

Samuël Delefortrie

**Optimizing the reliability of small-loop, frequency
domain electromagnetic survey data**

PhD supervisors	Prof. dr. ir. Marc Van Meirvenne and Dr. Philippe De Smedt Department of Soil Management, Faculty of Bioscience Engineering Ghent University
Dean	Prof. dr. ir. Marc Van Meirvenne
Rector	Prof. dr. Anne De Paepe

Samuël Delefortrie

**Optimizing the reliability of small-loop, frequency
domain electromagnetic survey data**

Thesis submitted in fulfilment of the requirements for the degree of Doctor (PhD) in
Applied Biological Sciences

Dutch translation of the title:

De betrouwbaarheid van small-loop, frequentie domein EM survey data op punt zetten

Citation:

Delefortrie, S., 2016. Optimizing the reliability of small-loop, frequency domain electromagnetic survey data, PhD thesis, Ghent University.

Notice of Rights

The author and the PhD supervisor give the authorisation to consult and to copy parts of this work for personal use only. Every other use is subject to the copyright laws. Permission to reproduce any material contained in this work in any form and by any means, should be obtained from the author.

Contents

Contents	xi
List of abbreviations and acronyms	xiii
Summary	xvii
Samenvatting (Dutch)	xix
Chapter 1 Introduction	21
1.1 Small-loop FDEM: merits and research significance	22
1.2 Research objectives	24
1.3 Structure of thesis	26
Chapter 2 Small-loop frequency domain electromagnetics	27
2.1 General EM principles	28
2.2 Small-loop FDEM operating principles	31
2.3 What's in a name?	42
Chapter 3 Positional accuracy surveys	45
3.1 Importance offsets between positioning and sensor data	47
3.2 Materials and methods	49
3.3 Results and discussion	58
3.4 Conclusions	68
3.5 Matlab scripts	69
Chapter 4 Signal instability	77
4.1 Drift compensation in literature	78
4.2 Materials and methods	80
4.3 Drift characterization and tie-line method evaluation	85
4.4 Tie-line vs. repeat line method	99
4.5 Discussion	105
4.6 Conclusions	107
4.7 Matlab scripts	107

Chapter 5	Absolute calibration and potential for conductivity modelling	115
5.1	Aim and strategy	116
5.2	Materials and methods	117
5.3	Results and discussion	126
5.4	Conclusions and future perspectives	136
Chapter 6	Absolute calibration and potential for susceptibility modelling	139
6.1	Problem statement and aim	140
6.2	Materials and methods	141
6.3	Results and discussion	149
6.4	Conclusions	158
Chapter 7	Final conclusions and perspectives	159
References		163
Curriculum vitae		173

List of abbreviations and acronyms

3D	three-dimensional
AC	alternating current
AMT	audio MT
B	magnetic induction (magnetic field associated with currents)
CPT	cone penetration testing
CSAMT	controlled source AMT
CSEM	controlled source EM
DC	direct current
DEM	digital elevation model
DOE	depth of exploration
DOI	depth of investigation
E	electric field
EC	electrical conductivity
ECa	apparent electrical conductivity
EM	electromagnetic
emf	electromotive force
EMI	electromagnetic induction
ERT	electrical resistivity tomography
$\mathbf{F}_{\text{electric}}$	electric force
$\mathbf{F}_{\text{magnetic}}$	magnetic force
FDEM/FEM	frequency domain EM
GPR	ground penetrating radar
GUI	graphical user interface
H	magnetic field strength

HCP	horizontal coplanar coil pair geometry
HEM	helicopter EM (aerial EM)
I	electric current
IP	induced polarization
LIN	low induction number
M	magnetization (magnetic dipole moment per unit volume)
MT	magnetotellurics
NRM	natural remanent magnetization
ppt	parts per thousand
PRP	perpendicular coil pair geometry
Q	electric charge
QP	quadrature-phase
R	resistance
RTK	real time kinematics
RMSE	root mean squared error
Sus	susceptibility
TDEM/TEM	time-domain EM
U	electric potential difference
UXO	unexploded ordnance
VCP	vertical coplanar coil pair geometry
VLF	very low frequency EM
β	induction number
δ	skin depth
ϵ	dielectric permittivity
κ	magnetic susceptibility
μ	magnetic permeability
ρ	electrical resistivity

σ	electrical conductivity
σ_a	apparent electrical conductivity
ω	angular wave frequency

Summary

Man has many desires. Some are lofty, like the desire to explore. This drive is why researchers have pursued greater knowledge and marvelled at nature's laws and mechanisms. One of the frontiers has been the surface of the planet we inhabit. For millennia, this frontier has been crossed by use of first hand observations and imagination. Since centuries, it has been possible to couple knowledge of physics with instrumental observations as well and the field of *geophysics* has been revolutionized.

Propelled by the momentum created by technological advances, EM methods have found a widespread application (among other geophysical methods) and they are increasingly used in an attempt to provide detailed subsurface information. In this work, one specific EM method, the *small-loop, frequency domain EM (FDEM) method*, is studied. Furthermore, the focus is on FDEM survey data, which refers to the collection of geophysical data for spatial studies. An increase in reliability of such data is pursued, which is of interest as optimizing the data reliability would allow to build more accurate subsurface conductivity and susceptibility models within a short timeframe. To further this aim, survey data were looked at critically to discern problematic areas and error sources. Following, assessments were made as well as attempts to (incrementally) improve the survey set-up, survey execution and processing schemes. Area survey data are collected for a wide array of (near-surface) applications including soil science (soil mapping, precision agriculture, ...), UXO detection, hydrogeology, etc.

It was possible to evaluate the positional accuracy, signal stability and absolute calibration of FDEM survey data. Following, efficient corrections were proposed and evaluated. Processing steps necessary to obtain accurate conductivity models were also looked into and a discussion on the accuracy potential is present. In addition, the depth of investigation was researched. Finally, a basic processing scheme, generalized for (generic) FDEM survey data *optimization* is proposed.

Samenvatting (Dutch)

De mens heeft vele verlangens. Sommige van deze verlangens zijn verheven, zoals het verlangen om te ontdekken. En juist hierdoor hebben onderzoekers naar de natuur gekeken en inzichten nagestreefd. Eén van de grenzen om te doorbreken was en blijft de oppervlakte van de planeet waar we leven. Sinds mensenheugenis is deze grens overschreden door middel van observaties en verbeelding. Sedert enkele eeuwen is het ook mogelijk om instrumentele observaties te koppelen aan een groeiende kennis van fysische verschijnselen. Dit heeft geleid tot een revolutie in het domein van de *geofysica*.

Voortgestuwd door het momentum dat was gecreëerd door technologische vooruitgang zijn EM methoden (onder andere) aangewend in vele toepassingsgebieden. Deze worden in toenemende mate gebruikt met als doel het bekomen van gedetailleerde informatie van de ondergrond. In dit werk wordt één specifieke EM methode belicht: de *small-loop, frequentie domein EM methode (FDEM)*. Het doel is de betrouwbaarheid van small-loop FDEM survey data optimaliseren. Met survey data wordt bedoeld: het verzamelen van geofysische data binnen een ruimtelijk kader. Dit is van nut aangezien meer betrouwbare data het zou toelaten om nauwkeurige conductiviteit- en susceptibiliteit modellen te bekomen binnen een korte tijd. Hiertoe zijn survey data kritisch beschouwd om de oorsprongen van foutbronnen te lokaliseren. Hieropvolgend, zijn beoordelingen uitgevoerd en is er gepoogd om de survey set-up, survey uitvoering en data verwerking te verbeteren. Survey data (en meer bepaald oppervlakte metingen) worden verzameld voor een brede waaier aan toepassingen zoals bodemkundige (precisie landbouw, bodeminventarisatie, ...), (hydro)geologische en ander (UXO detectie, ...).

Het is mogelijk gebleken om de nauwkeurigheid van positionering, signaal stabiliteit en absolute calibratie van FDEM survey te evalueren en correcties voor te stellen. De verwerking nodig om nauwkeurige conductiviteitsmodellen te bekomen is eveneens onderzocht en een discussie over het potentieel m.b.t. nauwkeurige modellen is aanwezig. Bijkomend, is de attenuatie van het signaal onder verschillende bodem-omstandigheden geëvalueerd. Tot slot wordt een verwerkingsschema, veralgemeend voor *optimalisatie* van (generische) FDEM survey data, voorgesteld.

Chapter 1

Introduction

“To see a world in a grain of sand
and a heaven in a wild flower,
hold infinity in the palm of your hand
and eternity in an hour.”

-- William Blake,
“Auguries of Innocence”

1.1 Small-loop FDEM: merits and research significance

The electrical method was one of the first geophysical exploration techniques to become widely used at the end of the 1920s in oil, gas, and mineral-deposit exploration. The development of a practical use of electrical fields to explore the earth's interior began with the pioneering work of the Schlumberger brothers (Zhdanov, 2010). Also during the 1920s the EM ground method was developed in Canada, the USA and Scandinavia for mining applications (Telford et al., 1991). In the decades since, the EM method has branched, with many different techniques now possible. Reviewing this particular branch, Everett (2012) recently asserted:

“Near-surface applied electromagnetic geophysics is experiencing an explosive period of growth with many innovative techniques and applications presently emergent and others certain to be forthcoming.”

One of the developments has been the small-loop Frequency Domain EM (FDEM) geophysical method. This technique is designed and used for near-surface investigations, which pertain to the outermost part of the earth's crust. Though a precise depth limit for near-surface applications is not set, Butler (2005) states:

“Many practitioners would argue that a significant percentage of near-surface applications involve depths of interest less than 10 meters, and most practitioners would agree that most common applications of near-surface geophysics involve depths less than 30 meters. However, there are occasional investigations to depths of 300 meters or more”.

The near-surface is of interest because it is the part of the crust that man interacts with.

Small-loop FDEM instruments employ one or several frequencies (in the low frequency range) that are transmitted by one or more (active) transmitter coils and picked up by one or several (passive) receiver coils. The coils are separated by a relatively small distance (usually some decimetres to several metres). Hence the small-loop denomination. Figure 2.7 situates the method relative to other geophysical methods.

The technique is applied for surveying because it allows mapping subsurface electrical conductivity and magnetic susceptibility. The surveys are generally land-based and the instruments have the following advantages (with regards to surveying):

- a simple design (allowing for relatively cheap and sturdy instruments);
- non-invasive data collection;
- good speed potential.

As a result surveys can be performed on-the-go to collect high-resolution data. The main (near-surface) application areas are listed in Table 1.1. Generally, the main uses are localizing specific features (detected as anomalies) and deriving subsurface variables from obtained conductivity or susceptibility maps. According to Butler (2005) near-surface application areas are characterized and distinguished by: shallow depths of investigation, requirements for high resolution, the possibility of near-real-time confirmation and survey choices and execution that are subject to health and safety concerns and constrained by regulations.

Table. 1.1 Main application areas of the small-loop FDEM technique. Listings of specific applications are not exhaustive and are given as examples. For a more exhaustive overview of selected applications see Everett (2012).

<i>Application area</i>	<i>Examples of applications</i>	<i>E.g.</i>
Archaeology	Locating and assessing archaeological sites	Tabbagh, 1986
	Locating artifacts/building foundations/...	Simpson et al., 2010
	Reconstructing human-landscape interactions	De Smedt et al., 2011
Environment	Locating buried cultural features	Bongiovanni et al., 2008
	Contaminant mapping	Martinelli et al., 2012
Geology	Stratigraphy	Shah et al., 2008
Hydrogeology	Mapping preferential flow paths	Triantafilis et al., 2013
	Groundwater quality assessment	Davies et al., 2014
Soils and agriculture	Mapping of moisture content/salinity	Lesch et al., 1992; Sheets and Hendrickx, 1995
	Clay content estimation	Saey et al., 2009
	Soil compaction	Islam et al., 2014
	Peat layer mapping	Altdorff et al., 2016
UXO	UXO characterization	Huang et al., 2007

It is remarked that there are alternative techniques which can be used for conductivity or susceptibility mapping. Yet no one technique is superior for all intents and purposes: each technique has shortcomings and limitations. Therefore, when designing a survey, the selection of technique(s) should be based on the target depth, target nature and survey requirements.

On the general philosophy of planning geophysical surveys, Reynolds (1997) adds:

“There is no short-cut to developing a good survey style; only by careful survey planning backed by a sound knowledge of the geophysical methods and their operating principles, can cost-effective and efficient surveys be undertaken within the prevalent constraints.”

The study of the potential and of the limitations of geophysical techniques is the subject of geophysics and scientific research contributes to a sound knowledge of the methods. Furthermore, Reynolds (1997) advocates the use of scientific trials:

“The success of geophysical methods can be very site-specific and scientifically-designed trials of adequate duration may be very worthwhile to provide confidence that the techniques chosen will work or that the survey design needs modifying in order to optimise the main survey.”

These remarks are still valid and as techniques and the way they are implemented evolve, continuous assessment of the technique’s potential is necessary. Only then can the full extent of their applicability be realized. This work should be read with this consideration in mind.

1.2 Research objectives

The main research objective consists of pursuing an increase in reliability of small-loop FDEM survey data. This is of interest as optimizing the reliability would allow to build more accurate subsurface conductivity and susceptibility models within a relatively short timeframe. To further this aim, FDEM surveys were looked at critically to discern problematic areas and error sources. Following, assessments were made as well as attempts to (incrementally) improve the survey set-up, survey execution and processing schemes.

Specific objectives, with regards to small-loop FDEM data, are to:

1. maximize positional accuracy;
2. assess signal stability and establish a calibration procedure;
3. assess absolute calibration;
4. investigate the depth of investigation;
5. obtain accurate conductivity and susceptibility models of the subsurface and determine the impact of systematic errors.
6. Fulfilling these objectives would allow a more quantitative use of the FDEM data for any given application.

It is remarked that there is a body of scientific literature available concerning these objectives. In addition, some of the applied methodologies are based on existing work or may merely constitute a novel application instead of a completely novel approach. Therefore, each objective will also entail providing references, an (concise) overview of made progress and a motivation for looking further into these matters.

Objective 1: Positional accuracy

To process spatially variable information collected during a survey, positioning systems are used. Severe positional inaccuracy (of the measurements) can result from errors in relating sensor data and position data when a spatial and/or temporal offset is present. These error sources are not well documented and measurement locations are often poorly estimated or not corrected during data processing when there is a spatial offset. A communication delay between logging device and positioning system or sensor can exacerbate the spatial offset problem and becomes more important with increasing survey speed. If spatial and temporal offsets adversely affect the required accuracy, a correction is necessary to maximize the reliability of the data. Therefore, accounting for (horizontal) spatial and temporal offsets between sensor and positioning data was researched.

Objective 2: Signal stability

Systematic measurement errors may impede realization of the full potential of FDEM data and can persist despite “factory” calibration of the instruments. FDEM instrument responses can suffer from signal instability (or drift) regardless of the application, meaning that a response at a given location may vary over time, despite no appreciable changes above or underneath the surface. Signal drift is unwanted as it may introduce global trends or abrupt changes in the data not related to the underground. To optimize data reliability it was recognized that the impact of drift needed to be assessed. A secondary objective is to establish an efficient drift correction procedure.

Objective 3: Absolute calibration

Another possible systematic error is due to incorrect absolute calibration. It is noted that correcting for signal instability may introduce or alter levelling offsets. To assess the impact of levelling offsets and correct for them, they first need to be detected. To this aim, accurate ancillary data were used to compare forward modelled and measured responses. Calibration is of the utmost importance when comparing data collected using several geophysical methods and when comparing data collected using the same technique at different times or with different instruments.

Objective 4: Depth of investigation

Due to the diffusive nature of the EM fields and the dependency of field attenuation on conductivity distribution that are employed when using the technique, the depth of investigation can be quite ambiguous. It is therefore an objective to examine the impact of high conductivity (of the subsurface) on the depth of investigation.

Objective 5: Validating quantative conductivity and susceptibility models

When striving to attain quantitative information on subsurface conductivity and susceptibility, FDEM data need to be inverted and, in doing so, systematic errors can impact the inversion results. The research objective is to obtain inverted FDEM data and validate the results before and after absolute calibration.

1.3 Structure of thesis

This work is divided into six chapters (see Fig. 1.1). Chapter two presents a concise FDEM background (including general EM principles as well as FDEM operating principles). Chapter 3 explores the first objective, i.e. the positional accuracy of FDEM data. It includes an evaluation of different methods for correcting spatial offsets, makes the case for the importance of temporal offsets and details the code used for applying different spatial offset corrections. Chapter 4 consists of the characterization and evaluation of FDEM signal instability and deals with a general purpose correction procedure to identify and tackle the issue. Chapter 5 involves a case study, designed specifically for studying the absolute calibration of FDEM responses as well as the effect of conductivity variations on the depth of investigation. Using accurate validation data, the accuracy potential of inverted FDEM data is touched on. Lastly, chapter 6, summarizes the main conclusions and holds the final perspectives.

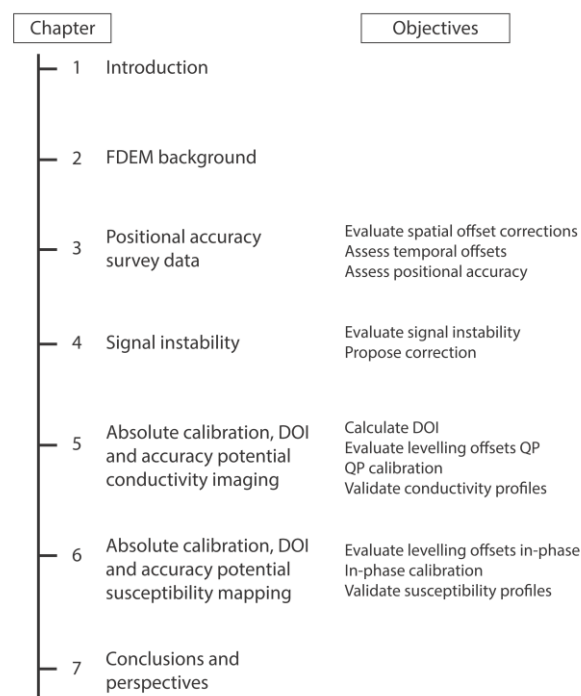


Fig. 1.1 Structure of the thesis

Chapter 2

Small-loop frequency domain electromagnetics

“All things by a mortal power,
Near or far
Hiddenly
To each other linked are,
That thou canst not stir a flower
Without the troubling of a star”

-- Francis Thompson,
“The Mistress of Vision”

2.1 General EM principles

In this section, some basic EM principles are provided as a background. For more detailed information on the physics of the electromagnetic induction method see Keller and Frischknecht (1966), Wait (1982) and West and Macnae (1991).

Electric and magnetic fields and properties

Electric and magnetic fields result from movements of electrically charged objects. The most direct expression of the distribution of (total) electric charge density (\mathbf{Q}), expressed in Coulomb, is the Coulomb law (here in differential form):

$$\nabla \cdot \epsilon_0 \mathbf{E} = \mathbf{Q} \quad (2.1.1)$$

with ' $\nabla \cdot$ ' the divergence operator and ϵ_0 the dielectric permittivity of free space (also called dielectric constant). The dielectric permittivity ϵ of a material, expressed in Farads per meter (F/m), is the measure of resistance to the formation of an electric field \mathbf{E} and ϵ_0 is the permittivity of free space.

\mathbf{E} , expressed in Volts per meter (V/m), can be defined as a vector field surrounding the electrically charged particles. Within this field, other electrically charged particles would be subject to an electrical force $\mathbf{F}_{\text{electric}}$, expressed in Newtons, defined by Coulomb's law as:

$$\mathbf{F}_{\text{electric}} = k \frac{\mathbf{Q}_1 \mathbf{Q}_2}{r^2} \quad (2.1.2)$$

with \mathbf{Q}_1 and \mathbf{Q}_2 the magnitude of two electrically charged particles, r the distance between them and k Coulomb's constant. In a conductive medium, the electric charges can flow from one place to another when there is an electrical potential difference U , expressed in Volts (V). This flow of charge constitutes an electric current I , expressed in Ampère (A). The relationship between the potential difference between two points and I is described in Ohm's law (with R the resistance in Ω):

$$R = \frac{U}{I} \quad (2.1.3)$$

The electrical resistivity ρ quantifies how strongly the conductor opposes the electrical current and is expressed in Ohms meter (Ωm):

$$\rho = R \frac{a}{l} \quad (2.1.4)$$

with l the length of the conductor in meters and a the cross-sectional area in units of meters squared. Electrical conductivity (σ), is the reciprocal of ρ and expresses how easily current can pass through a material. Its unit is Siemens per meter (S/m).

When in motion, charges generate another type of field in an electrical conductive medium. This is the induced magnetic field \mathbf{B} , expressed in Tesla (T), and can again be defined as a vector field surrounding the electrically charged particles. \mathbf{B} results from the moving electrical charges and the magnetic moment and ‘spin’ of elementary particles (i.e. particles without any substructure), and is commonly referred to as the magnetic induction or the magnetic flux density. Within this magnetic field \mathbf{B} , electrically charged particles are subject to a magnetic force $\mathbf{F}_{\text{magnetic}}$:

$$\mathbf{F}_{\text{magnetic}} = Q\mathbf{v} \times \mathbf{B} \quad (2.1.5)$$

Whereas an electric force depends only on the value of the total charge Q , the magnetic force also depends on the velocity v of the charge. However, ambiguities arise when defining the induced magnetic field outside of a vacuum, where magnetic materials themselves contribute internal magnetic fields to the total magnetic field. This makes it difficult to interpret which part of the total magnetic field comes from the external charges and current, and what the material itself contributes. Therefore, it is common to talk about the magnetic field strength \mathbf{H} (expressed in Ampère per meter (A/m)), which is independent of the medium in which the magnetic field is located and is given by:

$$\mathbf{H} = \frac{\mathbf{B}}{\mu} \quad (2.1.6)$$

with μ the magnetic permeability of the medium, expressed in Newton per Ampère squared (N A^{-2}). Based on μ (the degree of magnetization that a material obtains in response to an applied magnetic field), materials can be classified into diamagnetic, paramagnetic and ferromagnetic substances (Dearing, 1999). Diamagnetic materials have a permeability μ less than the permeability of free space (μ_0 ; also known as the magnetic constant), and are repelled by magnets. Materials that minutely increase \mathbf{H} are called paramagnetic and have a permeability larger than μ_0 . When a substance has a permeability hundreds or thousands times larger than μ_0 , it is classified as ferromagnetic.

The contribution of materials to an applied external magnetic field is called the magnetic susceptibility κ , which is dependent on \mathbf{H} and the strength of the magnetization \mathbf{M} (or magnetic dipole moment per unit volume), both expressed in A/m:

$$\kappa = \frac{\mathbf{M}}{\mathbf{H}} \quad (2.1.7)$$

As both \mathbf{M} and \mathbf{H} have the same unit, κ is dimensionless and expressed as the volume magnetic susceptibility or magnetic susceptibility per unit volume. Sometimes SI is written behind the

magnetic susceptibility value, referring to the international system of units (Système International d'Unités). The relationship with the between μ and κ , can be described by:

$$\mu = \mu_0(1 + \kappa) \quad (2.1.8)$$

with $(1 + \kappa)$ defined as the relative permeability of a material.

Electromagnetism

Electromagnetic fields are a manifestation of the interaction between electric charges: moving charges generate electric and magnetic fields, which exert an electrical and magnetic force on charged particles within their field of influence. Combined, these forces lead to the total electromagnetic force F , acting on a particle of electric charge Q as defined by the Lorentz force law:

$$\mathbf{F}_{\text{magnetic}} = Q\mathbf{v} \times \mathbf{B} \quad (2.1.9)$$

How electric charges act as a source for electromagnetic fields and how electric and magnetic fields affect each other, is described by Maxwell's equations. For geophysical EM methods, Maxwell's interpretation of Ampère's law and Faraday's law are of particular importance. Maxwell-Ampère's law describes how an electrical field \mathbf{E} induces a magnetic field \mathbf{H} . In a homogeneous, isotropic medium with an electrical conductivity σ and an electrical permittivity ε this can results in (in differential form):

$$\nabla \times \mathbf{H} = \sigma \mathbf{E} + \varepsilon \frac{\partial \mathbf{E}}{\partial t} \quad (2.1.10)$$

with $\partial/\partial t$ the partial derivative with respect to time (t) and ' $\nabla \times$ ' the curl operator. The right hand side of the equation represents the total current, which is the sum of the ohmic current flow ($\sigma \mathbf{E}$) and the displacement current ($\varepsilon \partial \mathbf{E} / \partial t$). This is particularly relevant for geophysical EM methods using low-frequencies since any magnetic field generated by the displacement current can usually be neglected at low frequencies.

The Faraday law describes how an electric field is created by a time-varying magnetic field. For a homogeneous, isotropic medium, this is given by:

$$\nabla \times \mathbf{E} = -\frac{\partial \mathbf{B}}{\partial t} \quad (2.1.11)$$

2.2 Small-loop FDEM operating principles

Loops

Electromagnetic coils (or loops) are electrical conductors in the shape of a coil, spiral or helix which are used in applications where electric currents interact with magnetic fields. An electric current can be passed through the wire of the coil to generate a magnetic field. Conversely, an external time-varying magnetic field passing through the interior of the coil generates an emf (electromotive force) in the conductor (Telford et al., 1991).

Following Ampère's law, a current through any conductor creates a circular magnetic field around the conductor. Coil shapes are used because they increase the magnetic field strength produced by a given current due to the magnetic fields generated by the separate turns of wire superposing (all pass through the centre of the coil) to produce a strong field there. Field strength is therefore proportional to number of turns. Following Faraday's law, a changing external magnetic flux induces a voltage in a conductor such as a wire. Again, the induced voltage can be increased by using a wound coil since the field lines intersect the circuit multiple times.

Some distinctions that can be made between EM coils are based on the:

- type of core: (ferro)magnetic cores can be used to multiply the magnetic field strength of a core, air cores denote coils without a magnetic core (i.e. no core or a nonmagnetic core);
- application of direct or alternating current (DC or AC);
- frequency of the AC.

When a stable, direct current is applied to a wound coil and the magnetization is also static, the (three-dimensional) field that is generated remains constant (Fig. 2.1). The magnetic field vectors of an EM coil can then be calculated using the Biot-Savart Law (Fig. 2.2).

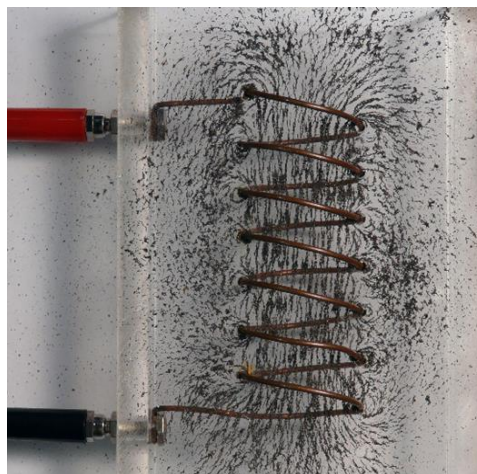


Fig. 2.1 Illustration of the magnetic field of a solenoid, visualised by use of iron fillings. (source: MIT physics demo, <https://www.flickr.com/photos/physicsdemos/>)

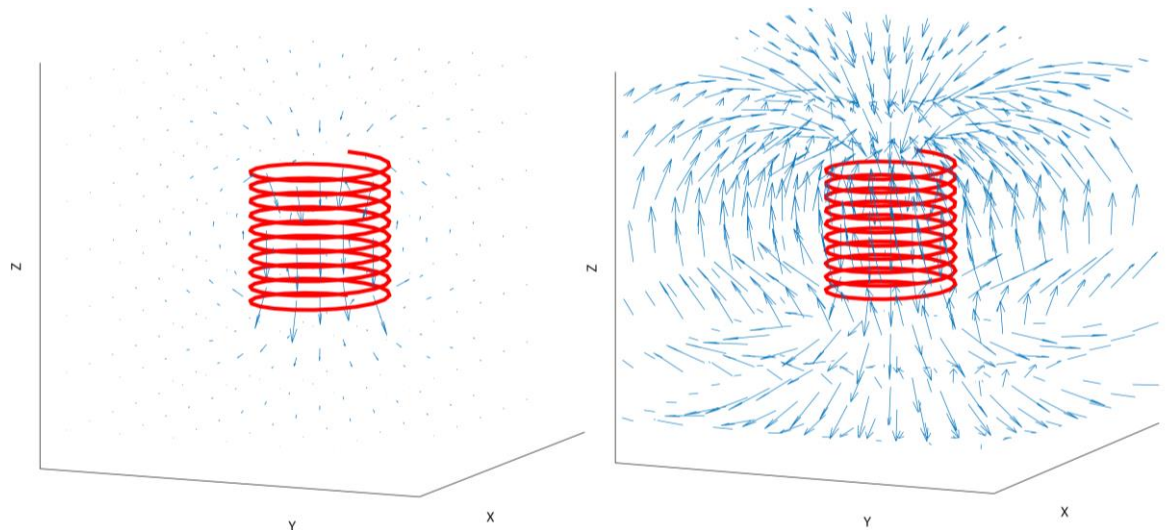


Fig. 2.2 3D illustration of the magnetic field of an air-core solenoid, calculated using the Biot-Savart Law. The (air core) solenoid is red and the magnetic field is depicted by a blue quiver plot which visualizes the field vectors with (left) the magnitude of the magnetic field and (right) the normalized field.

In contrast to the magnetostatic case (which is a special case of Maxwell's equations), applying an alternating current will cause polarity reversals at a specified rate (since the generated magnetic dipole will change orientation when the current flow reverses. Thus, calculating the generated magnetic field would require solving Maxwell's equations and a 4D representation.). For low frequencies (as are applied for the FDEM technique) the oscillating fields can be seen as magnetoquasistatic fields (which can be distinguished from the more commonly used far-field electromagnetic radiation).

Transmitter loop

In constructing portable FDEM systems, transmitters are an integral part. They generate the 'primary' magnetic field (\mathbf{H}_p): i.e. a time-varying EM signal with known waveform. Therefore, when using a controlled source method, the time variation of the primary field is controlled by the geophysicist. According to Telford et al. (1991) mobile transmitters can consist of:

- air-core coils: multiple-turn coils (100 turns or more) wound on insulating frames (diameter <1 m) or single turn coils of heavy gauge wire;
- a helical coil (or solenoid) wound on a ferrite or other high-permeability core (allowing a greatly reduced cross-section).

When a transmitter coil is placed near the subsurface, electrical currents (eddy currents) are induced in the subsurface according to Faraday's law. A current is possible due to the presence of mobile charge carriers. A geologic medium under investigation, which could include a conductive target and its host, is assumed to be electrically neutral (meaning any volume of the subsurface contains equal

numbers of positive and negative charge carriers). Only mobile charges play a role in shaping the low-frequency EM response (see Larsson, 2007). According to Everett (2013) a voltage develops along any arbitrary closed path within a conducting body that is exposed to a time-varying magnetic field. The mobile charge carriers migrate with an average drift velocity in response to the applied changing magnetic flux and the electrical conductivity σ is related to the density and mobility of the charge carriers by:

$$\sigma = nqm \quad (2.2.1)$$

where n is the number density of mobile charges, q is the mobile charge carrier, and m is the charge-carrier mobility (Gueguen and Palciauskas, 1994). The drift of mobile charges constitutes the induced current that acts as a secondary electromagnetic field (\mathbf{H}_s). In addition, magnetic particles in the soil become magnetized, or magnetically polarized by the primary field (Keller and Frischknecht, 1966), whereby the intensity of magnetization \mathbf{M} is determined by κ , following eq. 2.1.7. Consequently, magnetic polarization can also contribute to the characteristics of the secondary magnetic field.

Loop-loop system

Placing an additional coil or solenoid in the presence of an oscillating magnetic field, can cause a current to be induced in the wire. The following applies:

- a current is induced when the normal component of the magnetic field, parallel with the axis of the coil, is not zero;
- if the magnetic field does not vary, a current will no longer be induced;
- the voltage of the induced current is proportional to the magnetic field strength.

Like transmitter coils, receiver coils are made to be portable meaning they generally have many turns of fine wire and are used in conjunction with high-permeability cores (Telford et al., 1991). When a receiver is placed near the transmitting coil and the measured medium, both primary and secondary magnetic fields induce a current in the receiver, meaning that the resulting total field is picked up (with the secondary magnetic field superimposed on the primary field). The magnitude of the voltage is then directly proportional to the rate of change of the induced magnetic fields. Since it takes a finite amount of time to generate eddy currents and induce magnetic polarization in the subsurface in response to a time-varying magnetic field, a phase lag occurs between the primary and secondary magnetic field at the receiver coil (Beck, 1981). Therefore, the resulting total field has the same frequency as the primary field but differs in intensity, direction and phase.

The total field can be described as a complex-valued function consisting of both real and imaginary parts. The real part, which has the same phase as the primary field, is called in-phase. The imaginary

part, which shows a 90-degree phase difference from the transmitted signal, is called out-of-phase, outphase, or quadrature. When surveying, the magnetic part of the resulting electromagnetic (EM) field is detected by the receiver coil. Usually, the harmonic data are then sampled for the quadrature-phase (QP) and in-phase components of the ratio between the secondary and primary magnetic fields:

$$\text{in-phase} = \text{Re} \left(\frac{\mathbf{H}_s}{\mathbf{H}_p} \right) \quad (2.2.2)$$

$$\text{quadrature-phase} = \text{Im} \left(\frac{\mathbf{H}_s}{\mathbf{H}_p} \right) \quad (2.2.3)$$

with \mathbf{H} the total magnetic field and

$$\mathbf{H}_s = \mathbf{H} - \mathbf{H}_p \quad (2.2.4)$$

which illustrates that the waveform of the primary field has to be accurately known. It is remarked that most systems only measure one component of the magnetic field; the vertical component \mathbf{H}_z , although it can be measured in three orthonormal directions.

To measure the primary field strength, (some) systems make use of ‘bucking coils’ in addition to transmitter and receiver coils. These coils sense the primary magnetic field exclusively (ideally) and are therefore employed to measure the primary magnetic field in a continuous way, allowing to subtract the actual, measured primary field from the total magnetic field instead of the assumed primary field. However, all systems are designed to (ideally) ensure a stable primary field with known waveform and known field strength.

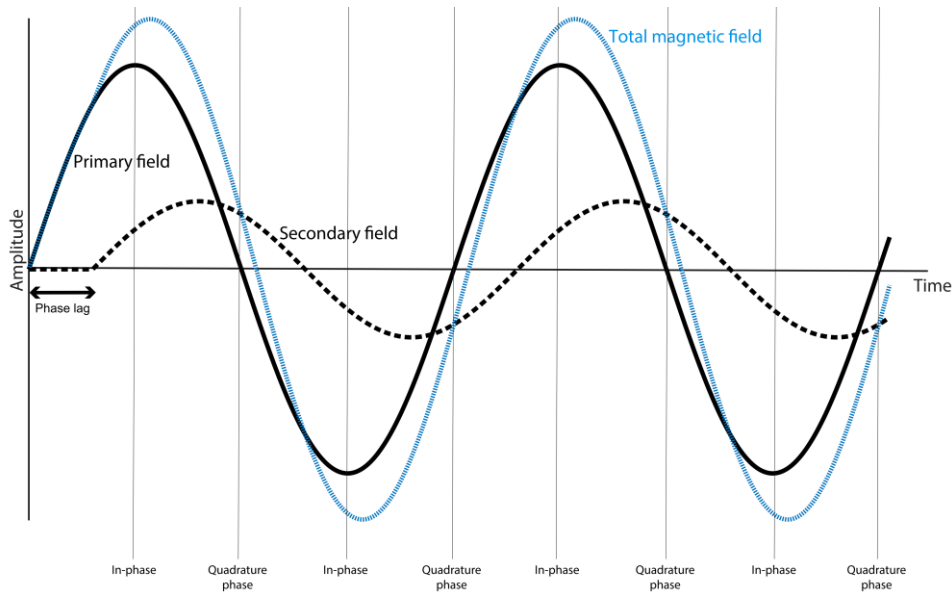


Fig. 2.4 Relationship between the primary (\mathbf{H}_p), secondary (\mathbf{H}_s) and total (\mathbf{H}) magnetic field, with indication of the in-phase and quadrature response.

The in-phase and quadrature responses are dimensionless and are usually expressed in parts per thousand (ppt) or parts per million (ppm). The response of the subsurface to the propagation of induced electromagnetic waves can then be used to deduce electric and magnetic properties of the measured subsurface volume. For transmitter-receiver separations greater than five loop diameters, the loops can be treated as a magnetic dipoles (Lange and Seidel, 2007).

Common coil orientations, or geometries, are the horizontal coplanar (HCP), the vertical coplanar (VCP) and the perpendicular (PRP) orientation (Fig. 2.5).

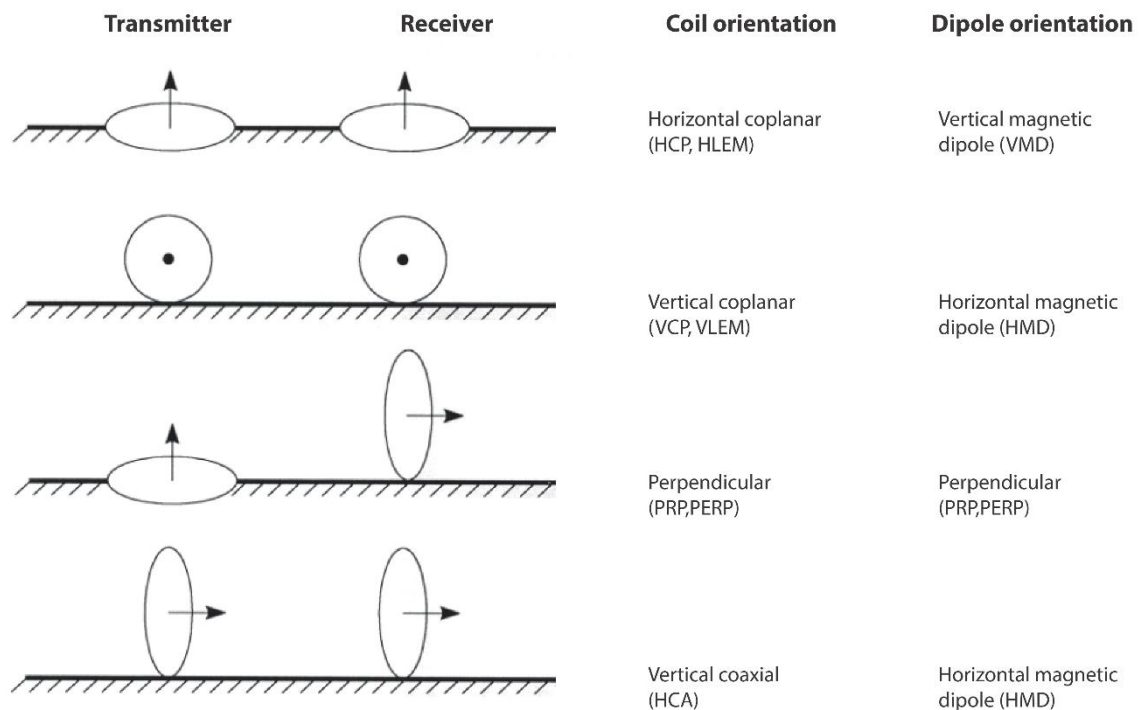


Fig. 2.5 Schematic representation of possible coil orientations. The dipole orientations are visualized and the names and abbreviations are listed. After Spies and Frischknecht (1991).

Commercially available systems

Details about the components and general make-up of FDEM systems are given by Telford et al. (1991) as well as Keller and Frischknecht (1966). In addition, general specifications such as coil configurations, EM frequency, etc. are detailed by the manufacturer: a summary of commercially available small-loop FDEM systems is given in Table 2.1.

Most systems make use of coils in the horizontal coplanar (HCP) geometry as it allows the largest depth of investigation for a given volume (cf. *infra*). Systems which allow any configuration and a variable coil separation (due to the coils not being housed in a fixed boom) allow flexibility but have

a lower survey speed potential, which is the main reason why they have been superseded by multi-receiver and multi-frequency instruments for most applications. The Dualem Inc. (Canada) instruments are multi-receivers that employ a dual geometry (both HCP and PRP coil configurations (e.g. Fig. 2.6).

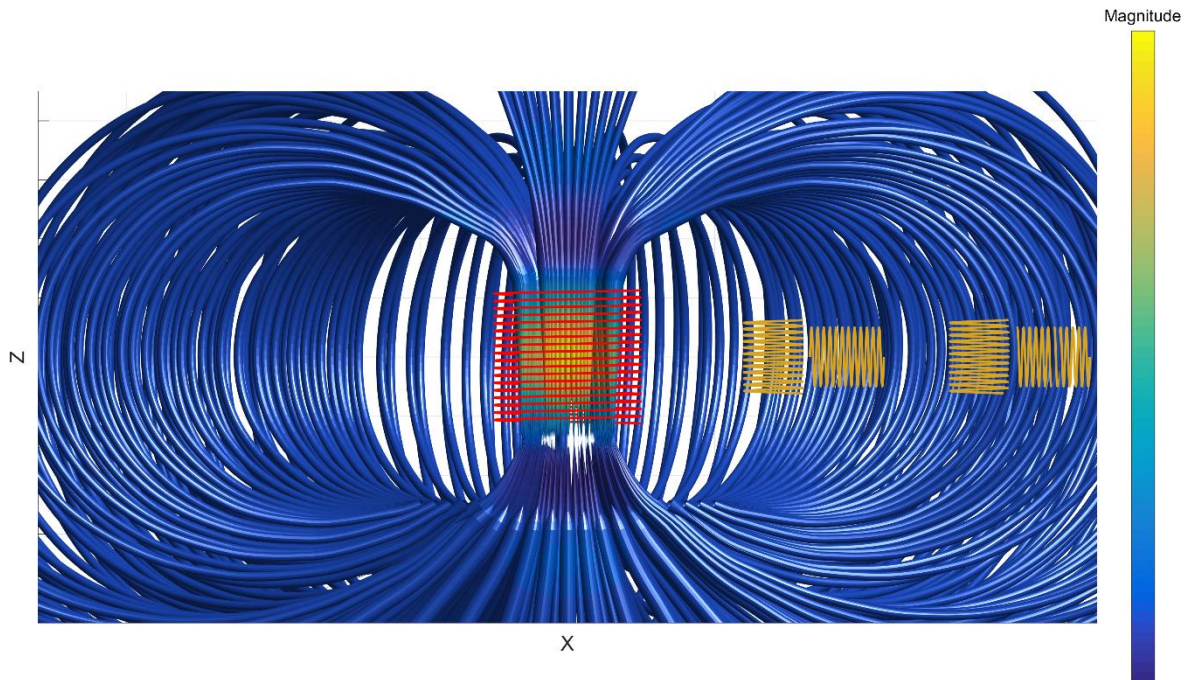


Fig. 2.6 Illustration of the Dualem 21S geometry. Coil configurations include 2 HCP configurations and 2 PRP configurations using one transmitter (red) and four receivers (yellow). The magnitude of the primary field was calculated using the Biot Savart Law (steady state magnetic field) and visualised using stream tubes.

Aside from transmitter and receiver loops the following components are required:

- An electronic oscillator (with amplifier) to provide a stable alternating current.
- A potentiometer or digital volt meter to measure the induced voltage. Its circuit may include a reference coil (or bucking coil), an attenuator and phase-shift compensation.
- Amplifiers to provide detectable signals.
- Temperature compensation circuitry.

Receiving coils and amplifiers can be tuned to the operating frequency to minimize signals due to atmospheric and power lines (Keller and Frischnecht, 1966).

All systems employ temperature compensation circuitry to obtain sufficiently stable measurements. Some insight of the importance of electronic temperature compensation can be gleaned from Mester et al. (2014) since they detail the calibration necessary to stabilize measurements of a FDEM prototype. Unfortunately, commercial manufacturers are not keen on providing exact information on how they establish factory calibration of their instruments (despite patents and copyright laws).

Table. 2.1 List of commercially available small-loop FDEM instruments. All coil separations listed under ‘coil configuration(s)’ are in m. Small-loop FDEM systems made for the sole purpose of metal detection have not been listed. Some companies also provide custom solutions.

Company	Small-loop FDEM system(s)	Frequency (kHz)	Coil configuration(s)	Remarks
Duaem Inc.	1S	9	1 HCP; 1.1 PRP	Can be used in VCP mode by rotating the instrument 90°: HCP --> VCP; PRP --> null
	2S		2 HCP; 2.1 PRP	
	21S		1 HCP; 1.1 PRP; 2 HCP; 2.1 PRP	
	21HS		0.5 HCP; 0.6 PRP; 1 HCP; 1.1 PRP; HCP2; 2..1 PRP	Can be fitted and calibrated with an internal GPS receiver (in this case the suffix ‘S’ is not added to instrument name).
	4S		4 HCP; 4.1 PRP	
	42S		HCP2; 2..1 PRP; 4 HCP; 4.1 PRP	
	421S		1 HCP; 1.1 PRP; HCP2; 2..1 PRP; 4 HCP; 4.1 PRP	
Geonics Ltd.	642S		HCP2; 2..1 PRP; 4 HCP; 4.1 PRP; 6 HCP; 6.1 PRP	
	EM-38-MK2	14.5	0.5 HCP; 1 HCP	Can be used in VCP mode by rotating the instrument 90°: HCP --> VCP
	EM-31-SH	9.8	2 HCP	
	EM-31-MK2	9.8	3.66 HCP	
	EM-34-3	6.4; 1.6; 0.4	10; 20; 40 m spacing between Tx and Rx	The coils can be used in any orientation since they are not housed in a fixed boom Same as EM-34-3 but with larger transmitter coil
	EM-34 XL	6.4; 1.6; 0.4	10; 20; 40 m spacing between Tx and Rx	
	EM-39(S)	39.2	0.5 HCA	Designed for borehole logging

Company	Small-loop FDEM system(s)	Frequency (kHz)	Coil configuration(s)	Remarks
GF instruments s.r.o.	CMD mini explorer	30	0.32 HCP; 0.71 HCP; 1.18 HCP	Can be used in VCP mode by rotating the instrument 90°: HCP --> VCP
	CMD tiny	60	0.45 HCP	
	CMD 1	10	0.98 HCP	
	CMD 2	10	1.89 HCP	
	CMD 4	10	3.77 HCP	
	CMD 6	10	5.79 HCP	
	CMD explorer	10	1.48 HCP; 2.82 HCP; 4.49 HCP	
	CMD DUO	0.925	10; 20; 40 m spacing between Tx and Rx	The coils can be used in any orientation since they are not housed in a fixed boom
Geophex Ltd.	GEM-2	0.03-93	1.66 HCP	Digital frequency synthesis; uses a bucking coil
GSSI Inc.	Profiler EMP-400	1-16	1.21 HCP	
IRIS instruments	PROMIS-10	0.11; 0.22; 0.44; 0.88; 1.76; 3.52; 7.04; 14.08; 28.16; 56.32	20-400 m spacing between Tx and Rx	Measures magnetic field components (Hx, Hy and Hz). The coils can be used in any orientation since they are not housed in a fixed boom
	PROMIS-4	0.11; 0.44; 1.76; 7.04; 28.16	10; 20; 40; 80 m spacing between Tx and Rx	

Investigation volume and depth of exploration limit

The investigation volume of FDEM measurements is influenced by:

- the distance between the transmitter and the receiver (coil separation);
- the orientation of the coils (coil geometry);
- propagation of the EM field in the subsurface;
- frequency of the transmitted EM signal.

The investigation volume is proportional with the distance between transmitter and receiver. It is also larger when the subsurface is more resistive (meaning conductive subsurface layers or objects can create a screening effect). The effect of the coil configuration (geometry) is harder to generalize. For each coil configuration, the relative weight of a subsurface (e.g. soil layers) to the sensor measurement can be expressed as a function of its depth z using Maxwell's equations and a given subsurface model.

Huang (2005) defines the depth of investigation (DOI) as a maximum depth at which a given target in a given host can be detected by a given sensor. He states that the DOI is affected by various properties of the target and host medium as well as factors related to the investigation modality, such as the sensor sensitivity, accuracy, frequency, coil spacing and configuration, ambient noise, data processing and interpretation methods. The DOI can be greater (i.e. under ideal conditions) or much less (i.e. under noisy conditions, e.g. high conductive host medium) than the skin depth. Unlike the well-defined skin depth, there is no definitive way to determine the DOI (Huang, 2005). The skin depth δ is defined as the depth at which the amplitude of an EM wave is attenuated to $1/e$ (37%) of its initial amplitude (Spies, 1989) and can be expressed as:

$$\delta = \sqrt{\frac{2}{\omega\mu\sigma}} \quad (2.2.5)$$

with ω the angular wave frequency ($2\pi f$), expressed in radians per second, μ the magnetic permeability and the electrical conductivity σ . In other words, the skin depth indicates the penetration depth of the electromagnetic signal, and is relative to the frequency of the EM wave and electrical conductivity of the subsurface.

Several approaches for the calculation of DOI have been presented:

- Estimating depth sensitivity responses for a given FDEM configuration (see Wait, 1962; Keller and Frischknecht, 1966; Callegary et al., 2007; Callegary et al., 2012) and applying a threshold value to the cumulative, and sometimes normalized) sensitivity response. Depth sensitivities are often calculated for a homogeneous subsurface and the 70% signal response is mostly used to derive the DOI (e.g. Allred et al., 2006; Abdu et al., 2007; Saey et al., 2009).

- Empirical formulas or tables which are based on model studies (e.g. Huang, 2005).
- Ward and Hohmann's (1988) method is based on the diffusion depth of a planar wave in a full-space.
- Oldenburg and Li (1999) use separate inversions with different parameters (with all things equal except the weight given to a reference model). By assessing the discrepancy between the inverted profiles they determine a DOI index.
- Christiansen and Auken (2012) proposed a method based on a recalculated sensitivity (Jacobian) matrix (during an inversion process). It can be used on any model type for which a sensitivity matrix can be calculated meaning it can be used for TEM or ERT surveys as well.

The profuse approaches illustrate the complexity of arriving at a single depth limit, which owes to the diffusive nature of low frequency EM methods. A very practical rule of thumb that can be applied is adopting the DOI provided by the manufacturer (which is generally the depth at which the cumulative sensitivity response is 70%, given a low-conductive homogeneous subsurface) and assuming it is almost halved when surveying high-conductive locations.

Deriving electrical and magnetic subsurface properties from FDEM measurements

Before detailing the derivation of subsurface electrical conductivity from FDEM responses, some definitions are in order. The electrical conductivity σ is used to denote the true electrical conductivity of a given subsurface volume. The apparent electrical conductivity σ_a is used to express the arithmetic average of σ within the sample volume of a FDEM measurement. Similarly, the apparent susceptibility κ_a can be defined as the arithmetic average of κ within the sample volume. The following applies:

- the σ_a and κ_a will depend on the subsurface conductivity and susceptibility, coil configuration, frequency, etc.;
- for a homogeneous subsurface $\sigma_a = \sigma$ and $\kappa_a = \kappa$ (assuming zero calibration errors and zero height of instrument);
- the σ_a is proportional to the QP response.
- the κ_a is proportional to the in-phase response.

Because both the FDEM responses and their derived, apparent subsurface properties are related to the FDEM sample volume, these data need to be inverted when striving to attain quantitative information on subsurface conductivity (or susceptibility).

The QP response of ground conductivity instruments is usually converted to apparent electrical conductivity, using the low-induction-number (LIN) approximation as formulated by McNeill (1980, Geonics Ltd., Technical Note 5):

$$\text{LIN } \sigma_a(\text{approximated } \sigma_a) = \frac{2}{\pi f s^2 \mu_0} \cdot \text{QP} \quad (2.2.6)$$

where f is the frequency (Hz), s is the coil separation (m) and μ_0 is the magnetic permeability of free space ($4 \pi 10^{-7}$ H/m). Within LIN conditions, the QP response is linearly proportional to σ_a . An instrument elevation of zero is assumed and the LIN approximation is no longer valid for large coil separations and/or high conductivities. As the subsurface conductivity increases, the skin depth decreases causing the induction number (defined as the ratio of the coil separation s over the skin depth) to rise. This effect is enhanced with increasing intercoil spacing. At high conductivities the LIN σ_a therefore becomes biased as the σ_a is increasingly underestimated for a given frequency and intercoil spacing. This shortcoming can be addressed by calculating the deviation from a linear relationship and correcting for it using (non-linearly approximated) tabulations or calculations of the FDEM responses with increasing induction number (Beamish 2011; Delefortrie et al., 2014a). Another approach consists of using both QP and in-phase responses to attain robust apparent conductivities (Guillemoteau et al., 2015).

The σ_a (LIN or otherwise) data can then be inverted. Another possibility is bypassing conversion of the responses altogether, and inverting QP and in-phase to obtain estimates of subsurface conductivity and/or susceptibility at different depths (Farquharson et al., 2003).

TDEM systems

Time-domain electromagnetics (or transient electromagnetics; abbreviated as TEM or TDEM) utilise transient pulses (instead of a continuous, fixed frequency signal) and measure the response decay for several frequencies. The transmitter may consist of a coil or a wire and there is a high customization potential with regards to the configuration. While there are many parallels with FDEM systems, the frequency range dimension and time series calibration do not easily allow a unified approach with regards to calibration.

2.3 What's in a name?

Ideally, names of scientific methods are well-defined, unambiguous and universally adopted. Unfortunately, clear definitions are sometimes lacking and various denominations are invariably used. To avoid (potential) confusion, a classification of prevalent EM techniques and possible denominations is given. A definition is also provided:

Small-loop FDEM is a technique that produces a time-varying electromagnetic field, thereby inducing EM fields in the subsurface. In its most simple configuration a transmitter coil produces a primary field with known waveform (using a fixed frequency), while a receiver coil picks up the total magnetic field, consisting of the primary and induced field. The distance between the coils is relatively small (usually several decimetres to several metres) and the frequency is relatively low (in the kHz range). Several frequencies and/or coil configurations are possible. Per measurement one transmitter is active.

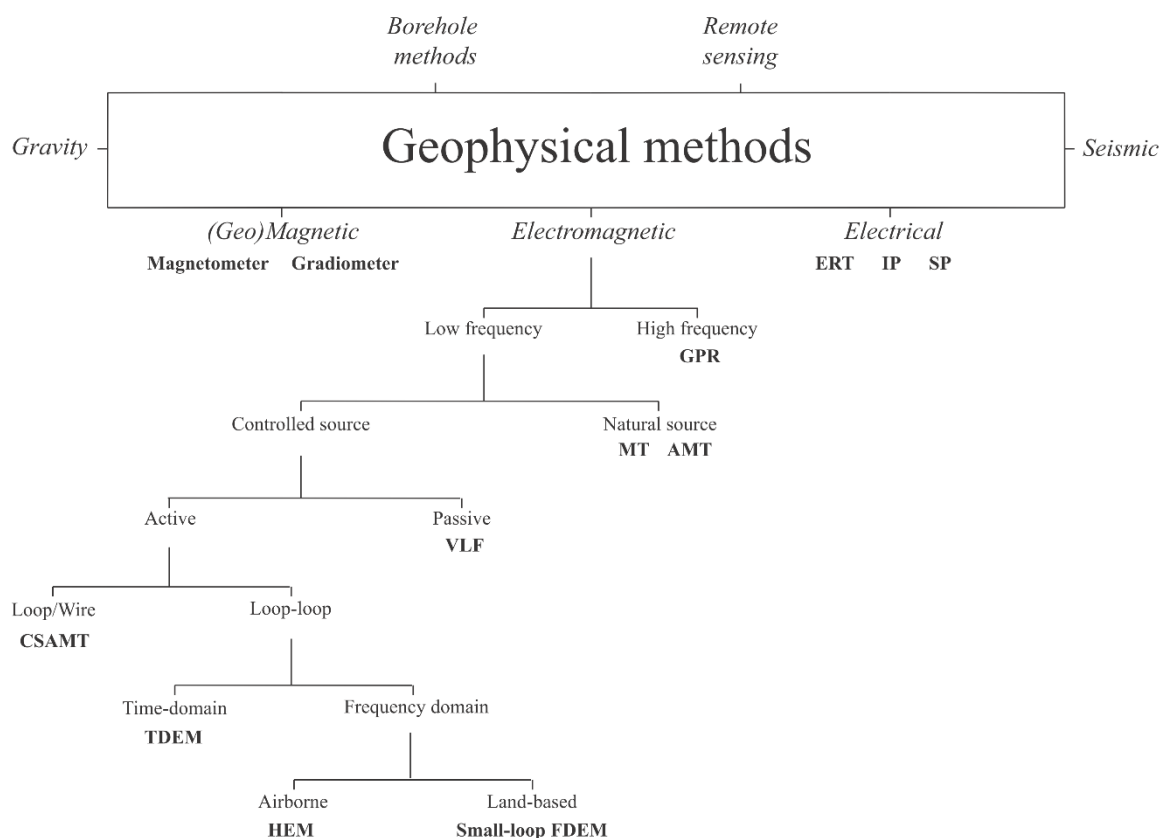


Fig. 2.7 Geophysical methods classification with emphasis on the EM technique. It is (loosely) based on an existing classification by Reynolds (1997) and is not exhaustive. Bold labels denote an instrument family.

Depending on the field, names other than ‘small-loop FDEM’ are sometimes used to refer to this technique, e.g.:

- ‘Loop-loop FDEM’ or ‘CSEM’: mostly used by geophysicists. These names are apt but do not distinguish between aerial, offshore and land-based FDEM.
- ‘EMI’: mostly used by soil scientists to denominate the loop-loop method or as an umbrella term. It refers to the general operating principle without additional specification.
- ‘Slingram-type’ EM or EMI: used sometimes in archaeological studies. ‘Slingram’ was the name given to the development of a fixed-boom loop-loop FDEM instrument by the Swedish geological survey in the 1920s.

This list is not exhaustive although aforementioned denominations are the most common in scientific literature. Because ‘small-loop FDEM’ is a more specific/clear denomination, it is the favoured option. The main reason for using names that are more specific owes to the fact that it is hard to generalize procedures, characteristics, calibrations or uses that apply equally to a broad family of EM instruments. However, for reasons of brevity, the small-loop FDEM technique will sometimes be referred to as ‘FDEM’. If any other EM method is discussed, the type will be explicitly stated.

The relation of the technique under consideration to other EM methods is summarized in figure 2.7. The classification also shows that loop-loop systems can operate in the time or frequency domain. Time domain systems emit electromagnetic pulses (generally using square waveforms) and measure the decay of the pulses with time whereas frequency domain systems make use of continuously emitted EM waves with fixed frequency.

Chapter 3

Positional accuracy surveys

“Position yourself well enough, and circumstances will do the rest”

-- Mason Cooley

This chapter was modified from:

- 1) Delefortrie, S., De Smedt, P., Saey, T., Van De Vijver, E., Van Meirvenne, M., 2014. An efficient calibration procedure for correction of drift in EMI survey data. *Journal of Applied Geophysics* **110**: 115-125.
- 2) Delefortrie, S., Saey, T., Van Meirvenne, M., 2015. Increasing positional accuracy of surveys: correcting for spatial offset and time lag. *Near Surface Geoscience*, Papers.
- 3) Delefortrie, S., Saey, T., De Pue, J., Van De Vijver, E., De Smedt, P., Van Meirvenne, M., 2016. Evaluating corrections for a horizontal offset between sensor and position data for surveys on land. *Precision Agriculture* **17** (3), 349-364.

3.1 Importance offsets between positioning and sensor data

When a positioning system and a data logger are used in surveys to record the position of a sample or sensor measurement, spatially variable information can be processed (Adamchuk et al., 2004). Motorizing a survey is preferable in many cases since it means faster data collection which can allow high resolution mapping or the covering of large areas in short time periods (e.g. Freeland et al., 2002). It is for instance advisable when performing a survey with a fixed-boom FDEM instrument. That said, on-the-go sensor data collection is employed for a variety of near-surface geophysical investigations and techniques. Applications include geological surveys, environmental investigations (e.g. Fitterman and Labson, 2005), UXO detection (e.g. Huang et al., 2006) and archaeological investigations (e.g. De Smedt et al., 2013). It has also become a widely used approach in soil science (Gottfried et al., 2012). Nonetheless, a motorized survey set-up can give rise to accuracy issues and practical problems (Sudduth et al., 2001). The necessary accuracy, resolution and sampling rate of position data vary according to the specific application, yet for all aforementioned purposes, accurate positioning is an important issue.

Potential reasons for positional inaccuracy related directly to the positioning system:

- Inaccurate positioning data. Currently, global navigation satellite system (GNSS) receivers, that are able to receive differential (DGNSS) or real-time kinematic (RTK) corrections, can offer sub-metre to sub-centimetre accuracies. A total station can provide very accurate (relative) coordinates as well, using the prism method. The choice of positioning system should reflect the survey scope. See Pérez-Ruiz et al. (2011) for a recommendation on positioning systems to be used in agriculture.
- The advertised, absolute accuracies of GNSS receivers or total stations may not be reached during field conditions, when the antenna or prism is subjected to shocks and vibration whilst situated on moving equipment or a vehicle. This can be mitigated in part by considering the placement and design of the mount.
- For GNSS systems, receiver accuracies can deteriorate rapidly when corrections are not coming through. In addition, atmospheric conditions can affect the accuracy as can as potential obstructions from the surrounding environment. Regarding total stations, there needs to be an unobstructed line of sight with the target. When the line of sight is interrupted a loss of accuracy can occur. The choice of positioning system should take into account the survey surroundings. Since a loss of accuracy can happen suddenly, a real-time visualisation of the positioning data is desirable.

Potential reasons for positional inaccuracy due to errors in relating the sensor data and position data:

- Communication delays between devices due to cable length or communication protocol (e.g. Banyś et al., 2013). This can lead to inaccurate time stamps during logging and compromises the synchronicity of measurements. High sampling speeds also require sufficiently high communication baud rates.
- Asynchronous measurements. Even without communication delays, a sensor measurement is never instantaneous (e.g. Böniger and Tronicke, 2010). Rather, a finite time interval passes during which a discrete measurement is made and this interval can also act as a noticeable time lag, relative to the position data.
- A spatial offset between sensor and position data can be present. Such an offset may be necessary to avoid interference with the sensor (e.g. Saey et al., 2012; Islam et al., 2014; Doolittle and Brevik, 2014) or may be the result of using a sensor array (e.g. Tabbagh et al., 2000). It can also be due to practical considerations such as mounting possibilities or having to use receiver data for navigation purposes as well. This can be the case for agricultural machinery and vehicles which require position data for guidance and to control implements with regards to precision farming (Speckmann, 2000).

A severe degradation of positional accuracy is possible when performing corrections for spatial offsets and quantification of induced error is difficult. In addition, a temporal offset (or time-lag) can be hard to determine as well. A communication delay between logging device and positioning system or sensor can exacerbate the spatial offset problem and becomes more important with increasing survey speed. As a consequence, the actual positional accuracy of sensor measurements is often omitted or unknown and a correction may be neglected during data processing. If the offset is relevant for the required accuracy, the measured positions have to be corrected (Gottfried et al., 2012), to maximize the reliability of the data.

Accounting for spatial offsets between FDEM instrument measurements and positioning data was researched by examining the use of several corrections. The aim was to identify the strengths and weaknesses of each applied correction, allowing recommendations for selecting an appropriate correction, and assessing the loss of accuracy due to the applied corrections. To evaluate the extent of positional accuracy loss, GNSS data (with RTK correction) were simultaneously collected at different locations along a survey set-up with a large horizontal spatial offset. More specifically, a GNSS receiver that was mounted on a towing vehicle, and two other receivers that were mounted on the front and end of an elongated sensor sled were used. The sled was connected to the vehicle using a flexible connection. Since the positional accuracies of the GNSS data were in the 20 mm range, it was possible to quantify the error of the predicted positions of the sled location for several corrections. It is noted that tilt of the receiver antenna has been not been considered in this work.

Nonetheless, antenna tilt can have a significant impact on positioning accuracy when terrain slope is high. The application of a total station is also not considered.

Accounting for temporal offsets between FDEM instrument measurements and positioning data is evaluated by visualizing FDEM after assignment of coordinates (corrected for a horizontal, spatial offset) and assessing the time lag based on linear anomalies in the data.

Though we focus on the case of an FDEM survey, the methodologies evaluated/proposed can be of value for all surveys requiring high positional accuracy and large spatial or temporal offsets between positioning data and measurement data.

3.2 Materials and methods

GNSS positioning systems

A detailed overview of the integration of GNSS data in (agricultural) geophysics is given by Grejner-Brzezinska (2008). Differential GNSS (DGNSS) and RTK solutions are widely accepted methods for accurate positioning and navigation. DGNSS is traditionally based on differential pseudorange measurements to compute its position (Landau et al., 2009) and the accuracy is in the sub-metre order. RTK correction makes use of carrier phase and Doppler measurements in addition to pseudoranges. The biggest advantages of RTK are its accuracy and productivity (the time needed to achieve the high accuracy with the positioning system). Disadvantages are its dependency on a reference station and its inability to work reliably over long distances from the reference station (Landau et al., 2009). In addition, this method is usually expensive.

Geographic coordinates (WGS84) were logged using the following GNSS systems:

- Receiver 1 (POS 1): Trimble Zephyr model 2, in conjunction with a Trimble SPS unit (Trimble Navigation Ltd., Sunnyvale, California, USA).
- Receiver 2 (POS 2): Trimble R10 (Trimble Navigation Ltd., Sunnyvale, California, USA)
- Receiver 3 (POS 3): Leica Viva GNSS-G15 system (Leica Geosystems, Heerbrugg, Switzerland).

These receivers made use of a telecom link to receive network-RTK corrections from the Flemish Positioning Service (FLEPOS) and are multi-receivers that are able to pick up signals of GPS and GLONASS satellites, thereby increasing the number of satellites used for positioning. For communicating with the receivers, the NMEA-0183 protocol was used. The output consisted of GGA strings. These detail essential GNSS fix data that provide 3D location, UTC (Coordinated Universal Time) time and accuracy data. The output was set to a 5 Hz logging rate.

Survey procedure and test location

The case of a motorized, FDEM survey set-up (where a multi-receiver instrument (array) is used) is considered. When using these sensors, no metallic objects should be in the vicinity so that measurements remain unaffected (e.g. Corwin and Lesch, 2005). This dictates that the antenna of the positioning system as well as the vehicle towing the instrument should keep a minimum distance. Thus a GNSS receiver can be positioned directly above the instrument (at sufficient height) though this has the following disadvantages:

- When one receiver is used for both track guidance and instrument positioning, guidance can be negatively affected.
- If the sled or cart topples (e.g. when surveying heavily ploughed terrain) the receiver may be damaged and a non-conductive mount is necessary.
- The higher the GNSS receiver is positioned, the higher the effect of sloping terrain (tilting of the antenna).

Of course, there are many possible solutions to such practical problems. Nonetheless, these solutions are generally costly, not always an option and a horizontal offset correction may need to be performed anyway (sensor arrays automatically give rise to horizontal offsets). It is noted that some instruments may even include a built-in positioning solution yet as there are many cases in which spatial offsets are present, it is worth looking into.

The spatial offset present in FDEM survey set-ups can be relatively large (e.g. several metres), which is useful for an evaluation since larger offsets result in more pronounced differences between offset corrections. The considered field set-up is shown in Figure 3.1. A polyethylene sled was towed by an all-terrain vehicle making use of a flexible connection (two ropes). The sled ran parallel to the driving direction and the offset between the front of the sled and the vehicle was variable (over a limited range) since the slackness of the ropes can vary. GNSS receiver 1 was mounted on the vehicle while the two other receivers were mounted near the front and rear of the elongated sensor sled. Receiver 1 was located above the point of attachment of the flexible connection to the vehicle (which acts as a pivot for the towed equipment). The (slightly variable) distance between receivers 1 and 2 was approximately 3.6 m (with the ropes taut) and the fixed distance between receiver 2 and 3 was 2.07 m. The sled and the vehicle GNSS receiver mount were lined up so that, ideally, there was only an in-line spatial offset when driving straight lines.

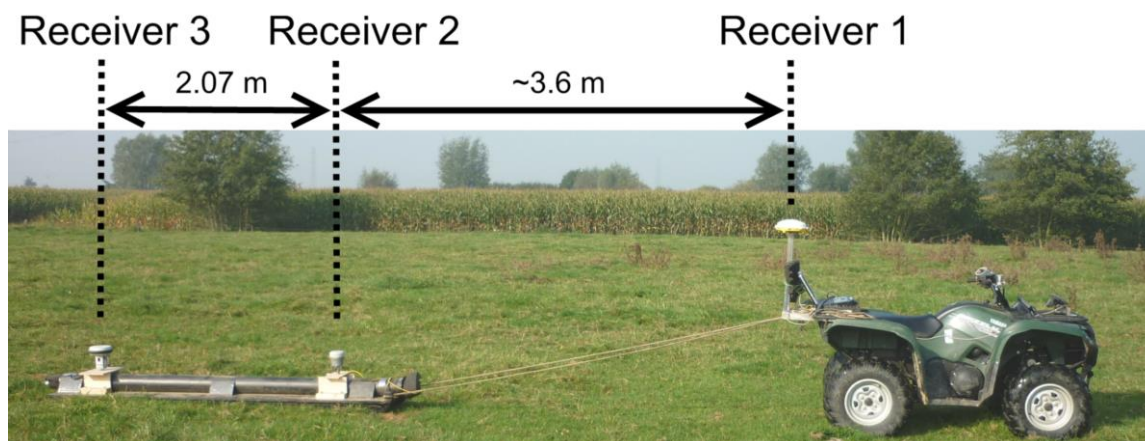


Fig. 3.1 FDEM survey set-up: a vehicle towing an elongated poly-ethylene sled by use of two ropes. Three GNSS receivers are mounted on the vehicle and the sled: receiver 1 is denoted as POS 1, receiver 2 as POS 2 and receiver 3 as POS 3.

All data were collected in Belgium. Central coordinates of the survey field are x: 543,195 m and y: 5,663,570 m - UTM 31 geographic coordinate system. The survey was performed on 18 August 2014. Weather conditions were clear. The field was a pasture with an average terrain slope of 0.7 %. The difference between the maximum and minimum height was ~0.7 m in the survey area (~0.5 ha). All figure axes show local coordinates.

Two surveys were performed. Figure 3.2 shows the survey tracks of both (with the survey track corresponding to the first receiver). The survey speeds are displayed by use of a colour coding. The surveys were conducted by driving parallel (straight) lines, using real-time navigation. The first survey was a slow, high resolution survey. The second survey was performed to vary the survey speed and track turn radii more.

Before starting the surveys, the GNSS data were logged whilst stationary for about 5 to 10 min. Out of 3,000+ stationary measurements, 99% were within ~20 mm of the median coordinate for all receivers. The measures of accuracy of the systems themselves indicated a slightly better accuracy (~10 mm). Thus enabling accurate tracking and analysis of the movement of both towing vehicle and sled (Figure 3.3).

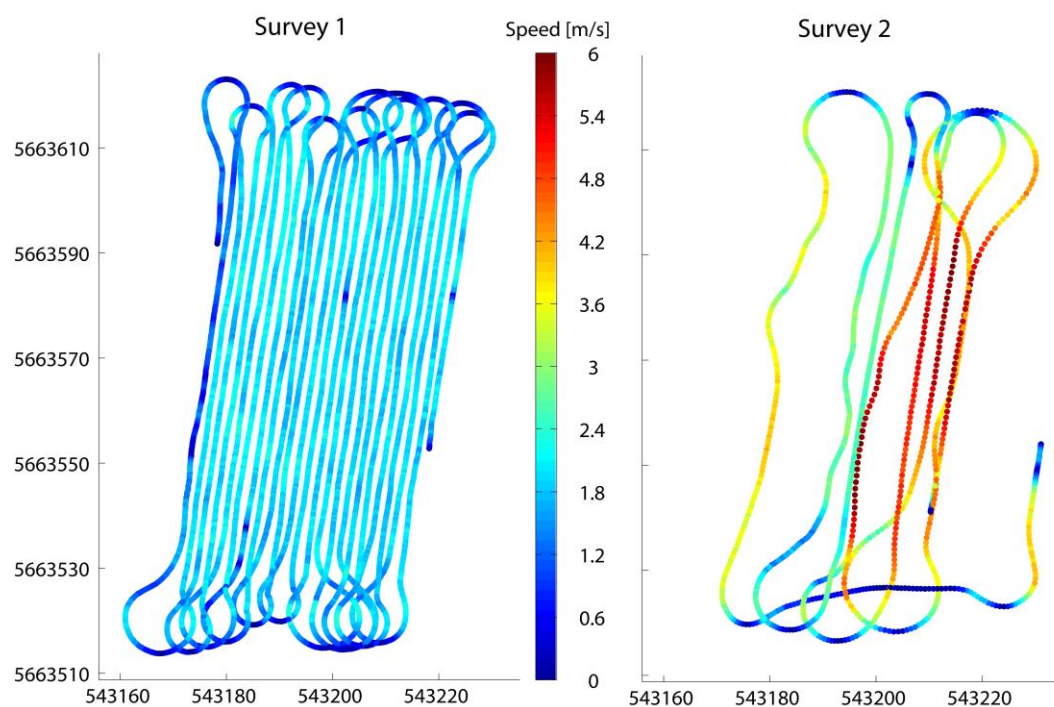


Fig. 3.2 Positioning surveys performed at the same field. Colour coding of the positioning data (belonging to the receiver on the vehicle) visualizes the survey speed.

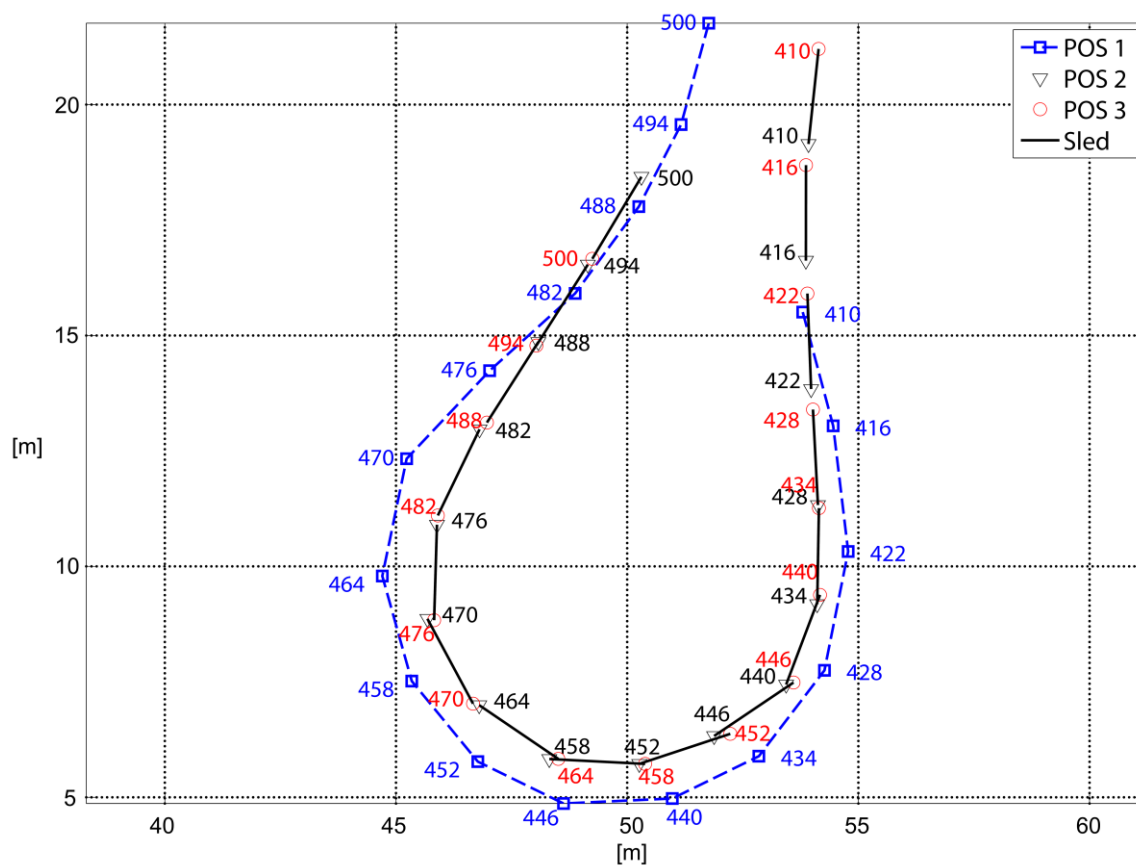


Fig. 3.3 Illustration of tracking of the logged positions along the survey set-up.

Data processing

All data processing was done in Matlab (The Mathworks Inc, Natick, USA). The WGS84 spherical coordinates were logged and transformed to Cartesian coordinates in the UTM geographic coordinate system (with x the horizontal axis, y the vertical axis and X and Y the system coordinates). The initial, stationary recordings were deleted after which the data of the different GNSS receivers were synchronized using the logged satellite time. Only time stamps shared by all receivers were kept. Duplicate position data, within less than 1 mm of each other, were removed from all data collected. This was done to remove standstill position data, which might produce biased statistics. No smoothing or clipping of inaccurate data was otherwise performed.

The following subsections detail the corrections that were evaluated. It is noted that only a horizontal (spatial) offset, in the direction of travel, was considered.

Direction vector shift

For a given position $\mathbf{P}_i (P_{i,x}, P_{i,y})$, the corrected value $\mathbf{S}_i (S_{i,x}, S_{i,y})$ is calculated by deriving the driving direction (velocity vector), obtained through comparison with a subsequent or previous position, and shifting the coordinate along this direction. The incremental index of the positions is denoted by ‘ i ’ and ranges from 1 to the number of GNSS positions. Mention of this correction is made by Aspinall et al. (2008) though they do not go into detail. It is presumably the most widely used correction for a horizontal offset (shift) yet very few authors provide information on the choice of spatial offset correction. The implementation used (see Figure 3.4, left), executes a search of the previous positions along the survey track (using the cumulative distance along the survey track) and selects the previous coordinate that is closest to \mathbf{P}_i minus the horizontal offset along the survey track. As a consequence, the calculated driving direction is less prone to small direction corrections and GNSS inaccuracies. If, for instance, the position \mathbf{P}_{i-3} is selected, the correction performed is:

$$S_{i,x} = P_{i,x} - \frac{dX}{\sqrt{dX^2 + dY^2}} * \text{horizontal offset}$$

$$S_{i,y} = P_{i,y} - \frac{dY}{\sqrt{dX^2 + dY^2}} * \text{horizontal offset}$$

with

$$dX = P_{i,x} - P_{i-3,x}$$

$$dY = P_{i,y} - P_{i-3,y}$$

and ‘horizontal offset’ denoting a scalar (horizontal distance of the spatial offset).

To calculate the initial corrected positions, where no previous positions within the horizontal offset distance are available, the same method was used by taking the subsequent position (that is within a distance of at least a metre) instead of previous positions. Removing the initial positions (of the corrected data) that are within the offset distance is also an option.

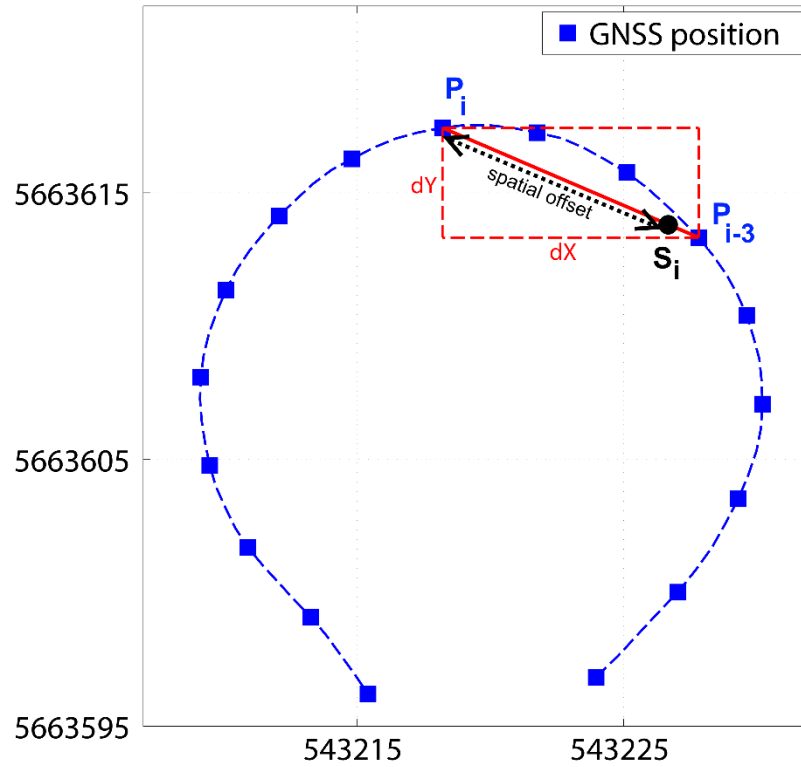


Fig. 3.4 The direction vector method involves calculating the direction vector between two positions. The desired horizontal offset is then off-set in this direction.

Constrained shift

The constrained method has been described by Delefortrie et al. (2014b). The essence of this method is that the allocation of corrected coordinates is limited to the survey track. Firstly, a piecewise cubic polynomial interpolation is performed, resulting in a near continuous survey track (see Figure 3.5). As a result, the position \mathbf{P}_{sel} with (interpolated) coordinates closest to position \mathbf{P}_i minus the horizontal offset along the survey track (using the cumulative distance) can be found and allocated as the corrected coordinate:

$$S_{i,x} = P_{sel,x}$$

$$S_{i,y} = P_{sel,y}$$

The smaller the time step used in the interpolation, the higher the potential accuracy. A time step of 0.01 s was used for the corrections shown in this chapter. A flowchart to implement this correction is given in Figure 3.6. To calculate the initial corrected positions, where no previous positions within the horizontal offset distance are available, the direction vector method was used (with a search for subsequent points that are within a distance of at least a metre).

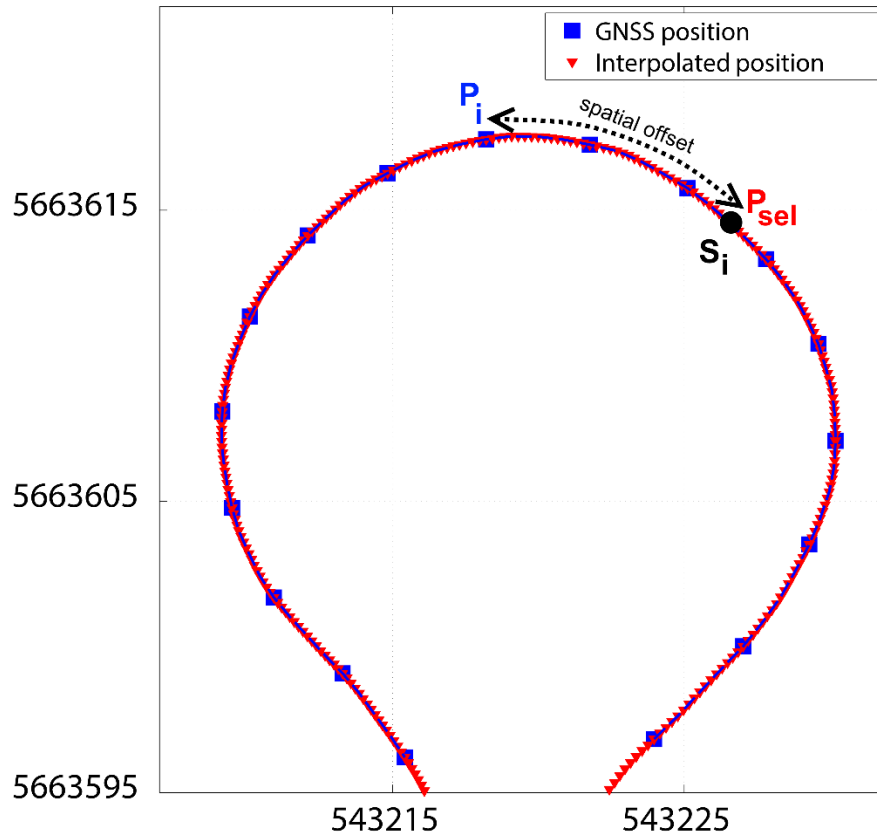


Fig. 3.5 The constrained method makes use of a piecewise polynomial interpolation of successively visited positions. The (interpolated) position closest to P_i minus the desired offset (along the survey track) is then equated to the shifted position.

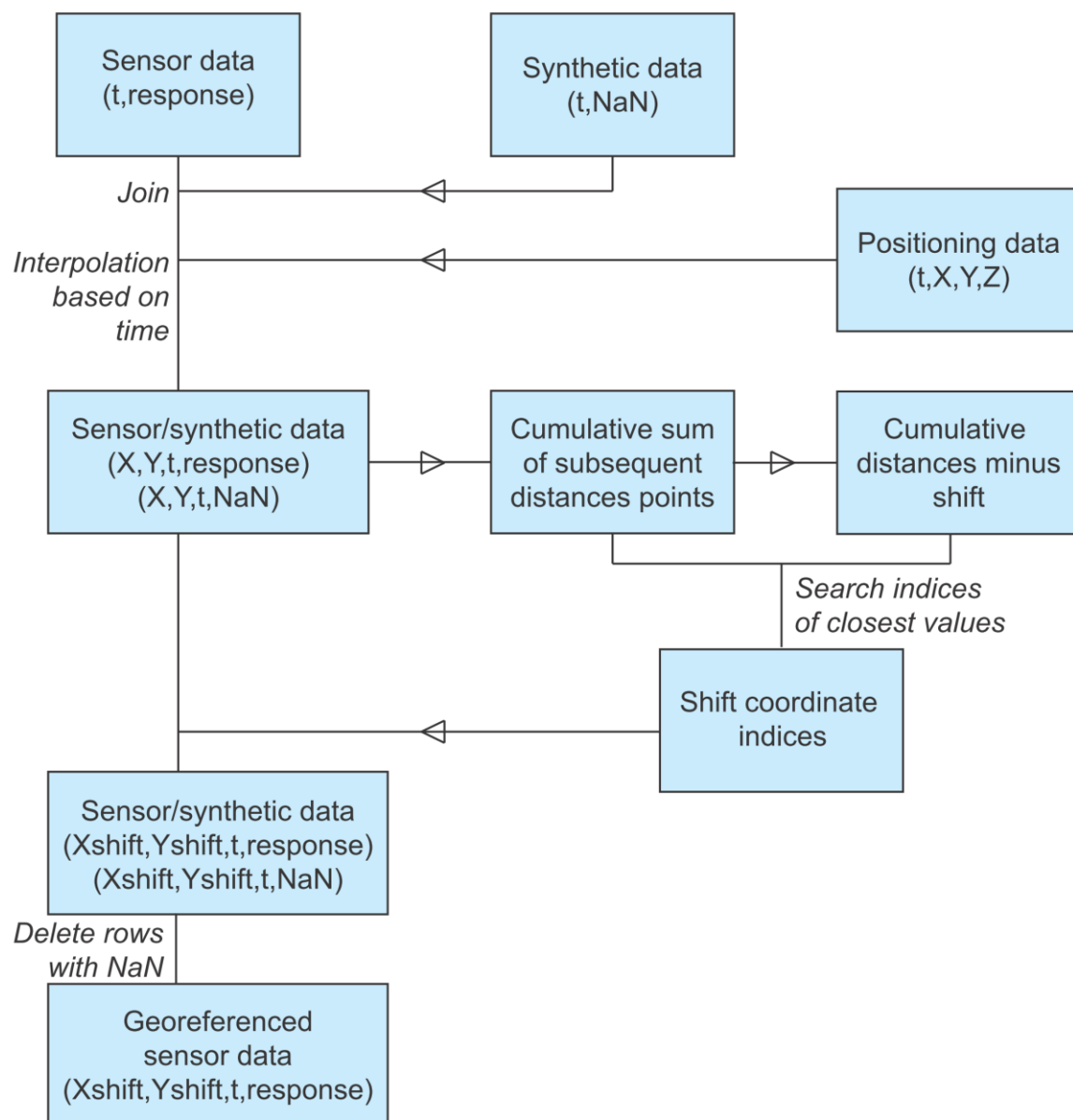


Fig. 3.6 Flowchart summarizing the applied routine for correcting a spatial offset between sensor and positioning data. ‘NaN’ stands for ‘not a number’, which is a no-data identifier; ‘t’ indicates data timestamps. Alternatively, XY locations can be allocated to the sensor data (based on time stamps) prior to the addition of synthetic data.

Kinematic correction

Gottfried et al. (2012) have developed a kinematic approach to account for a spatial offset when a cart or sled is towed by a vehicle equipped with a positioning system. The approach mainly consists of using a tractrix equation, which is a mathematical description of a pursuit at a constant distance of a towed object (Garlick et al., 1993). The equations governing movement of a sled or cart were given by Gottfried et al. (2012) and are reproduced here using terminology consistent with the other methods above:

$$S_{i+1,x} = S_{i,x} + \frac{\left[A \cos \alpha + \exp\left(\frac{dP}{shift}\right) * shift * \sin \alpha * \sin \varphi \right]}{\exp\left(\frac{2*dP}{shift}\right) * \left(\frac{1+\cos \varphi}{2}\right) + \left(\frac{1-\cos \varphi}{2}\right)} + \frac{B_x}{C}$$

$$S_{i+1,y} = S_{i,y} + \frac{\left[A \sin \alpha + \exp\left(\frac{dP}{shift}\right) * shift * \cos \alpha * \sin \varphi \right]}{\exp\left(\frac{2*dP}{shift}\right) * \left(\frac{1+\cos \varphi}{2}\right) + \left(\frac{1-\cos \varphi}{2}\right)} + \frac{B_y}{C}$$

with

$$A = \exp\left(\frac{2 * dP}{shift}\right) * (dP - 2 * shift) * \left(\frac{1 + \cos \varphi}{2}\right) + dP * \left(\frac{1 - \cos \varphi}{2}\right)$$

$$B_x = shift * \sin \alpha * \sin \varphi - shift * \cos \alpha * (1 + \cos \varphi)$$

$$B_y = -shift * \sin \alpha * (1 + \cos \varphi) - shift * \cos \alpha * \sin \varphi$$

$$C = \left(\frac{1 + \cos \varphi}{2}\right) + \left(\frac{1 - \cos \varphi}{2}\right)$$

and

$$\cos \alpha = \frac{P_{i+1,x} - P_{i,x}}{dP}$$

$$\sin \alpha = \frac{P_{i+1,y} - P_{i,y}}{dP}$$

$$dP = \sqrt{(P_{i+1,x} - P_{i,x})^2 + (P_{i+1,y} - P_{i,y})^2}$$

$$\sin \varphi = \frac{(P_{i,x} - S_{i,x})_{trans}}{\text{horizontal offset}}$$

$$\cos \varphi = \frac{(P_{i,y} - S_{i,y})_{trans}}{\text{horizontal offset}}$$

The subscript ‘trans’ denotes that the coordinate has been transformed to the field coordinate system, which is a system that takes into account the vehicle motion (see Zhang and Qiu, 2004; Gottfried et al., 2012). This can be implemented using:

$$(P_{i,x} - S_{i,x})_{trans} = \cos \alpha * (P_{i,x} - S_{i,x}) + \sin \alpha * (P_{i,y} - S_{i,y})$$

$$(P_{i,y} - S_{i,y})_{trans} = -\sin \alpha * (P_{i,x} - S_{i,x}) + \cos \alpha * (P_{i,y} - S_{i,y})$$

To calculate the corrected coordinates using the kinematic correction, an initial estimate of the corrected position is required. This was calculated by using the direction vector method. In addition, a condition was implemented so that the corrected position was calculated only if there was forward movement between the position of interest and its previous position: if $\cos \varphi < 0$ then $S_{i+1} = S_i$. It is noted that the kinematic correction as described herein is only valid for the case of towing a sled behind the receiver, contrary to the other described methods, which can be used for the case of a

sensor mounted in front of the position data. For more information on the kinematic correction, see Gottfried et al. (2012).

3.3 Results and discussion

Spatial offset

The positions of receivers 2 and 3 were predicted (POS 2* and POS 3*), using the above mentioned corrections, from the positioning data of receivers 1 and 2 (POS 1 and POS 2) respectively. Comparing the predicted locations with the actual positions allowed quantifying and visualizing the prediction error, which is defined as the horizontal distance between predicted and actual positions. It is noted that the following analysis is only valid for sufficiently flat terrain and that the colour scale of the figures does not show the full range.

Figure 3.7 shows error maps for POS 2* for the first survey. Not surprisingly, the most noticeable difference between the correction procedures is in the track turns. The kinematic approach outperforms the other methods since these do not account for a possible rotation of the sled connection around the pivot during track turns. The direction vector method and constrained method produce very similar results though the results of the latter appear slightly smoother. Figure 3.8 shows error maps for POS 3* for the same survey, starting from POS 2. In this case, the kinematic correction seems to over-correct in the track turns. It can be seen that, except for very tight track turns, a shift along the rigid sled should be constrained to the survey track.

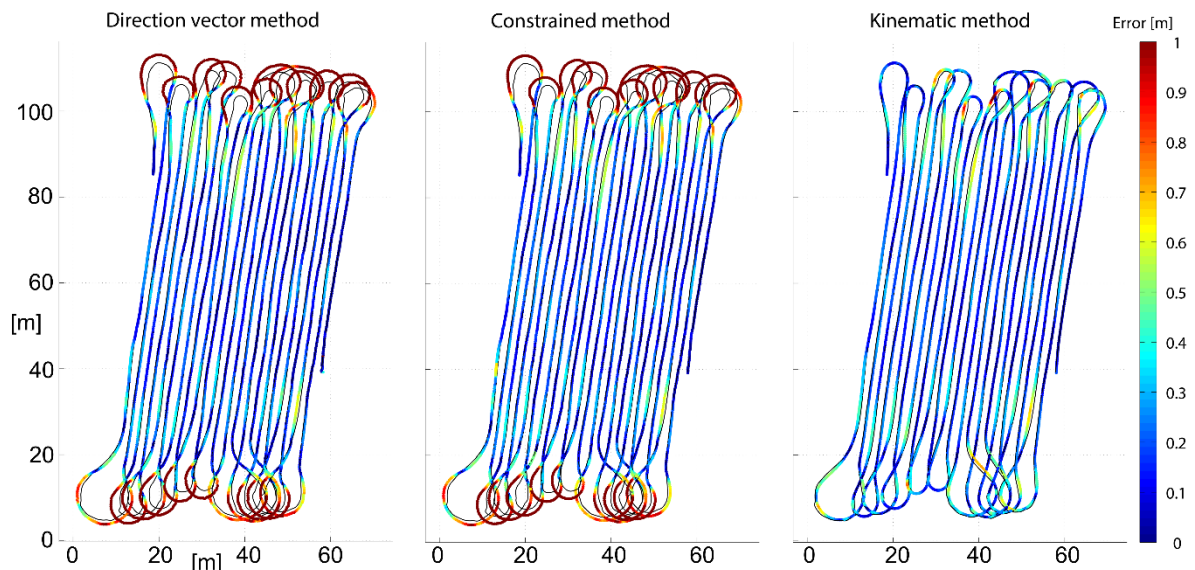


Fig. 3.7 Comparison of the predicted and logged positions of receiver 2 for the first survey, starting from receiver 1 positions. The predicted positions are plotted as points which are colour coded to visualize the distance from the corresponding logged position. The actual, logged track is plotted as a black line.

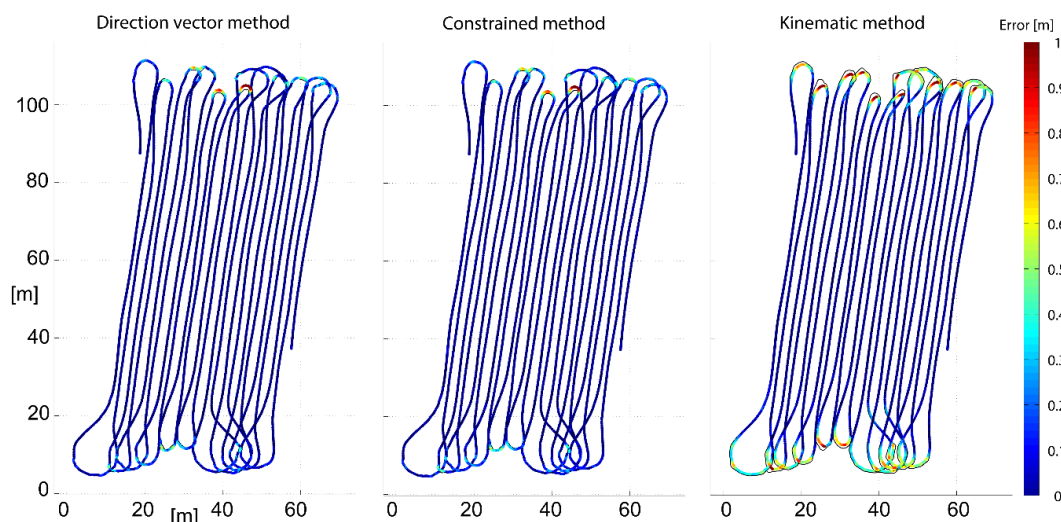


Fig. 3.8 Comparison of the predicted and logged positions of receiver 3 for the first survey, starting from the receiver 2 positions. The predicted positions are plotted as points which are colour coded to visualize the distance from the corresponding logged position. The actual, logged track is plotted as a black line.

Figure 3.9 shows error maps for POS 2* for the second survey. The results show that the direction vector and constrained method on the one hand and the kinematic correction on the other are generally complementary: the former perform well in wide track turns with a large radius whereas the latter performs well in tight track turns. A possible explanation for the over-correcting of POS 2 in the wide tracks, by the kinematic correction, is that the tractrix equations neglect possible centrifugal forces during turns. The error maps for POS 3*, starting from POS 2 are not shown since the results are similar to survey 1.

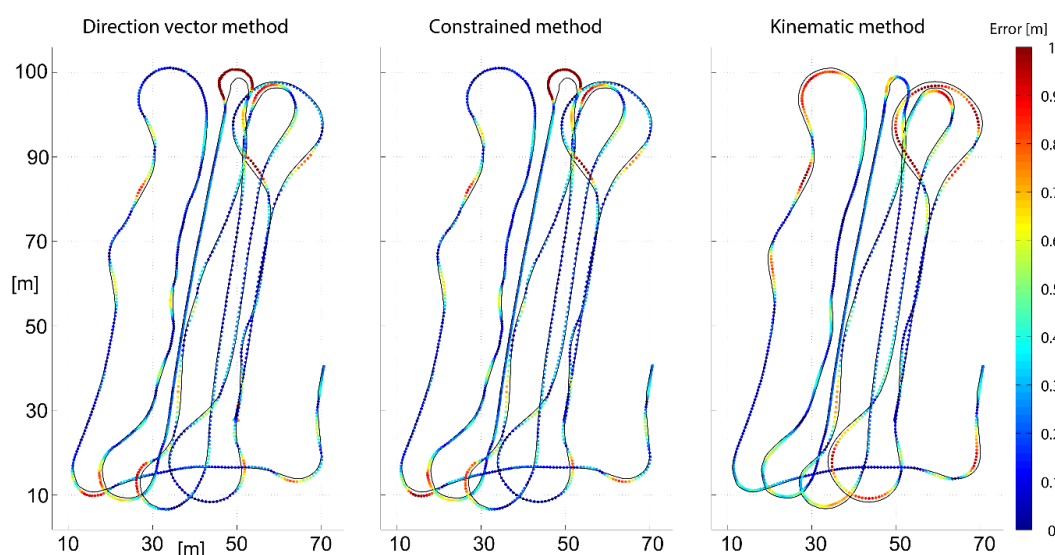


Fig. 3.9 Comparison of the predicted positions and logged positions of receiver 2 for the second survey, starting from receiver 1 data. The predicted positions are plotted as points which are colour coded to visualize the distance from the corresponding logged position. The actual, logged track is plotted as a black line.

To verify the visual results, the root-mean-square errors (RMSE) were calculated to act as a measure of the difference in predicted coordinates and observed coordinates (Tables 3.1 and 3.2). A sub-division of the survey track was made to assess the goodness of correction in the track turns and straight track data separately. For these sub-divisions the in-line error and cross-track error, with regards to the movement direction of the actual GNSS positions under scrutiny, were calculated as well. Generally, the error was larger in the turns of the survey tracks than in the straight track data and the in-line error was always (significantly) smaller than the cross-track error. That means that, even in straight sections, the sled did not follow the line of the GNSS track precisely. This cross-track error is not desirable since a large terrain slope as well as terrain features such as tractor and tillage tracks may exacerbate the error. This might be improved by re-designing the method of connection and taking the topography into account. When comparing between the prediction errors for POS 2* and POS 3* it is obvious that the errors along the rigid sled were always significantly smaller than the POS 2* errors.

Table 3.1 RMSE [m] of the predicted positions for survey 1 (number of points = 6,580). Kin = kinematic method, Con = constrained method, Dir = direction vector method, Cross-track = error perpendicular to the logged position data, In-line = in-line error. The best all-round RMSE values for a given comparison are highlighted.

Prediction	POS 1 → POS2*			POS 2 → POS3*			POS 1 → (POS2* →) POS3*				
Method	Kin	Con	Dir	Kin	Con	Dir	Kin + Kin	Con	Dir	Kin + con	Kin + dir
All track data	0.26	0.70	0.70	0.25	0.10	0.10	0.36	0.88	0.89	0.29	0.29
Cross-track	0.25	0.66	0.66	0.24	0.05	0.04	0.34	0.77	0.80	0.27	0.27
In-line	0.07	0.23	0.23	0.09	0.05	0.04	0.12	0.42	0.40	0.11	0.11
Track turns	0.33	1.23	1.25	0.47	0.19	0.18	0.55	1.57	1.61	0.39	0.39
Cross-track	0.31	1.15	1.17	0.44	0.17	0.17	0.50	1.38	1.43	0.35	0.35
In-line	0.12	0.43	0.43	0.16	0.08	0.07	0.21	0.78	0.74	0.18	0.18
Straight track	0.23	0.24	0.23	0.03	0.02	0.02	0.24	0.24	0.23	0.23	0.23
Cross-track	0.23	0.23	0.23	0.03	0.02	0.02	0.23	0.24	0.23	0.23	0.23
In-line	0.04	0.04	0.04	0.01	0.00	0.00	0.04	0.04	0.04	0.04	0.04

From the previous results, it follows that a combination of the assessed methods is likely the best approach to predict the location of a point along the length of the sled. This is confirmed by the RMSE for the predicting of POS 3, starting from POS 1 (see Tables 3.1 and 3.2). A horizontal offset correction involving a kinematic correction (to predict the location of the front of the sled) followed by a direction vector or constrained shift (along the sled) was found to be best practice for the survey set-up under consideration. It is also clear from Tables 1 and 2 that an increase in driving speed has led to higher RMSE for the second survey, concerning the prediction of POS 2. Quite likely, the

greater variation in speed resulted in more distance variation between POS 1 and POS 2 due to stretching of the ropes when going faster and inertia of the sled when slowing down.

Table 3.2 RMSE [m] of the predicted positions for survey 2 (number of points = 1,402).

Prediction	POS 1 → POS2*			POS 2 → POS3*			POS 1 → (POS2* →) POS3*				
Method	Kin	Con	Dir	Kin	Con	Dir	Kin + Kin	Con	Dir	Kin + con	Kin + dir
All track data	0.44	0.64	0.65	0.25	0.09	0.09	0.58	0.80	0.82	0.49	0.49
Cross-track	0.41	0.55	0.57	0.23	0.08	0.08	0.54	0.66	0.70	0.46	0.46
In-line	0.15	0.31	0.31	0.08	0.04	0.03	0.21	0.45	0.43	0.19	0.19
Track turns	0.57	1.00	1.07	0.40	0.15	0.14	0.80	1.30	1.33	0.66	0.66
Cross-track	0.53	0.86	0.92	0.38	0.13	0.13	0.75	1.06	1.11	0.60	0.61
In-line	0.21	0.52	0.54	0.12	0.07	0.05	0.29	0.76	0.73	0.27	0.27
Straight track	0.35	0.31	0.31	0.11	0.04	0.04	0.39	0.32	0.32	0.36	0.36
Cross-track	0.33	0.30	0.29	0.11	0.04	0.03	0.37	0.30	0.30	0.34	0.34
In-line	0.10	0.10	0.10	0.04	0.01	0.01	0.13	0.11	0.11	0.12	0.12

An important consideration, when relating the RMSE with the level of accuracy of the receivers, is that the corrections have resulted in a significant deterioration of the initial positioning accuracy (Table 3.3 shows the maximum errors for the methods). Nonetheless, the obtained accuracy will suffice for most any type of application. It also follows that the accuracy of the receiver is an unreliable measure for the sensor data positioning accuracy. Another reason to give sufficient attention to a horizontal offset correction is that the highest achievable accuracy can be very different for the straight track data and track turn data. Since the surface area pertaining to vehicle turns can make up a sizeable part of the total survey area, this is worth evaluating.

Table 3.3 Maximum error [m] of the predicted positions for surveys 1 and 2 (number of points = 6,580 and 1,402 respectively). The lowest maximum errors for a given comparison are in bold.

Prediction	POS 1 → POS2*			POS 2 → POS3*			POS 1 → (POS2* →) POS3*				
Method	Kin	Con	Dir	Kin	Con	Dir	Kin + Kin	Con	Dir	Kin + con	Kin + dir
Survey 1	1.10	3.11	3.22	1.95	1.21	1.30	1.88	4.62	4.89	1.67	1.68
Survey 2	1.23	2.88	3.12	0.97	0.49	0.51	1.60	3.93	4.31	1.26	1.31

Table 3.3 Maximum error [m] of the predicted positions for surveys 1 and 2 (number of points = 6,580 and 1,402 respectively). The lowest maximum errors for a given comparison are in bold.

Whilst a horizontal offset correction does limit the loss in positional accuracy, a deterioration of the logged positions is likely. The best solution would be to avoid a spatial offset altogether. If this is

not possible, a good choice of correction is important since a given correction should not be used indiscriminately. Table 3.4 summarizes the (dis)advantages of the correction methods and recommendations for their use. However, Tables 3.1 and 3.2 also show that the performances of the corrections are generally quite similar when only evaluating the straight track data. It follows that when these are considered exclusively, careful selection of an appropriate correction is less important. The same can be said for cases where the spatial offset is limited. Figure 3.10 shows that the assessed methods produce similar results for small horizontal offsets whereas the differences become more pronounced with increasing offset.

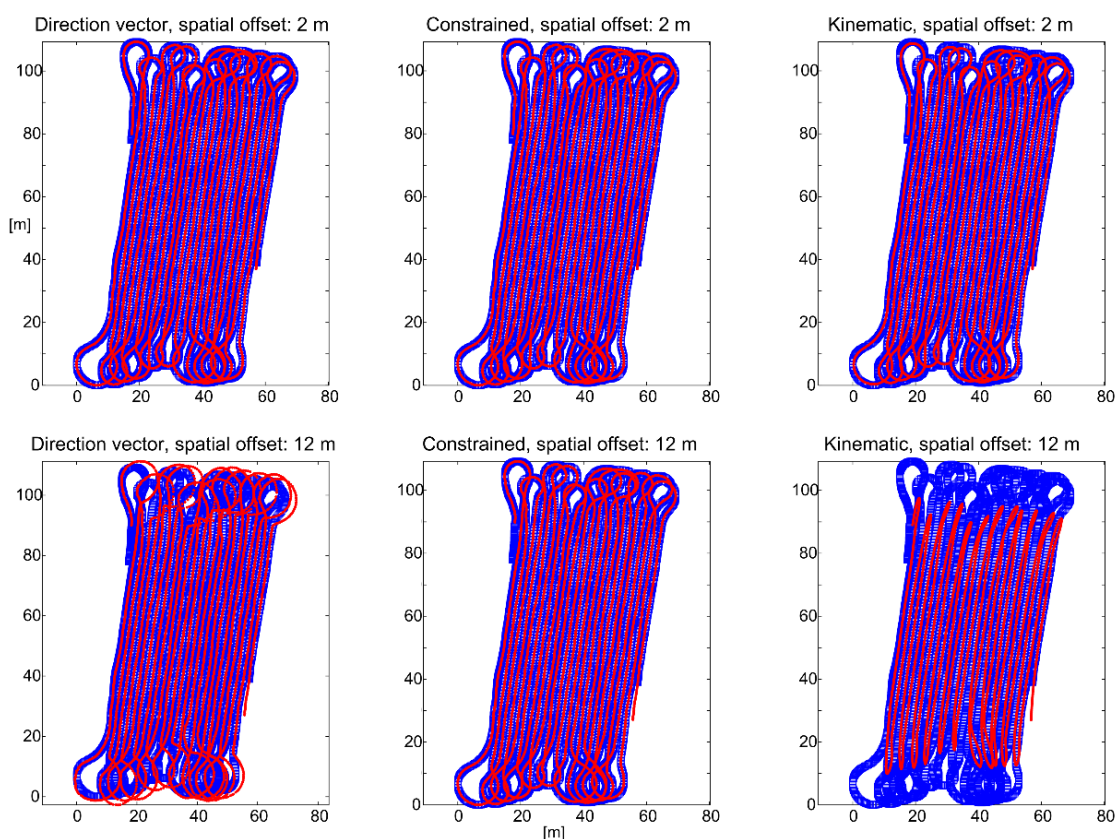


Fig 3.10 Illustration of differences between the correction methods for a small spatial offset and a large spatial offset. The predicted positions are plotted as red points and the original data (before correction) are plotted as blue squares.

Table 3.4 Summary of the (dis)advantages of the correction methods and recommendations for their use.

Method	Use when	Advantages	Disadvantages
Direction vector	ease of implementation and execution speed outweigh accuracy in the track turns or when only straight track data is processed	Easy to implement. Highest potential for a very fast implementation	Less robust. When the horizontal offset is large this correction can become unstable
Constrained	the corrected position is constrained to the positioning track	Robust. Not influenced by length of spatial offset. Performance is easy to gauge	Good accuracy only when the constrained assumption is valid
Kinematic	the connection between the sled and the vehicle mount can rotate around the pivot	Takes into account rotation of the sled-vehicle connection around the pivot. Well suited for tight track turns	Purely mathematical approach. The performance can be hard to gauge. Quite complex

Table 3.4 Summary of the (dis)advantages of the correction methods and recommendations for their use.

Temporal offset

When visualising FDEM data, the location of the out-of-phase or in-phase (volume) positions should reflect the location of the coil configuration midpoint (i.e. a 1 m HCP configuration would require an extra 0.5 m shift from the location of the transmitter toward the receiver).

To test the presence of a time-lag between the sensor output and positioning data a FDEM survey, collected in Zeeland (The Netherlands), was looked into. The survey was performed using a Dualem 21S, which has four receivers at different locations (and thus requires four spatial offset corrections). The aim was archaeological: to detect remains of past buildings that no longer show any traces on the surface. The dataset was chosen because it contained clear linear anomalies as well as point anomalies in the out-of-phase and in-phase data. The spatial offset between the front of the sensor and GNSS receiver was measured and the sensor data were corrected for a horizontal spatial offset. To this aim, both GNSS and sensor data were logged synchronously and timestamped during the survey after which the GNSS data were shifted (for the recorded in-line offset) to estimate the FDEM instrument midpoints by using a tractrix correction to estimate to position of the front of the instrument followed by a constrained correction to estimate the midpoint locations. To conclude the spatial offset correction, the shifted XY coordinates were assigned to the sensor data based on the recorded timestamps by applying a piecewise cubic polynomial interpolation (1D). Starting from the original GNSS positions (Figures 3.11 and 3.12, left), this produced the spatial offset corrected maps (Figures 3.11 and 3.12, middle).

The uncorrected grids showcase the general subsurface trends regarding conductivity and susceptibility but are heavily impacted by a zig-zag pattern. This is due to the survey execution,

which consisted of turning at the end of each survey line and sequentially scanning the entire area. Clearly an improvement in positioning accuracy is reached by correcting for the spatial offset, but a zig-zag pattern persists (though to a lesser extent). This is due to the sensor data lagging behind the positioning data during logging. To visually determine the time-lag, a graphical user interface (GUI) was created to display a series of gridded maps with an incremental addition of a time lag, specified by user input (e.g. 6 maps: +0s, +0.2s, ..., +0.8s, +1s). The map which best represented the linear anomalies was then selected. Out of experience (by performing this step on hundreds of datasets) it has become apparent that for the Dualem instruments, a time of lag of 0.6s or more is no exception. Such a lag is no longer negligible in many cases. At a slow speed of 2 m/s this would produce a noticeable (and undesirable) effect and at higher speeds the effect would become pronounced. While the influence would be less for low resolution surveys, it is a crucial element in correctly visualising and processing high resolution FDEM data. The importance for the exact positioning of features such as drainage tiles and UXO cannot be overstated.

The exact source for the time-lag is hard to determine. It is presumably mainly due to the FDEM instrument since it is assumed that:

- the GNSS timestamp is highly accurate
- the GNSS receiver does not contribute to a time-lag (considering a survey-grade receiver)
- the effect due to cable length is negligible (all cables < 10 m).

It is noted that when a survey is conducted by always moving a FDEM instrument in the same direction (and orientation), no zig-zag pattern will be visible and all measurements will shift in the same direction. It is also possible that there are no linear features present in the data, making it hard to visually assess the presence of a time-lag. There are two options if a high positional accuracy is required but no visual assessment can be made:

- researching whether the time-lag remains constant for a given instrument and always applying a time-lag that is found to be representative
- performing a test at each survey location before or after surveying; this might consist of passing perpendicularly in both directions over a steel rod for example, and assessing the time-lag based on a shift in the responses collected in different directions

Unfortunately, an additional complicating factor with regards to FDEM data positioning is the asymmetric response of PRP configurations. Whereas a well-designed HCP configuration should provide symmetrical responses, PRP responses can still display zig-zag patterns over strong anomalies even after spatial and temporal offset correction (Fig. 3.13) when these anomalies are traversed in different orientations.

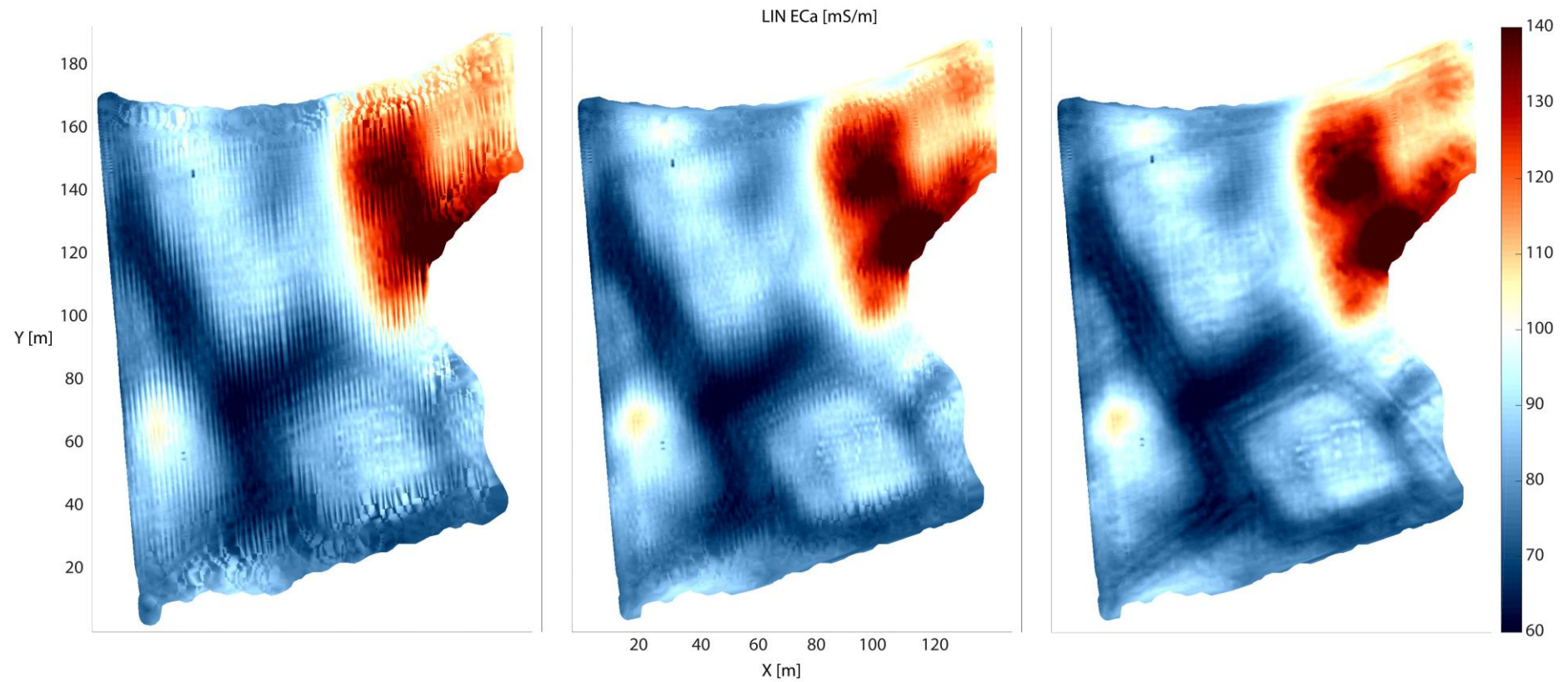


Fig 3.11 HCP2 LIN σ_a grids: (left) data without spatial offset correction or time lag correction; (centre) data after spatial offset correction and (right) data after spatial offset correction and a time lag correction of 0.8 s. The scattered data were gridded using a linear interpolation. The coordinates shown are relative coordinates. The colour scale does not show the full range.

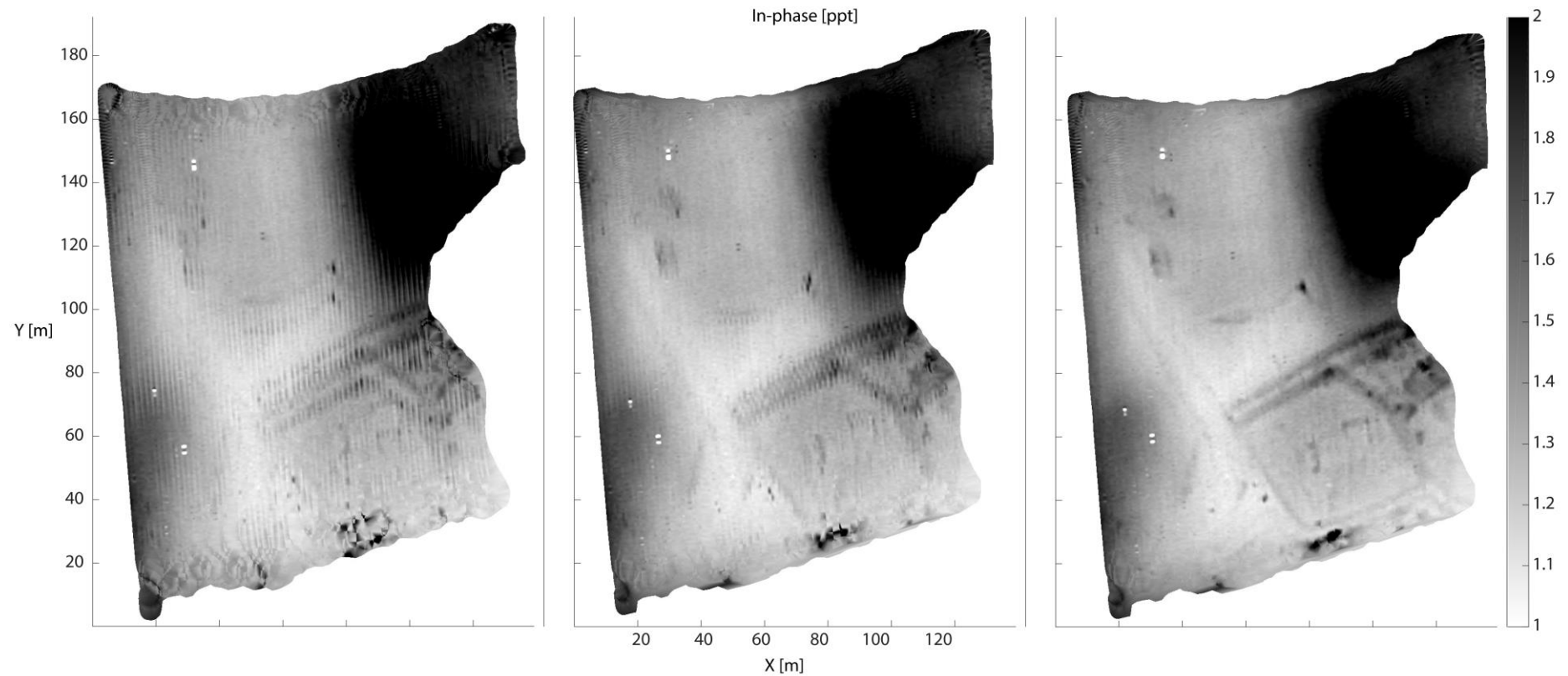


Fig 3.12 HCP2 in-phase grids: (left) data without spatial offset correction or time lag correction; (centre) data after spatial offset correction and (right) data after spatial offset correction and a time lag correction of 0.8 s. The scattered data were gridded using a linear interpolation, the coordinates shown are relative coordinates and the colour scale does not show the full range.

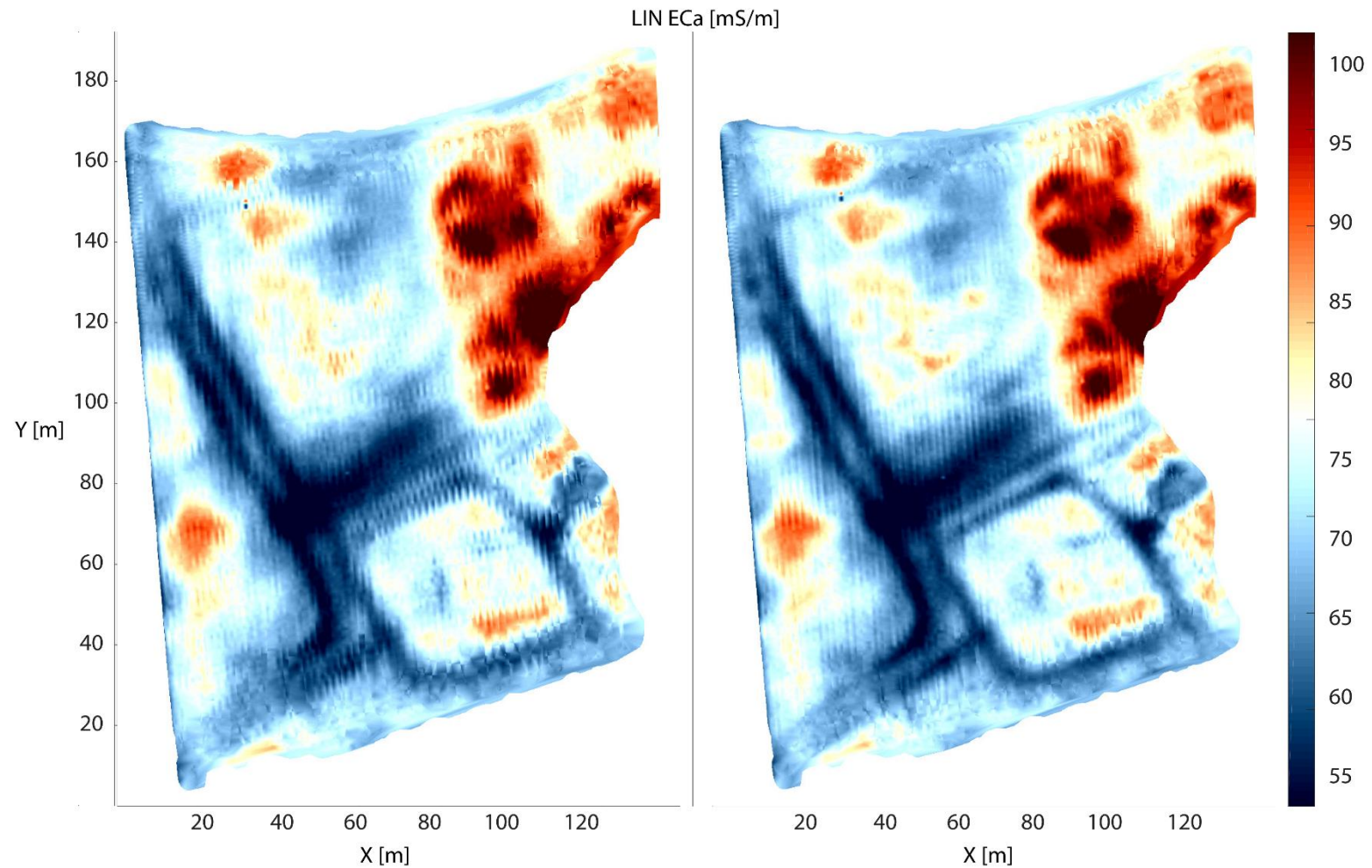


Fig 3.13 PRP4 LIN σ_a grids: (left) data after spatial offset correction and (right) data after spatial offset correction and a time lag correction of 0.8 s. The scattered data were gridded using a linear interpolation, the coordinates shown are relative coordinates and the colour scale does not show the full range

3.4 Conclusions

Spatial offset corrections were developed for a specific purpose and while they can be applied universally, their performance (accuracy-wise) is not constant. Therefore, a given correction should not be used indiscriminately. For the considered cases (high-resolution surveys that use a connection which rotates around a pivot on the towing vehicle), a horizontal offset correction involving a kinematic correction (to predict the location of the front of the sled) followed by a direction vector or constrained shift (for predictions along the sled) was found to be best practice. However, it is important to note that the assessed correction methods resulted in very similar errors when regarding only the straight track data. The main differences were in the track turn data, which may be less important for some applications. However, when surveying small plots the track turns may constitute >10 % of the entire survey area. Moreover, the strengths and weaknesses of the applied corrections were evaluated, allowing selection of an appropriate correction for a given survey implementation (Table 4).

It is clear that positional accuracies of sensor data cannot be equated to the positioning system accuracies when spatial offsets are present. Relating logged position data to other survey data is routinely done with little regard for spatial (and temporal) offsets despite the risk of severe positional accuracy deterioration. This is a weak link, given the fact that both survey data resolution and positioning system accuracy keep increasing. The proposed methodology, which consists of validating the positions obtained using several positioning systems to accurately assess the prediction errors, will surely improve the under-exposed science of correcting for spatial offset and time lags. Conversely, this methodology can also be used to optimize the survey set-up, given a certain correction, by evaluating the effect of sled or cart design on positional accuracy.

Future venues that can be explored are the application of hybridized correction methods or development of more accurate models. Yet technological advances are most likely to enhance positional accuracy in a generally applicable way. Nonetheless, corrections as described in this chapter remain useful because they can be applied retrospectively and are free.

It has been shown that temporal offsets cannot be overlooked when performing FDEM surveys. Though precise time-lag detection is technically challenging, temporal offset assessment can be done in a practical way. Making use of the capabilities of GUI's and making a visual assessment seems like a viable and efficient solution. A complication is the sometimes asymmetric response of some FDEM coil configurations.

3.5 Matlab scripts

Constrained spatial offset correction

```
function out_data = shift_constrained(XY,time_d,shift,timestep)
% Copyright 2014 Samuël Delefortrie <samuel.delefortrie@ugent.be>

% Programmed by: Samuël Delefortrie
% Affiliation: ORBit, UGent, Belgium
% Created in: Matlab 2013a

% References:
% Delefortrie, S. et al., 2016.
% Evaluating corrections for a horizontal offset between sensor and
% position data for surveys on land.
% Precision Agriculture 17 (3), 349-364.

% CONSTRAINED IN-LINE SHIFT: Constrained spatial offset correction
% Input
% 'XY': array of column vectors. [m].
%   cartesian XY coordinates [m] in the first two columns
% 'time_d': columnvector containing positioning time stamps. [s].
%   time is assumed to be always increasing [s]
% 'shift': spatial offset [m].
%   positive: sensor is behind the GNSS receiver
%   negative: sensor is in front of the GNSS receiver
% 'timestep': [s]. Optional. Default is 0.03 s
%   Smaller timestep means higher accuracy
% Output
% 'out_data': column array with shifted coordinates

% Argument checking
narginchk(3,4);
if (nargin < 4); timestep = 0.03; end
if shift == 0; out_data = XY; return; end

% Number crunching
% Add an identifier to time data and separate data
time_d(:,2) = 0;
XY = XY(:,1:2);
S_data = XY(:,3:end);

% Add synthetic time data to sensordata for improving shift error
Syn_S = (round(time_d(1,1))+1e-5:timestep:round(time_d(end,1))-1e-5)';
Syn_S(:,2) = NaN;
Syn_data = sortrows([time_d;Syn_S],1);

% Piecewise polynomial interpolation of GPS data to sensor data
XY_track(:,1) = pchip(time_d(:,1), XY(:,1), Syn_data(:,1)); % X
XY_track(:,2) = pchip(time_d(:,1), XY(:,2), Syn_data(:,1)); % Y

% Calculate x and y difference subsequent XY coordinates
XY_diff = [0,0;(XY(2:1:end,1:2) - XY(1:1:end-1,1:2))];
% Calculate distance subsequent XY coordinates
XY1S_dis = sqrt(XY_diff(:,1).^2 + XY_diff(:,2).^2);
% Cumulative sum of distance (total distance with time)
```

```
XY_dis_cum = cumsum(XY1S_dis)';

% Calculate X and Y difference subsequent XY track coordinates
XY_diff_track = [0,0;(XY_track(2:1:end,1:2) - XY_track(1:1:end-1,1:2))];
% Calculate distance subsequent XY track coordinates
XY1S_dis_track = sqrt(XY_diff_track(:,1).^2 + XY_diff_track(:,2).^2);
% Cumulative sum of track distance
XY_dis_cum_track = cumsum(XY1S_dis_track)';
% Shift total distance with time
XY_dis_cum_shift = XY_dis_cum_track - shift;

% Find indices of XYshiftcumsum in XYcumsum
[~,ind] = histc(XY_dis_cum_shift,...
    [-inf,(XY_dis_cum_track(1:end-1)+XY_dis_cum_track(2:end))/2,inf]);
ind = ind'; excl = isnan(Syn_data(:,2)); ind(excl) = [];
XY_shift = XY_track(ind,:);

% Calculate initial positions
if shift >= 0
    % Find values where intial positions need to be predicted
    ind_sel = find(XY_dis_cum < shift,1,'last');
    % Find probable driving direction
    ind_sel2 = find(XY_dis_cum > shift & XY_dis_cum < 100,1,'first');
    if isempty(ind_sel2)
        ind_sel2 = 2;
    end
    dx2 = XY(ind_sel2,1)-XY(1,1);
    dy2 = XY(ind_sel2,2)-XY(1,2);
    Dist2 = sqrt(dx2^2 + dy2^2);
    % Calculate initial positions
    XY_shift(1:ind_sel,1) = XY(1:ind_sel,1) - shift * dx2(1)/Dist2(1);
    XY_shift(1:ind_sel,2) = XY(1:ind_sel,2) - shift * dy2(1)/Dist2(1);
else
    % Find values where final positions need to be predicted
    ind_sel = find(XY_dis_cum > XY_dis_cum(end) + shift,1,'first');
    dx2 = XY(ind_sel:end,1)-XY(ind_sel-1:end-1,1);
    dy2 = XY(ind_sel:end,2)-XY(ind_sel-1:end-1,2);
    Dist2 = sqrt(dx2.^2 + dy2.^2);
    Dist2_cum = cumsum(Dist2);
    % Find probable driving direction
    ind_sel2 = find(XY_dis_cum > XY_dis_cum(end) + shift -2,1,'first');
    dx3 = XY_shift(end,1)-XY_shift(ind_sel2,1);
    dy3 = XY_shift(end,2)-XY_shift(ind_sel2,2);
    Dist3 = sqrt(dx3^2 + dy3^2);
    % Calculate initial positions
    XY_shift(ind_sel:end,1) = XY_shift(ind_sel,1) ...
        + Dist2_cum(1:end) * dx3/Dist3;
    XY_shift(ind_sel:end,2) = XY_shift(ind_sel,2) ...
        + Dist2_cum(1:end) * dy3/Dist3;
end

% Put XY shifted coordinates in the array
out_data = XY_shift;
out_data = [out_data,S_data];

end
```

Direction vector spatial offset correction

```
function out_data = shift_dir_vec(XY,shift,dist_find)
% Copyright 2014 Samuël Delefortrie <samuel.delefortrie@ugent.be>

% Programmed by: Samuël Delefortrie
% Affiliation: ORBit, UGent, Belgium
% Created in: Matlab 2013a

% References:
% Delefortrie, S. et al., 2016.
% Evaluating corrections for a horizontal offset between sensor and
% position data for surveys on land.
% Precision Agriculture 17 (3), 349-364.

% DIRECTION VECTOR SHIFT: in-line direction vector offset correction
% Input
% 'XY': array of column vectors. [m].
% cartesian XY coordinates [m] in the first two columns
% 'shift': spatial offset [m].
% positive: sensor is behind the GNSS receiver
% negative: sensor is in front of the GNSS receiver
% dist_find: preferred distance between points for direction
% calculation [m]
% Output
% 'out_data': column array with shifted coordinates

% Argument checking
narginchk(2,3);
if shift == 0; out_data = XY; return; end

% Separate data
XY = XY(:,1:2);
S_data = XY(:,3:end);

% Cumulative sum of distance (total distance with time)
XY_diff = [0,0;(XY(2:1:end,1:2) - XY(1:1:end-1,1:2))];
Dist = sqrt(XY_diff(:,1).^2 + XY_diff(:,2).^2);
XY_dis_cum = cumsum(Dist);

% Shift cumulative distance
XY_dis_cum_shift = XY_dis_cum - dist_find;

% Find indices of XYshiftcumsum in XYcumsum
[~,ind] = histc(XY_dis_cum_shift',...
    [-inf;(XY_dis_cum(1:end-1)+XY_dis_cum(2:end))/2;inf]);

% Find direction vectors and do not allow distances of 0
diffx = XY(:,1) - XY(ind,1);
diffy = XY(:,2) - XY(ind,2);
Dist = sqrt(diffx.^2 + diffy.^2);
Dist(Dist == 0) = 1e-10;
diffx_R = diffx ./ Dist;
diffy_R = diffy ./ Dist;
```

```
% Calculate shifted coordinates
XY_shift(:,1) = XY(:,1) - diffX_R * abs(shift);
XY_shift(:,2) = XY(:,2) - diffY_R * abs(shift);

% Calculate initial positions
if shift >= 0
    % Find values where initial positions need to be predicted
    ind_sel = find(XY_dis_cum < shift,1,'last');
    % Find probable driving direction
    ind_sel2 = find(XY_dis_cum > shift & XY_dis_cum < 100,1,'first');
    dx2 = XY(ind_sel2,1)-XY(1,1);
    dy2 = XY(ind_sel2,2)-XY(1,2);
    Dist2 = sqrt(dx2^2 + dy2^2);
    % Calculate initial positions
    XY_shift(1:ind_sel,1) = XY(1:ind_sel,1) - shift * dx2(1)/Dist2(1);
    XY_shift(1:ind_sel,2) = XY(1:ind_sel,2) - shift * dy2(1)/Dist2(1);
else
    % Find values where final positions need to be predicted
    ind_sel = find(XY_dis_cum > XY_dis_cum(end) + shift,1,'first');
    dx2 = XY(ind_sel:end,1)-XY(ind_sel-1:end-1,1);
    dy2 = XY(ind_sel:end,2)-XY(ind_sel-1:end-1,2);
    Dist2 = sqrt(dx2.^2 + dy2.^2);
    Dist2_cum = cumsum(Dist2);
    % Find probable driving direction
    ind_sel2 = find(XY_dis_cum > XY_dis_cum(end) + shift -2,1,'first');
    dx3 = XY_shift(end,1)-XY_shift(ind_sel2,1);
    dy3 = XY_shift(end,2)-XY_shift(ind_sel2,2);
    Dist3 = sqrt(dx3^2 + dy3^2);
    % Calculate initial positions
    XY_shift(ind_sel:end,1) = XY_shift(ind_sel,1) ...
        + Dist2_cum(1:end) * dx3/Dist3;
    XY_shift(ind_sel:end,2) = XY_shift(ind_sel,2) ...
        + Dist2_cum(1:end) * dy3/Dist3;
end

% Put XY shifted coordinates in the output array
out_data = XY_shift;
out_data(:,3:2+size(S_data,2)) = S_data;

end
```

Kinematic spatial offset correction

```
function out_data = shift_tractrix(XY,shift)
% Copyright 2012 Tom Gottfried <tom.gottfried@tum.de>

% Programmed by: Jan De Pue and Samuël Delefortrie
% Affiliation: ORBit, UGent, Belgium
% Created in: Matlab 2013a

% References:
% Gottfried T., Auerswald K., Ostler U., 2012, Kinematic correction
% for a spatial offset between sensor and position data in on-the-go
```

```
% sensor applications.
% Computers and Electronics in Agriculture 84, 76-84

% Delefortrie, S. et al., 2016.
% Evaluating corrections for a horizontal offset between sensor and
% position data for surveys on land.
% Precision Agriculture 17 (3), 349-364.

% KINEMATIC IN-LINE SHIFT: kinematic spatial offset correction
% Input
% 'XY': array of column vectors. [m].
% cartesian XY coordinates [m] in the first two columns
% 'shift': spatial offset [m].
% only positive: sensor is behind the GNSS receiver
% Output
% 'out_data': column array with shifted coordinates

% Argument checking
narginchk(2,2);
if shift == 0; out_data = XY; return; end

% Distances of subsequent points
nP = size(XY,1);
dX = XY(2:end,1) - XY(1:end-1,1);
dY = XY(2:end,2) - XY(1:end-1,2);
Dist = sqrt(dX.^2 + dY.^2);
Dist(Dist == 0) = 1e-12;
P_dPcum = cumsum(Dist);

% Predict location initial point
ind_sel = find(P_dPcum > 1 & P_dPcum < 100,1,'first') + 1;
if isempty(ind_sel); ind_sel = 2; end
% ind_sel = ind_sel(1);
dx2 = XY(ind_sel,1) - XY(1,1);
dy2 = XY(ind_sel,2) - XY(1,2);
Dist2 = sqrt(dx2^2 + dy2^2);
% Dist2(Dist2 == 0) = 1e-12;
out_data = zeros(nP,2);
out_data(1,1) = XY(1,1) - shift * dx2/Dist2;
out_data(1,2) = XY(1,2) - shift * dy2/Dist2;

% Alpha
cosalpha = dX./Dist;
sinalpha = dY./Dist;

% Pre-allocated calculations
Cst_1 = exp(2*Dist/shift);
Cst_2 = Dist - 2*shift;
Cst_1x2 = Cst_1 .* Cst_2;
Cst_3 = exp(Dist./shift);
Cst_4 = shift .* cosalpha;
Cst_5 = shift .* sinalpha;

for LoopInd = 1:nP-1
    if Dist(LoopInd) == 0
        % Static shift
        out_data(LoopInd+1,1:2) = out_data(LoopInd,1:2); % XY coordinates
```

```
else
    % Tractrix shift
    Diff_XY_S_x = XY(LoopInd,1) - out_data(LoopInd,1);
    Diff_XY_S_y = XY(LoopInd,2) - out_data(LoopInd,2);

    Diff_transform_x = cosalpha(LoopInd) * Diff_XY_S_x ...
        + sinalpha(LoopInd) * Diff_XY_S_y;
    Diff_transform_y = -sinalpha(LoopInd) * Diff_XY_S_x ...
        + cosalpha(LoopInd) * Diff_XY_S_y;

    cos_phi = Diff_transform_x/shift;
    sin_phi = Diff_transform_y/shift;

    if cos_phi >= 0
        Cst_6 = (1+cos_phi) / 2;
        Cst_7 = (1-cos_phi) / 2;

        Cst_s1 = Cst_1x2(LoopInd) * Cst_6 + Dist(LoopInd) * Cst_7;
        Cst_s2 = Cst_1(LoopInd) * Cst_6 + Cst_7;
        Cst_s3 = (Cst_5(LoopInd) * sin_phi - Cst_4(LoopInd) ...
            * (1 + cos_phi)) / (Cst_6 + Cst_7);
        Cst_s4 = ((- Cst_5(LoopInd) * (1 + cos_phi)) ...
            - (Cst_4(LoopInd) * sin_phi)) / (Cst_6 + Cst_7);

        out_data(LoopInd+1,1) = out_data(LoopInd,1) ...
            + (cosalpha(LoopInd) * Cst_s1 + (Cst_3(LoopInd) ...
            * Cst_5(LoopInd) * sin_phi)) / Cst_s2 ...
            - Cst_s3;

        out_data(LoopInd+1,2) = out_data(LoopInd,2) ...
            + (sinalpha(LoopInd) * Cst_s1 - (Cst_3(LoopInd) ...
            * Cst_4(LoopInd) * sin_phi)) / Cst_s2 ...
            - Cst_s4;
    else
        % Static shift
        out_data(LoopInd+1,1:2) = out_data(LoopInd,1:2);
    end
end
end

end
```

Lateral offset correction

```
function out_data = shift_lateral(XY,xv,yv,dist_find)
% Copyright 2014 Samuël Delefortrie <samuel.delefortrie@ugent.be>

% Programmed by: Samuël Delefortrie
% Affiliation: ORBit, UGent, Belgium
% Created in: Matlab 2013a

% LATERAL SHIFT: direction vector spatial offset correction
% Input
% 'XY': array of column vectors. [m].
```

```
% cartesian XY coordinates [m] in the first two columns
% 'xv': longitudinal distance to be shifted [m]
% 'yv': lateral distance to be shifted [m]
% dist_find: preferred distance between points for direction
% calculation [m]
% Output
% 'out_data': column array with shifted coordinates

% Argument checking
narginchk(2,4);
if (nargin < 4); dist_find = 4; end
if xv == 0 && yv == 0; out_data = XY; return; end

% Cumulative sum of distance (total distance with time)
XY_diff = [0,0;(XY(2:1:end,1:2) - XY(1:1:end-1,1:2))];
Dist = sqrt(XY_diff(:,1).^2 + XY_diff(:,2).^2);
XY_dis_cum = cumsum(Dist);

% Shift cumulative distance
XY_dis_cum_shift = XY_dis_cum - dist_find;

% Find indices of XYshiftcumsum in XYcumsum
[~,ind] = histc(XY_dis_cum_shift',...
    [-inf;(XY_dis_cum(1:end-1)+XY_dis_cum(2:end))/2;inf]);

% Find direction vectors and do not allow distances of 0
diffx = XY(:,1) - XY(ind,1);
diffy = XY(:,2) - XY(ind,2);
Dist = sqrt(diffx.^2 + diffy.^2);
Dist(Dist == 0) = 1e-10;
cos_beta = diffx ./ Dist;
sin_beta = diffy ./ Dist;

% Adjust initial predictions
ind_sel = find(XY_dis_cum < dist_find,1,'last');
cos_beta(1:ind_sel) = cos_beta(ind_sel+1);
sin_beta(1:ind_sel) = sin_beta(ind_sel+1);

% % Increase robustness
% cos_beta = smooth(cos_beta,10);
% sin_beta = smooth(sin_beta,10);

% Discrete points on pathway of point of attachment (A)
G_to_A = zeros(size(XY,1),2);
G_to_A(:,1) = cos_beta*xv - sin_beta*yv;
G_to_A(:,2) = sin_beta*xv + cos_beta*yv;
out_data(:,1:2) = XY(:,1:2) - G_to_A;

end
```


Chapter 4

Signal instability

“There is nothing stable in the world
Uproar's your only music.”

-- John Keats

“Cambia lo superficial
Cambia también lo profundo
Cambia el modo de pensar
Cambia todo en este mundo”

-- Julio Numhauser,
“Todo cambia”

This chapter was modified from:

Delefortrie, S., De Smedt, P., Saey, T., Van De Vijver, E., Van Meirvenne, M., 2014. An efficient calibration procedure for correction of drift in EMI survey data. *Journal of Applied Geophysics* 110: 115-125.

4.1 Drift compensation in literature

Regardless of the application, FDEM instrument response(s) may suffer from a drift with time, which is recognized as a systematic data error by Minsley et al. (2012) together with incorrect instrument calibration and improper data levelling. Signal drift can be visualized by performing a stationary recording (e.g. Gebbers et al., 2009), and is characterized as a systematic variation that exceeds the random signal noise over time, despite no appreciable changes above or underneath the surface. It is unwanted as it decreases the reliability of collected data: global trends and/or abrupt changes not related to the underground can be introduced in the data.

When the signal-to-noise ratio (S/N) is low, instrument drift becomes a critical disturbance since the magnitude may near the observed response (Grellier et al., 2013). Inversely, the error becomes less significant when the signal-to-noise ratio is high (Abdu et al., 2007). Yet even when the S/N is high, a relatively limited drift is unwanted given the high level of accuracy of modern instruments. Beamish (2011) states that the reference level of accuracy in apparent conductivity data may be less than 0.25 mS/m, though this is influenced by the sampling interval, instrument accuracy and survey setup.

The cause for signal drift is not unambiguous. It has long been clear that the temperature dependency of circuit elements can cause slow shifts in null values (Keller and Frischnecht, 1966). However, Robinson et al. (2004) concluded that differential heating of instrumentation is but one factor contributing to drift. They suggested that it may be caused by a combination of instrument factors such as circuit design, placement of temperature compensation sensors and coil performance under heating. Thus it is important to realize that any instability encountered, when using a commercially available instrument, is residual. Commercially available sensors employ temperature compensation circuitry (which accounts for differential temperature variations of the instrument) and other internal compensations (such as accounting for ambient temperature variations). It follows that attempting to relate drift to ambient or internal variations can be obfuscated due to this. Sudduth et al. (2001) performed various accuracy tests with an FDEM sensor and inferred that ambient temperature variations could not be consistently related to drift.

The need to compensate for effects of drift has been recognized by several authors and different procedures for compensation have been developed:

- Robinson et al. (2004) recommended turning on the instrument 2 hours ahead of surveying at the location as well as shading the sensor to limit (differential) heating. This approach is time consuming and the authors recognized that drift may only partially be corrected for by field compensation. It was also suggested that the coil temperature may be recorded to

exclude potentially inaccurate data. Abdu et al. (2007) likewise advocated field compensation such as shading the sensor and choosing a cooler day.

- Sudduth et al. (2001) and Abraham et al. (2006) proposed the use of repeat measurements at a fixed calibration point or transect during a survey for drift assessment and correction. Such an approach is time-consuming and results in a very discrete evaluation of drift. If the evolution of drift is too sparsely logged or calculated (viewed over time), accurate compensation for an abrupt drift may not be possible.
- Use of a calibration line that crosses the entire survey area within a short time frame. Hereby, coincident calibration and survey data (or cross-over points) are collected. The use of a so-called tie-line has been used frequently for HEM surveys (Siemon, 2009) but is not recommended due to discrepancies in tie line data owing to altitude differences. The use of a calibration line for drift correction of land-based surveys was mentioned by Simpson et al., (2009) though no methodological information or evaluation was provided.
- Grellier et al. (2013) advocated the use of nulling measurements every 5 to 20 measurements during a survey, at the then held position, to calculate drift offset. The calibration requires the instrument to be held 1.5 m above ground. Following, the ratio between apparent conductivity in horizontal coplanar orientation and vertical coplanar orientation is determined and the deviation with this ratio is calculated. They found that this method is considerably more efficient than performing repeat measurements at one location during a survey. However, the procedure is time-consuming.
- Procedures requiring other geophysical data (Deszcz-Pan et al., 1998; Minsley et al., 2012). However, accurate ancillary data are not always available (in sufficient quantity). In addition accurate forward modelling and laborious processing is required.
- Filtering of survey data to account for systematic errors: data are processed after collection to conform to an expected statistical profile. This approach does not inform about the absolute value of drift, and does not discern between a trend caused by drift and a trend due to variation in the subsurface.

The drift correction procedure proposed in this chapter aims at (1) a near continuous evaluation of drift of both out-of-phase and in-phase responses for land-based FDEM data, without use of ancillary data or need of time consuming repeat measurements, as well as (2) a drift compensation that is suitable for various drift effects and survey setups. For this purpose, a calibration line that crosses the entire survey area within a short time frame is employed. Comparison of coincident calibration and survey data (or tie-line data) can then be used to model and subtract the drift. This is performed by applying outlier detection and removal, followed by curve fitting of the residuals. Suitability for different survey setups and drift effects is examined, and the benefits and drawbacks of the procedure are discussed.

The different drift compensation strategies are summarized in Table 1.

Table 4.1 Strategies for mitigating or correcting for FDEM signal instability available in scientific literature.

<i>Method</i>	<i>Strategy</i>	<i>References</i>
Field compensation	Choosing a cool day	Abdu et al. (2007)
	Shading of the instrument	Robinson et al. (2004)
	Allowing a “warm-up” time	Robinson et al. (2004)
Nulling	Lifting of instrument during survey and comparing output with calculated response ratios	Grellier et al. (2013)
Collection of repeat measurements	Fixed calibration point	Abraham et al. (2006)
	Repeat transect	Sudduth et al. (2001)
	Area calibration line (Tie lines)	Simpson et al. (2009)
Collection of ancillary data	Using ERT	Minsley et al. (2012)
	Using borehole information	Moghadas et al. (2012)
Prior assumptions	Levelling	Siemon (2009) –for HEM

4.2 Materials and methods

Data collection

Multi-receiver FDEM data were collected using a Dualem 21S and 421S. During surveying, the instrument was positioned in a polyethylene sled that encased the instrument at an elevation (inter-coil centre line) of 0.16 m. For area investigation, the sled was towed by an all-terrain vehicle (ATV) by use of a flexible connection (two ropes). The sled ran parallel to the driving direction and the offset between the front of the sensor and the vehicle was around 3.5 m. Geographic coordinates were logged using a GNSS system which was located on the vehicle. All area survey data were collected in Belgium, The Netherlands and the UK. When performing a stationary recording, the instrument was located in an open field, with no power lines or leads above surface or underground to minimize ambient interference.

Data processing

Duplicate points of the FDEM data were removed by requiring subsequent points (viewed in time) to be at least 6 cm apart. A spatial and temporal offset correction was performed on all area survey data, using the methods discussed in chapter 3.

A Hampel filter is a moving window, nonlinear filter that detects local outliers in a time-series (Pearson, 2002). These can then be deleted or replaced by the local median. The code used for applying the filter can be found in Nielsen (2012) –written in Matlab- or Smith (2013) –written using

C-. Input parameters are half-width of the filter window and a threshold to determine upper and lower bounds outside of which point data are considered outliers. More details about the Hampel filter can be found in Pearson (2002). By comparing the Hampel filter with moving average or median filters applied to several FDEM datasets, it was found that is generally more suitable for noisy time series with sudden breaks or erratic behaviour.

B-splines are spline functions constructed from polynomial pieces, joined at certain values of x (time, when working with time series), the knots or spline breaks. Once the breaks are given, the B-splines can be computed recursively, for any desired degree of the polynomial. A short overview of B-splines and their construction can be found in Eilers and Marx (1996). The (Matlab) code used for the curve fitting by use of B-splines can be found in Lundgren (2010). Both Hampel parameter selection and B-spline fitting was performed by user specification in a GUI.

To warrant an accurate drift correction based on tie-line data, the execution of the calibration line has to be conceptually sound. It should: (i) cross the entire survey area, preferably with several passes more or less perpendicular to the survey lines to achieve a good balance between area coverage and time needed for the calibration line (ii) allow comparison over the entire survey time range (iii) be kept as brief as possible (e.g. < 15 min) (iv) be executed at a low, constant speed and (v) preferably be performed when the instrument has had a sufficiently long ‘warm-up’ (e.g. 20 minutes).

Tie-line comparison data can be expressed as simple residuals ($z_{\text{res}} = z_{\text{survey}} - z_{\text{cal}}$ or the inverse) at the comparison locations. Measurements recorded at the same place at different times might deviate due to signal drift. However, instrument noise, which ambient interference may exacerbate, contributes to calculated differences as well. Since instrument drift is a systematic error it may be recognized as a pattern exceeding the instrument noise level. In addition, other sources of deviation between the calibration and survey data, also occur:

- Positional accuracy of the measurements affects the comparison of calibration and survey points. If there is a temporal or spatial offset between sensor and positioning data a correction is crucial (see Chapter 6).
- Difference in orientation of the instrument at coincident points (see Figure 4.1) is another cause for discrepancy and may even give rise to extreme outliers (e.g. above underground metallic objects). Topography may exacerbate differences: aside from a difference in planar direction it may give rise to a difference in the pitch and roll of the sensor.



Fig 4.1 FDEM survey tracks of high resolution datasets with indication of well-executed calibration lines (red): (top) 3.5 ha survey at Hoeke (Belgium); (middle) 3.8 ha survey at Damme (Belgium); (bottom) 7.1 ha survey near Stonehenge (UK). The coordinates shown are WGS84 coordinates.

When comparing calibration and survey data, (large-scale) systematic variations are assumed to be caused by instrument instability and can therefore only be modelled when such change can be discerned. The trends present in tie-line data can be obscured by aforementioned causes, related to the difference between the calibration and survey data, since errors can stack and introduce uncertainty (exceeding instrument noise levels). This creates the need for a statistical approach where it is opportune to have sufficient comparison points. It follows then that it is best to not limit the tie-line data to coincident points but, rather, to use a search windows and include several neighbouring locations if present within this window. If enough comparison locations are present, fitting a smooth, polynomial curve to the residuals is believed to model the drift. Thus, to model and subtract the drift, outlier removal and curve fitting are recommended.

Figure 4.2 summarizes the drift correction procedure. The correction consists in comparing the instrument responses at every calibration point and the survey points within a specified (circular) search window. For every pair, the time of the survey data is stored and the difference in response is calculated. Outlier detection, curve fitting and visualization of the residuals (a time series) is then possible. When spline fitting, the number of spline breaks or the exact location of the breaks is entered or pre-set as well as the order of the spline. The modelled drift can then be evaluated at every survey measurement (based on its time) and corrected for.

It is important to have a good understanding of the vertical scale when assessing drift. Outliers may complicate this and can adversely affect the fit when modelling drift by use of B-splines. Where they should be removed, a Hampel filter offers an adequate solution. The moving window filter also allows visualizing nominal data, which is similar to a local median for the time series. This nominal data may be equated to the estimated drift and can be evaluated for all survey points by linear interpolation. Nonetheless, the use of curve fitting is preferred since it allows more flexibility and user control (the procedure can be parameter sensitive). It is also noted that extrapolation of the modelled drift is not justifiable.

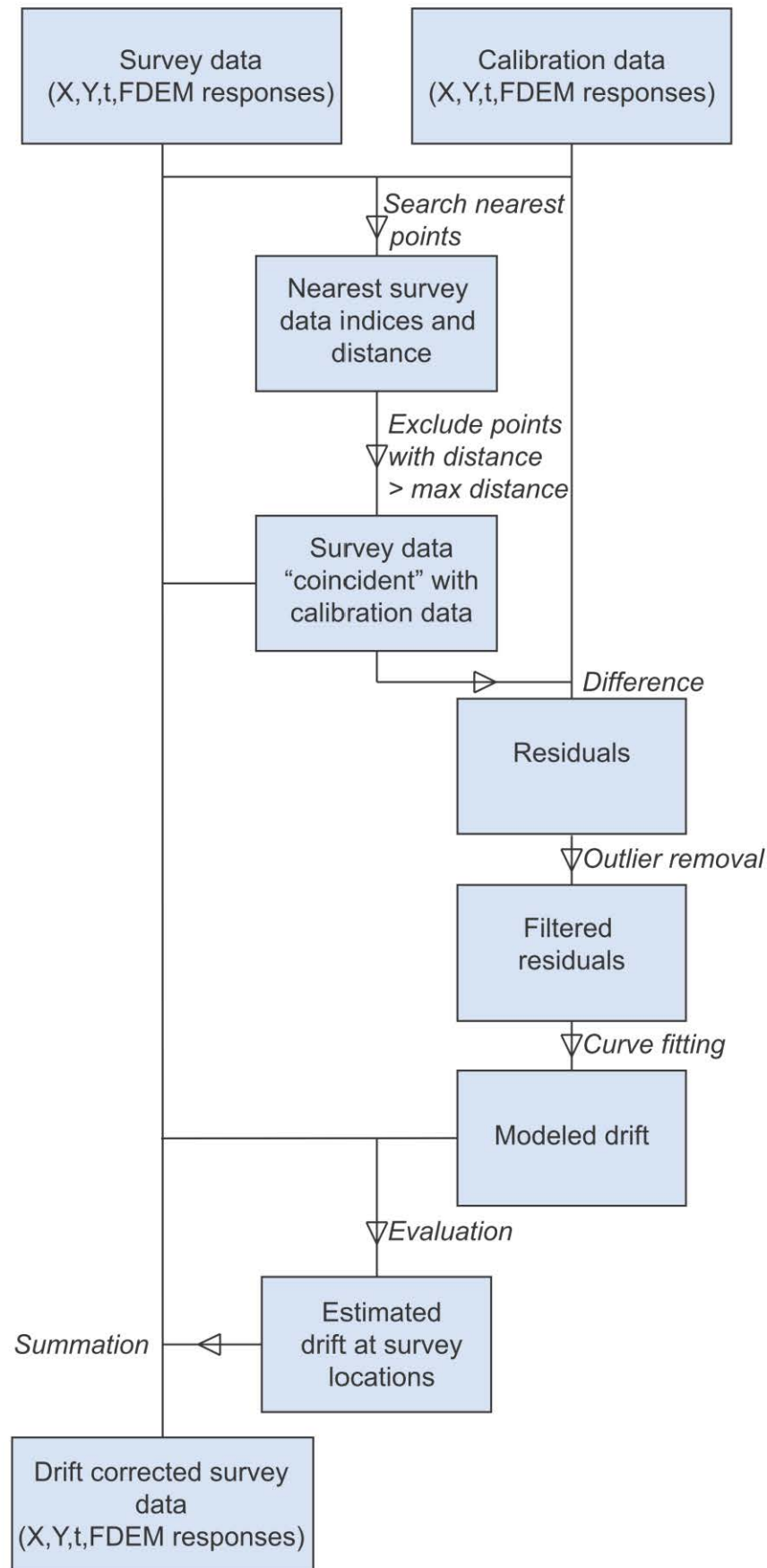


Fig 4.2 Flowchart summarizing the proposed routine for drift compensation.

4.3 Drift characterization and tie-line method evaluation

Stationary measurements

The temporal variation of instrument response, at a fixed location, is visualized on Figure 4.3. It is apparent that some (Dualetm) responses are more stable than others:

- The PRP QP responses are very stable, showing no or limited, linear drift.
- The HCP QP and in-phase responses show a quadratic trend with time. The greatest instability is encountered right after powering the sensor and complete stabilization with time may or may not occur.
- The PRP in-phase responses are rather unstable and show erratic behaviour.

Other stationary recordings have shown similar results and it follows that the drift of a coil configuration can be characterized (to a degree). It is also clear that a drift correction procedure has to be flexible since there are a wide range of drift effects (linear, quadratic and/or periodic trends as well as erratic behaviour).

To evaluate the noise levels of the signals, a moving window of ten seconds was utilised to calculate local ranges over the time series. These were then averaged to represent the noise levels (Table 2). It is noted that noise levels are influenced by ambient interference and by the sampling interval. Furthermore, it is clear that the noise level increases with increasing coil separation.

Table 4.1 Averaged local ranges (moving time window of 10 s) for the stationary recording data (sampling interval of 8 Hz). These values are an indication of the coil configuration noise levels.

	<i>LIN σ_a (mS/m)</i>	<i>Out-of-phase (ppt)</i>	<i>In-phase (ppt)</i>
HCP1	0.8	0.01	0.02
1PRP4	0.5	0.01	0.01
HCP2	1.0	0.07	0.07
2PRP4	0.9	0.07	0.07

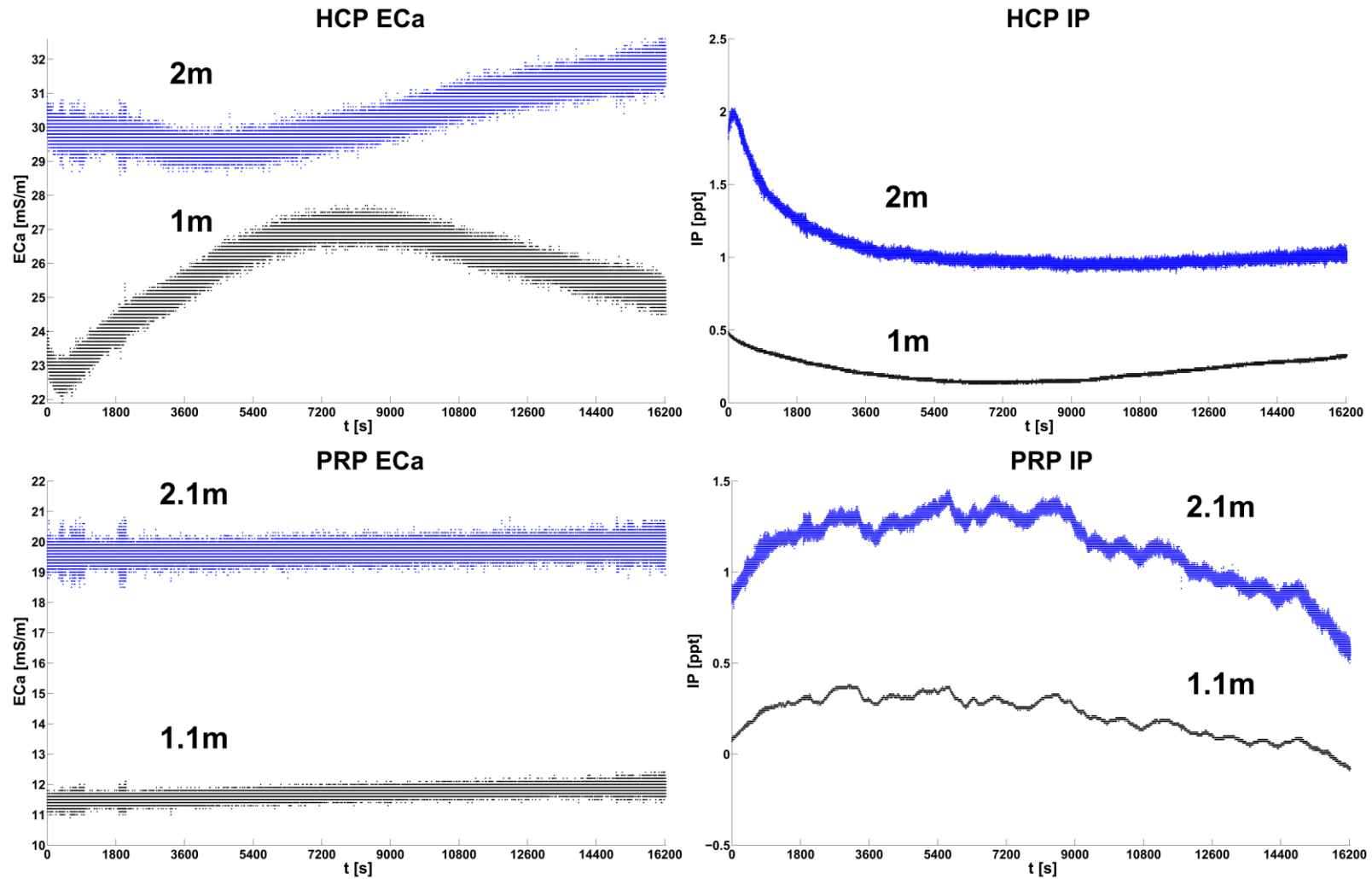


Fig 4.3 A 4.5 h stationary recording collected in Flanders with a Dualem 21S (129 600 measurement points for each response). The uppermost curves (black) are the 2 or 2.1 m coil configurations whilst the lower most curves (blue) are the 1 or 1.1 m coil configurations. The QP responses have been converted to LIN σ_a using the LIN approximation.

The main premise of the proposed drift correction is that the calibration data does not suffer from signal drift, or rather, that signal drift does not exceed instrument noise, given a small enough time window. The data suggest that this premise is viable for a five minute calibration line recording. Generally, the variation does not exceed the noise level in such a short time interval. However, performing the calibration line immediately after powering the instrument should be avoided, given that the greatest signal instability is usually encountered in this moment.

Application of drift correction procedure

The procedure detailed in this chapter was applied to many area surveys (> 100). A selection of modelled signal instabilities was made to illustrate the benefits and discuss the (dis)advantages of the procedure. Figure 4.4 exemplifies the use of the Hampel filter for HCP1 in-phase data collected in the UK. The uppermost plot shows that differences in response can be very large, due to high contrasting small-scale anomalies and/or presence of metal. Metal objects especially, may give rise to a vastly differing response when the orientation and position of the sensor differs. On all subsequent plots, outlier detection and removal was performed.

Case 1

An archaeological survey was conducted near Bruges in the framework of the FWO (Fund scientific research Flanders) project “Medieval Bruges and its outer ports. A landscape archaeological contribution to the Zwin-debate”. The area is located within the Belgian coastal plain and the near-surface is characterized mainly by Holocene clayey to loamy sand deposits with a possible presence of peat. The comparison of calibration and survey data as well as the modelled drift for a dataset collected are visualized in Figure 4.5. The dataset is a high resolution dataset: the survey lines are ~ 1 m apart and the distance between measurements along the survey track are ~ 20 cm. Similarly to the stationary recordings, the HCP QP (or out-of-phase) and in-phase drift are characterized as quadratic trends whereas PRP QP drift is characterized by high stability. The PRP in-phase responses are less stable, which was also concluded from the stationary recordings. It follows that a drift correction is not always necessary. Nonetheless, the need for drift compensation can be evaluated only when the drift is assessed. It is noted that when only some signals are significantly affected by drift, this poses a problem for processing that involves combination of the signals (e.g. principal component analysis of the signals).

Figure 4.5 and 4.6 visualize the PRP2 in-phase and HCP1 QP data before and after drift compensation. It is clear that the broad bands of the PRP2 in-phase data, caused by instability of the signal, are compensated for though some residual corrugations are left in the data due to the high instability and noise of this signal.

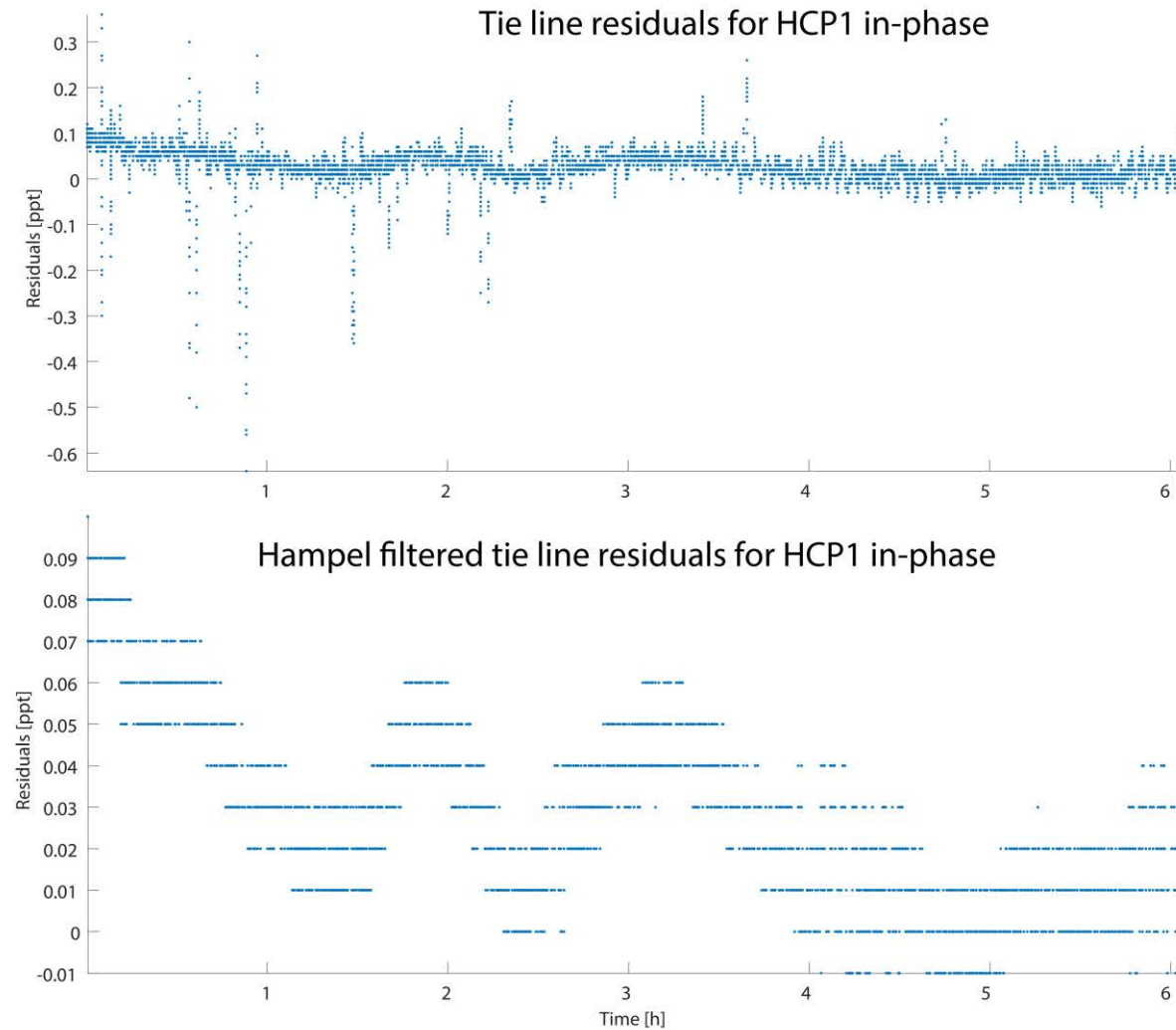


Fig 4.4 Tie line residuals (calibration minus survey data) for the HCP1 in-phase response of a UK survey before (top) and after outlier detection and removal (bottom). The following parameters were used for the hamper filter: a window of 300 [] and threshold of 1 []. The local range of the residuals is usually around one to three times the noise level of a response.

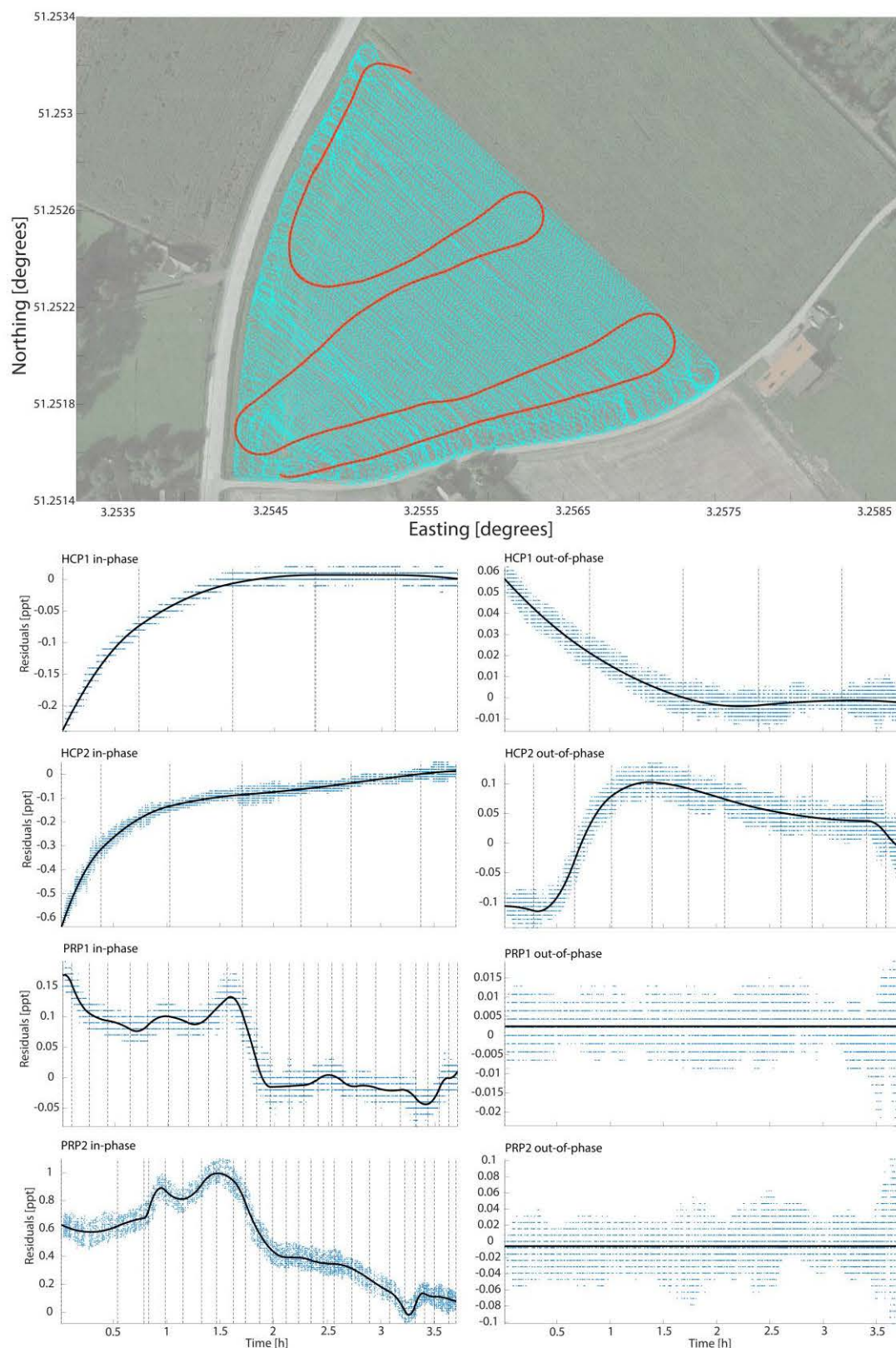


Fig 4.4 (top) Survey track for a high-resolution dataset (2.6 ha) collected in Belgium with indication of the calibration line (red). WGS84 coordinates are shown. The calibration line was collected in 6.5 min. (bottom) Hampel filtered tie line residuals (calibration minus survey data) for the Dualem 21S responses. Hampel filter window: 300 [] and threshold: 1 []. Because the calibration line was collected after the area survey, the tie line residuals near the end of the survey become (close to) zero. The fitted splines are black and the breaks are visualized using vertical dotted lines.

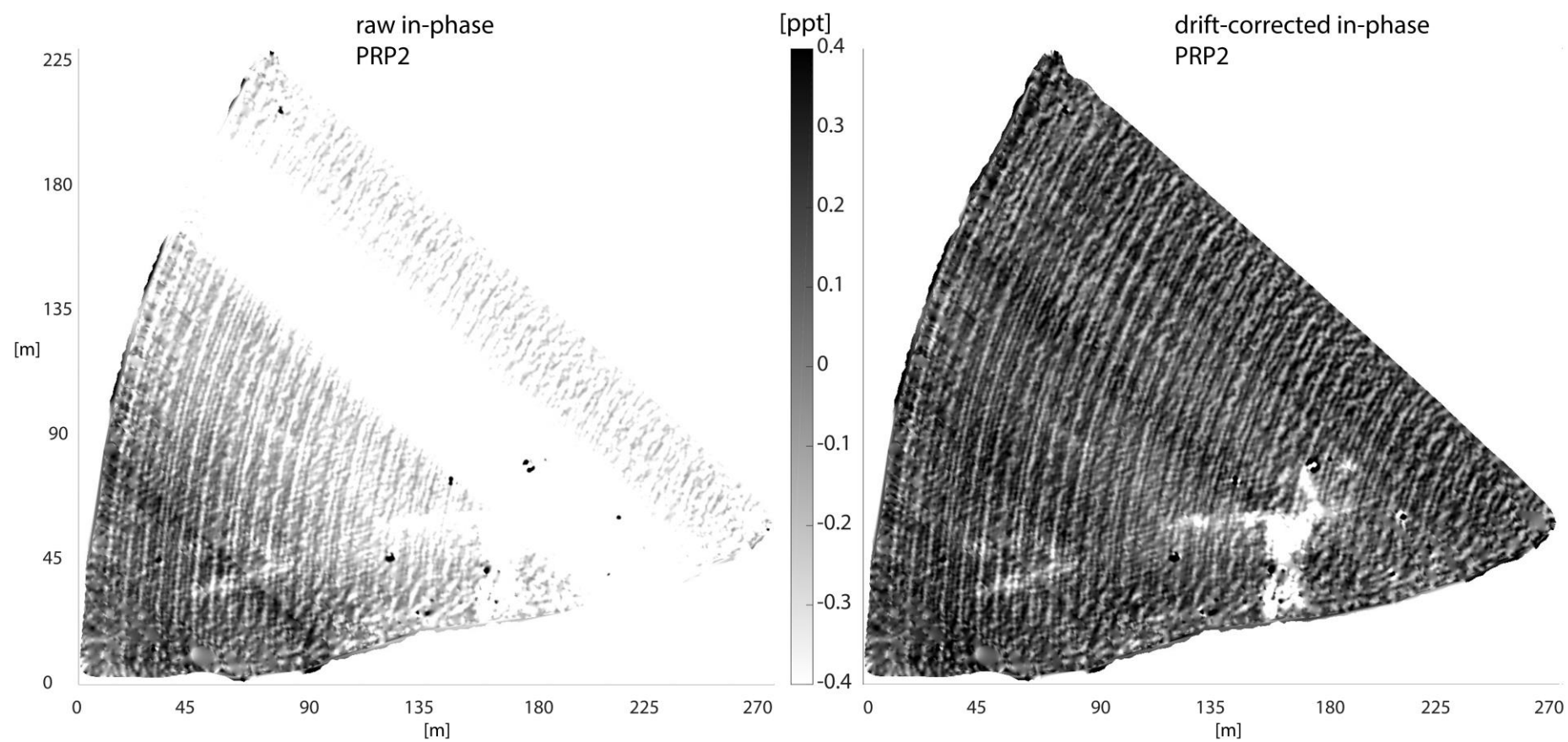


Fig 4.5 PRP2 in-phase response before and after drift compensation. See Fig. 4.4 for the modelled drift. Local coordinates are shown.

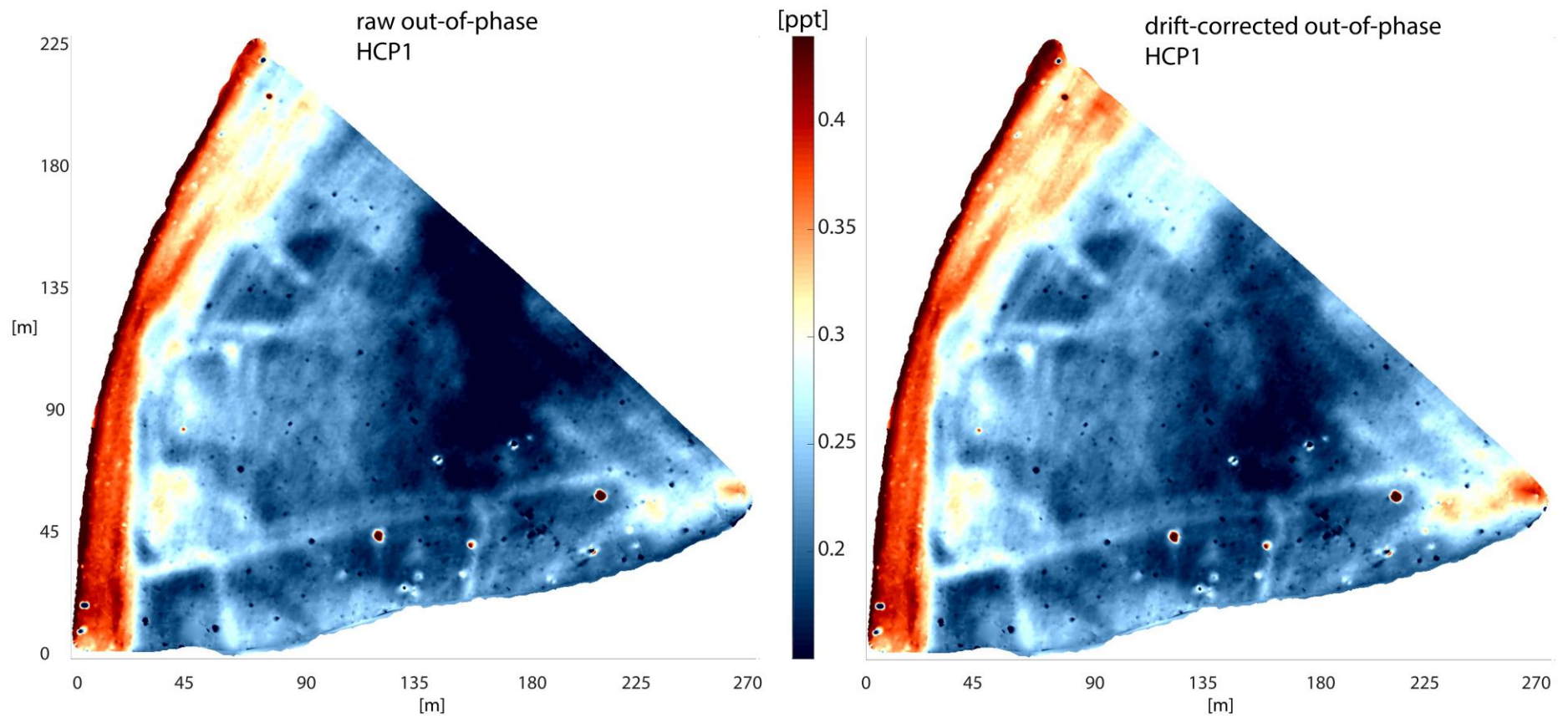


Fig 4.6 HCP1 out-of-phase response before and after drift compensation. See Fig. 4.4 for the modelled drift. Local coordinates are shown.

Case 2

FDEM data were collected in Assenede (Belgium) on farmland overlying Quaternary deposits. In the subsurface a salt lens was present owing to past tidal entries (during the Holocene) in these parts: conductivities of up to 500 mS/m were measured at 1.5 m depth.

When regarding an area with high conductivity, the tie-line data are strikingly more noisy (Fig 4.7) –when applying the same hampel filter parameters. This was not due to higher ambient interference and the major contributor was therefore likely a greater sensitivity to instrument geometry in high conductive environments.

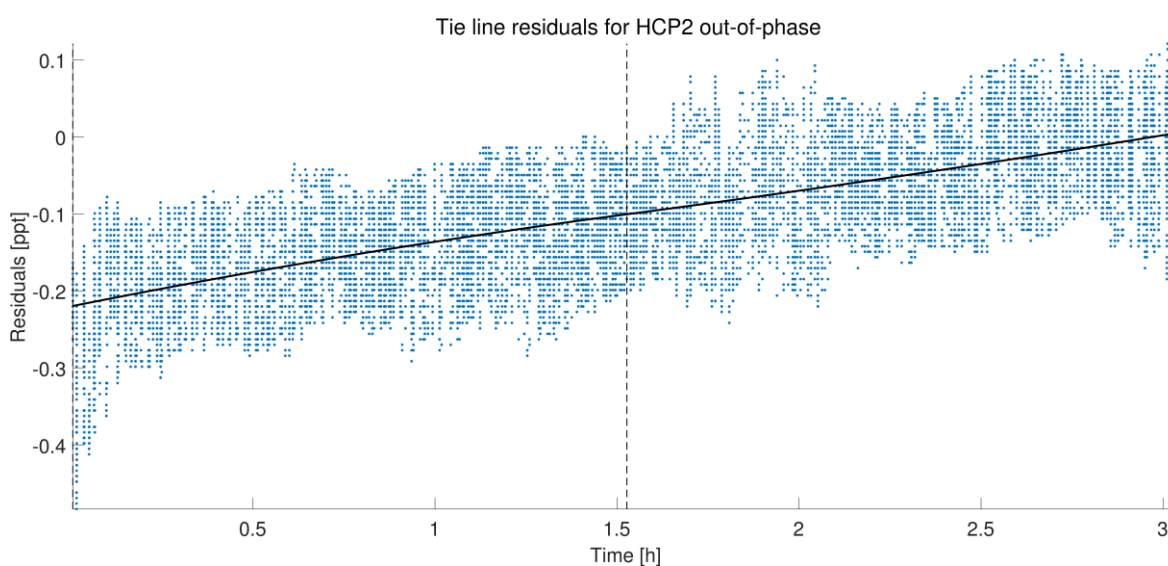


Fig 4.7 Hampel filtered tie line residuals (calibration minus survey data) for the HCP2 response (Dualem 21S) collected at an area with high conductivity. Hampel filter window: 300 [] and threshold: 1 [].

Case 3

The tie-line residuals for a dataset collected by ‘Vandenborne Aardappelen’ (a potato farmer) are visualized in Figure 4.8. The subsurface is characterized by sandy deposits. It concerns a high resolution dataset gathered for precision agriculture practices: the survey lines are ~5 m apart and the distance between measurements along the survey track are ~30 cm. The drift characteristics of the responses are again analogous to the instabilities seen in the stationary recordings. The main differences with the first case are the lower conductivity of the underground (subsurface consisting of mostly sandy deposits, characterised by a conductivity of < 10 mS/m) and the larger distance between survey lines. Despite the coarser survey modality, which results in a more discrete evaluation of drift (there is less comparison data), the tie-line data are generally not very noisy which enables an accurate drift correction. The importance thereof is clearly seen in figure 4.9: due to

collection of the east-west lines prior to the collection of the west-east lines the signal instability is apparent as well as the levelling using the proposed drift correction procedure.

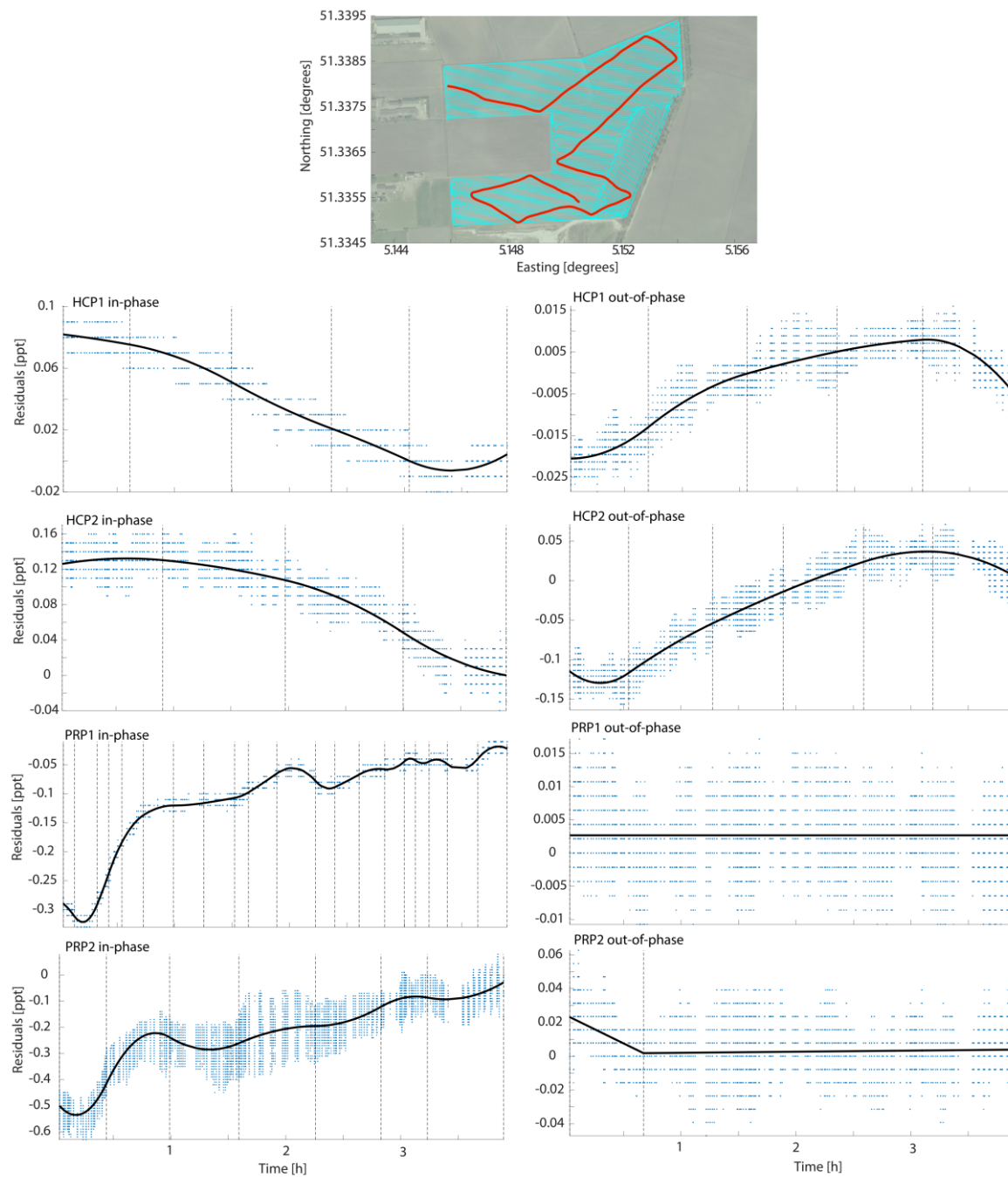


Fig 4.8 (top) Survey track for a 17.5 ha dataset collected in the Netherlands with indication of the calibration line (red). The calibration line was collected in 15 min. (bottom) Hampel filtered tie line residuals (calibration minus survey data) for the Dualcam 21S responses. Hampel filter window: 300-500 [] and threshold: 1 []. Because the calibration line was collected after the area survey, the tie line residuals near the end of the survey become (close to) zero. The coordinates are WGS84 coordinate.

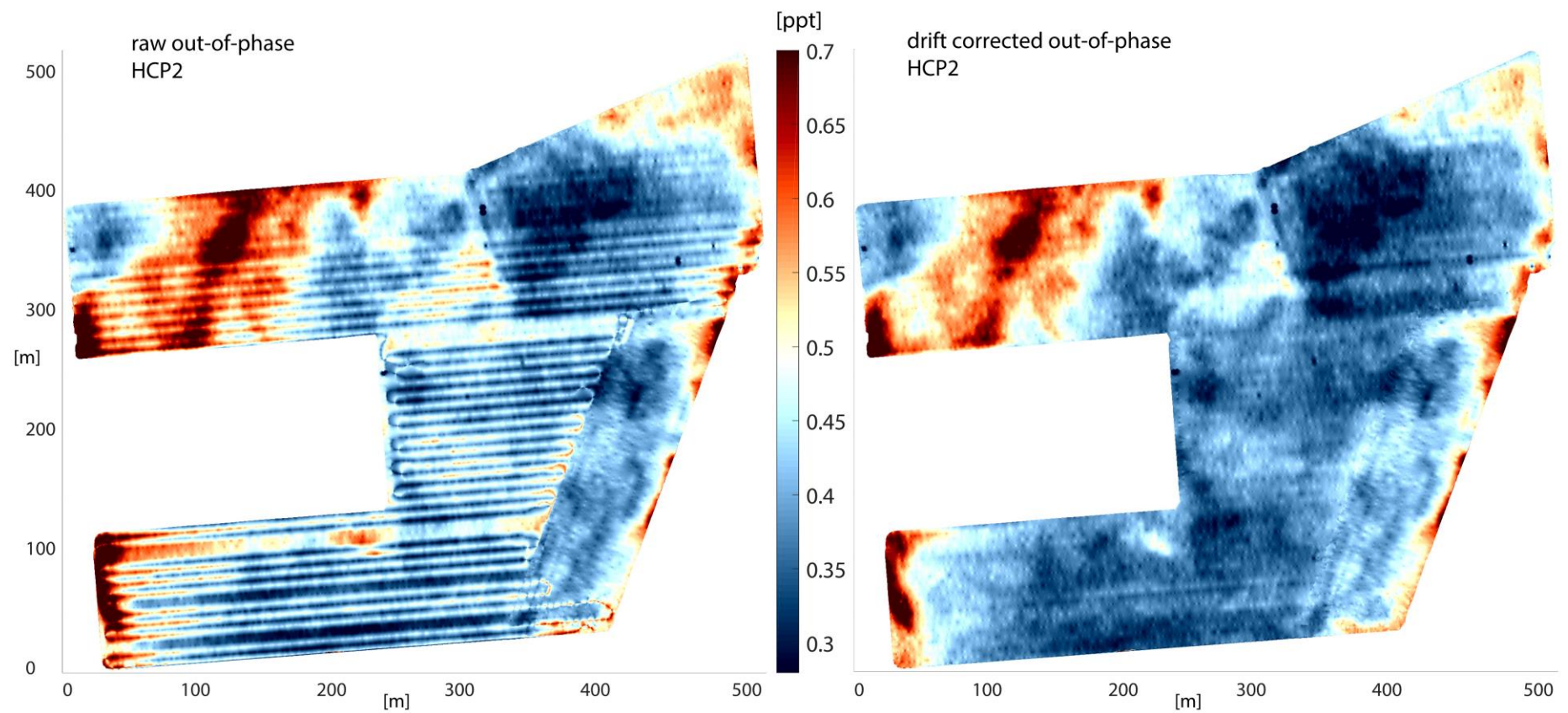


Fig 4.9 HCP2 out-of-phase response before and after drift compensation. See Fig. 4.8 for the modelled drift. Local coordinates are shown.

Case 4

Lastly, we consider a survey performed in the UK. It concerns a high resolution dataset of 9.7 ha gathered for an archaeological investigation: the survey lines are ~ 1.2 m apart and the distance between measurements along the survey track are ~ 25 cm. The subsurface can be characterized mainly as Cretaceous chalk overlain by Quaternary loamy deposits. The survey track and tie-line residuals are visualized in Figure 4.10 while Figure 4.11 visualizes the PRP1 in-phase response before and after drift correction.

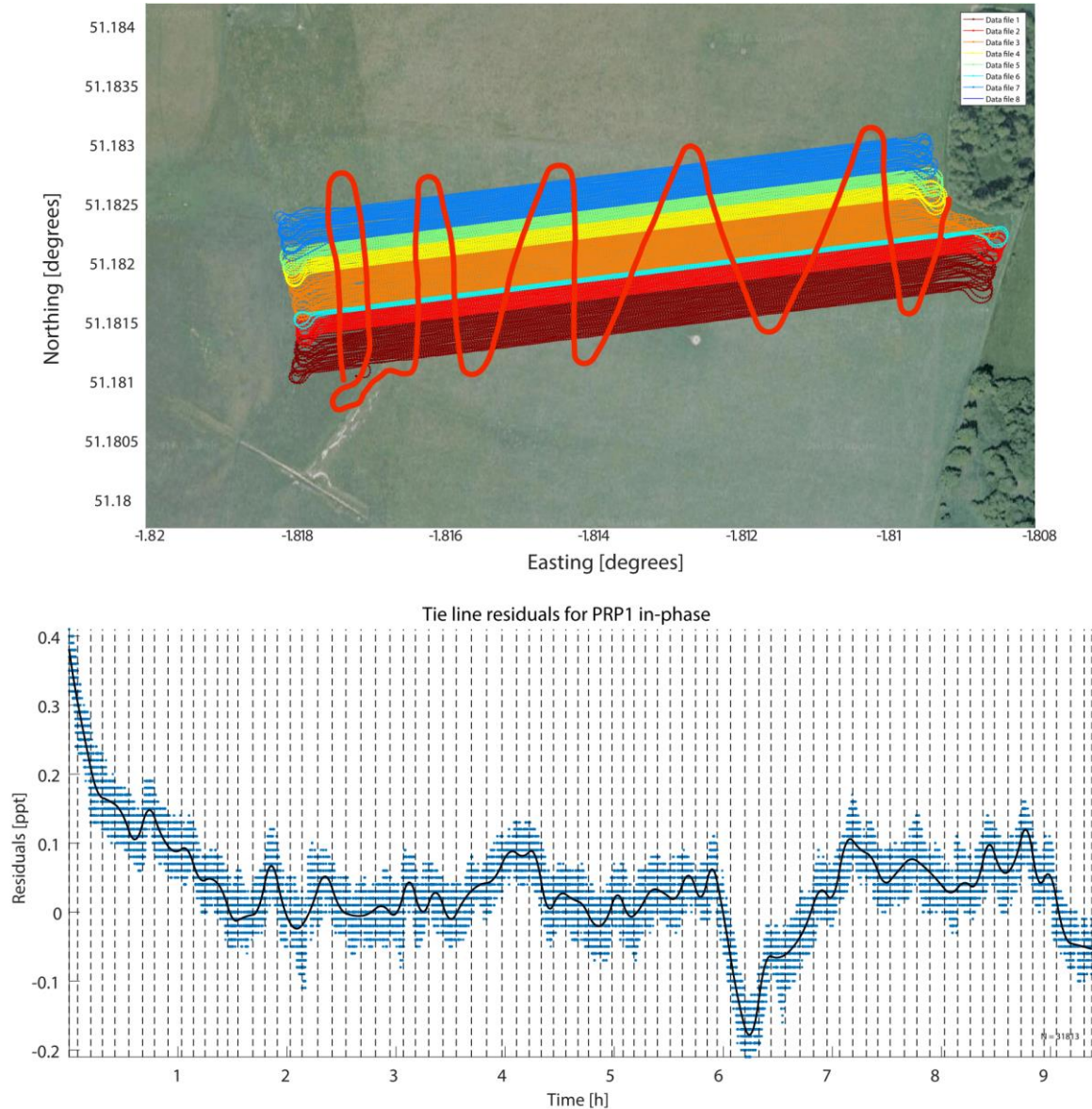


Fig 4.10 (top) Survey track for a 9.7 ha dataset collected in the UK with indication of the calibration line (red). The calibration line was collected in 16 min. (bottom) Hampel filtered tie line residuals (calibration minus survey data) for the PRP1 in-phase response (Duallem 21S). Search window: 1.5 m; number of search neighbours: 8; Hampel filter window: 300 [] and threshold: 1 []. The coordinates are WGS84 coordinates.

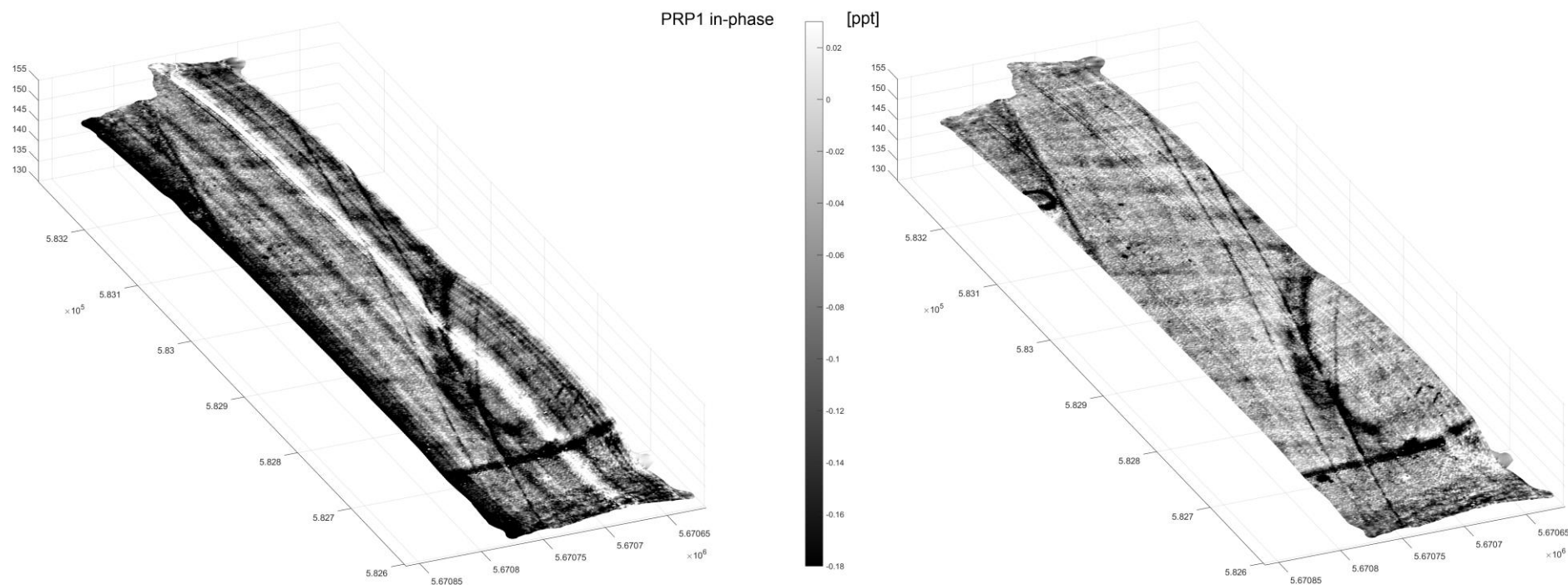


Fig 4.11 PRP1 in-phase response before and after drift compensation. The interpolated grids are draped over the height model. See Fig. 4.11 for the modelled drift. The coordinates are Cartesian UTM coordinates.

Again the results show the importance of a (near-)continuous evaluation of signal instability. However, sufficient tie line data is necessary to allow accurate drift modelling for long area surveys and this requirement conflicts with the necessity for a brief (and thus stable) calibration line. Fortunately, it is possible to evaluate the validity of the calibration itself by colour coding the tie-line residuals using the calibration data time. If there is a pattern whereby the residuals marked by a later time have an offset (in the vertical range) compared to the early (calibration time) residuals, then surely the calibration line was not stable enough for the purpose of an accurate drift correction. An example is given in Fig. 4.12; here no such offset between early and late time residuals is present, which vouches for the validity of the correction.

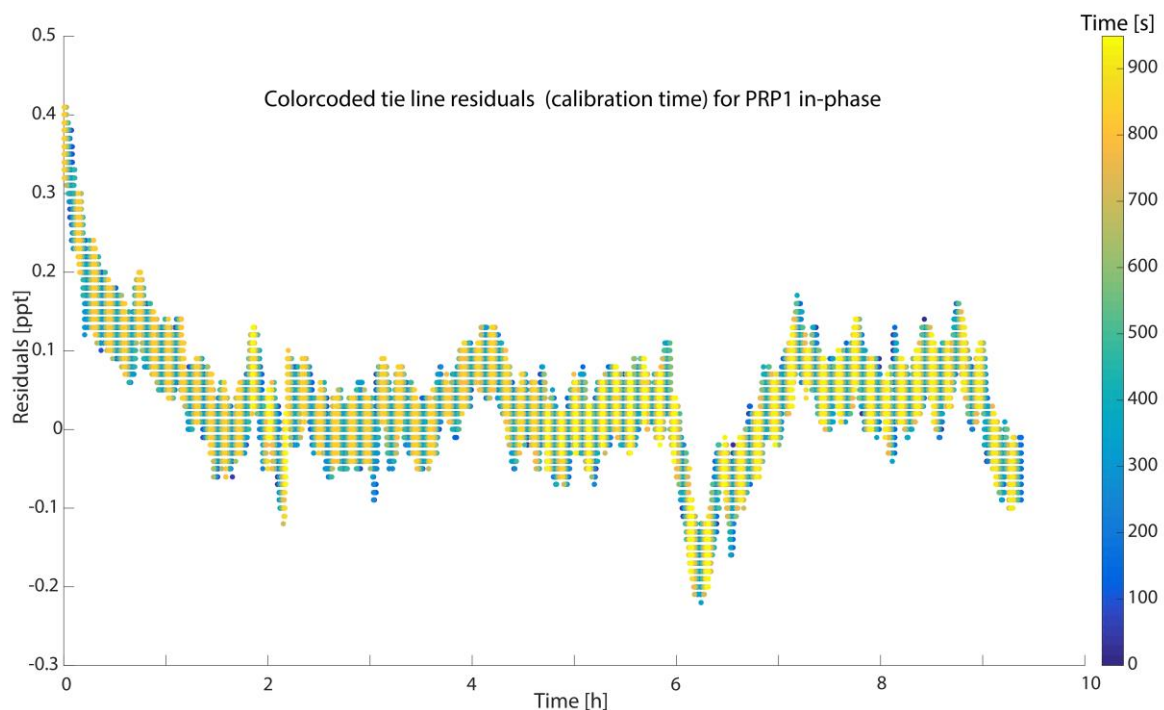


Fig 4.12 Hampel filtered tie line residuals (calibration minus survey data) for the PRP1 in-phase response (Dualem 21S). Here colour coded using the calibration line time.

Likewise, the residuals can be colour coded using the distance between comparison pairs (sensor and calibration data). This type of data reveals that it is acceptable to take a search window of >1 m.

Some final remarks pertain to the drift corrected survey data. Fig. 4.14 showcases the raw and corrected PRP1 in-phase data: in this particular case, it is clear that the survey data has been levelled due to the background conductivity and susceptibility being (more or less) constant. This is not always the case; high resolution surveys often reveal large scale variation in conductivity (which can also influence the in-phase data). It follows that correcting for drift does not necessarily produce data with a constant background value and that statistically levelling data without use of a calibration line is only sometimes justified. Figure 4.14 also makes clear that only a relative compensation is performed and not an absolute calibration. More so, an offset might be introduced during the levelling procedure as it is obviously unknown when the absolute calibration is most correct during the survey.

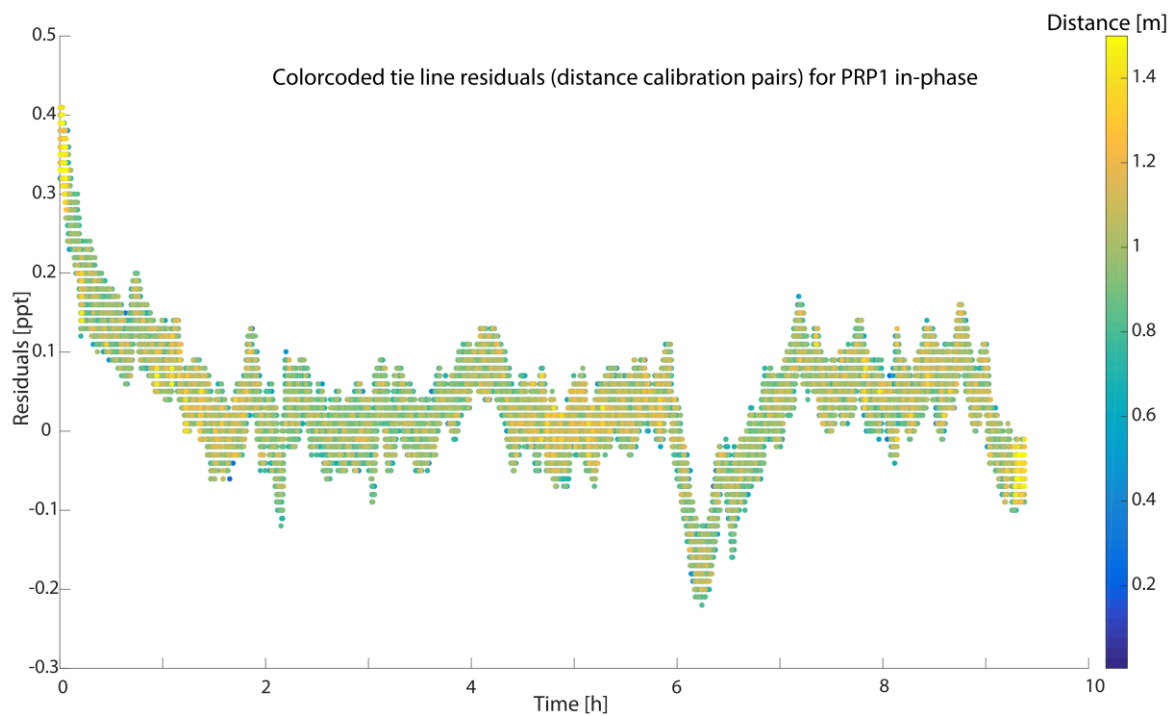


Fig 4.13 PRP1 in-phase residuals (same as fig. 4.11, bottom). The interpolated grids are draped over the height model. See Fig. 4.11 for the modelled drift.

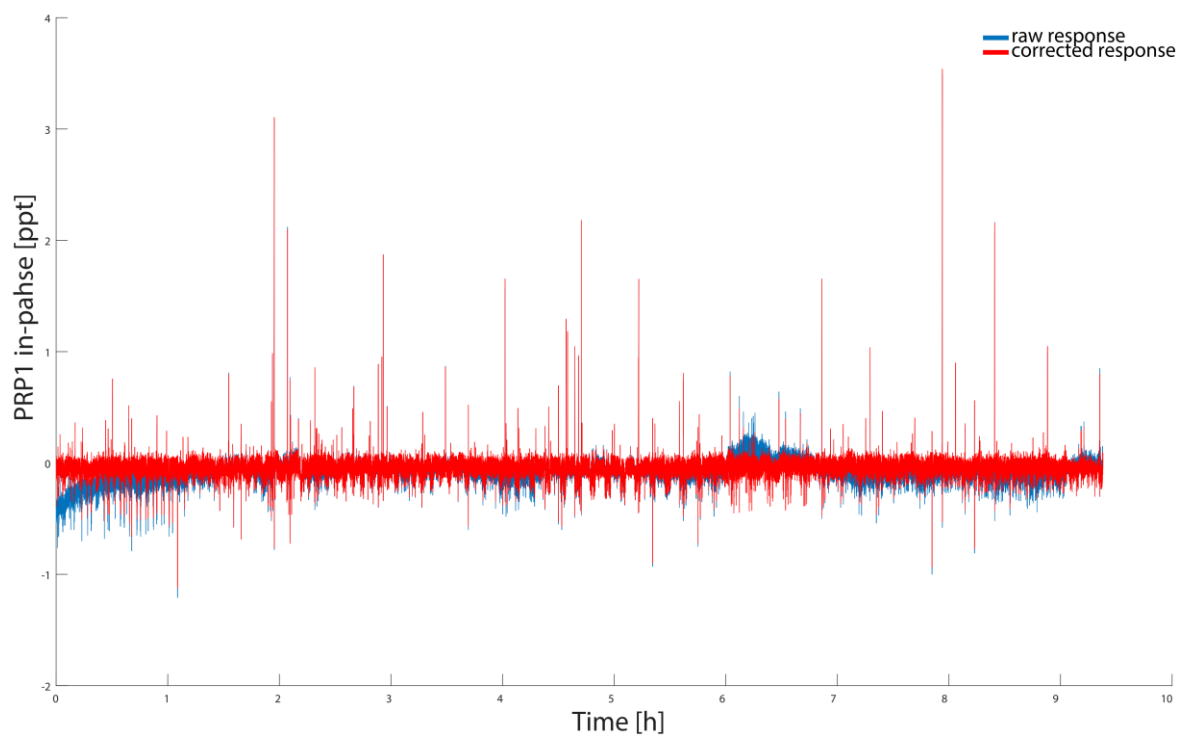


Fig 4.14 PRP1 in-phase: raw and drift corrected survey data.

4.4 Tie-line vs. repeat line method

The tie-line calibration method was explored in this chapter since it was thought to be the most practical (least time consuming) and least subjective approach for land-based FDEM surveys. A test was performed to find out whether it incurs an accuracy penalty compared to a similar approach that makes use of a repeat transect during a survey. In theory, the repeat transect methods should allow for a more accurate correction since the comparison data do not suffer from varying instrument orientations and more comparison data can be collected. However, using this method, the drift evaluation can be more sparse (especially in the case of long survey transects).

Both types of calibration line (tie-line and repeat transect) were collected and applied to a 0.5 ha, high resolution, archaeological dataset collected at Wervershoof (the Netherlands). The duration of the survey was ~1.4 hours and the tie line was collected after concluding the area survey. The tie line duration was ~2.5 minutes and was performed ~11 minutes after finishing the area survey.

The survey track with indication of the calibration lines is visualized on Fig. 4.15. The repeat transect was collected every other line to be able to gauge the maximum obtainable accuracy. Consequentially, all area survey lines (excluding the repeat transect) were collected with the same instrument heading.

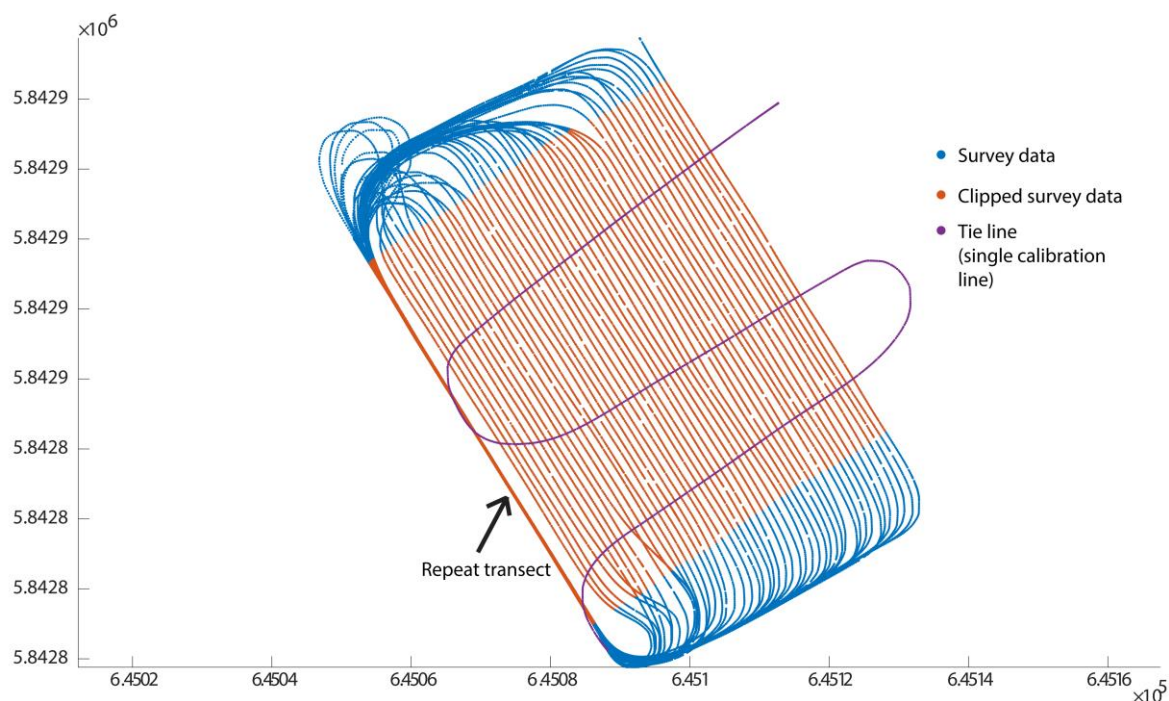


Fig 4.15 GNSS survey track test: clipped survey data, tie line and repeat transect (first survey line, indicated with arrow). The coordinates are WGS84 coordinates.

After data collection, the data were corrected for spatial and temporal offsets. Following, the comparison data were gathered for both calibration lines using a k nearest neighbour search. The repeat transect comparison data were found using a circular search window of 0.1 m and included only the nearest neighbour (in the case of multiple data points within the search window). The single calibration line (area tie line) comparison data were found using a 0.5 m circular window and included up to 3 nearest neighbours. Outlier detection was not performed to facilitate comparison and due to the absence of extreme outliers in the comparison data (due to absence of small scale conductors in the area). The QP residuals (fig. 4.16 and 4.17) highlight the differences between both approaches: the repeat transect residuals are more sparse (here very slightly) yet also more equivocal whereas the tie-line residuals are more prone to larger differences (higher range) and outliers. Nonetheless, after spline fitting similar trends are revealed and it is apparent that the QP responses did not suffer from a large drift due to the short survey time. Note that differences between the fits are well within the noise level of the coil configurations (~ 0.5 to 1 mS/m).

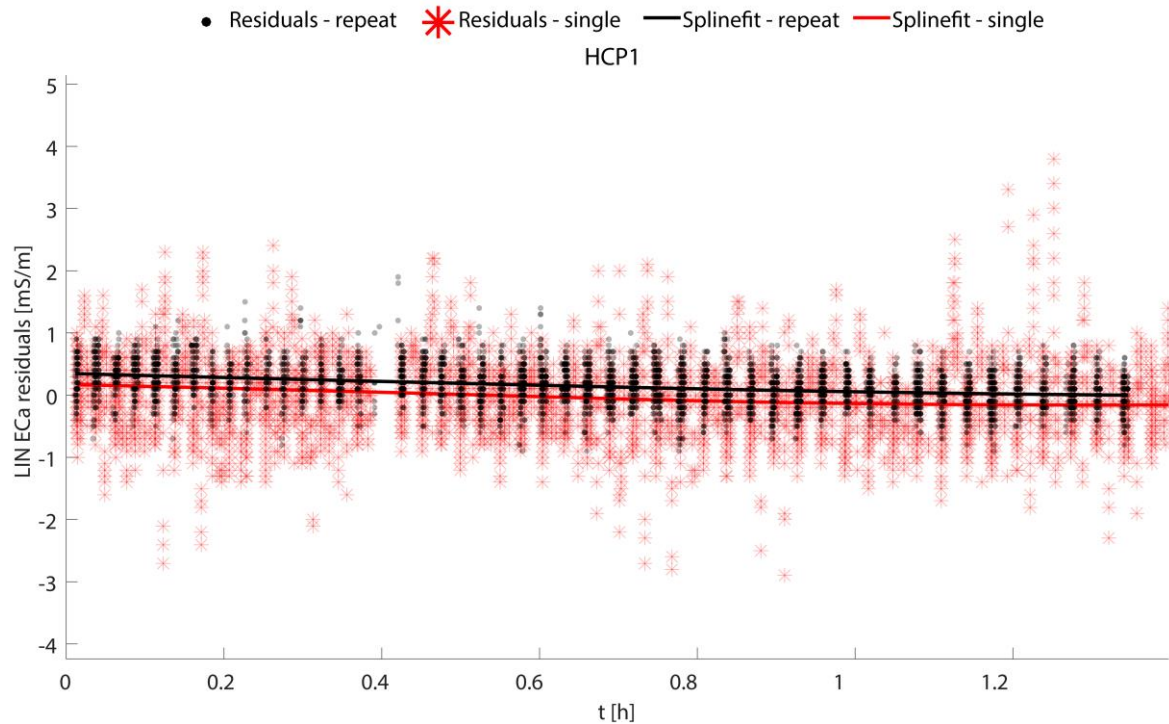


Fig 4.16 Tie line (red markers) and repeat transect (black markers) residuals for the HCP1 QP response (given as LIN ECa) with indication of the fitted splines. The residuals have been given a transparency of 70% to visualize the density. The ‘repeat’ designation refers to the repeat transect residuals and fit thereof. The ‘single’ designation refers to the single calibration line (or tie-line) residuals and fit thereof.

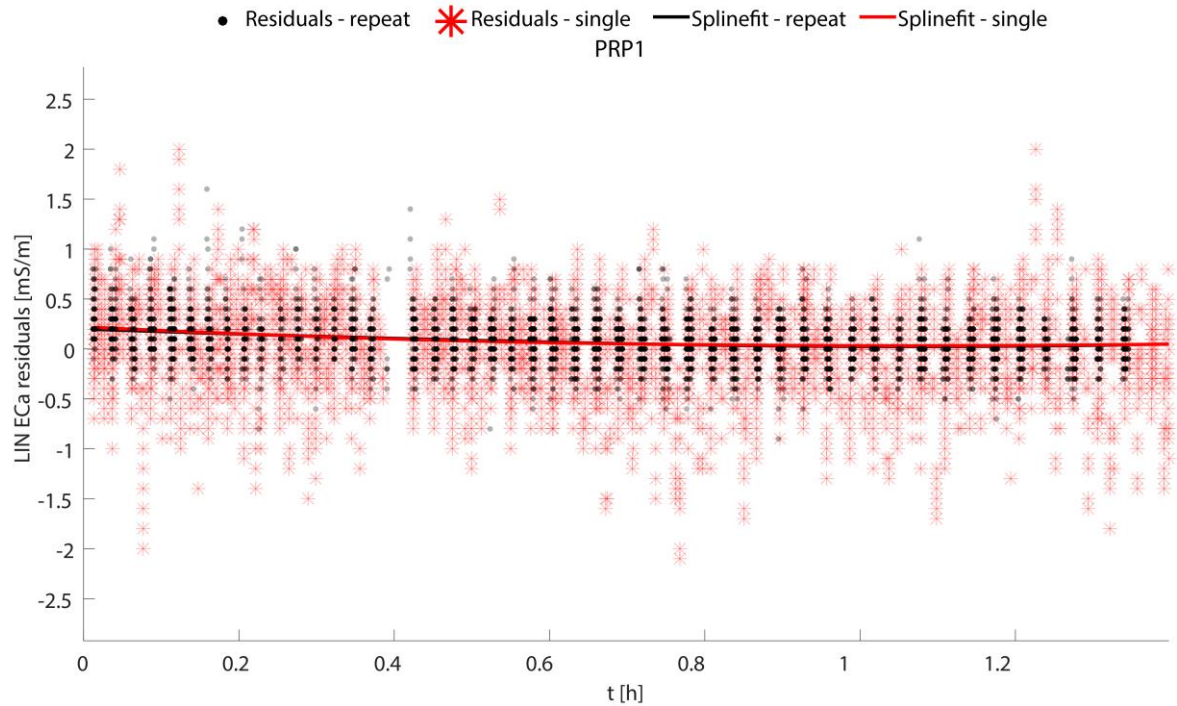


Fig 4.17 Tie line (red markers) and repeat transect (black markers) residuals for the PRP1 QP response (given as LIN ECa) with indication of the fitted splines. The residuals have been given a transparency of 70% to visualize the density. Both fitted splines overlap almost perfectly.

Regarding the in-phase residuals (Fig. 4.18 and 4.19) some additional remarks can be made. Strikingly, the range of the residuals are very similar using both approaches. This likely points to a higher (small-scale) heterogeneity of subsurface conductivity compared to the subsurface susceptibility. Whereas the fitted splines agree completely for the HCP1 in-phase response, the modelled signal instabilities for the PRP1 in-phase reveal an offset slightly above the noise level (despite a very similar trend). This is due to the short break (~11 minutes) between the collection of the survey data and the tie line, during which the response must have drifted.

Fig. 4.20 visualizes the resulting in-phase maps: both uncorrected and corrected using both approaches. Taking into account all previous results, an accuracy gain (or loss) using any of the aforementioned methods, was not demonstrable. The only difference between the maps shown on Fig. 4.20 is the offset due to slightly different calibration level (i.e. difference between last repeat transect line and tie-line level) which has no bearing on the relative compensation that was endeavoured.

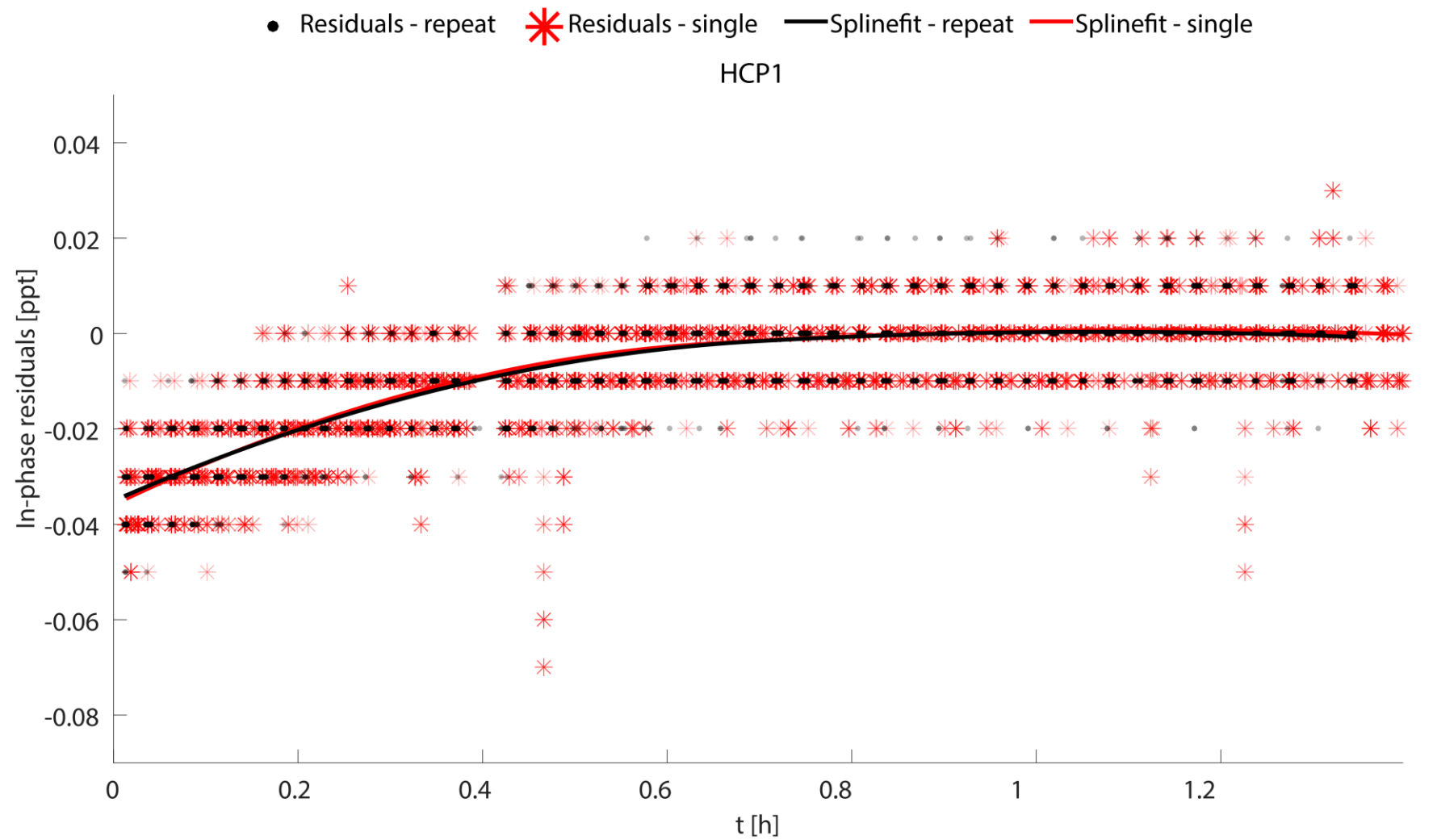


Fig 4.18 Tie line (red markers) and repeat transect (black markers) residuals for the HCP1 in-phase response with indication of the fitted splines. The residuals have been given a transparency of 70% to visualize the density. Both fitted splines overlap almost perfectly.

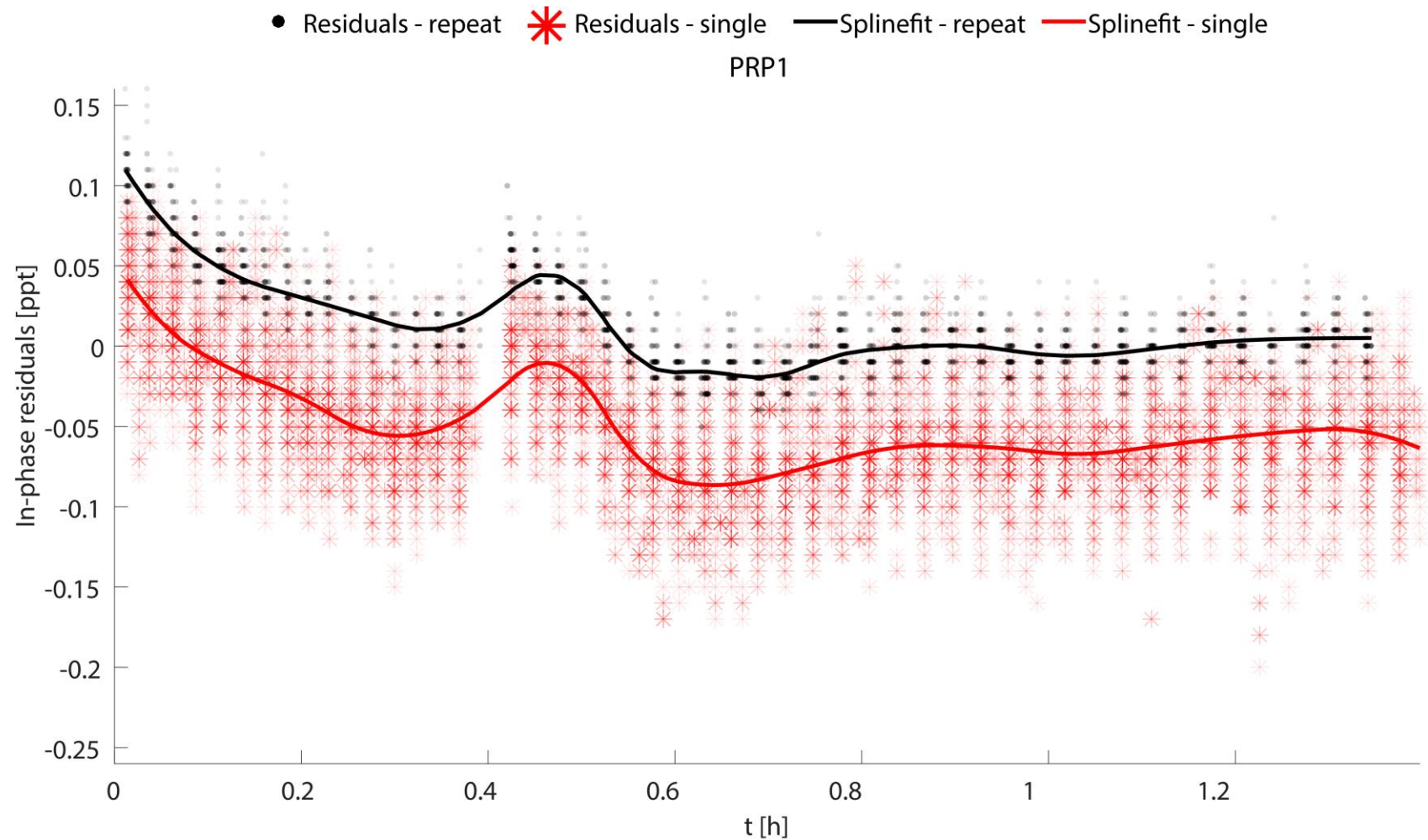


Fig 4.19 Tie line (red markers) and repeat transect (black markers) residuals for the PRP1 in-phase response with indication of the fitted splines. The residuals have been given a transparency of 70% to visualize the density. The residuals break around 0.4 h is due to a pause in data collection.

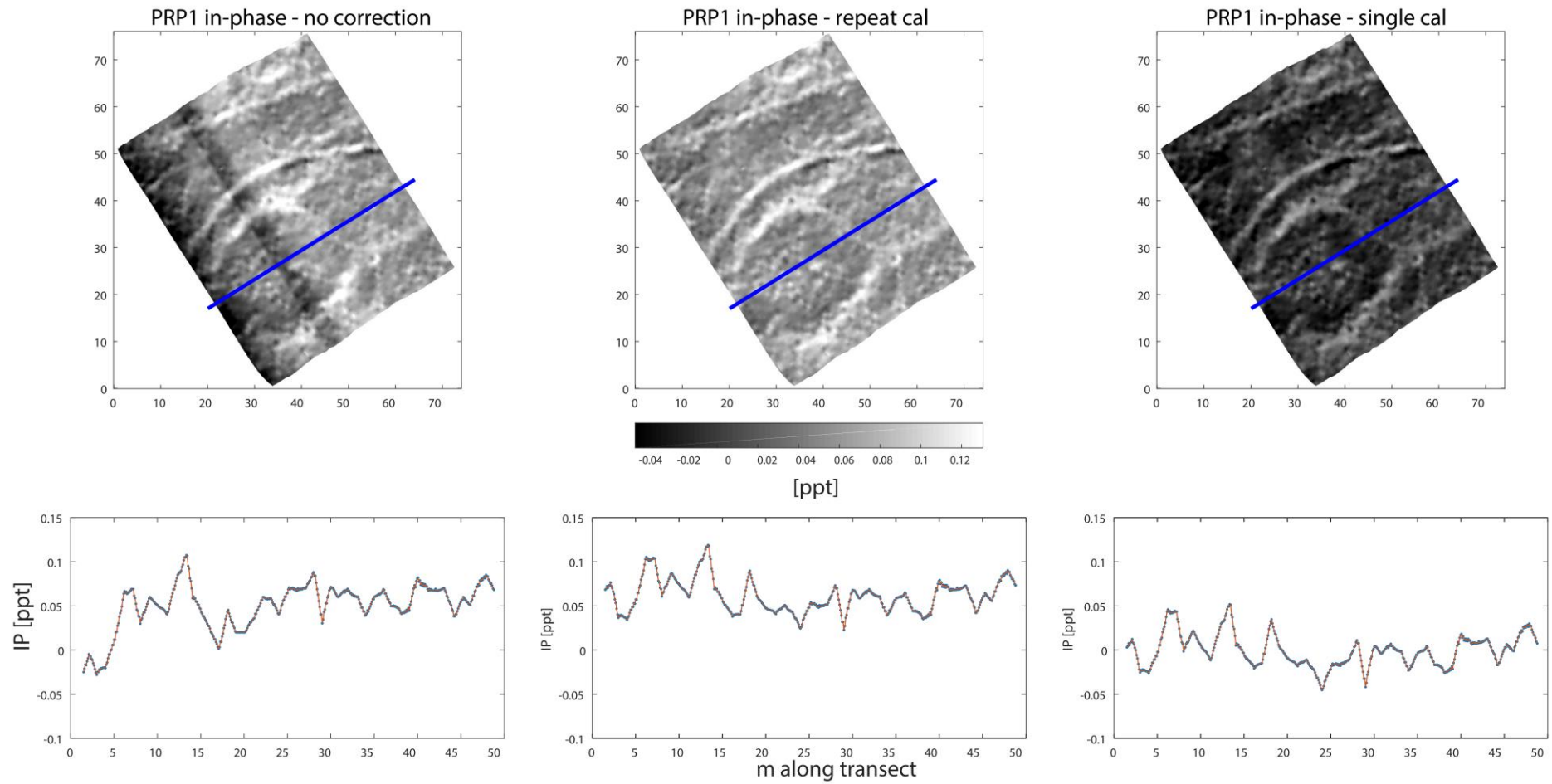


Fig 4.20 (top) PRP1 in-phase maps before and after correction with both the repeat transect and tie line calibration method. (bottom) in-phase profiles for the transects (marked blue on the above maps)

4.5 Discussion

The results can be summarized as follows:

- FDEM signal instability can be characterized (to a certain degree) by assessing (several) stationary recordings: trends/erratic behaviour/amplitude of the instability.
- Tie line data can be successfully used to assess and correct for signal instability. A correction does generally require outlier removal and robust spline fitting as the comparison data often results in noisy residuals.
- Having compared the tie-line approach with the repeat transect approach, it seems that the latter does not require outlier detection and removal and leads to more equivocal residuals. However, while the tie-line method may require additional processing, an accuracy loss was not demonstrable. Thus, given the impracticality of the repeat transect method, it is not generally advisable. This restricts its use to validation purposes and perhaps surveys in (small) areas with an extreme presence of small-scale conductors.
- The accuracy that can be achieved using a calibration line is influenced by many factors. It will be impacted positively with decreasing ambient interference, instrument noise, subsurface heterogeneity, presence of metal and with increasing survey resolution.
- Signal instability correction is absolutely necessary for surveys with a long duration if an accurate collection of in-phase data is desired. It is also of great importance for low conductivity settings.
- The corrections applied are relative compensations (i.e. they are not absolute).

A drift compensation procedure has to be versatile, especially considering real survey conditions: ambient temperatures may vary strongly, there may be unplanned pauses between measurements and restarting or replacing the sensor during a survey (causing recalibration) may be necessary. Furthermore, it may be unfeasible to frequently return to a given location or collect a lot of ancillary data in order to correct for signal drift. In addition, stationary recordings show that a near continuous evaluation is preferred as results show that drift may be erratic. For all the aforementioned reasons the proposed drift correction is a boon, allowing to maximize the reliability of collected data and allowing flexibility for varying drift situations and problems.

Although the presented tie-line approach was applied to only one type of FDEM sensor, the correction is generally applicable and expeditious. It is good practice to log several stationary recordings during different atmospheric conditions to assess which instrument responses are prone to drift and whether the drift may be characterized (e.g. consistent observation of a linear drift for the Dualem σ_a PRP responses). Such a priori knowledge may then be used in modelling the signal drift by curve fitting, especially if the process is fully automated.

The crux of the correction procedure is that a calibration line covering the survey area, performed in a sufficiently short amount of time, does not suffer from significant drift. The data presented suggests that this generally holds true, yet performing the calibration line immediately after powering the instrument should be avoided. If the stability of the calibration line is doubted it can be assessed (see Fig. 4.12). Should a calibration line be corrupt, inadequate or lacking it can be performed at a later time as long as there is no substantial change in subsurface conductivity (e.g. due to changes in moisture content).

Enough comparison locations are necessary since the differences between calibration line and survey data are not solely due to drift and since drift may be abrupt. Too few comparison points over time may preclude accurate drift correction. However, as the highest obtainable sampling frequency keeps rising with continual instrumental developments, a drift compensation procedure as described herein will only become increasingly relevant with time.

In utilising the drift procedure it should be assessed if the desired accuracy can be reached. Compensation for drift that is smaller in magnitude than instrument noise level is possible in theory, though unlikely. It is noted that correcting for high (random) noise levels is not possible using the described method: a sufficiently stable signal (in the sense of low stochastic noise) was postulated.

It is noted that a similar use of a calibration line has been employed in a variety of domains. Siemon (2009) examined its use for the levelling of helicopter EM data and found that tie-line levelling is often not useful when applied to FDEM instrument responses because they are nonlinearly dependent on the instrument altitude. This is clearly not the case with ground-based EM data, which does not suffer from elevation offsets at cross-over points. We also note that applying the drift correction procedure to QP or LIN σ_a data is essentially the same (owing to the linear approximation).

If the desired accuracy is not reached, it can still be valuable to apply a tie-line calibration to compensate for large deviations before applying another method. This way the residual drift (with smaller magnitude) can be tackled easier and with less ambiguity (e.g. De Smedt et al., 2016).

4.6 Conclusions

By using the tie-line calibration procedure detailed in this chapter, a relative compensation with regards to the (stable) calibration data is performed. While signal stability can be achieved in this manner, an absolute calibration is not realized. This means that multiple calibration lines will give rise to different results and whether this is due to changes in temperature or other physical parameters is not easily distinguished between. However, given the results obtained, the procedure is for all intents and purposes an excellent first step in processing EMI data as it allows to maximize the reliability of collected data with regards to signal stability.

In addition to increasing data repeatability, using tie-line data collected at different moments in time and comparing the data with drift corrected area data can lead to insights in temperature and moisture dependency of conductivity and susceptibility data as well as possible calibration issues.

4.7 Matlab scripts

Here included is a simple GUI (written in Matlab 2015a) to perform tie line data search, outlier removal and spline fitting. To run without errors it requires the following function which can be found on Matlab File Exchange:

Hampel filter (this function needs to be compiled for the user OS with MEX)

<http://nl.mathworks.com/matlabcentral/fileexchange/40147-hampel-filter-in-c++>

Splinefit

<http://nl.mathworks.com/matlabcentral/fileexchange/13812-splinefit>

Export_fig

<http://nl.mathworks.com/matlabcentral/fileexchange/23629-export-fig>

Draggable:

<http://nl.mathworks.com/matlabcentral/fileexchange/4179-draggable>

Example

```
% LOAD
% load sensor data
load s_sensdat.mat
% load calibration data
load s_cal.mat

% ARRANGE + SET PARAMETERS + CALL GUI
% Put data in structure
Struct.sensdat = s_sensdat.HCP1; Struct.caldat = s_cal.HCP1;
% Name, unit and column number of variable to be compared
Struct.var_name = 'HCP1 IP';
Struct.var_unit = '[ppt]';
Struct.var_col_nr = 6;
% Column number and unit of time stamps data
Struct.time_col_nr = 4;
Struct.time_unit = '[h]';
% Search parameters
Struct.maxdist = 1.0;           % search window size [m]
Struct.no_neighbours = 5;      % number of neighbours
% Call GUI
fh = GUI_tie_line(Struct); waitfor(fh);

% After selecting a splinefit to correct the data, use the variable
% 'spline_eval_sensdat' that is present in the workspace after selecting a
% fit in the GUI
sensdat_corr = sensdat_corr(:,Struct.var_col_nr) + spline_eval_sensdat;
```

Tie-line GUI

```
% Copyright 2015 Samuël Delefortrie <samuel.delefortrie@ugent.be>

% Programmed by: Samuël Delefortrie
% Affiliation: ORBit, UGent, Belgium
% Created in: Matlab 2015a

% References:
% Delefortrie, S. et al., 2016.
% An efficient calibration procedure for correction of drift
% in EMI survey data
% Journal of Applied Geophysics 110, 115-125
% http://dx.doi.org/10.1016/j.jappgeo.2014.09.004

function fh = GUI_tie_line(Struct)
%%%%%%%%%%%%%%%%%%%%%%%%%%%%%%%%%%%%%%%%%%%%%%%%%%%%%%%%%%%%%%%%%%%%%%%%%%%%%%
% Find residuals
%%%%%%%%%%%%%%%%%%%%%%%%%%%%%%%%%%%%%%%%%%%%%%%%%%%%%%%%%%%%%%%%%%%%%%%%%%%%%%
% Search nearest points cal - survey data
[IDX,Dist] = knnsearch(Struct.sensdat(:,1:2),Struct.caldat(:,1:2)...
    , 'k',Struct.no_neighbours);
```



```
% Multiply calibration data according to number of neighbors in search
Cal = repmat(Struct.caldat,Struct.no_neighbours,1);

% Create one-column vectors and exclude points > maxdist
IDX = IDX(:); Dist = Dist(:);
excl = Dist > Struct.maxdist;
IDX(excl) = []; Cal(excl,:) = []; Dist(excl,:) = [];

% Obtain residuals and data relevant to the residuals
% Residuals
Tie_line_res = Cal(:,Struct.var_col_nr) ...
    - Struct.sensdat(IDX,Struct.var_col_nr);
% Time survey data
Tie_line_res(:,2) = Struct.sensdat(IDX,Struct.time_col_nr);
% Time calibration line
Tie_line_res(:,3) = Cal(:,Struct.time_col_nr);
% Distance cal - survey points
Tie_line_res(:,4) = Dist;

% Sort rows
Struct.Tie_line_res = sortrows(Tie_line_res,2);

%%%%%%%%%%%%%%%%%%%%%%%%%%%%%%%%%%%%%%%%%%%%%%%%%%%%%%%%%%%%%%%%%%%%%%%%
% Build the figure for the GUI.
%%%%%%%%%%%%%%%%%%%%%%%%%%%%%%%%%%%%%%%%%%%%%%%%%%%%%%%%%%%%%%%%%%%%%%%%
% Create the GUI window
Struct.fh = figure('units','normalized','outerposition',[0 0.05 1 0.90],...
    'Name','Spline fitting','NumberTitle','off');
fh = Struct.fh;
% Create the axes for image display
Struct.ax = axes('units','norm','position',[.07 .1 .90 .7]...
    , 'fontsize',10,'nextplot','replacechildren');
% Outlier removal
Struct.Outl_txt_pieces=uicontrol('style','text','unit','norm',...
    'position',[.05 .96 .055 .02],'fontsize',10,'string','Hampel filter:');
Struct.Hwindow_txt_pieces=uicontrol('style','text','unit','norm',...
    'position',[.10 .96 .06 .02],'fontsize',8,'string','window [ ]');
Struct.Hampel_window = uicontrol('style','edit','unit','norm',...
    'position',[.16 .96 .04 .025],'fontsize',10,'string',' ');
Struct.Hampel_T_txt_order=uicontrol('style','text','unit','norm',...
    'position',[.10 .93 .06 .02],'fontsize',8,'string','Threshold [ ]');
Struct.Hampel_T = uicontrol('style','edit','unit','norm',...
    'position',[.16 .93 .04 .025],'fontsize',10,'string',' ');
% Spline fit
Struct.spline_txt=uicontrol('style','text','unit','norm',...
    'position',[.25 .96 .06 .02],'fontsize',10,'string','Spline fit:');
Struct.txt_pieces=uicontrol('style','text','unit','norm',...
    'position',[.30 .96 .06 .02],'fontsize',8,'string','Breaks');
Struct.no_pieces = uicontrol('style','edit','unit','norm',...
    'position',[.35 .96 .20 .025],'fontsize',10,'string',' ');
Struct.txt_order=uicontrol('style','text','unit','norm',...
    'position',[.30 .93 .06 .02],'fontsize',8,'string','Order');
Struct.order = uicontrol('style','edit','unit','norm',...
    'position',[.35 .93 .05 .025],'fontsize',10,'string',' ');
Struct.but_spline = uicontrol('style','pushbutton','unit','norm',...
    'position',[.32 .88 .08 .04],'fontsize',10,'string','Spline calc');
% Spline select
```

```

Struct.spline_select_txt=icontrol('style','text','unit','norm',...
    'position',[.60 .96 .06 .02],'fontsize',10,'string','Spline select:');
Struct.but_export = uicontrol('style','pushbutton','unit','norm',...
    'position',[.66 .96 .08 .04],'fontsize',10,'string','Select spline');
Struct.but_no_corr = uicontrol('style','pushbutton','unit','norm',...
    'position',[.66 .88 .08 .04],'fontsize',10,'string','No correction');
% Evaluation of fit and residuals
Struct.eval_txt=icontrol('style','text','unit','norm',...
    'position',[.80 .96 .06 .02],'fontsize',10,'string','Eval:');
Struct.but_res_corr = uicontrol('style','pushbutton','unit','norm',...
    'position',[.85 .96 .08 .04],'fontsize',10,...
    'string','Plot res after cor');
Struct.but_sens_corr = uicontrol('style','pushbutton','unit','norm',...
    'position',[.85 .92 .08 .04],'fontsize',10,...
    'string','Plot dat after cor');
Struct.but_col_codeT = uicontrol('style','pushbutton','unit','norm',...
    'position',[.85 .88 .08 .04],'fontsize',10,...
    'string','Color code res time');
Struct.but_col_codeD = uicontrol('style','pushbutton','unit','norm',...
    'position',[.85 .84 .08 .04],'fontsize',10,...
    'string','Color code res dist');

%%%%%%%%%%%%%%%%%%%%%%%%%%%%%%%%%%%%%%%%%%%%%%%%%%%%%%%%%%%%%%%%%%%%%%%%
% Draw the first frame
%%%%%%%%%%%%%%%%%%%%%%%%%%%%%%%%%%%%%%%%%%%%%%%%%%%%%%%%%%%%%%%%%%%%%%%%
Struct.clr = [0,0.4470,0.7410];
axes(Struct.ax); set(gca,'FontSize',20); axis tight
plot(Struct.Tie_line_res(:,2),Struct.Tie_line_res(:,1),'.',...
    'Color',Struct.clr,'MarkerSize',8);
ylabel(['Residuals ' Struct.var_unit],'FontSize',20);
xlabel(['Time ' Struct.time_unit],'FontSize',20);
title(['Tie line residuals for ' Struct.var_name]);
assignin('base','Tie_line_res',Struct.Tie_line_res)
text(0.95,0.05,['N = ' num2str(numel(Struct.Tie_line_res(:,2)))]...
    ',Units','normalized')

% Display spline fit that was passed along with the structure, if present
if isfield(Struct,'splinefit')
    if ~isempty(Struct.splinefit)
        % Spline fit
        D_splinefit = Struct.splinefit;
        D_breaks = D_splinefit.breaks;
        D_spline_eval = ppval(D_splinefit,Struct.Tie_line_res(:,2));
        % Plot
        children = get(gca,'children'); delete(children);
        plot(Struct.Tie_line_res(:,2),Struct.Tie_line_res(:,1),'.',...
            'Color',Struct.clr,'MarkerSize',8); hold on
        plot(Struct.Tie_line_res(:,2),D_spline_eval,'k','Linewidth',2);
        for i = 1:size(D_breaks,2)
            break_h(i) = line([D_breaks(i) D_breaks(i)],get(Struct.ax,'YLim'),...
                'Color',[0 0 0],'Linewidth', 1,'LineStyle','--'); %#ok<AGROW>
        end
        % Display breaks in GUI editbox
        set(Struct.no_pieces,'string',num2str(roundn(D_breaks,-2)));
        set(Struct.order,'string',num2str(D_splinefit.order));
        % Make breaks available across callbacks
        assignin('base','spline_breaks',D_breaks)
    end
end

```

```

        assignin('base','splinefit',D_splinefit)
        % Make breaks draggable and set callback
        draggable(break_h,'h','endfcn',@update_value)
    end
else
    Struct.splinefit = [];
    assignin('base','splinefit',[])
end

%%%%%%%%%%%%%%%%%%%%%%%%%%%%%%%%%%%%%%%%%%%%%%%%%%%%%%%%%%%%%%%%%%%%%%%%%%%%%%
% Callbacks
%%%%%%%%%%%%%%%%%%%%%%%%%%%%%%%%%%%%%%%%%%%%%%%%%%%%%%%%%%%%%%%%%%%%%%%%%%%%%%
% callback outlier detection
set([Struct.Hampel_window,Struct.Hampel_T],'Callback'...
    ,{@outlfunction,Struct});
% callback spline fit
set([Struct.no_pieces,Struct.order,Struct.but_spline],'Callback'...
    ,{@set_spline,Struct});
% callback select fit
set([Struct.but_export,Struct.but_no_corr],'Callback'...
    ,{@export_function,Struct});
% evaluation options
set([Struct.but_res_corr,Struct.but_sens_corr,...
    Struct.but_col_codeT,Struct.but_col_codeB]...
    ,'Callback',{@eval_function,Struct});
end

% Callback for change in hampel filter parameters
function []=outlfunction(varargin)
[h,Struct] = varargin{[1,3]};
    switch h
        case Struct.Hampel_window
            Hampel_window = str2num(get(h,'string')); %#ok<*ST2NM>
            Hampel_T = str2num(get(Struct.Hampel_T,'string'));
        case Struct.Hampel_T
            Hampel_window = str2num(get(Struct.Hampel_window,'string'));
            Hampel_T = str2num(get(h,'string'));
    end

    if ~isempty(Hampel_window) && ~isempty(Hampel_T)
        [~,Idx_hamp,~,~] = hampeFilter(Struct.Tie_line_res(:,1),...
            Hampel_window,Hampel_T);
        Struct.Tie_line_res(Idx_hamp,:) = [];

        axes(Struct.ax); % axis tight
        children = get(gca,'children'); delete(children);
        plot(Struct.Tie_line_res(:,2),Struct.Tie_line_res(:,1),'.',...
            'Color',Struct.clr,'MarkerSize',8);
        text(0.95,0.05,['N = ' num2str(numel(Struct.Tie_line_res(:,2)))]...
            ,'Units','normalized')

        assignin('base','Tie_line_res',Struct.Tie_line_res)
    end
end

% Callback for change in spline fit parameters
function []=set_spline(varargin)

```

```

[h,Struct] = varargin{[1,3]};
switch h
    case Struct.no_pieces
        breaks = str2num(get(h,'string'));
        order = str2num(get(Struct.order,'string'));
    case Struct.order
        breaks = str2num(get(Struct.no_pieces,'string'));
        order = str2num(get(h,'string'));
    case Struct.but_spline
        breaks = evalin('base','spline_breaks');
        order = str2num(get(Struct.order,'string'));
end

if ~isempty(breaks) && ~isempty(order)
    Tie_line_res = evalin('base','Tie_line_res');

    % Spline fit
    D_splinefit = splinefit(Tie_line_res(:,2),Tie_line_res(:,1),...
        breaks,order,'r');
    D_breaks = D_splinefit.breaks;
    D_spline_eval = ppval(D_splinefit,Tie_line_res(:,2));

    % Plot
    children = get(gca,'children'); delete(children);
    plot(Tie_line_res(:,2),Tie_line_res(:,1),'.',...
        'Color',Struct.clr,'MarkerSize',8); hold on
    plot(Tie_line_res(:,2),D_spline_eval,'k','Linewidth',2);
    for i = 1:size(D_breaks,2)
        break_h(i) = line([D_breaks(i) D_breaks(i)],...
            get(Struct.ax,'YLim'),'Color',[0 0 0]...
            ,'Linewidth', 1,'LineStyle','--'); %#ok<AGROW>
    end
    text(0.95,0.05,['N = ' num2str(numel(Tie_line_res(:,2)))]...
        ,'Units','normalized')

    % Display breaks in GUI textbox
    set(Struct.no_pieces,'string',num2str(roundn(D_breaks,-2)));

    % Make breaks available across callbacks
    assignin('base','spline_breaks',D_breaks)
    assignin('base','splinefit',D_splinefit)

    % Make breaks draggable and set callback
    draggable(break_h,'h','endfcn',@update_value)
end
end

% Callback when dragging one of the breaks using the mouse
function update_value(break_h)
    old_pos = getappdata(break_h,'initial_extent');
    old_pos = old_pos(1);
    new_pos = get(break_h,'XData');
    new_pos = new_pos(1);

    if new_pos ~= old_pos
        zzz = evalin('base','spline_breaks');
        zzz(zzz==old_pos) = new_pos;
    end
end

```

```

        assignin('base','spline_breaks',zzz);
    end

end

%%%%%%%%%%%%%%%%%%%%%%%%%%%%%%%%%%%%%%%%%%%%%%%%%%%%%%%%%%%%%%%%%%%%%%%%%%%%%%
function []=export_function(varargin)
[h,Struct] = varargin{[1,3]};
    switch h
        case Struct.but_no_corr
            spline_eval_sensdat = Struct.sensdat(:,Struct.time_col_nr) .* 0;
            assignin('base','spline_eval_sensdat',spline_eval_sensdat);
            assignin('base','splinefit',[]);
        case Struct.but_export
            splinefit = evalin('base','splinefit');
            if ~isempty(splinefit)
                spline_eval_sensdat = ...
                    ppval(splinefit,Struct.sensdat(:,Struct.time_col_nr));
            else
                spline_eval_sensdat = ...
                    Struct.sensdat(:,Struct.time_col_nr) .* 0;
            end
            assignin('base','spline_eval_sensdat',spline_eval_sensdat);
        end
    close(Struct.fh);
end

%%%%%%%%%%%%%%%%%%%%%%%%%%%%%%%%%%%%%%%%%%%%%%%%%%%%%%%%%%%%%%%%%%%%%%%%%%%%%%
function []=eval_function(varargin)
[h,Struct] = varargin{[1,3]};
    switch h
        case Struct.but_res_corr
            % Evaluate splinefit at residual timestamps and correct
            D_splinefit = evalin('base','splinefit');
            Tie_line_res = evalin('base','Tie_line_res');
            D_spline_eval = ppval(D_splinefit,Tie_line_res(:,2));
            res_corr = Tie_line_res(:,1) - D_spline_eval;

            figure; hold on
            plot(Tie_line_res(:,2),Tie_line_res(:,1),'.',...
                'color',Struct.clr,'MarkerSize',10);
            plot(Tie_line_res(:,2),res_corr,'r*','MarkerSize',6);
            ylabel(['Residuals ' Struct.var_unit],'FontSize',20);
            xlabel(['Time ' Struct.time_unit],'FontSize',20);
            title(['Tie line residuals for ' Struct.var_name]);
            legend('residuals','corrected residuals');
        case Struct.but_sens_corr
            % Evaluate splinefit at sensdat timestamps and correct
            D_splinefit = evalin('base','splinefit');
            D_spline_eval = ppval(D_splinefit,...
                Struct.sensdat(:,Struct.time_col_nr));
            res_corr = Struct.sensdat(:,Struct.var_col_nr) + D_spline_eval;

            figure; hold on
            plot(Struct.sensdat(:,Struct.time_col_nr),...
                Struct.sensdat(:,Struct.var_col_nr),...
                'color',Struct.clr,'MarkerSize',10);

```

```

        plot(Struct.sensdat(:,Struct.time_col_nr),res_corr,...
            'r','MarkerSize',6);
        ylabel(['Sensdat ' Struct.var_unit],'FontSize',20);
        xlabel(['Time ' Struct.time_unit],'FontSize',20);
        title(['Tie line splinefit correction ' Struct.var_name]);
        legend('sensdat','corrected sensdat');
    case Struct.but_col_codeT
        % Color code time of calibration for every tie line pair
        Tie_line_res = evalin('base','Tie_line_res');
        Tie_line_res = sortrows(Tie_line_res,3);
        Tie_line_res(:,3) = Tie_line_res(:,3) - min(Tie_line_res(:,3));

        figure; set(gca,'FontSize',20); axis tight
        scatter(Tie_line_res(:,2),Tie_line_res(:,1),25,...
            Tie_line_res(:,3),'filled');
        ylabel(['Residuals ' Struct.var_unit],'FontSize',20);
        xlabel(['Time ' Struct.time_unit],'FontSize',20);
        title(['Colorcoded tie line residuals (calibration time) ' ...
            Struct.var_name]);
        h = colorbar; title(h, ['Time ' Struct.time_unit]);
    case Struct.but_col_codeD
        % Color code distance from calibration point
        % for every tie line pair
        Tie_line_res = evalin('base','Tie_line_res');
        Tie_line_res = sortrows(Tie_line_res,4);

        figure; set(gca,'FontSize',20); axis tight
        scatter(Tie_line_res(:,2),Tie_line_res(:,1),25,...
            Tie_line_res(:,4),'filled');
        ylabel(['Residuals ' Struct.var_unit],'FontSize',20);
        xlabel(['Time ' Struct.time_unit],'FontSize',20);
        title(['Colorcoded tie line residuals' ...
            ' (distance calibration pairs) ' Struct.var_name]);
        h = colorbar; title(h,'Distance');
    end
end

```

Chapter 5

Absolute calibration and potential for conductivity modelling

A man with a watch knows what time it is. A man with two watches is never sure

-- Segal's law

5.1 Aim and strategy

Systematic and random measurement errors impede realization of the full potential of FDEM data. Calibration is of the utmost importance when comparing data collected using several electrical and (electro)magnetic geophysical methods (Benech et al., 2002) and even when comparing data collected using the same technique at different times or with different instruments. Systematic errors persist despite “factory” calibration of the instruments (see Mester et al., 2014). Quantitative information on subsurface conductivity and susceptibility can be obtained through data inversion but systematic errors might impact the inversion results severely. Systematic errors include signal drift and incorrect data levelling. A summary overview of FDEM calibration strategies can be found in Minsley et al. (2012) -for helicopter and land-based data- and Thiesson et al. (2014) -for land-based data. A brief overview on drift correction strategies for ground-based FDEM data is provided in chapter 2. Other problems impacting accurate mapping of subsurface conductivity and susceptibility are the approximations involved in relating the measured fields to ground conductivity and susceptibility. In addition, inversion results can be heavily dependent on (opaque) parameters and, when applying 1D inversions, FDEM 2D/3D geometrical effects (see Frischknecht et al., 1991) can distort the results. Aforementioned error sources and problems can lead to wildly inaccurate results when applying 1D inversions. For calibration purposes, collection of both ERT profiles (Lavoué et al., 2010 and Minsley et al., 2012) and ground cores (Moghadas et al., 2012) have been reported.

In this chapter, arable land was surveyed using a multi-configuration FDEM instrument to explore the potential for accurate conductivity mapping. The collected responses showcased a broad range, indicating fresh to salt groundwater. Due to high conductivities, linear approximations (between the QP responses and EC) were no longer valid (Beamish 2011) and the depth of investigation was uncertain (Callegary et al. 2007), complicating an accurate delineation and characterization of the salt lens. This necessitated a custom approach, tailored to allow validation of the FDEM data and EC models derived thereof. The survey strategy consisted in performing a FDEM survey and recording a (single) calibration line for drift correction. In addition, FDEM height soundings and CPT-EC logs were collected at specific locations, to be used in calibration and for validation purposes. All data were gathered in a two day time span to ensure maximum correspondence of all temperature and moisture dependent data.

The survey strategy consisted in performing a FDEM survey and recording a (single) calibration line for drift correction. In addition, FDEM height soundings and cone penetration testing (CPT) logs (including an EC module) were collected at specific locations, to be used in for validation purposes. All data were gathered in a two day time span to ensure maximum correspondence of all temperature and moisture dependent data.

The conductivity logs (CPT-EC) were used to calculate theoretical instrument responses at several locations. These theoretical responses were compared to the experimental results in order to evaluate the levelling of the FDEM data. The logs were also used as reference data to obtain optimal inversion parameters and assess the estimated depth of investigation.

5.2 Materials and methods

Data collection and processing

Within LIN conditions, the QP response is linearly proportional to subsurface conductivity (EC). The LIN approximation is no longer valid for large coil separations and/or high conductivities. This shortcoming can be addressed by calculating the deviation from a linear relationship and correcting for it (Beamish 2011; Delefortrie et al., 2014a) or by using both QP and in-phase responses to attain robust apparent conductivities (Guillemoteau et al., 2015). The resulting, corrected σ_a data can then be inverted (e.g. Guillemoteau et al., 2015). Another possibility consists of avoiding approximate relationships altogether by solving Maxwell's equations to calculate the FDEM responses of a layered earth for given layer conductivities, susceptibilities and permittivities (or an assumption of zero permittivity considering the negligible effect it has on FDEM responses (Ward and Hohmann, 1987)). This is sometimes referred to as the “full solution” and this approach allows inverting QP and IP responses to obtain estimates of subsurface conductivity and/or susceptibility at different depths (Farquharson et al., 2003). For the modelling and inversion of FDEM data in this paper, the latter approach was favoured and only the QP and IP data were used.

For the FDEM data collection, multi-receiver data were recorded using a DUALEM 421S sensor (DUALEM Inc., Milton, Canada). On 29/09/2015 an FDEM survey was conducted in the survey area, using the DUALEM 421S in HCP mode. The sampling frequency was 8 Hz and the instrument elevation (intercoil centre line) was 0.16 m. The data were collected along parallel lines, 4 m apart, at a speed of ~10 km/h. The acquisition direction was east-west and geographic coordinates were logged using a dGNSS system. After collection, all measurements were corrected for the spatial offsets between the GNSS antenna and the coil configuration midpoints using the methods discussed by Delefortrie et al. (2016) as well as a time lag. Following, the data were corrected for signal drift using a calibration line as described in Delefortrie et al. (2014b). The processed data were then interpolated to grids (1 x 1 m) using natural neighbour interpolation (Sibson, 1981), which served as the basis for all subsequent data handling. Figure 5.2 shows the resulting HCP1 map. No treatment for random errors was performed (such as a low pass filter) since the signal to noise ratio was considered excellent (due to the high conductivities and low interference). The noise levels for the QP data were estimated to be 0.03 ppt for the 1 m separations, 0.10 ppt for the 2 m separations and 0.20 ppt for the 4 m separations (see also chapter 2).

On 30/09/2015 additional FDEM soundings were performed at 11 selected locations along two transects (Fig 5.2). The soundings consisted of logging the instrument responses at 9 heights (0.08 to 2.08 m with 0.25 m increments) in the HCP as well as the VCP mode. At each height, the instrument signals were logged for 1 – 1.5 minutes (Fig. 5.1). For each recording (9 coil configurations x 9 heights x 11 locations), the median was calculated and stored. At the same locations and on the same day, CPT data were collected using a 200 kN CPT system. The CPT probe had a cross-sectional area of 15 cm² and simultaneously measured cone resistance (total force acting on the cone divided by the projected area of the cone), q_c , and sleeve friction (total force acting on the sleeve of the cone divided by the area of the sleeve), F_s . The friction ratio, R_f , is defined as the ratio F_s/q_c . Soil properties such as grain size, and soil consolidation govern q_c and R_f (Lunne et al., 1997). A CPT measurement at a particular depth is influenced by the subsurface several cone diameters around the tip (Robertson and Campanella, 1983). In addition, a module to measure electrical conductivity, by use of an electrode array, was mounted below the tip of the cone (Gouda Geo-Equipment B.V., Warmond, The Netherlands). This module was calibrated before application, using salt baths with known conductivity (cf. Hilhorst, 1998) and the module was nulled before collection of every log. Figures 5.3 and 5.4 show the CPT and CPT-EC data for all locations. Limitations of the CPT technique are that the cone cannot penetrate hard materials. The advantages are the speed of execution, the objectivity, the collection of several subsurface parameters (depending on the cone used) and the high vertical resolution.

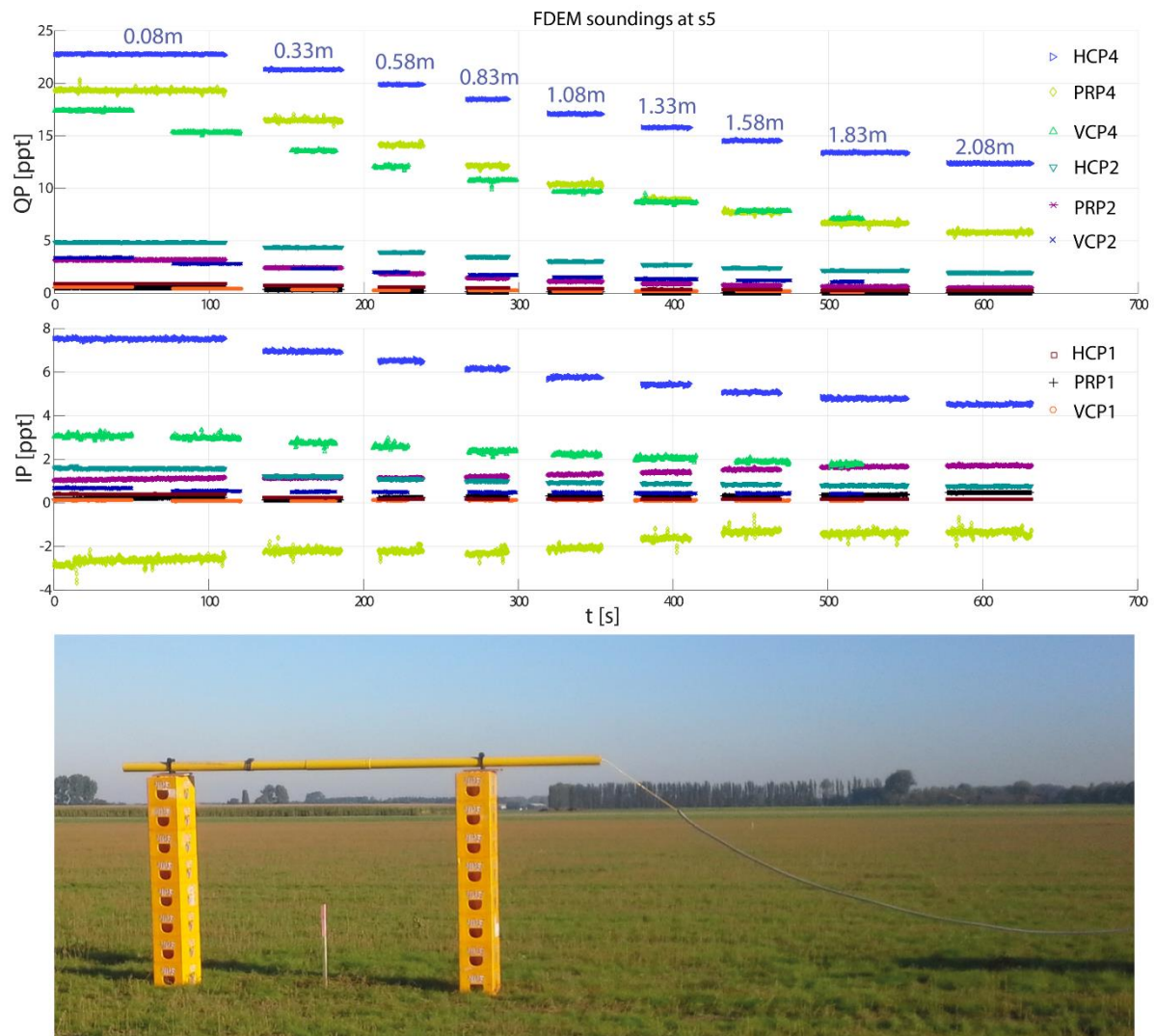


Figure 5.1. (Top graphs) FDEM height sounding example at location ‘s5’: QP and in-phase responses of both HCP/PRP and VCP mode for the DUALEM 421S at 9 heights (0 to 2 m with 0.25 m increments). The instrument elevation (intercoil centre line) is listed on the upper plot. (Bottom picture) photograph of height sounding set-up in the survey area with the instrument at a height of 2 m. The midpoints of the coil configurations are at slightly different locations along the instrument (within 1.5 m of each other) meaning there is a small spatial offset with regards to location ‘s5’ for some coil configurations. During the heights soundings the instrument was positioned in an E-W direction.

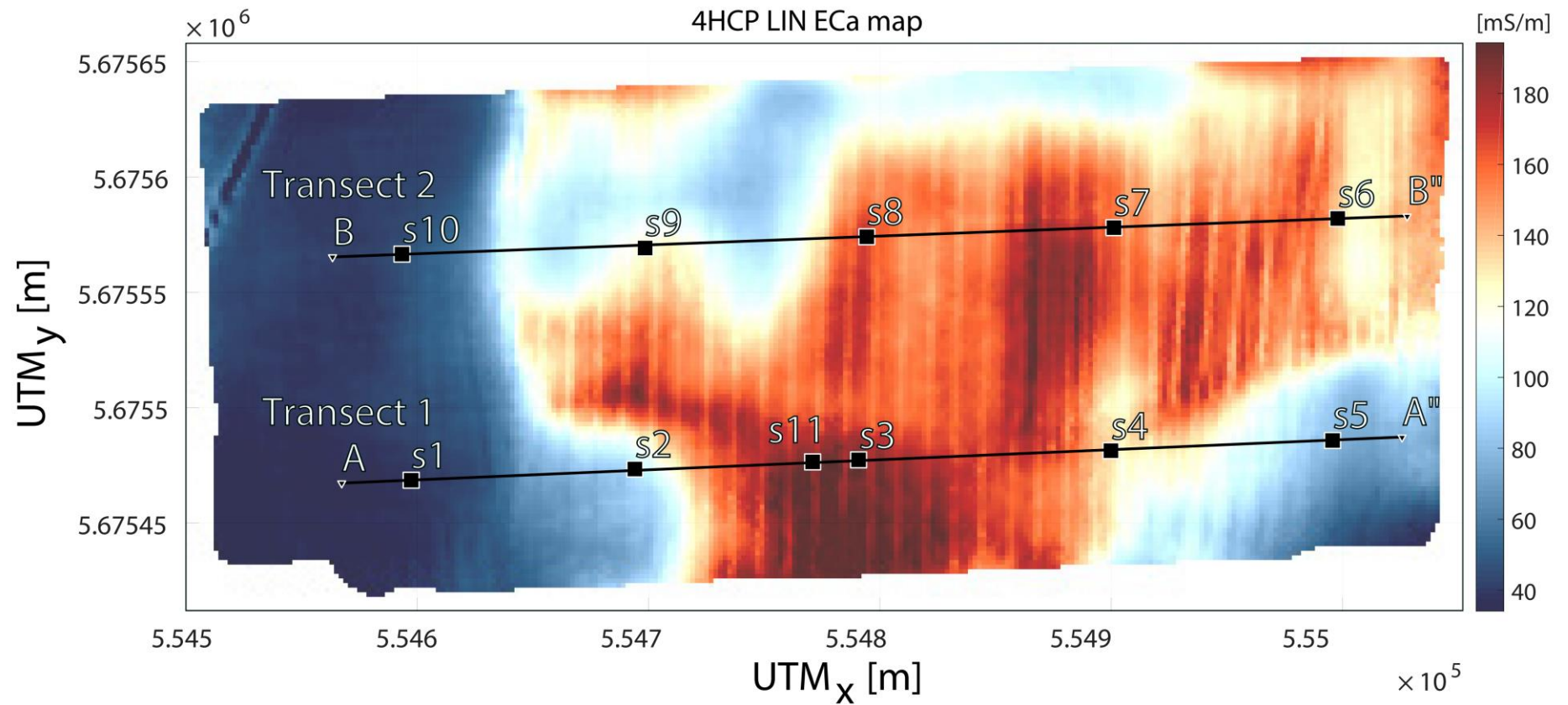


Figure 5.2. Initial FDEM survey result: 4HCP LIN ECa map. The black crosses show the locations of the CPT logs and FDEM soundings along two transects. Axes show UTM coordinates [m]. In the northwest corner (edge of map) a gas lead can be seen in the data. An extensive drainage network with north-south orientation is prominently visible in higher conductivity zone.

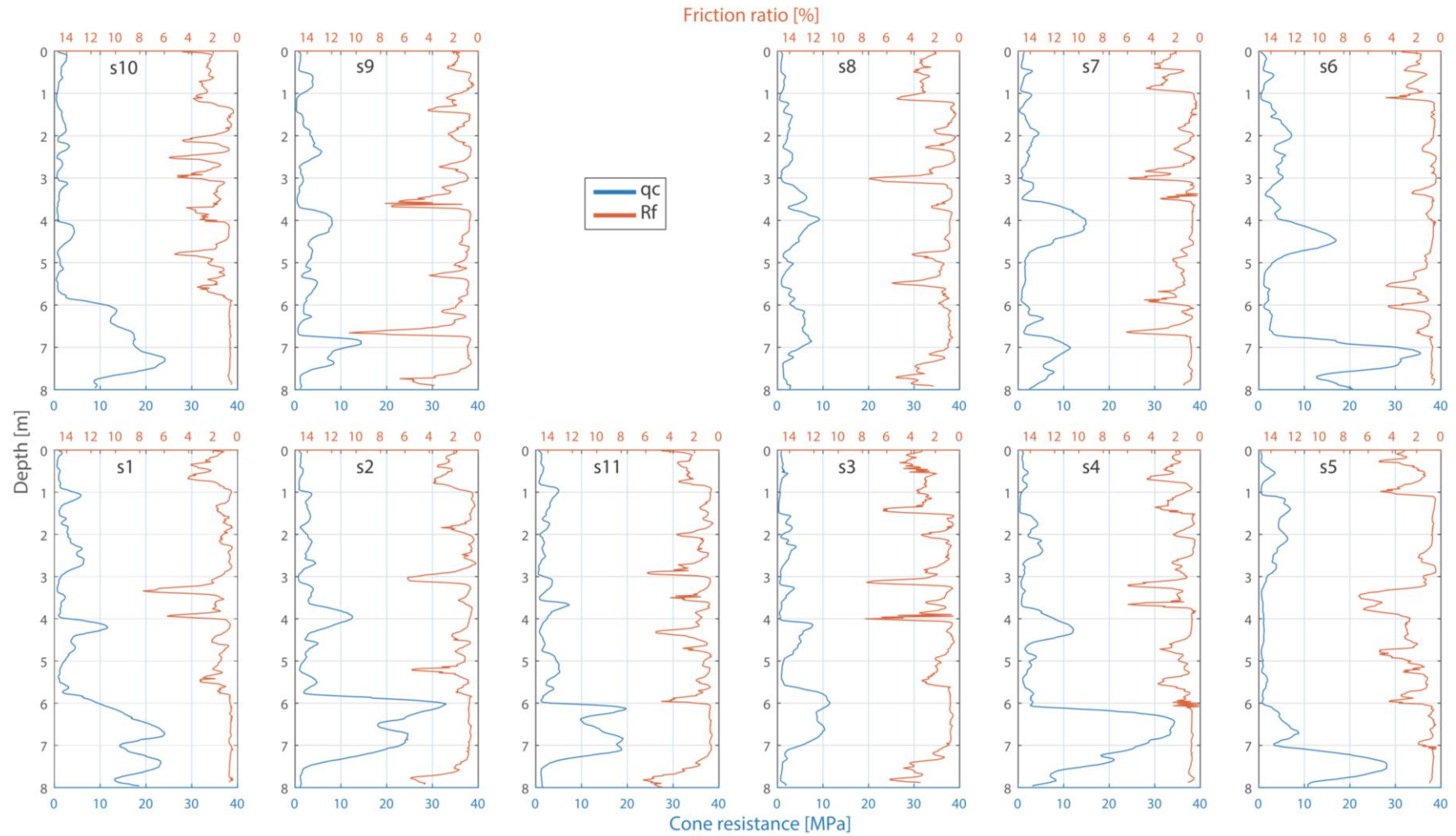


Figure 5.3. CPT logs taken along two transects in the survey area. The cone resistance (q_c) is plotted as a blue line on the left side of the plots (with the corresponding axes at the bottom) and the friction ratio (R_f) is plotted as an orange line on the right side of the plots (with the corresponding axes on top). The order of the plots is the same as on the transect lines (see Fig. 5.2).

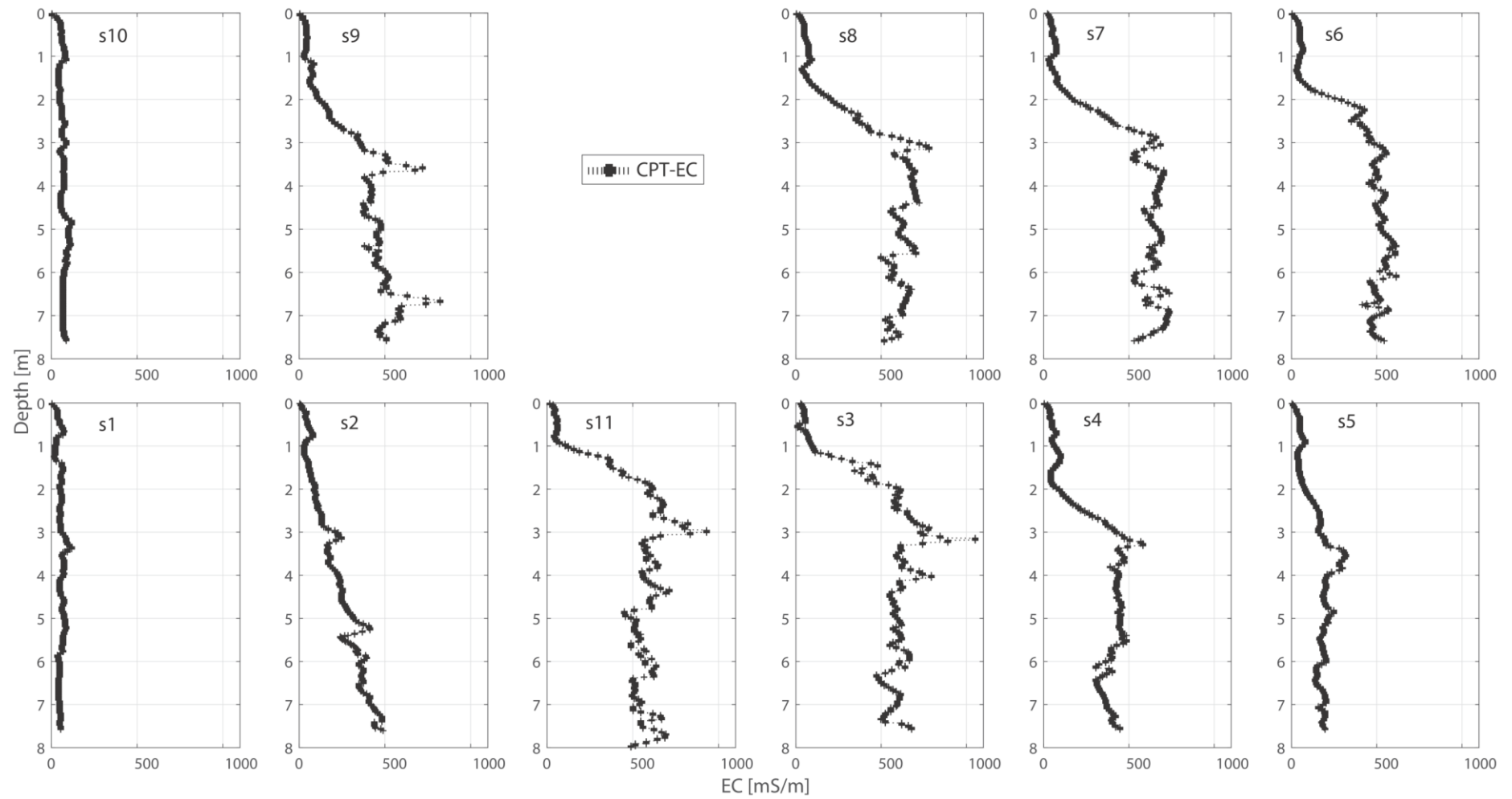


Figure 5.4. CPT-EC logs taken at the survey area. All axes have the same limits. The order of the plots is the same as on the transect lines (see Fig. 5.2).

The forward model EM1DFMFWD, that was used to compute the magnetic field values for the given coil configurations over a layered half-space, employs the matrix propagation approach described in Farquharson et al. (2000). The method uses the z-component of the Schelkunoff F-potential (Ward and Hohmann 1987). An alternative development (with the same results) is given by Minsley (2011) and is applied in the FEMIC code (Elwaseif et al. 2017).

For inverting the data, the EM1DFM (Farquharson 2000) code was applied. The fixed trade-off parameter inversion type was used and the inversion parameters were selected through trial and error by considering the inversion misfits, the robustness of the inversion parameters and by comparing the inverted results with the conductivity logs. A reference (homogenous) background of 200 mS/m and 0 susceptibility was passed along. The noise levels were indicated for the various coil configurations as well. Generally put, the inversion aims at constructing the simplest model that adequately reproduces the observations by posing the inverse problem as an optimization problem in which the model is sought that minimizes the objective function:

$$\Phi = \phi_d + \beta \phi_m$$

with

$$\phi_d = \| W_d (d - d^{obs}) \|^2$$

and (in the case of only inverting for conductivity)

$$\phi_m = \alpha_s \| W_s (m - m_{ref}) \|^2 + \alpha_z \| W_z (m - m_{ref}) \|^2$$

where ϕ_d represents the data misfit or the l2-norm (represented by $\| \cdot \|$, indicating the root square error) of the weighted differences between the observed and forward modelled responses. The weights W_d are given according to the noise indications for each observation. ϕ_m is the model structure. The two terms correspond to the “smallest” and “flattest” terms for the conductivity parts of the model (governed by the coefficients α_s and α_z respectively). W_s and W_z contain weights related to the model layer thicknesses while m and m_{ref} pertain to the (conductivity) model and reference model. By iteratively solving the objective function the non-linear problem is linearly approximated during each iteration. The iterative solver employs by the least squares solution, using the Paige and Saunders subroutine (1982). Finally, β is a user defined trade-off parameter which balances the relative share of the data misfit and model structure. For more information on the implementation of the EM1DFM forward model, the objective function of the inversion and the exact definitions of the inversion parameters, we refer to Farquharson et al (2003), Oldenburg and Li (2005) and the manual of the program: <https://www.eoas.ubc.ca/ubcgif/iag/sftwrdocs/em1dfm/em1d-man.html>.

The 3D forward code Marco 4.4.0 (Raiche 2008) was applied as well for a simulation of the possible impact of (lateral) small-scale heterogeneities. It can be used for the 3D forward calculation of

responses for a layered medium with the inclusion of a set of arbitrary prisms by use of the integral equation method. Unfortunately the theoretical background of the software is not well documented though a list of references supporting the code can be found at: [http://www.amirainternational.com/web/documents/downloads/p223f/software/P223%20Modelling%20software January%202008.pdf](http://www.amirainternational.com/web/documents/downloads/p223f/software/P223%20Modelling%20software%20January%202008.pdf).

A depth of investigation (DOI) of the FDEM data was estimated at each validation location and consisted of:

- (i) forward calculation of the instrument response (4HCP) using conductivity profiles → “original” response;
- (ii) iterating the forward calculation for the profiles with increased conductivities along incremental depths of the profile → “simulated” responses;
- (iii) calculating the difference between the “simulated” responses and the “original” response → simulated sensitivity for all depths;
- (iv) normalizing the cumulative sensitivities;
- (v) determining a sensitivity threshold by performing aforementioned steps on a synthetic low-conductivity profile and taking the value encountered at the maximum DOI (explained below) as the response threshold → gauging step;
- (vi) applying the threshold to the desired profile → local DOI.

It follows that this procedure allows quantifying the decrease in depth sensitivity along a given conductivity profile compared to a synthetic low-conductivity profile. For the results in this paper, the CPT-EC data were considered for step 1. Every 10 cm, 1 S/m was added for calculating the sensitivities (step 2) since a sufficiently large value was needed to provide contrast in the case of high conductivity CPT-EC profiles. The cumulative of the simulated sensitivities ($sens$) was calculated using: $sens_{cum,i} = \sum_{j=1}^i sens_j$ and the normalization was performed by: $tmp_i = sens_{cum,i} - \min(sens_{cum})$ and $sens_{norm,i} = \frac{tmp_i}{\max(tmp)}$ (step 4). The synthetic low-conductivity profile consisted of a homogeneous 1 mS/m profile (step 5).

The gauging step is applied to decrease the subjectivity of the procedure by considering a substantiated reference; for the 4HCP coil configuration a maximum DOI of 6.2 m was considered (i.e. the manufacturer’s DOI limit). Yet despite the gauging step, the discretisation of the profiles, the added conductivity value and conductivity of the synthetic profile all influence the results, meaning the method cannot be considered completely objective. Furthermore, it needs mentioning that EM methods are diffusive in nature making the determination of a single DOI limit ambiguous (Christiansen and Auken 2012).

Study area

The survey area is arable land located in Assenede, Belgium; the central (UTM 31) coordinates are X: 554 750 m, Y: 5 675 600 m. The land has been levelled and is located at a height of approx. 3 - 3.5 m above the mean lower low sea-water level at the Belgian coast. The surface area is ~11 ha and the subsurface consists of Quaternary deposits, comprised of unconsolidated marine and continental sediments overlying Pleistocene sediments. The CPT data allow us to characterize the subsurface in more detail (Fig. 5.3): at most locations clayey sand to clay is present up to a depth of < 6 m. Intermittently, thin peat layers (characterized by a high R_f and low q_c) are present in these clayey deposits. Underlying these sediments are sandy deposits (high q_c). Groundwater was registered at a depth of 1 m at location 's10'.

The conductivity logs (Fig. 5.4) show a good qualitative correlation with the preliminary results of the FDEM survey (Fig. 5.2) and showcase the significant variation in salinity of the groundwater in the subsurface as well as the shallowness of the salt lens. At locations where salt water is present, there is a steep rise in EC downwards from 1 to 1.5m depth with a maximum EC being reached at ~3m depth (in most cases). When comparing the CPT data with the CPT-EC data, it is evident that local (elevated) peaks in EC correlate with thin peat layers (only at locations with salt groundwater). The highest conductivity encountered is ~1100 mS/m, at location 's3'.

The FDEM survey (see Fig. 5.2) resulted in qualitative maps of the variation in conductivity and shows the presence of a gas lead in the northwest corner as well as an extensive drainage network (associated with lower conductivity zones) with north-south orientation and a spacing of ~10 m. Because of the drainage pipes, some FDEM responses were “tripled” (meaning the traverses displayed complex response signatures consisting of several peaks) due to the size and conductivity contrast of these anomalies (see Callegary et al. 2012; Delefortrie et al. 2014a). In addition, the PRP maps showed zig-zag patterns over local anomalies due to the asymmetric responses (not shown) and differing headings of the collected data lines. According to information provided by the farmer two drainage networks are present at a depth of ~0,7 – ~1,2 m (one recent: PU pipes, and one older: brick drainage).

5.3 Results and discussion

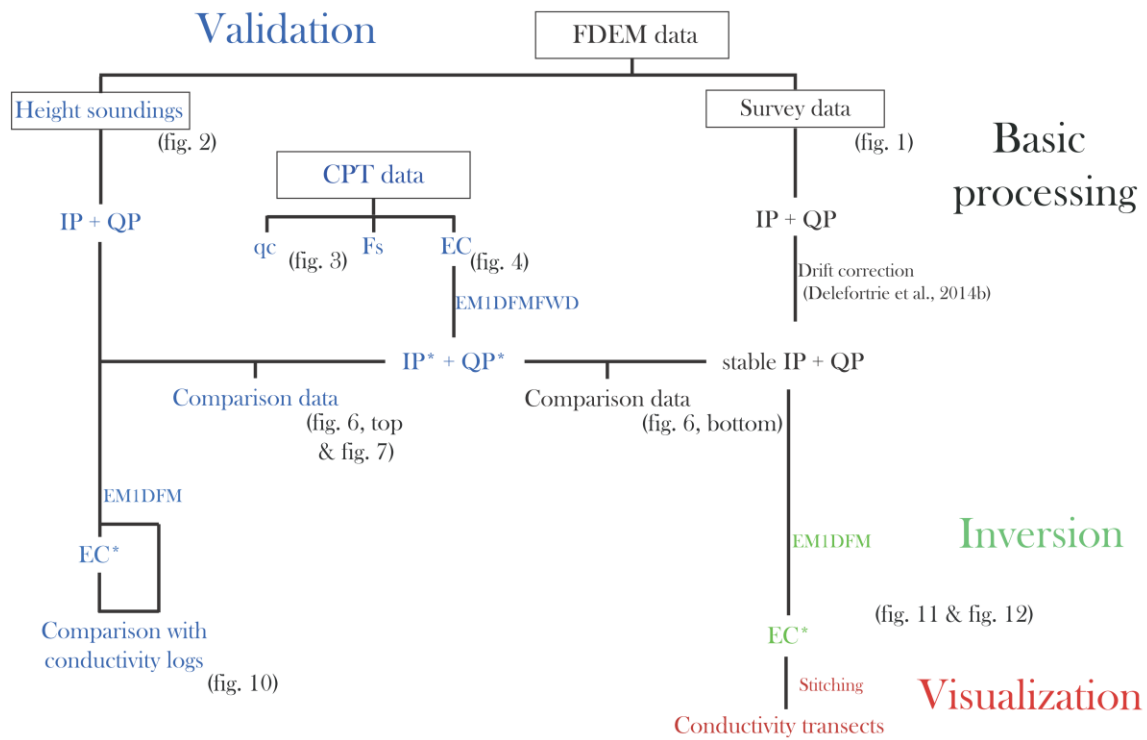


Figure 5.5. Flowchart summarizing the data processing with regards to the basic processing, validation and inversion of the FDEM data.

A flowchart of the data processing concerning the validation and inversion of the FDEM data is given in Fig. 5.5. To ascertain the presence of calibration errors in the FDEM data, the FDEM responses measured at the validation locations were compared with the 1D forward calculated responses (QP* and IP*) based on the CPT conductivity logs. Discrepancies between measured and calculated responses in both components can result from: (i) FDEM calibration errors (ii) CPT-EC calibration errors (iii) incorrect positioning of the instrument over the surface (including roll and pitch) (iv) subsurface heterogeneity (comparing volume data with local measurements) (v) measurement noise (vi) erroneous assumptions present in the forward modelling procedure and (vii) an erroneous basement conductivity. The basement conductivity taken at each validation location, was the last registered conductivity of each CPT conductivity log.

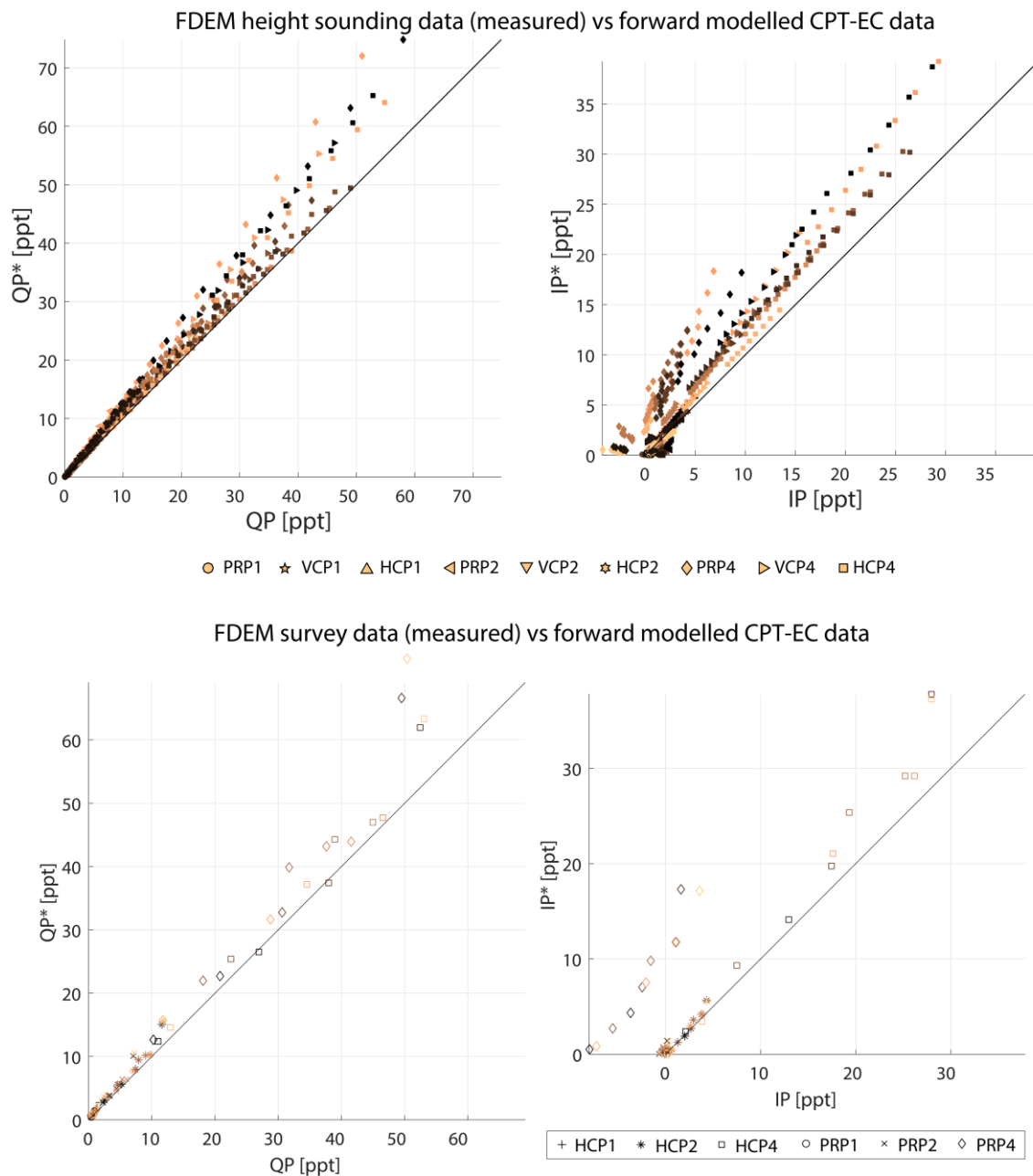


Figure 5.6. Scatterplots of forward modelled FDEM responses (QP* and IP*) using EM1DFWD based on the conductivity profiles from the CPT-EC logs and the actual, measured FDEM data (QP and IP). Subsurface susceptibility was assumed to be zero. The colour coding of the data corresponds with the validation location. (top) shows the comparison data for the height sounding FDEM data (11 locations x 9 heights x 9 configurations) and (bottom) shows the comparison data for the area survey FDEM data (11 locations x 1 height x 6 configurations).

Figure 5.6 shows the scatterplots with the (EM1DFMFWD) forward modelled CPT-EC data and FDEM heights soundings (top) and the forward modelled CPT-EC data and FDEM survey data below (bottom). Several things can be gleaned from this figure:

1. - The QP* vs QP comparison data show excellent correlations, which advocates the combined use of CPT-EC and FDEM data and suggests a sound forward modelling procedure. In addition, both the survey and height sounding data provide similar results (top and bottom plots). This confirms a limited signal instability (compared to the conductivity variation) for the height sounding data (it was not drift corrected); cf. Delefortrie et al. (2014b). The potential advantage of collecting height sounding data lies in attaining more data (per location) which may be useful if few validation points are present (as is the case).
2. The in-phase* vs in-phase responses do not show strictly excellent correlations: although there is a resemblance to the QP data (because the in-phase is also influenced by the high conductivities), several configurations showcase erratic comparison data with poor correlation. It is striking that the bottom IP* vs IP plot shows less erratic data. This is due to the (less stable) in-phase responses having been drift corrected; cf. Delefortrie et al. (2014b).
3. The amplitude of the responses drops significantly with increasing instrument height

Because of the uncertainty in the comparison data (which precludes accurate detection of levelling offsets) and the lack of susceptibility validation data (a zero susceptibility was assumed) an attempt at inverting in-phase data was not undertaken.

Figure 5.7 again shows the QP* vs QP data but with the data separated for every coil configuration. In addition, the coefficients of determination are listed together with the coefficients of a linear fit. It is remarked that the height sounding data are not uncorrelated for a given coil configuration. From these detailed plots, the following can be deduced:

1. Despite the excellent correlation for the QP* vs QP data, there seems to be an obvious bias as well as a large uncertainty (which increases with increasing QP) present in the comparison data. Whereas the slope coefficients indicate a significant bias, the limited intercepts of the linear fits reveal a good correspondence at low QP values.
2. The large discrepancies preclude the use of this data for accurate detection of levelling offsets.
3. Looking closer at the HCP4 comparison data (upper right plot Figure 5.7), it is apparent that with decreasing instrument height and increasing QP, the discrepancies are habitually larger, yet the effect varies along with the location. The largest discrepancies are linked to the validation locations 's3' and 's11'. Similar observations can be made for the other configurations.

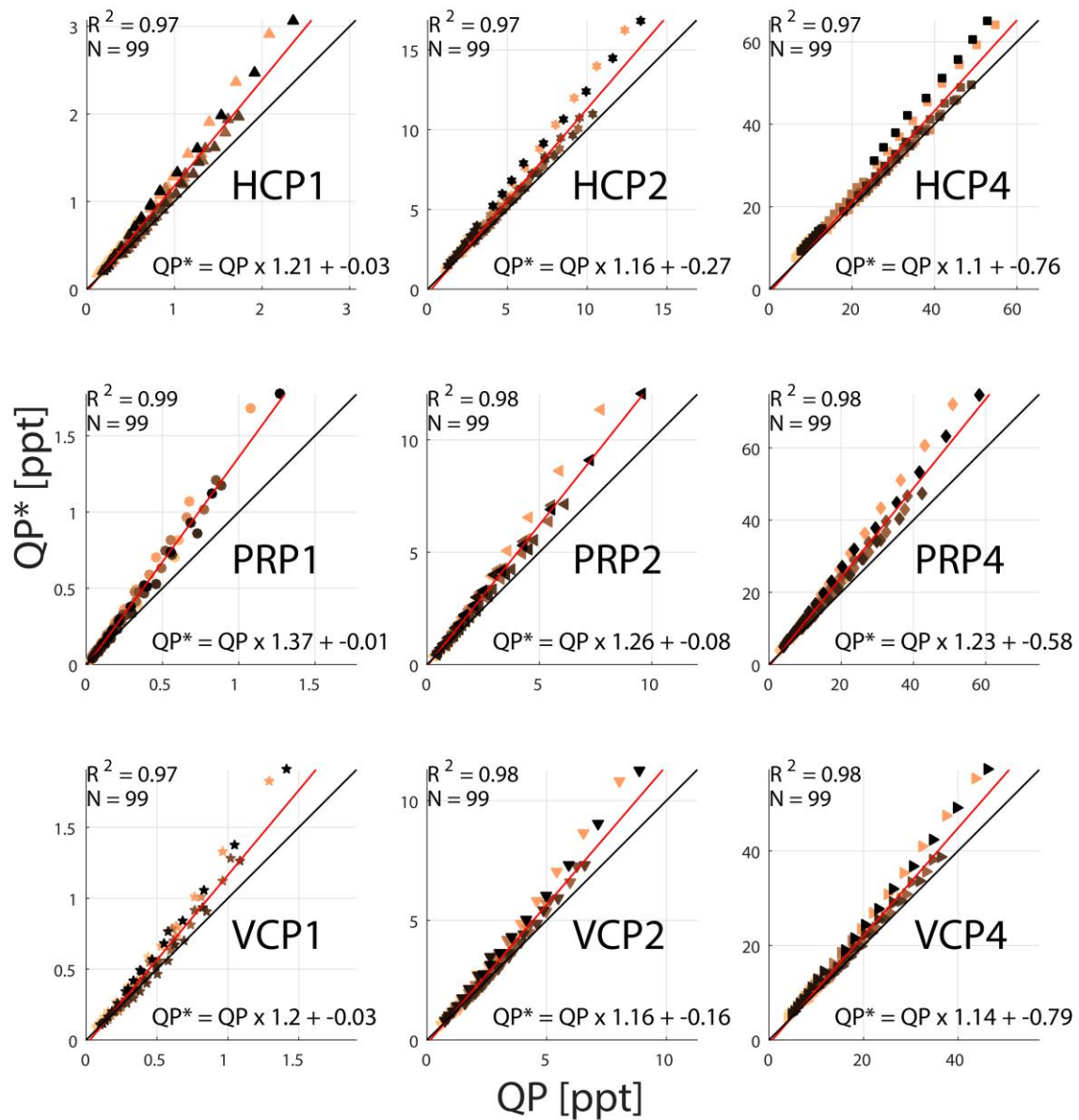


Figure 5.7. Scatterplot of forward modelled FDEM responses (QP^*) using EM1DFWD based on the conductivity profiles from the CPT-EC logs and the actual, measured height sounding FDEM data (QP). The data are separated according to coil configuration type. Same data as shown in Figure 6 top.

Due to the many factors (and stacking of errors) possibly contributing to the QP^* - QP discrepancies, it is hard to interpret the scatterplots and impossible to estimate the impact of every factor. Nonetheless, it can be reasoned that the trends present in the comparison indicate a strong effect due to the presence of subsurface heterogeneities: alternative hypotheses cannot sufficiently explain the occurrence of discrepancies that vary so much with location. A likely cause for this would be the presence of the extensive drainage network (cf. Fig. 5.2). To verify this hypothesis, a simple, synthetic model was used to assess the effect of small scale heterogeneities: a two layered model with two low conductivity features with large lateral extensions (1 x 1 x 100 m), representing the drainage pipes, was used to approximate the situation at locations ‘s3’ and ‘s11’. These dimensions

are quite large to take into account impact of drainage installation (soil excavation and placement of permeable material) that goes beyond just the presence of a pipe in the subsurface. Figure 5.8 shows the synthetic model and the 3D and 1D forward modelled E-W traverses (perpendicular to the drainage tiles) for the 4HCP configuration. This is a simulation and by no means a perfect representation of the truth. However, the results indicate that it might explain for most of the discrepancies seen in Figure 5.7:

1. Small bodies with a strong conductivity contrast are shown to have a large effect.
2. The 3D forward responses are consistently lower, compared to the 1D responses
3. The effect of the heterogeneities decreases with increasing instrument height
4. It is remarked that the validation locations were located in between the (lower conductivity) linear anomalies detected during the area survey to avoid damaging the drainage/CPT cone. Though it seems these zones do not necessarily coincide with the drainage tiles, the varying distances with regards to such a feature would explain the large variation between locations despite similar QP responses.
- 5.

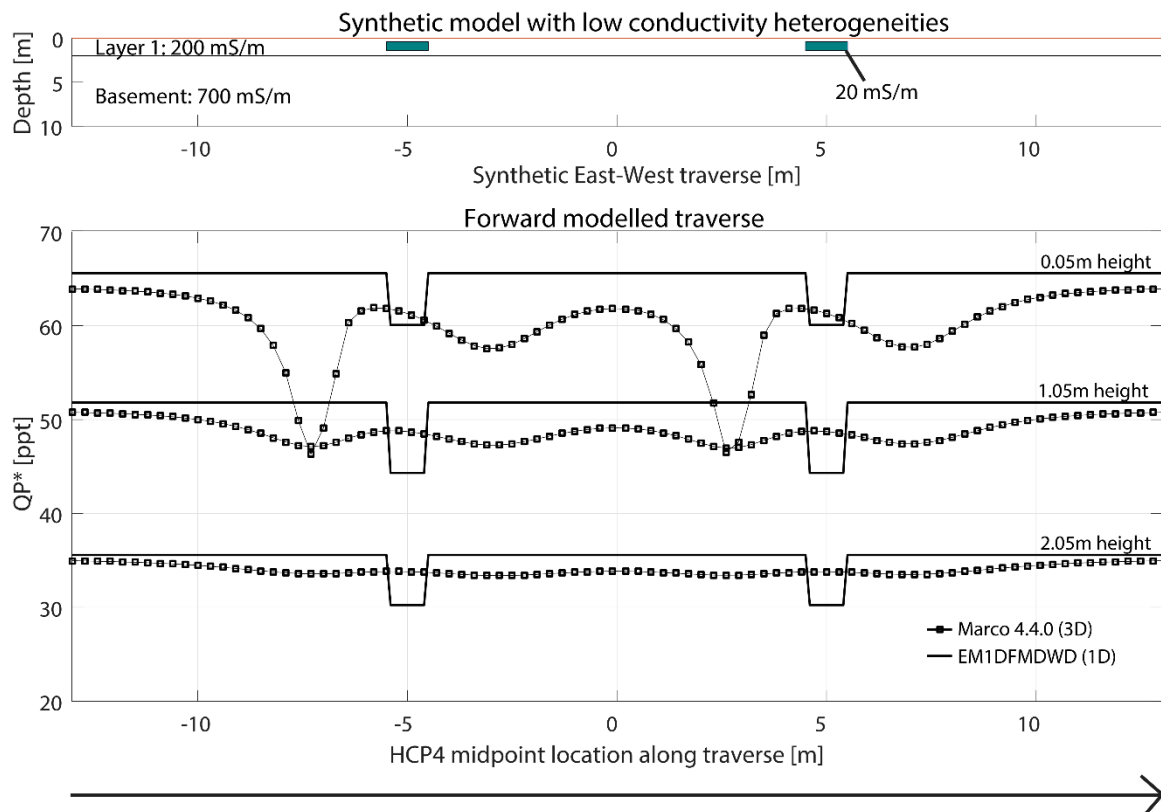


Figure 5.8. Simulation of effect of lateral heterogeneity due to drainage tiles. (top) show the synthetic model and (bottom) shows the forward modelled 1D and 3D responses for the 4HCP configuration.

The only way to prove this would be to collect more validation data at the drainage locations. However, other simulations were done for varying conductivities and configurations and the results do lend strength to the hypothesis; which would attribute the large uncertainty of the comparison data to the erroneous assumption of lateral homogeneity while still allowing excellent correlations. It is noted that the exact location, orientation, conductivity contrast, model, discretization, traverse direction, etc. have a large impact on the 3D modelling.

Following the previous discussion, the 0.05m height sounding data were inverted (using EM1DFM) to verify whether 1D inversions might still be of any use. The local DOI was calculated for each conductivity log (Fig. 5.9) using the approach described in the material and methods and the resulting EC* profiles are visualized on Fig. 5.10. Clearly, the shallow presence of salinity and high conductivities lower the maximum DOI significantly. From the EC* data it is obvious that the inverted data are more apt for assessing the general trend of conductivity with depth than allowing for an accurate conductivity reconstruction; large deviations are present and spikes in the EC data are not reconstructed. The largest deviations (from the conductivity logs) are associated with the high conductivity zones and the disparities are (unsurprisingly) greatest at ‘s3’ and ‘s11’. This does show that the QP vs QP* plot can be seen as an assessment of (1D) inversion accuracy in itself; revealing biases and uncertainties beforehand in a way that would not be possible from (e.g.) assessment of inversion misfits. Nonetheless, the similarity concerning data range and EC trend showcase that a robust representation could still be reached through 1D inversion. Naturally, this was also influenced by the applied inversion parameters: β : 150, α_s : 1×10^{-4} and α_z : 1. These indicate that, during the iterative process a lot of weight was given to the model structure and that a flat model was preferred. More data-driven inversions or inversions with a large “smallest” structure resulted in less robust inversions that were quite unrealistic.

For further comparison and validation, the survey data were inverted (EM1DFM) along the transects seen on Fig. 5.2. The stitched EC* profiles are visualised on Fig. 5.11 and the inversions misfits can be seen on Fig. 5.12. Again the inversion parameters used were: β : 150, α_s : 1×10^{-4} and α_z : 1. These results further corroborate the previous validation. At some locations, the underestimation of EC* (compared to EC) due to lateral heterogeneity can clearly be seen. In addition, both figures 5.11 and 5.12 again reveal the significant impact of the drainage tiles: large corrugations are present in the raw, survey data and the resulting inversion shows large lateral discrepancies (which are especially apparent in the zone below the estimated DOI).

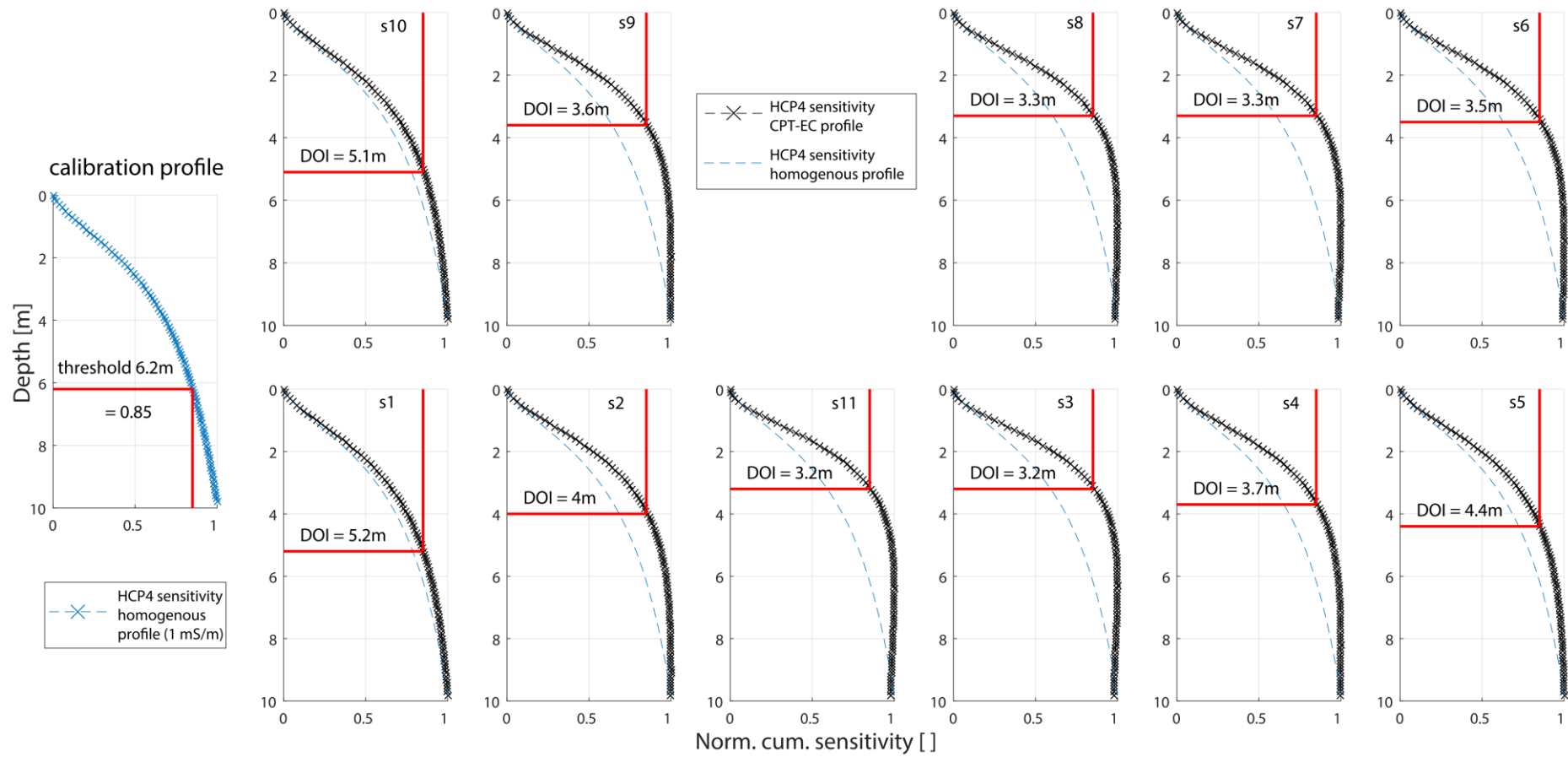


Figure 5.9. Sensitivity plots of the 4HCP QP survey response for the validation locations as well as a sensitivity plot for a synthetic, calibration profile. The estimated depths of investigations are given.

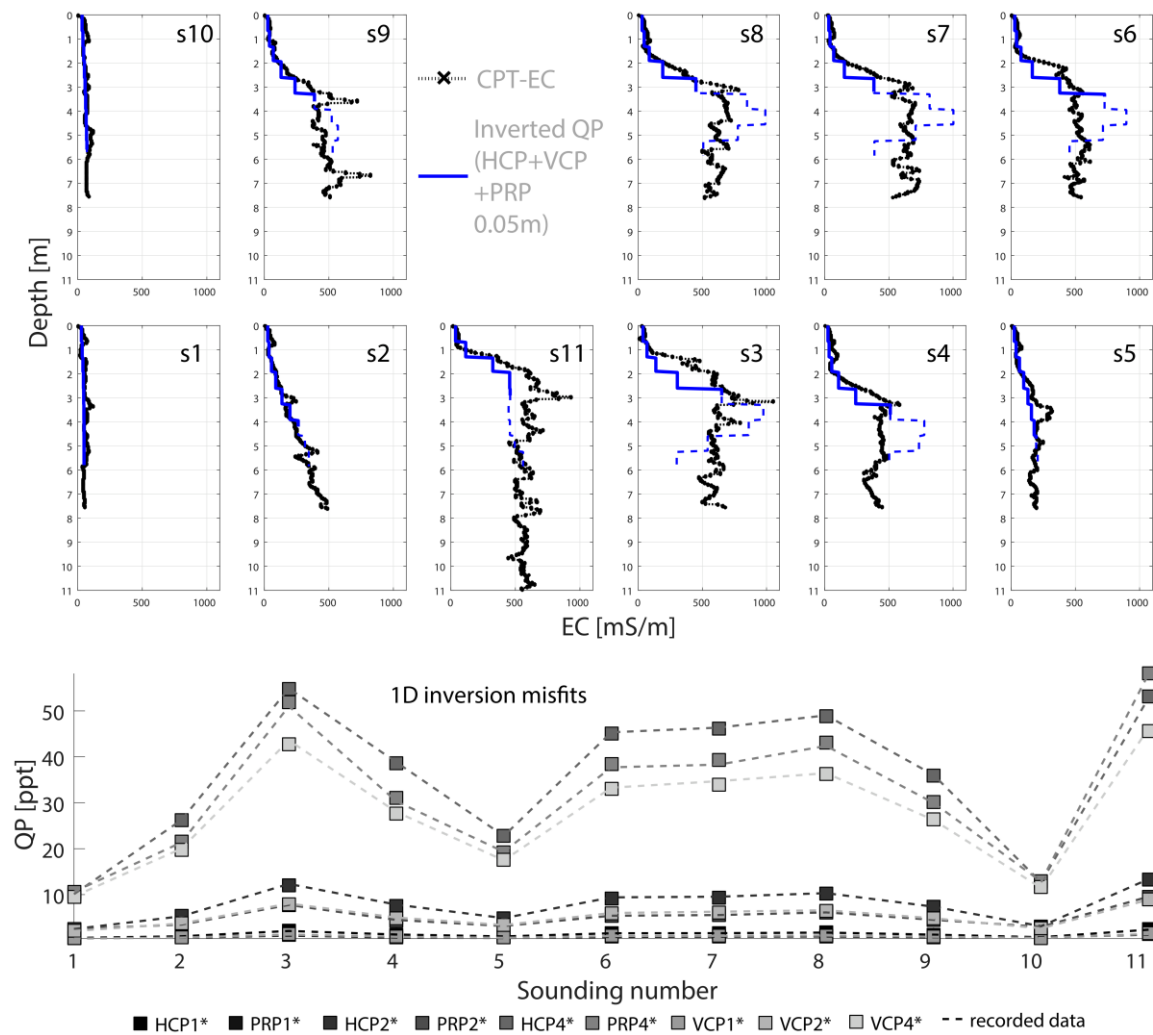


Figure 5.10. (top) CPT-EC logs plotted together with the inversion results of the QP responses (EC*) of the FDEM height sounding data. The FDEM data were inverted using the EM1DFM program and the fixed trade-off method was applied (with trade-off = 150 / acs = 1×10^{-4} / acz = 1). Only the QP responses were inverted. The EC* profile is presented as a dashed line below the estimated DOI. (bottom) Inversion misfits. The forward calculated responses of the inverted EC* profiles are plotted by use of squares and the measured FDEM responses are plotted using dashed lines.

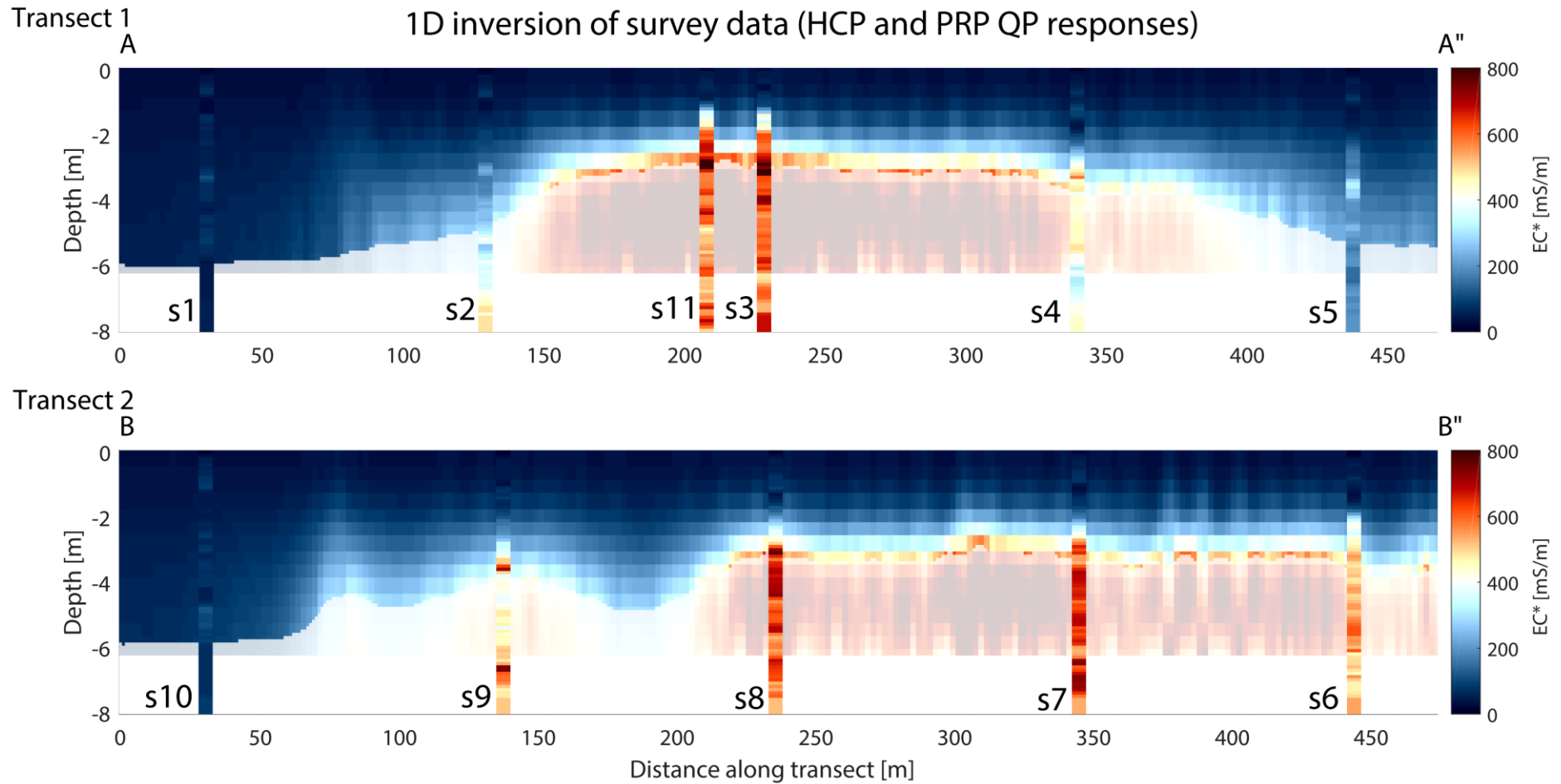


Figure 5.11. Stitched, inverted profiles (unsmoothed EC*) along the transects shown on Fig. 5.2. The FDEM data were inverted using the EM1DFM program and the fixed trade-off method was applied (with trade-off = 150 / acs = 1×10^{-4} / acz = 1). Only the QP responses were inverted. The validation profiles are also visualized (CPT conductivity profiles). The inverted model was made transparent below the calculated DOI.

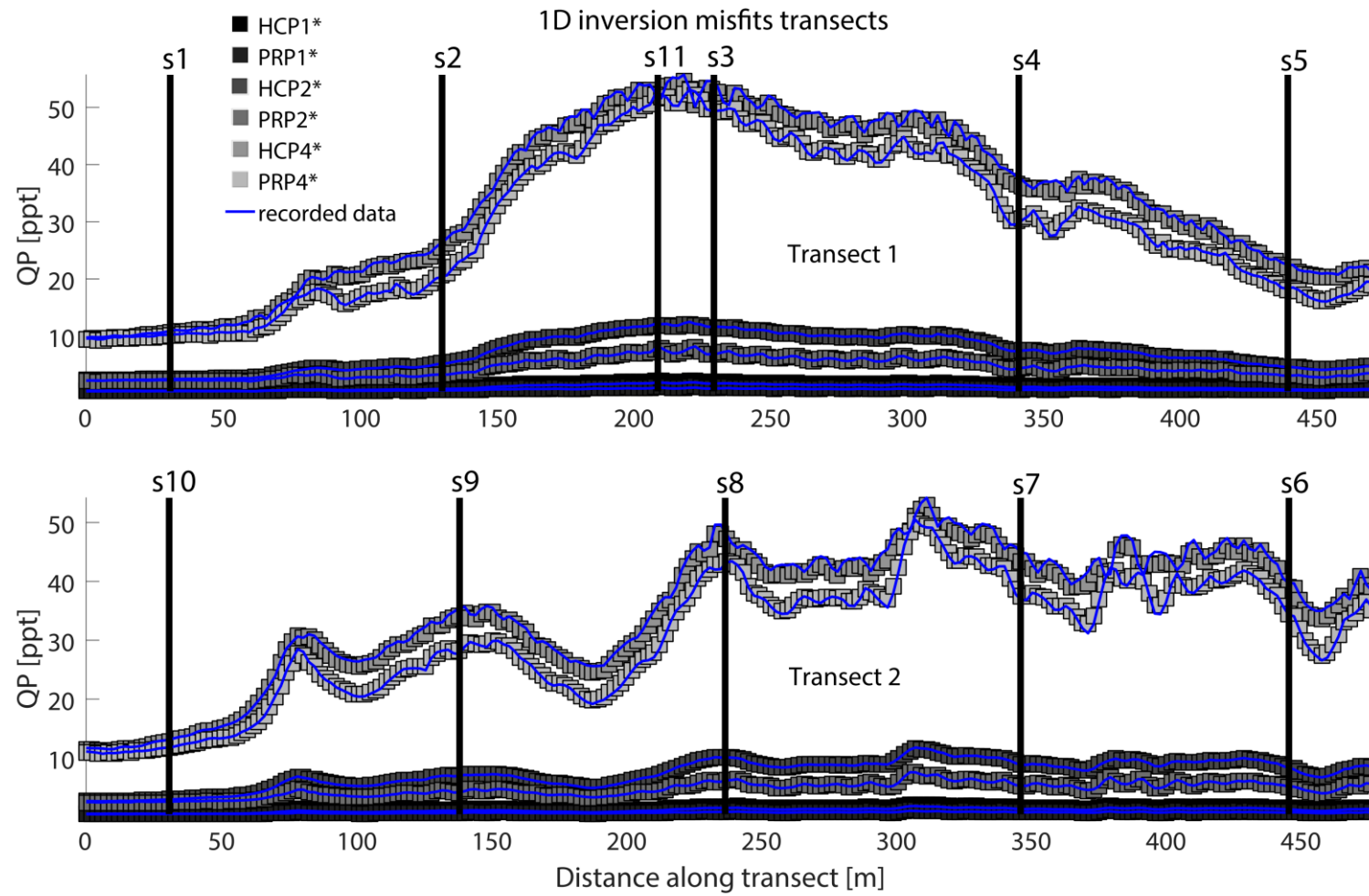


Figure 5.12. Inversion misfits associated with the inversion results shown in Fig. 5.11. The forward calculated responses of the inverted EC* profiles are plotted by use of squares and the measured FDEM responses are plotted using dashed lines.

5.4 Conclusions and future perspectives

Geophysical case studies are mostly tales of caution. The case described herein is no different: heavily diminished DOI due to high conductivities, complex instrument responses, subjectivity regarding inversion parameters, erroneous assumptions, ... all add uncertainty to FDEM results. It follows that the ease of use of FDEM instruments is mitigated by the data complexity. Making matters worse, properly validating geophysical data is laborious, which is exactly why validation is often lacking. Nonetheless, advances in instrumentation are running parallel with theoretical advances and are driving the rapid growth of ground FDEM applications. Bridging the gap between theoretical advances and practical limitations, and validating the data, as endeavoured in this chapter, is crucial for realizing the full potential of FDEM data.

Given the excellent correlations of the measured FDEM data and forward modelled conductivity logs, CPT-EC data is very likely an excellent addition to or alternative to DC electrical resistivity profiles or ground cores for validation purposes and assessment of FDEM calibration. The high vertical resolution of the CPT technique especially complements well with FDEM survey data, which allows extensive area surveys but has a low vertical resolution.

The sensitivity of FDEM responses to (contrasting) subsurface heterogeneities can be seen as an advantage of the technique, allowing adequate detection of such features. However, when attempting to obtain a general subsurface model through inversion, it seems the impact of heterogeneity can be significant: it can preclude to detection of levelling offsets and add a large uncertainty to 1D inversions. Since the impact of small heterogeneities decreases with increasing survey height, it may be interesting to investigate what other effects instrument height has on 1D inversions (e.g. decreased resolution, ...) and determine if it may be worthwhile to adjust the instrument height with survey objective.

To avoid an erroneous assumption of lateral heterogeneity, 2D or 3D approaches can be employed. However, it remains to be seen if the potential advantages (accuracy) can offset the disadvantages (complexity of the forward modelling, computation speed, subjectivity regarding the starting model, more inversion parameters, ...). One can also wonder if an accurately discretized 2D/3D starting model and a survey technique do not constitute a *contradictio in terminis*.

Though it was not possible to demonstrate the impact of levelling offsets in this chapter, pursuing the evaluation and correction of FDEM data offsets, specifically, would allow answering the following questions:

1. Are the benefits of absolute calibration worthwhile or is it more useful to pursue improvements in constrained inversion methodologies that take into account possible data offsets?
2. Is laborious (absolute) calibration always necessary if quantitative data analysis is desired or can the “factory calibration” of FDEM instruments be improved on?

Research to provide such a framework should: i) repeat the inclusion of ancillary data when performing FDEM surveys to ascertain whether QP levelling errors vary for different conditions and instruments and ii) expand the procedure towards in-phase data by collecting susceptibility logs.

Chapter 6

Absolute calibration and potential for susceptibility modelling

“All models are wrong, but some models are useful.”

-- George E.P. Box

6.1 Problem statement and aim

Applying the FDEM method to obtain information on the subsurface conductivity is well documented and a wide array of approaches have been investigated (Santos et al., 2004; Saey et al., 2012; Grellier et al., 2013; Guillemoteau et al., 2015). However, the potential for susceptibility mapping is often overlooked. Especially in environments with low susceptibility (e.g. most sedimentary environments) it is generally assumed that the background susceptibility is negligible. Nonetheless, the heterogeneity of the near surface and the impact of anthropogenic disturbances on the soil causes sufficient variation in susceptibility for it to be detectable using small-loop FDEM systems (see De Smedt et al., 2014; Thiesson et al., 2017). Because the S/N is generally low, it is challenging to study the potential for susceptibility mapping. Exacerbating the problem are systematic errors and the complexity of correlation with susceptibility associated with the in-phase responses.

To summarize from the previous chapters, we can view the in-phase response as a combination of the following:

- a response (non-linearly) proportional to subsurface susceptibility. The sensitivities of the in-phase to subsurface susceptibility for a given coil configuration are complex since these can be positive or negative depending on the depth and since the exact sensitivities depend on the subsurface susceptibility distribution.
- a response proportional to the subsurface conductivity distribution (due to the coupling of out-of-phase and in-phase; see Farquharson et al., 2003). When the conductivity is low this response is negligible.
- systematic errors (see Minsley et al., 2012; Delefortrie et al., 2014b).
- random errors.

Due to the complexity of the in-phase depth sensitivities and the QP - in-phase coupling, any attempt at relating the in-phase with subsurface susceptibility requires the use of a forward model that takes into account the full solution of Maxwell's equations (and where both conductivity and susceptibility contributions are taken into account). In addition, the previous chapters showcase the difficulty in handling FDEM in-phase data: these responses can be erratic, are more prone to drifting (see chapter 4) and comparison with ground truths suggests that levelling offsets can be severe (see chapter 5). To make matters worse, the impact of systematic errors can be hard to ascertain. However, (ancillary) subsurface susceptibility data can be used to (dis)prove the importance of in-phase absolute calibration though accurate in-situ susceptibility is required. Therefore, an additional case study, aimed at focussing on the in-phase calibration as well as the potential of FDEM data for susceptibility

modelling, was performed. This chapter is analogous to the approach used in assessing levelling offsets and modelling accuracy of the quadrature phase data as described in chapter 5.

6.2 Materials and methods

Study area

The case studied pertains to data collected in the framework of an archaeological survey. The motivation for selecting this dataset was the presence of highly local in-phase anomalies in the data as well as a relatively large variation in susceptibility in the subsurface (considering the geological background). The ~1.3 ha survey area was situated near the Knowlton circles (Dorset, UK) and can be described as gently sloping farmland. From aerial pictures, the subsurface was thought to contain a henge monument as well as an irregular burial monument.

Generally, the shallow geology at the site is characterized by Cretaceous chalk of the Portsdown Chalk Formation overlain by Quaternary, siliciclastic deposits. Based on information found on the Geology of Britain viewer (British Geological Survey), the chalk Bedrock was formed approximately 71 to 84 million years ago and often consists of a calcareous ooze of the microscopic remains of plankton, especially the disc shaped calcite plates or coccoliths that make up the spherical coccolithophores. Lithological information collected at the site (cf. *infra*) confirmed a chalk substrate (at shallow depth) overlain by silty sand.

Data collection and processing

For the FDEM data collection, multi-receiver data were recorded using a DUALEM 21S sensor (DUALEM Inc., Milton, Canada). On 28/07/2016 an FDEM survey was conducted in the survey area, using the DUALEM 21S in HCP as well as VCP mode. The sampling frequency was 8 Hz and the instrument elevation (intercoil centre line) was 0.16 m. The data were collected along parallel lines, 1 m apart, at a speed of ~8 km/h. The acquisition direction was southwest-northeast and geographic coordinates were logged using a dGNSS system. After collection, all measurements were corrected for the spatial offsets between the GNSS antenna and the coil configuration midpoints using the methods discussed by Delefortrie et al. (2016) as well as a time lag. Following, the data were corrected for signal drift using a calibration line as described in Delefortrie et al. (2014b). The processed data were then interpolated to grids (0.5 x 0.5 m) using natural neighbour interpolation, which served as the basis for all subsequent data handling. Figures 6.1 and 6.2 show the resulting in-phase and LIN ECa maps.

The FDEM maps clearly show in-phase anomalies in different signals that can be related to the known presence of a henge and other prehistoric remnants. The PRP in-phase signals are heavily affected by pattern that occurs with an orientation almost perpendicular to the driving direction: this is thought to be the effect of ploughing. Whereas the PRP2 in-phase appears to suffer from remanent drift, the instability correction of the other signals was deemed successful.

The LIN ECa maps reveal the low conductivity of the environment as well as the presence of small-scale anomalies (see HCP1) which are likely due to small metal objects near or on the surface. Though the S/N ratio is small, there are congruous LIN ECa variations in the different maps.

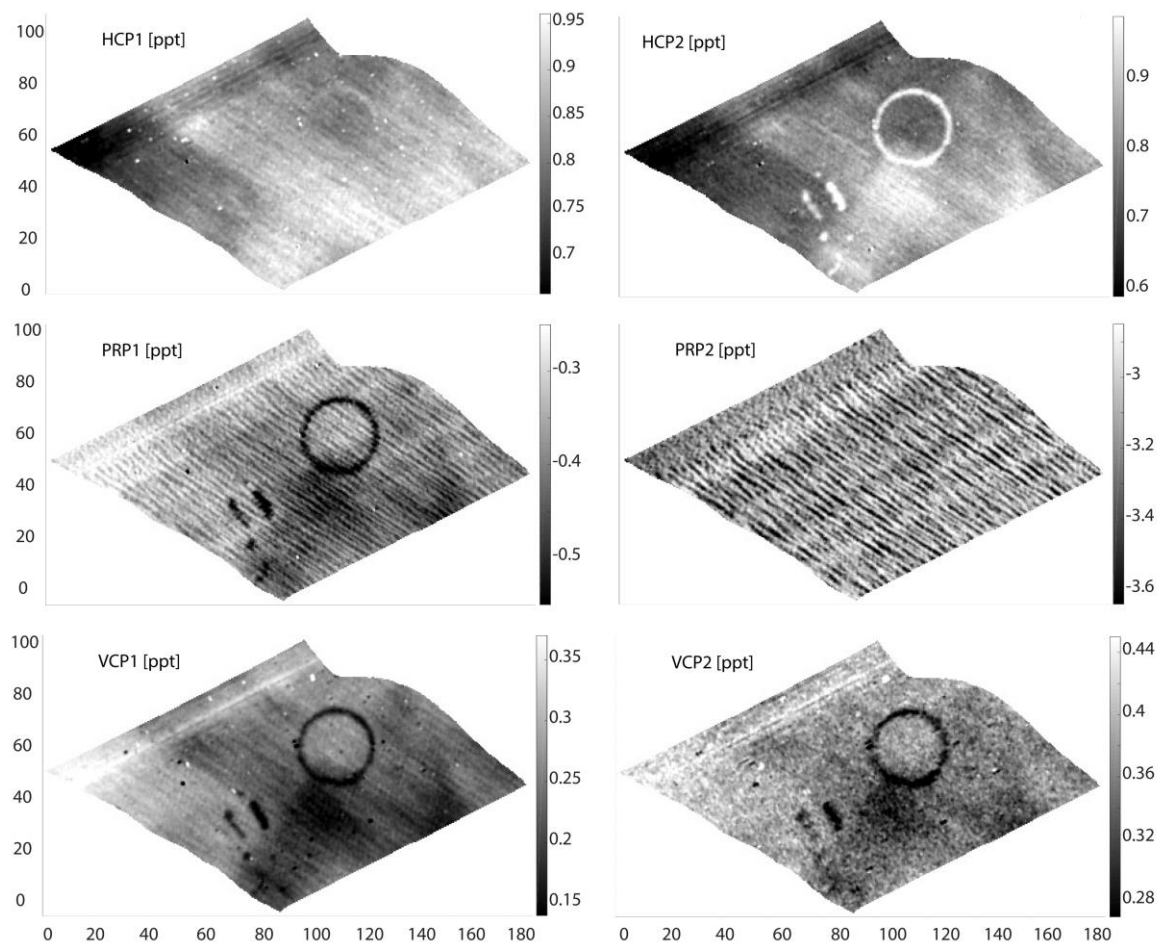


Figure 6.1. Initial FDEM survey result: Dual-em in-phase maps. Axes show local coordinates [m]. The PRP2 response is affected by corrugations due to remanent drift.

Figure 6.3 shows the validation locations and the location of an inversion transect indicated on the HCP2 in-phase map.

A treatment for random errors was performed since the signal to noise ratio was considered poor: a simple 2D median filter was applied to all grids with a square, smoothing window of 1 x 1 m. A small smoothing window was selected to arrive at more robust maps without smoothing the regions of interest too much. Most low-pass procedures will inherently smooth the data causing all local anomalies to be decreased in amplitude. An illustration hereof is provide in Figure 6.4; it shows the filtered in-phase signals overlain on the unfiltered signals along the transect indicated on figure 6.3. This is a simple albeit very important step as decreasing the peak amplitudes of the local anomalies (that are of interest) can have a significant effect during inversion when the S/N is low.

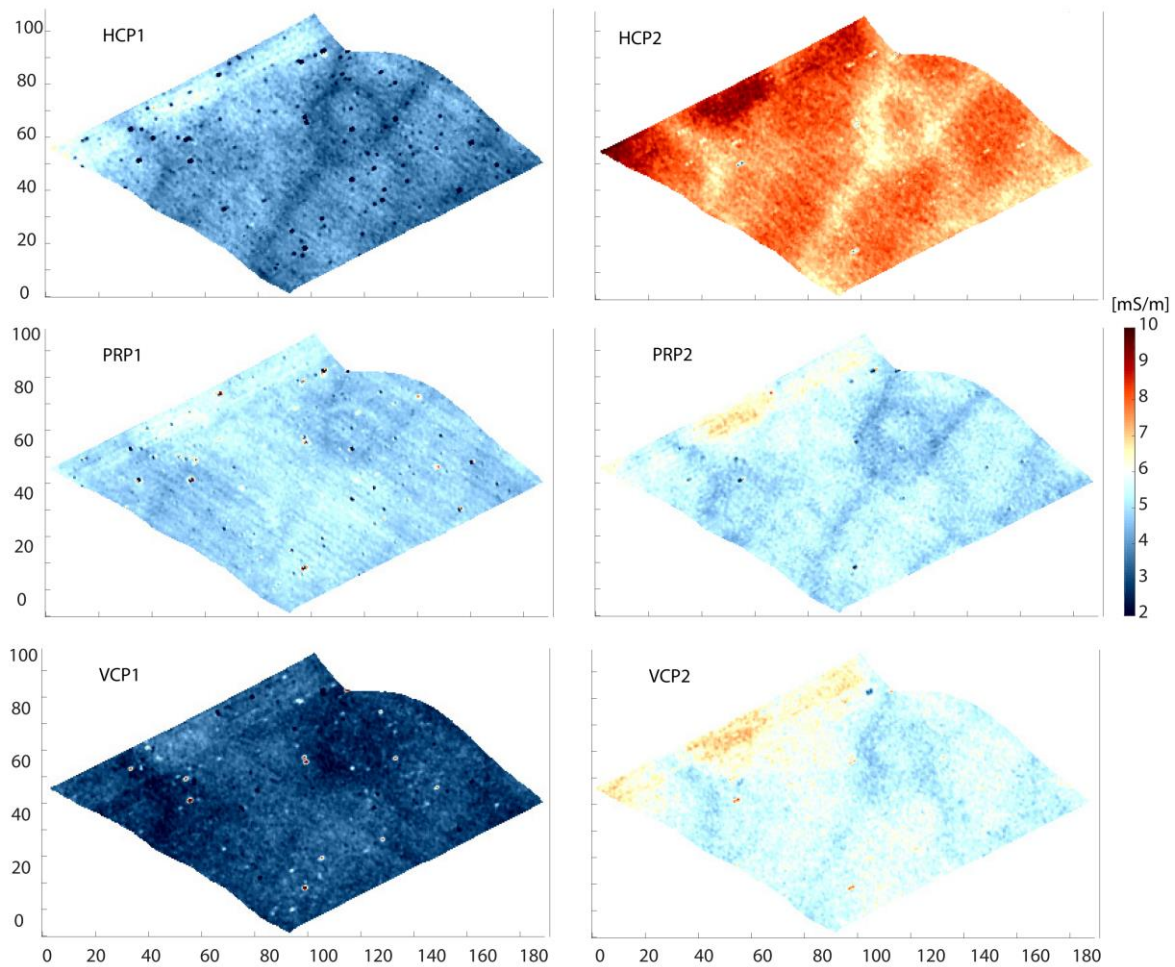


Figure 6.2. Initial FDEM survey result: Dualem LIN σ_a maps. Axes show local coordinates [m].

The noise levels for the in-phase and quadrature data were estimated to be 0.02 ppt for the 1 m separations and 0.04 ppt for the 2 m separations.

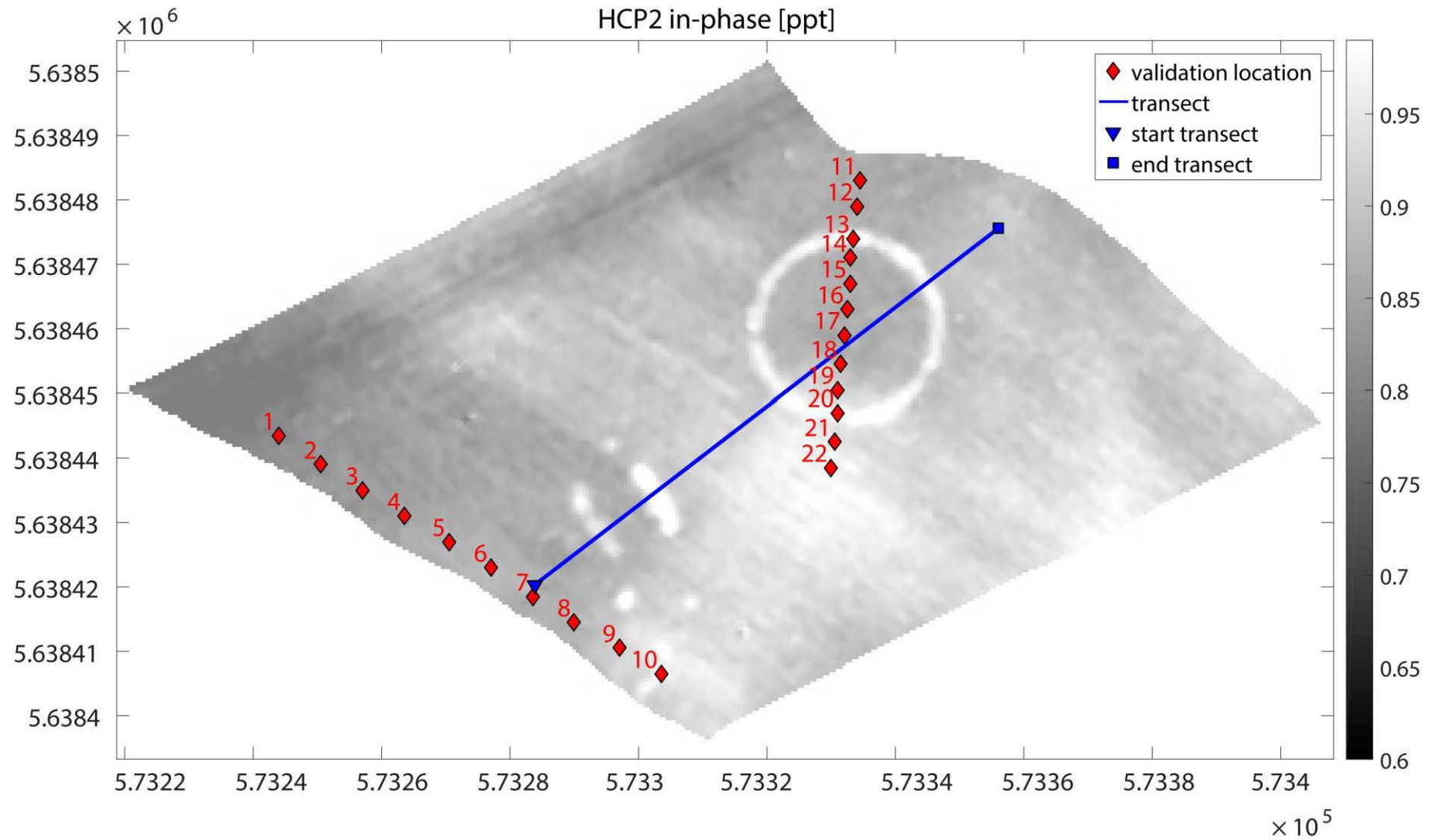


Figure 6.3. HCP2 in-phase map with indication of validation locations (red) and inversion transect (blue). Axes show geographic WGS84 coordinates.

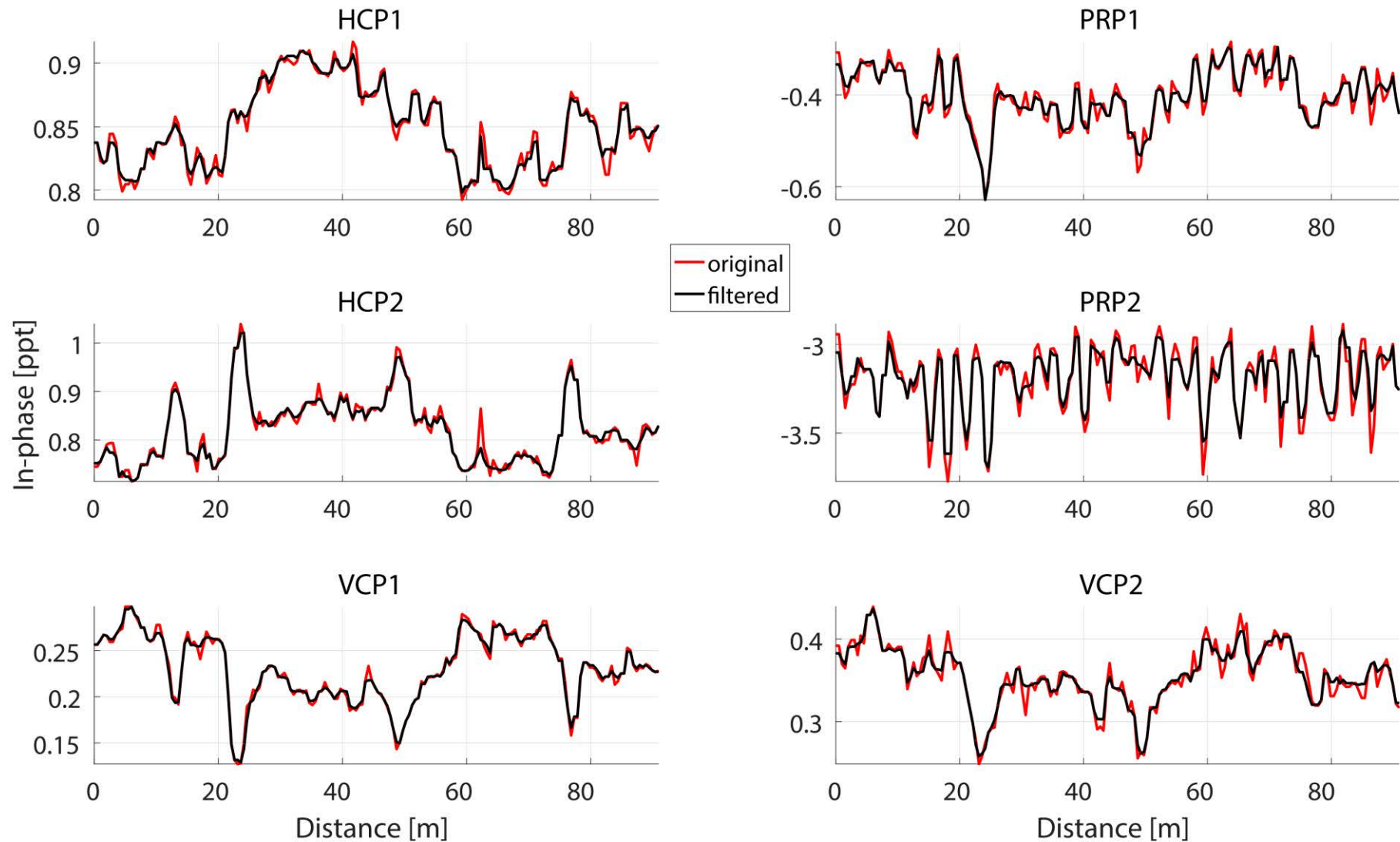


Figure 6.4. 2D median filtered, in-phase signals overlain on the unfiltered data along the transect shown on fig. 6.3.

On 28-29/07/2016 and 10-12/08/2016 the following validation data were collected at each validation location:

- a lithological description was made using a 10 cm (diameter) hand auger. The depth of the upper boundary of the chalk substrate was noted. The boundary between the Quaternary mantle (silty sand) and the Cretaceous chalk substrate was fairly sharp (as opposed to diffuse) and was visible due to the contrast between the white chalk and brownish sediments on top of it.
- during the lithological description, conductivity data were gathered using a UMP-1 (UGI GmbH, Germany). Due to practical limitations, no validation data deeper than 1 m (from the surface) were collected.
- susceptibility data were collected using a 2.5 cm gouge auger and a MS2H probe (Bartington instruments, England). The MS2H probe has a 0.5 cm horizontal signal-depth penetration around its tip and a vertical resolution of 1.25 cm. The κ measurements were taken at 5 or 10 cm intervals, down to at least 50 cm depending on the depth of the chalk substrate. The background susceptibility of the chalk was found to be 0 and therefore the susceptibility measurements were generally made until the background) susceptibility was reached.

The validation locations were chosen to attempt to get validation data for the entire range of conductivity and susceptibility of the plot which is necessary to assess the absolute calibration in a similar way as seen in chapter 5.

Figures 6.5 and 6.6 show the validation profiles (σ and κ) with indication of the observed chalk boundary depth. Clearly the chalk has a background value of 0 susceptibility whereas the Quaternary mantle has a more elevated susceptibility (in the order of $100 \text{ E-}05 \text{ []}$). The contrast is apparent yet the sudden decrease in κ at the layer boundary does not always coincide (exactly) with the observed chalk depth. This is likely due leaching and mixing caused by agricultural practices.

Also shown on figures 6.5 and 6.6 are the extrapolated profiles. These profiles were calculated as they will be used in the forward modelling of the instrument responses (theoretical QP and in-phase signals) and in doing so, a “basement” conductivity/susceptibility has to be detailed. It has therefore been assumed that the last conductivity or susceptibility of the chalk remains unchanged with increasing depth (until the max depth of exploration for a given coil configuration). Obviously, extrapolation is ill-advised in any case and especially given a heterogeneous sedimentary environments. Nonetheless, it was reasoned that the chalk substrate might be fairly homogeneous in itself and particularly with regards to the substrate susceptibility. Whether these assumptions can be used, will be discussed in the results.

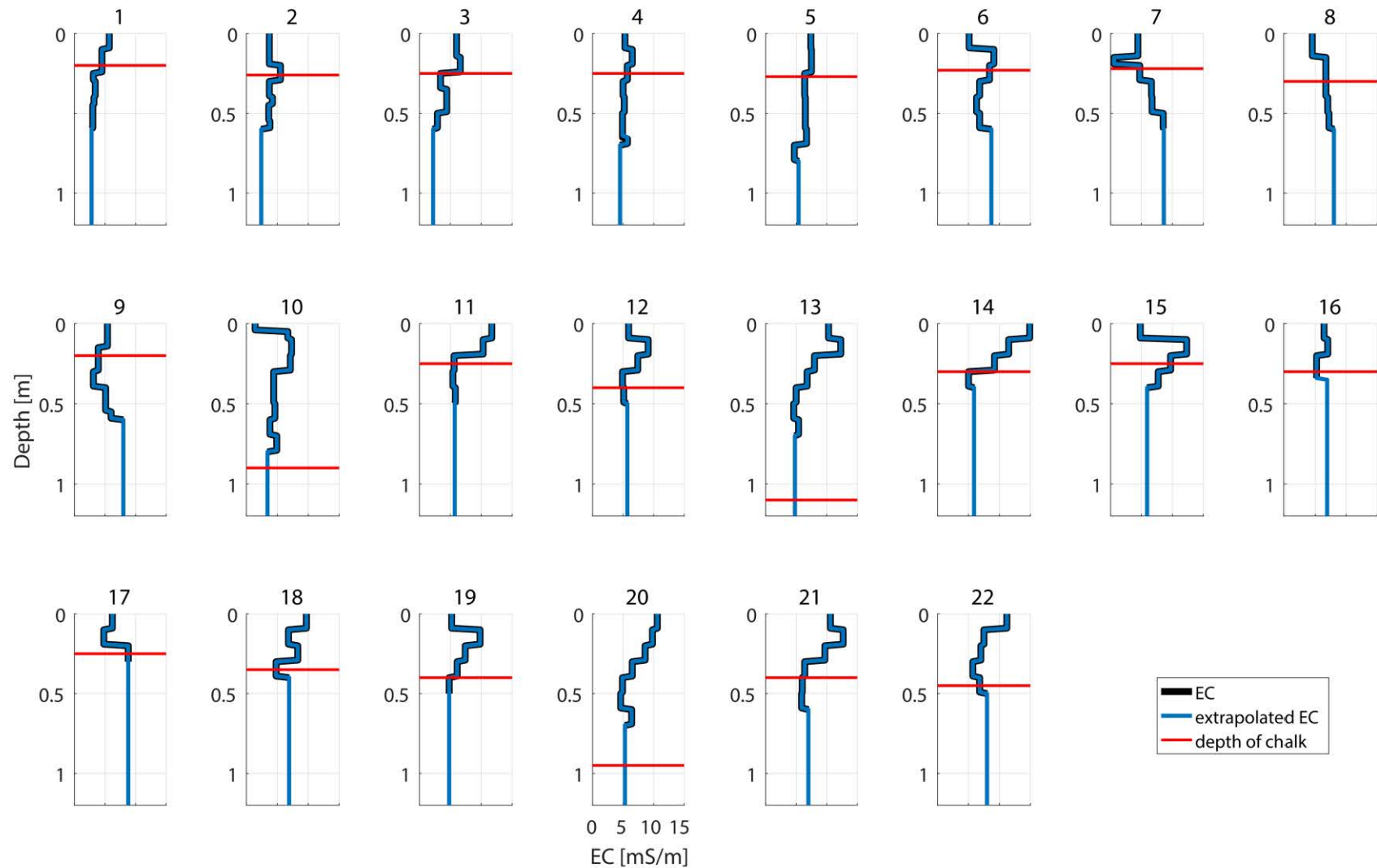


Figure 6.5. EC profiles collected at the validation locations. All axes have the same limits.

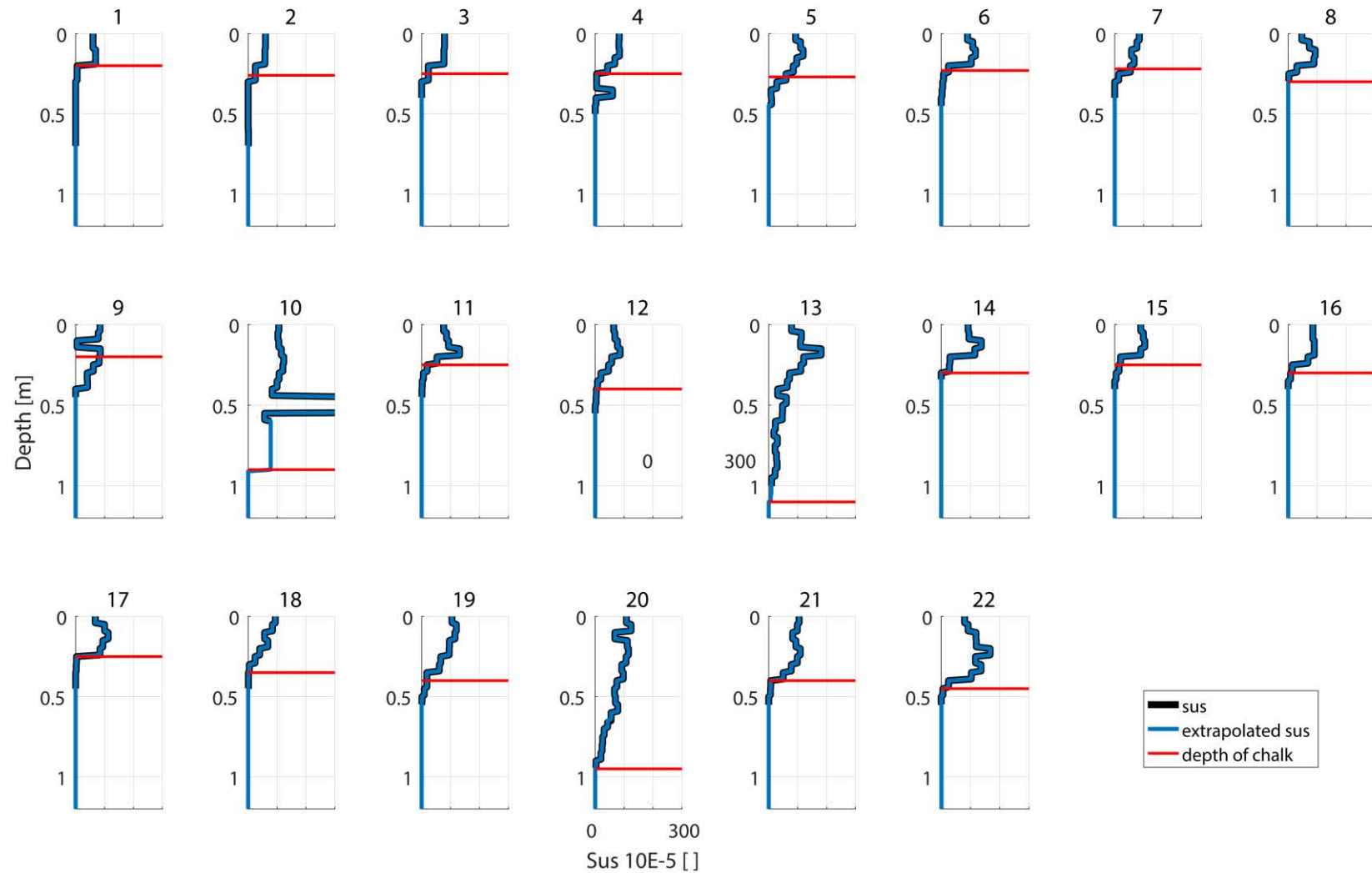


Figure 6.6. κ profiles collected at the validation locations. All axes have the same limits. Profile 10 is partially cut of: the susceptibility measured in the field at a depth of 0.5 m was 900 E-05 [].

Forward modelling and inversion

There are not many cases (available in scientific literature) where small-loop FDEM data have been used to model subsurface susceptibility. This is due to the complexities and calibration issues related to the responses. In addition, the S/N ratio of the in-phase is often low in sedimentary environments, where small-loop FDEM instruments are often applied. However, recently Thiesson et al. (2017) described the potential of linear inversions of apparent susceptibility data. This approach has not been followed owing to the contentiousness of the method: it can be reasoned that the complex relation of in-phase depth sensitivities and susceptibility distribution precludes the usefulness of apparent susceptibilities (which assumes homogeneous investigation volumes). Nonetheless, it is outside the scope of this chapter to investigate the accuracy of this method.

Analogous to the previous chapter, the forward modelling and inversion of the FDEM data were performed using EM1DFWD and EM1D (Farquharson, 2000; Farquharson et al., 2003), which were designed specifically for taking into account the coupling of QP and in-phase responses. The line-search inversion type was used and the inversion parameters were selected through trial and error by considering the inversion misfits, the robustness of the inversion parameters and by comparing the inverted results with the validation data (to assess problems of over or under fitting). A general reference model was passed along: a 25 cm uppermost layer with a κ of 100 E-05 [] and a basement half space of $0 []$. Though a reference model was passed along, most weight was given to the response misfits during the inversion procedure. The noise levels were indicated for the various coil configurations as well.

6.3 Results and discussion

To ascertain the presence of systematic errors in the FDEM data, the (extrapolated) validation profiles were used to calculate forward responses (QP* and in-phase*) for all coil configurations and these responses were compared with the measured responses. Figure 6.7 shows the scatterplots. The following can be noted:

- The QP* data show little to no correlation with the measured data. This is likely due to the extrapolated conductivity profiles being a bad representation of the real conductivity variation at greater depths. Indeed, the scattering seems greater for larger coil separations. In addition, it might be due to inaccuracy of the validation data, subsurface heterogeneity and the low S/N of the FDEM data.
- Except for the PRP2 data, a good correlation can be observed for the in-phase data. This suggest that the assumption of zero susceptibility for the chalk substrate is warranted. Despite the decent correlation, relatively large offsets with the 1:1 line are noticed.

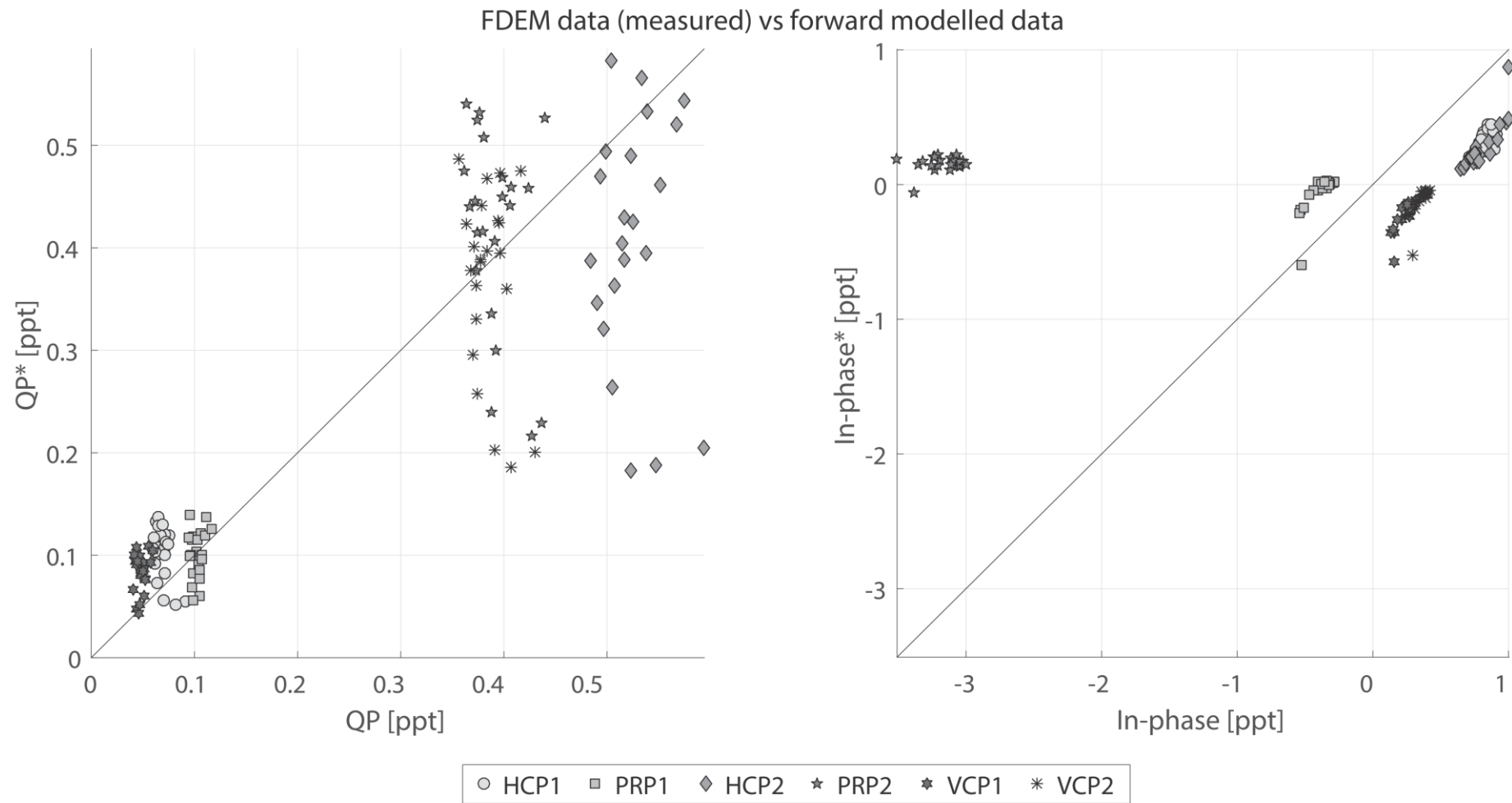


Figure 6.7. Scatterplots of forward modelled FDEM responses (QP* and in-phase*) using EM1DFWD based on the collected (and extrapolated) conductivity and susceptibility profiles and the actual, measured Dualem data (QP and in-phase).

Notably, the in-phase data are clustered, suggesting different calibration offsets for different coil configurations. A robust linear regression seemed most suitable to correct for the trends present in the in-phase comparison data because of the presence of outliers (and assuming an average error of zero in the absence of calibration errors). The fits obtained through robust, linear regression can be viewed on figure 6.8, which also shows the equations for the fitted lines as well as the coefficient of determinations. The right side of figure 6.8 displays the linearly transformed data, which of course now adheres to the 1:1 line. It can also be seen that the main effect of the transformation consists of simple shifts which are necessary due to levelling offsets in the data. Whether a strictly constant shift (i.e. “zero-order” regression) might be more justified than a linear or higher order transformation is not clear from the data. By repeating the experiment this should become apparent. Due to the lack of correlation of the PRP2 data (in-phase* vs in-phase) this signal was disregarded. The cause for the lack in correlation is unknown.

As the QP data cannot be reliably levelled and since the aim of this chapter was to assess levelling and inversion of in-phase data, the QP data was not looked into further. However, subsurface conductivity cannot be completely ignored as it influences the in-phase as well. Therefore, a background conductivity of 5 mS/m was assumed for the entire area. Due to the low conductivity, which results in a negligible contribution to the forward response calculation of the in-phase, and the limited variation in the LIN ECa data this is a conservative assumption. Nonetheless, in higher conductivity settings this should not be overlooked and wrongfully assuming a homogeneous conductivity would lead to untrustworthy results.

Due to the magnitude of the levelling offsets present in the in-phase data, with regards to the variation of these responses, it is obvious that the offsets will have an important effect on any quantitative use of these data. Regardless, the following questions remain unanswered:

- Can the (levelled or unlevelled) in-phase data be inverted successfully (i.e. can a quantitatively realistic susceptibility model be calculated) or do the complex sensitivities and the low S/N impede successful inversion?
- How severe is the effect of the levelling offsets?

To answer these questions both calibrated and uncalibrated in-phase data were inverted using the same inversion parameters. EM1DFM was used, with application of the line-search method, which was found to give sufficiently robust results (for the calibrated data). The inversion results along the transect indicated on figure 6.3 are shown on figure 6.9 whereas the misfits are plotted on figures 6.10 and 6.11. The most important parameters used were: $\alpha_s = 0.1$ and $\alpha_z = 1$ (see previous chapter). The models (fig. 6.9) are unsmoothed and were interpolated to a 2D grid using nearest neighbour interpolation. Only the in-phase responses were inverted.

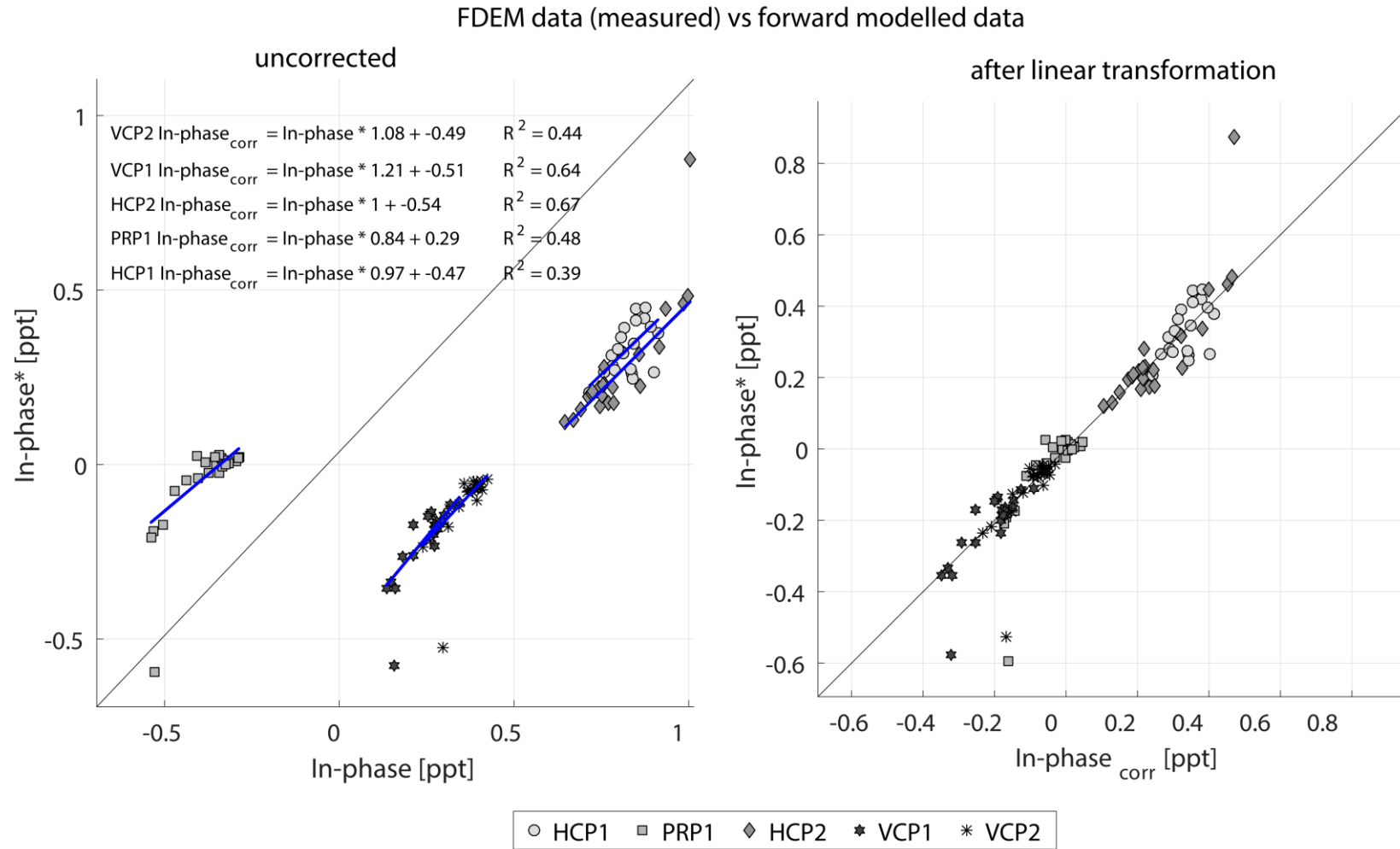


Figure 6.8. (left) Scatterplot of forward modelled FDEM responses (in-phase*) using EM1DFWD based on the collected (and extrapolated) conductivity and susceptibility profiles and the actual, measured Dualem data (in-phase) without the PRP2 data. The linear transformations, calculated using robust, linear regression, are indicated in the comparison plots. (right) same data after linear transformation.

It is not in the scope of this chapter to elaborate on the implementation of the EM1DFM forward model, the objective function of the inversion and the exact definition of the inversion parameters. For this information we refer to Farquharson et al (2003), Oldenburg and Li (2005) and the manual of the program: <https://www.eoas.ubc.ca/ubcgif/iag/sftwrdocs/em1dfm/em1d-man.html>.

When comparing the inversion results, the results are obvious and it is unsurprising that the inversion of the uncalibrated data has failed. Regarding the uncalibrated data: no convergence was reached for any sounding during the inversion due to the discrepancies between the forward modelled and uncalibrated responses. Instead, after reaching a local minimum the iterative evaluation of the objective function was halted. This resulted in an unrealistic model (see fig. 6.9). In addition, the inversion results were not robust (small changes in inversion parameters caused large differences in the final models). Generally, inversions always resulted in a perfectly horizontally layered earth which can again be ascribed to the incorrect levelling of the data. The inversion results for the calibrated in-phase responses, on the other hand, were more robust and suggest that fairly realistic models can be attained. The susceptibility change around the upper boundary of the chalk is not abrupt in the inverted model though the susceptibility values are similar to the ones collected in-situ. This is not unexpected (the validation data were used in the overall calibration of the in-phase data) yet it does illustrate the impact of data levelling. It is noted that this sizeable impact was due to the magnitude of the levelling offsets nearing the magnitude of the responses.

Similar to the results shown in chapter 5, the reconstructed susceptibilities are closer to averaged (actual) susceptibilities than perfect reconstructions with sharp boundaries. This is exemplified in figure 6.12 which shows the validation profiles and 1D inversion results. This was influenced by the inversion parameters where the flattest component was many times larger than the smallest component, which was chosen due to the desire in achieving a robust solution despite working with data characterized by a low S/N case. So while a fairly accurate (though inherently smoothed) and, more importantly, robust image was obtained, it precluded the reconstruction of sharp boundaries. Nonetheless, this is seen as a good result, considering the diffusive nature of the method and the low S/N of the data.

The depth of investigation of the susceptibility image was not calculated. A method similar to the one described in chapter 5 could be attempted but reference DOI's are not available for the in-phase responses and the complex sensitivities may preclude robust normalization of the sensitivities. A more suitable method for attempting to study the DOI for the in-phase responses might be the method proposed by Oldenburg and Li (1999).

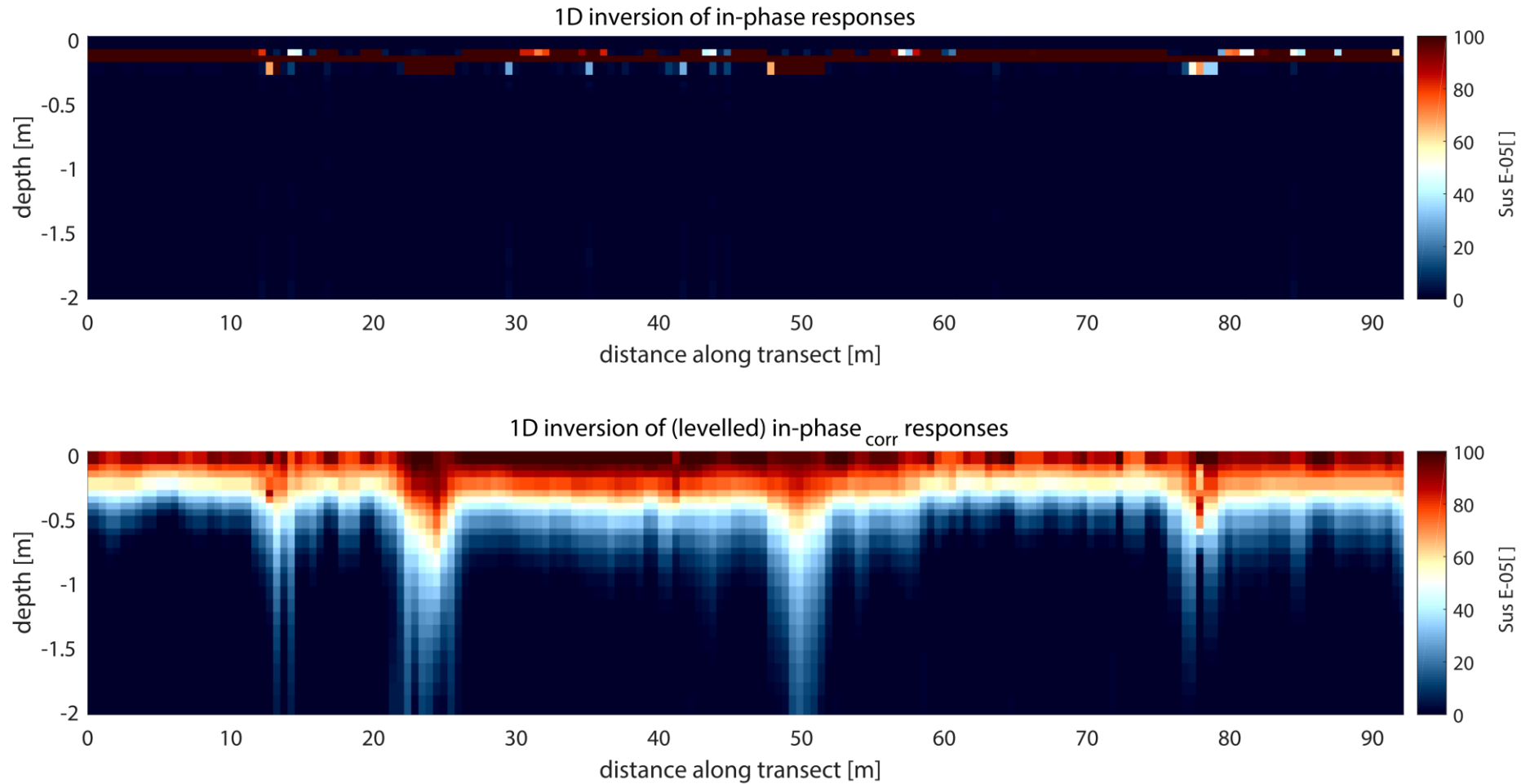


Figure 6.9. 1D (nearest neighbour interpolated) inversion results of the in-phase responses along the transect indicated on fig. 6.3, that cuts through the most prominent in-phase anomalies: (top) susceptibility model calculated using the in-phase responses that were not levelled using the comparison data (bottom) susceptibility model calculated using the in-phase_{corr} responses that were linearly transformed using the comparison data. The responses were inverted using the EM1DFM program and the line-search method was applied (with $\text{chifac} = 1$ / decrease in misfit = 0.8 / $\alpha_s = 0.1$ and $\alpha_z = 1$). Only the in-phase responses were inverted, assuming a background conductivity of 5 mS/m. These profiles are not smoothed.

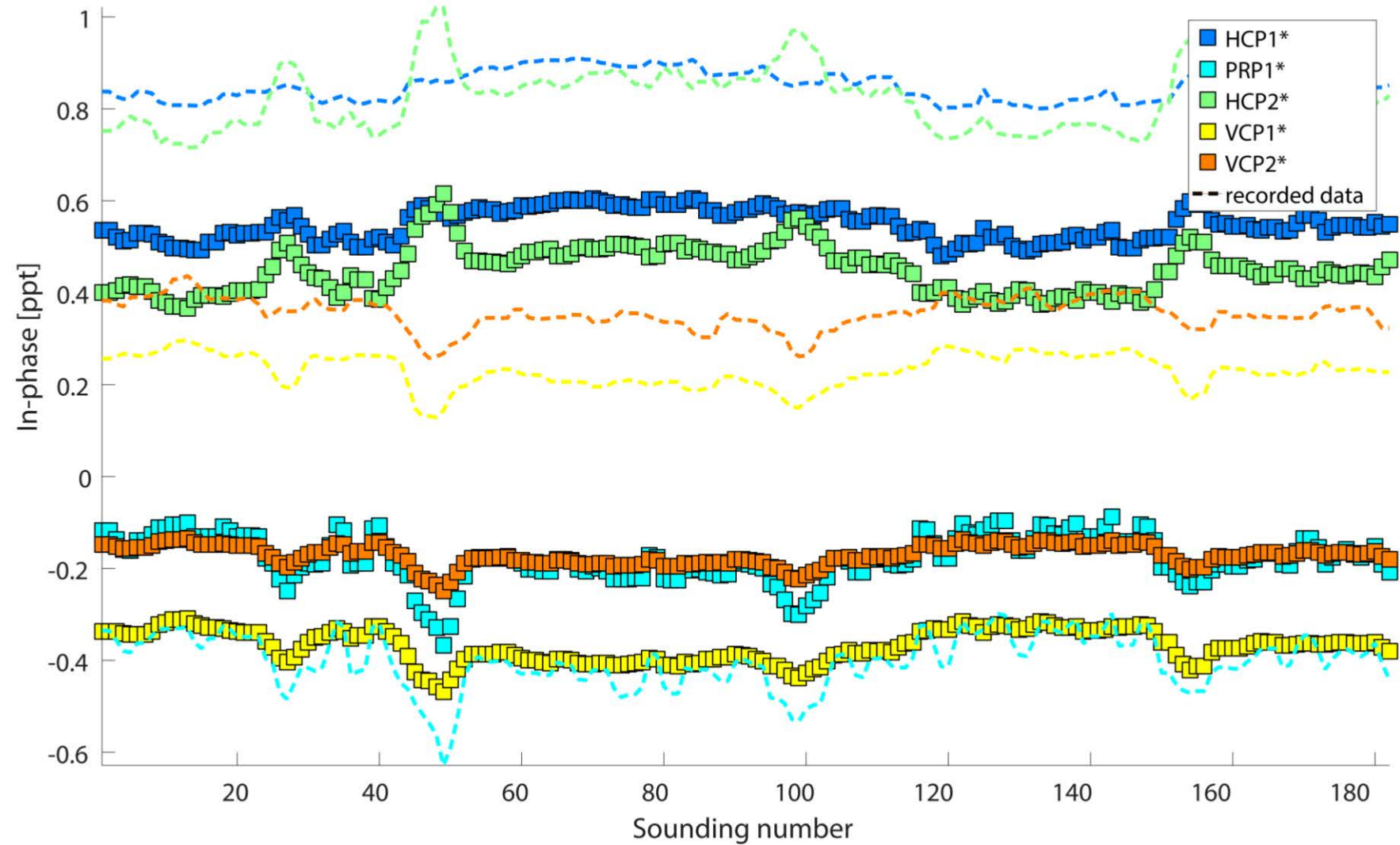


Figure 6.10. Fit of the data with the forward calculated responses of the inversion results shown in Fig. 6.9 (top). The forward calculated responses of the inverted susceptibility profiles are plotted by use of squares and the measured FDEM responses (input of inversion) are plotted using dashed lines.

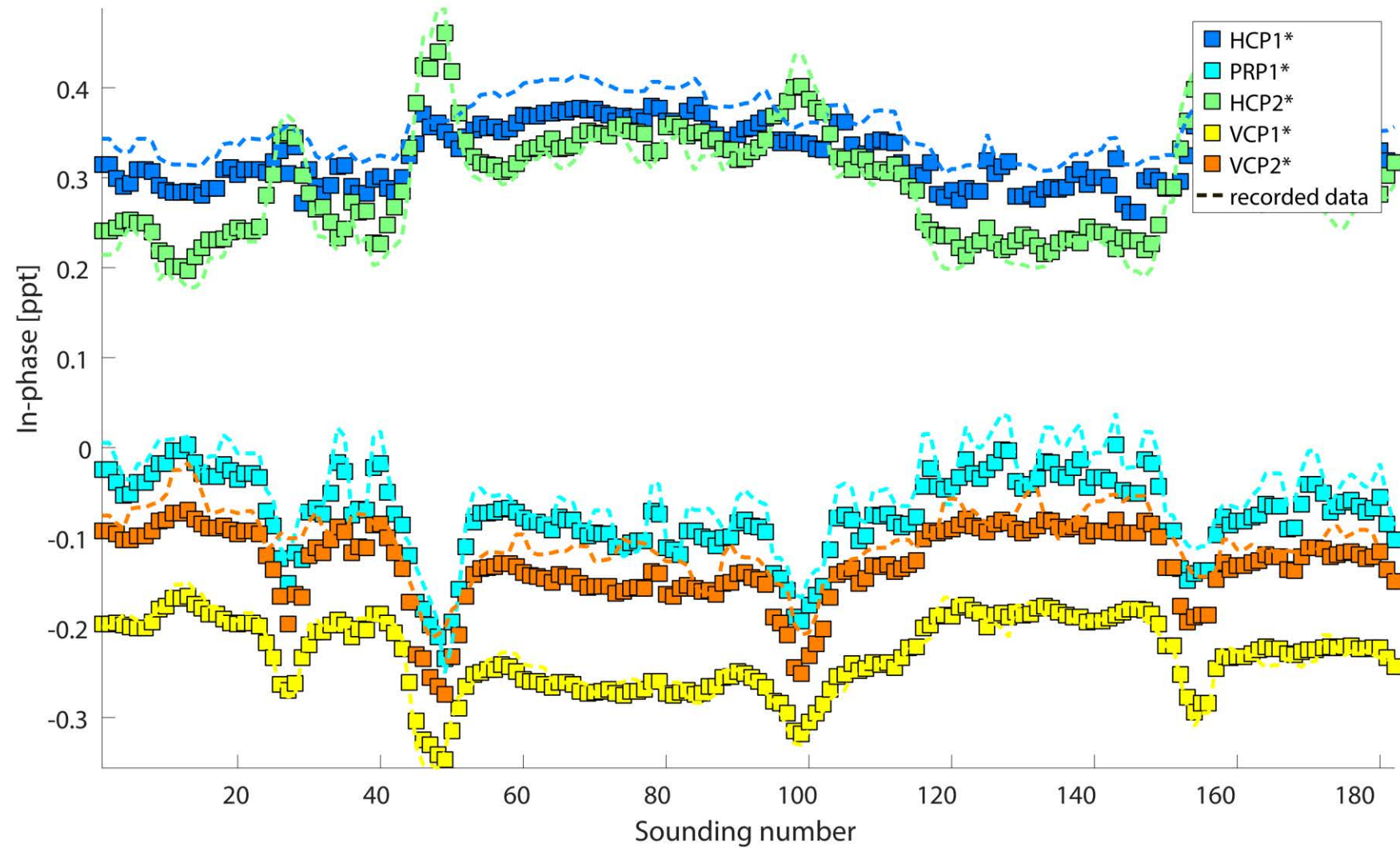


Figure 6.11. Fit of the data with the forward calculated responses of the inversion results shown in Fig. 6.9 (bottom). The forward calculated responses of the inverted susceptibility profiles are plotted by use of squares and the measured FDEM responses (input of inversion) are plotted using dashed lines.

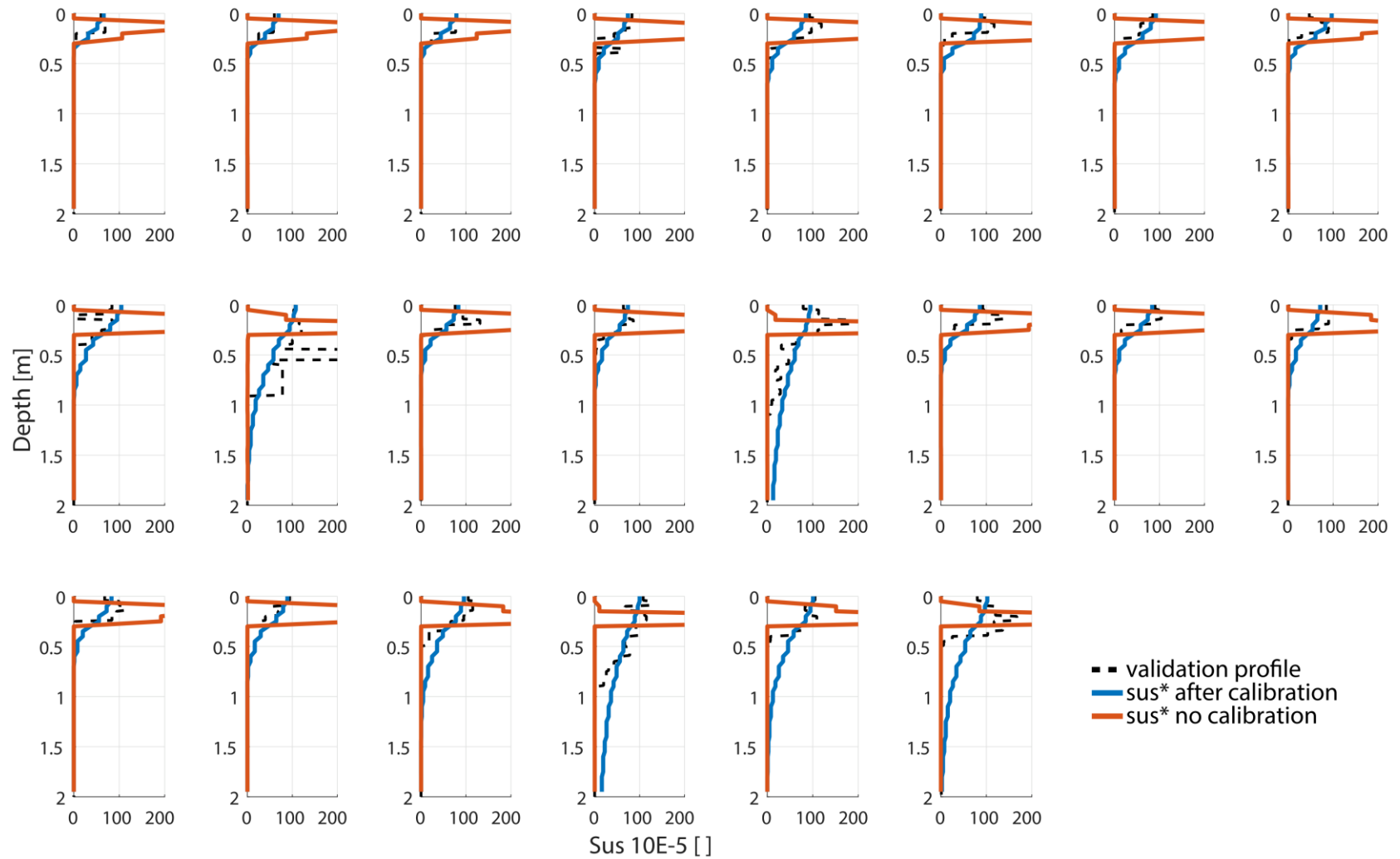


Figure 6.12. 1D inversion profiles overlain on the validation profiles. Sus* is the estimated susceptibility (obtained by inversion of the FDEM in-phase data).

6.4 Conclusions

The results have shown that:

- Levelling offsets present in in-phase data can near or exceed the magnitude of the responses.
- To invert in-phase data in an environment characterized by low susceptibility, absolute calibration is crucial. The same can be said for any other quantitative use of the data.
- Despite in-phase responses being impacted by low S/N, systematic errors and despite the complexity of correlation with susceptibility, it was possible to approximately reconstruct susceptibility profiles.
- By attempting to attain more robust inversion results, more averaged profiles were arrived at, suggesting a smoothing penalty. This is mainly a result of the ill-posedness of the problem as well as the assumption of lateral homogeneity (1D approach) at the level of the measuring volumes.

It follows that at current, the potential of small-loop FDEM for susceptibility mapping is largely untapped. Therefore more attention needs to go toward permanently solving the problem of absolute calibration or, if this is unfeasible, design a less laborious approach.

Chapter 7

Final conclusions and perspectives

“We shall not cease from exploration
And the end of all our exploring
Will be to arrive where we started
And know the place for the first time.”

-- T. S. Eliot,
“Little Gidding”

The general aim of this research was to optimize the reliability of small-loop FDEM survey data. The focus was on (high resolution) area surveys and the following issues were scrutinized: spatial and temporal offsets due to instrumentation and survey modality; FDEM signal instability and relating FDEM responses with subsurface conductivity and susceptibility to assess absolute calibration.

The results have shown that it is both necessary and worthwhile to investigate instrument offsets and calibration issues. Necessary because there are calibration issues that need resolving. Worthwhile because it has been shown that it is possible to increase the reliability of the data. To give an overview we return to the initial objectives:

Objective 1: Positional accuracy

It was possible to evaluate the impact of spatial and temporal offsets on the positional accuracy of (FDEM) survey data, when utilising a GNSS receiver. To mitigate to the errors, corrections were proposed, applied and evaluated. For small spatial offsets, the error can be mitigated to within the receiver's positional accuracy while for larger offsets and the case of towed sled, a loss of accuracy does occur. It was also found that the presence of temporal offsets should not be overlooked, especially with the tendency toward faster surveys.

Objective 2: Signal stability

& objective 3: Absolute calibration

The signal instability of FDEM responses was characterized for one type of systems and a general purpose, efficient correction was proposed (i.e. the collection of tie line data for calibration). Following, the correction was evaluated thoroughly. The adopted procedure was found to be an excellent first step in calibration of high resolution land-based FDEM surveys. However, after acquiring a stable signal, controversy surrounding the exact levelling of the signals persists. This is not an issue when viewing the data in a qualitative manner but is a necessary consideration for quantitative use. Accurate, absolute calibration is of the utmost importance when comparing data collected using several geophysical methods and when comparing data collected using the same technique at different times. However, to study levelling offsets in FDEM survey data, accurate ancillary data are required as well as an accurate forward modelling procedure, which renders comparative studies laborious. Two cases were investigated and though it is hard to generalize, the data suggest that:

- the in-phase responses are severely impacted by systematic errors: large signal drift was encountered (cf. chapter 4) and levelling offsets were detected (cf. chapter 6) after drift

correction. The magnitude of the detected levelling offsets did not seem to exceed the magnitude of the signal instabilities: meaning that both errors are likely two sides of the same coin i.e. they are both a result of the signal instability associated with a given coil configuration.

- the quadrature-phase responses seem to have been calibrated more consistently. The drift associated with the QP responses was less erratic.
- whereas signal stability assessments/corrections are always necessary, the usefulness of levelling offsets detection and correction decreases with increasing S/N of the responses.

Objective 4: Depth of investigation

A straightforward method for estimating the depth of investigation was introduced. It was only applied to one case study and not tested as a general purpose method. In addition, it was not tested for in-phase responses. However, it might be a simple alternative compared to more elaborate methods for small-loop FDEM systems. The employment of a reference depth may be useful and it has been shown that the impact of conductivity on DOI is of great importance.

Objective 5: Obtaining quantitative conductivity and susceptibility models

It was possible to obtain and validate both conductivity and susceptibility models using small-loop FDEM data. Generally put, the resulting models were a success, though the smoothing (associated with the diffuse nature of the measurements and a smoothing penalty caused by selection of robust inversion parameters) precludes the reconstruction of sharp boundaries. Nonetheless, the acquired, inverted results can allow quantitative (albeit averaged) representations of the subsurface. It is noted that a successful inversion in a low S/N environment was not possible without calibrating for systematic errors.

Perspective

Given the results and proposed corrections, it is possible to present a general processing scheme for small-loop FDEM data (Fig. 7.1). What is lacking in the processing chain is a procedure that mitigates the effect of random errors (e.g. low pass filtering of the data). It is also noted that the absolute calibration, as performed in chapters 5 and 6, is unlikely to have great practical value due to the laborious nature of the procedure. More research is therefore required to draw more general conclusions and hopefully attain a general purpose and practical correction.

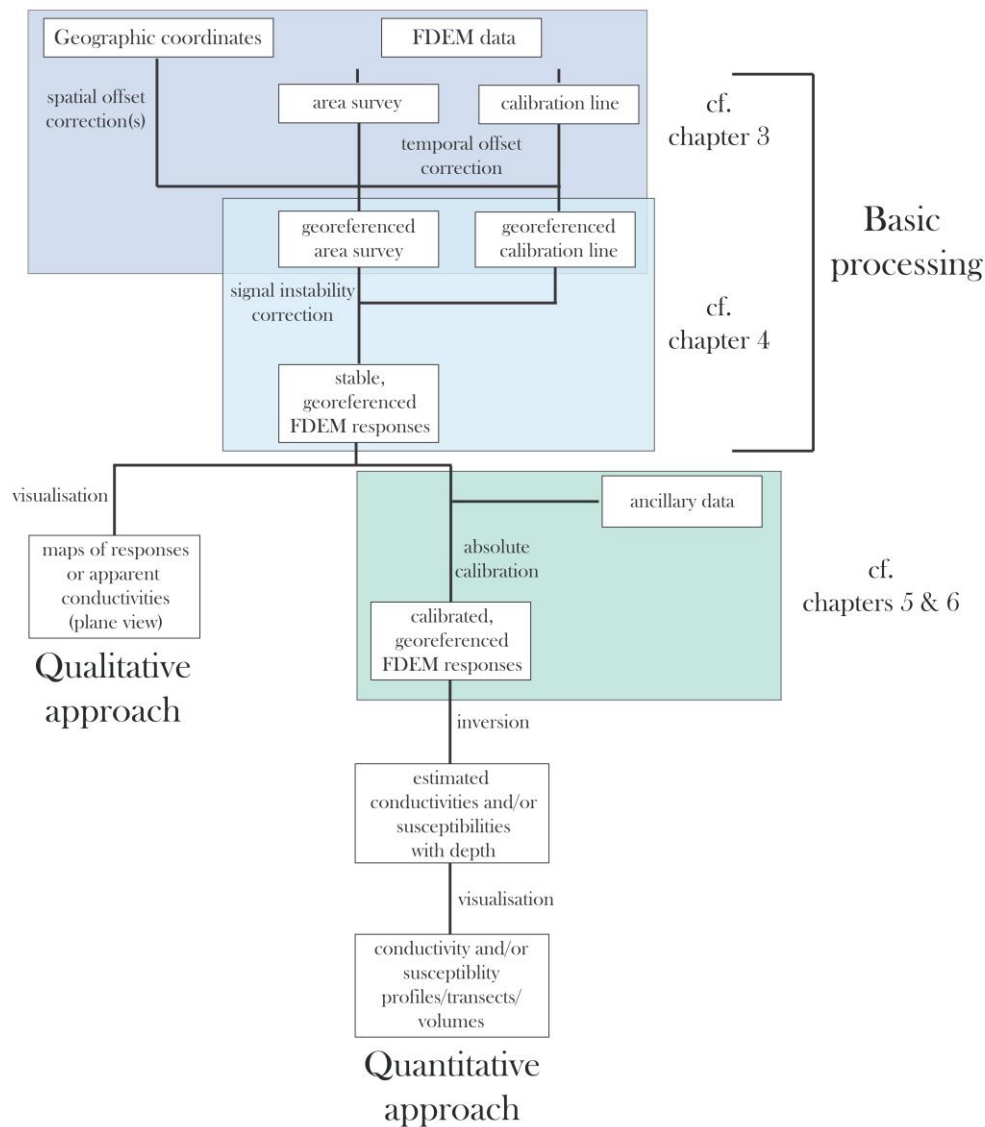


Figure 7.1. Proposed processing scheme of small-loop FDEM data

The relevance of FDEM data optimization for near-surface and soil study applications is obvious: calibrating for systematic and random errors will allow more quantitative use of FDEM data which can benefit subsurface visualization and 3D modelling. The importance for monitoring purposes, i.e. 4D evaluations, is equally great.

Finally, the only way to permanently increase the reliability of the instruments, is for manufacturers and researchers to pool their information. If an increase in reliability is desired, it is in the interest of manufacturers of FDEM instruments to support research which ascertains the calibration and accuracy potential of FDEM instruments by giving exact information on “factory calibration”. Furthermore, it is in the interest of researchers to share code/data/detailed procedures. In addition, the way forward in promoting the use of small-loop FDEM instruments requires user-friendly software and hardware.

References

- Abdu, H., Robinson, D.A., Jones, S.B., 2007. Comparing bulk soil electrical conductivity determination using the Dualem-1S and EM38-DD electromagnetic induction instruments. *Soil Science Society of America Journal* **71**, 189–196. <http://dx.doi.org/10.2136/sssaj2005.0394>
- Abraham, J.D., Deszcz-Pan, M., Fitterman, D.V., Burton, B.L., 2006. Use of a handheld broadband EM induction system for deriving resistivity depth images. Symposium on the Application of Geophysics to Engineering and Environmental Problems., pp. 1782–1799.
- Adamchuk, V.I., Hummel, J.W., Morgan, M.T., Upadhyaya, S.K., 2004. On-the-go soil sensors for precision agriculture. *Computers and Electronics in Agriculture* **44**, 71-91. <http://dx.doi.org/10.1016/j.compag.2004.03.002>
- Allred, B.J., Reza Ehsani, M., Saraswat, D., 2006. Comparison of electromagnetic induction, capacitively-coupled resistivity, and galvanic contact resistivity methods for soil electrical conductivity measurement. *American Society of Agricultural and Biological Engineers* **22**(2): 215-230.
- Altdorff, D., Bechtold, M., van der Kruk, J., Vereecken, H., Huisman, J.A., 2016. Mapping peat layer properties with multi-coil offset electromagnetic induction and laser scanning elevation data. *Geoderma* **261**: 178-189. <http://dx.doi.org/10.1016/j.geoderma.2015.07.015>
- Aspinall, A., Gaffney, C.F., Schmidt, A., 2008. *Magnetometry for Archaeologists* (eds. Conyer, L.B. and Kvamme, K.L.). 1-208. Lanham, Maryland, USA: Altamira Press
- Banyś, P., Engler, E., Heymann, F., Noack, T., 2013. Timestamp Discrepancies in Multisensor NMEA Environment during Survey Voyage. *Scientific Journals Maritime University of Szczecin* **36**, 22-26
- Beamish, D., 2011. Low induction number ground conductivity meters: Corrections procedure in the absence of magnetic effects. *Journal of Applied Geophysics* **75**, 244-251. <http://dx.doi.org/10.1016/j.jappgeo.2011.07.005>
- Beck, A.E., 1981. Physical Principles of Exploration Methods: An Introductory Text for Geology and Geophysics Students. John Wiley, New York.
- Benech, C., Tabbagh, A., and Desvignes, G., 2002. Joint interpretation of EM and magnetic data for near-surface studies. *Geophysics* **67**, no. 6, 1729-1739. <http://dx.doi.org/10.1190/1.1527074>
- Bongiovanni, M.V., Bonomo, N., de la Vega, M., Martino, L., Osella, A., 2008. Rapid evaluation of multifrequency EMI data to characterize buried structures at a historical Jesuit Mission in Argentina. *Journal of Applied Geophysics* **64**: 37-46. <http://dx.doi.org/10.1016/j.jappgeo.2007.11.006>

- Böniger, U., Tronicke, J., 2010. On the potential of kinematic GPR surveying using a selftracking total station: evaluating system crosstalk and latency. *IEEE Transactions on Geoscience and Remote Sensing* **48**, 3792–3798
- Butler, D.K. (Ed.), 2005. *Near-surface geophysics. Investigations in geophysics*. Society of Exploration Geophysicists.
- Callegary, J. B., Ferré, T. P. A., and Groom, R. W., 2007. Vertical spatial sensitivity and exploration depth of Low-Induction-Number electromagnetic induction instruments. *Vadose Zone Journal* **6**, 158-167. <http://dx.doi.org/10.2136/vzj2006.0120>
- Callegary, J. B., Ferré, T. P. A., and Groom, R. W., 2012. Three-dimensional sensitivity distribution and sample volume of low-induction-number electromagnetic-induction instruments. *Soil Science Society of America Journal* **76**, 85-91.
- Christiansen, A. V., and Auken, E., 2012, A global measure for depth of investigation: *Geophysics* **77**(4): WB171-WB177. <http://dx.doi.org/10.1190/geo2011-0393.1>
- Corwin, D.L., Lesch, S.M., 2005. Characterizing soil spatial variability with apparent soil electrical conductivity: I. Survey protocols. *Computers and Electronics in Agriculture* **46**, 103–133
- Davies, G., Huang, J., Monteiro Santos, F.A., Triantafilis, J., 2014. Modeling Coastal Salinity in Quasi 2D and 3D Using a Dualem-421 and Inversion Software. *Ground Water* **53**: 424-431. <http://dx.doi.org/10.1111/gwat.12231>
- De Smedt, P., Van Meirvenne, M., Meerschman, E., Saey, T., Bats, M., Court-Picon, M., De Reu, J., Zwertvaegher, A., Antrop, M., Bourgeois, J., De Maeyer, P., Finke, P.A., Verniers, J., Crombé, P., 2011. Reconstructing palaeochannel morphology with a mobile multicoil electromagnetic induction sensor. *Geomorphology* **130**: 136–141. <http://dx.doi.org/10.1016/j.geomorph.2011.03.009>
- De Smedt, P., Saey, T., Lehouck, A., Stichelbaut, B., Meerschman, E., Islam, M.M., et al., 2013. Exploring the potential of multi-receiver EMI survey for geoarchaeological prospection: A 90 ha dataset, *Geoderma* **199**, 30-36. <http://dx.doi.org/10.1016/j.geoderma.2012.07.019>
- De Smedt, P., Saey, T., Meerschman, E., De Reu, J., De Clercq, W., Van Meirvenne, M., 2014. Comparing apparent magnetic susceptibility measurements of a multi-receiver EMI sensor with topsoil and profile magnetic susceptibility data over weak magnetic anomalies. *Archaeological Prospection* **21**:103–12.

- De Smedt, P., Delefortrie, S., Wyffels, F., 2016. Identifying and Removing Micro-drift in Ground-based Electromagnetic Induction Data. *Journal of Applied Geophysics* **131**, 14–22. <http://dx.doi.org/10.1016/j.jappgeo.2016.05.004>
- Dearing, J.A., Hay, K.L., Baban, S.M.J., Huddleston, A.S., Wellington, E.M.H., Loveland, P.J., 1996. Magnetic susceptibility of soil: an evaluation of conflicting theories using a national data set. *Geophysical Journal International* **127**: 728-734.
- Delefortrie, S., De Smedt, P., Saey, T., Van De Vijver, E., Van Meirvenne, M., 2014b. An efficient calibration procedure for correction of drift in EMI survey data. *Journal of Applied Geophysics* **110**, 115-125. <http://dx.doi.org/10.1016/j.jappgeo.2014.09.004>
- Delefortrie, S., Saey, T., Van De Vijver, E., De Smedt, P., Missiaen, T., Demerre, I., Van Meirvenne, M., 2014a. Frequency domain electromagnetic induction survey in the intertidal zone: limitations of low-induction-number and depth of exploration. *Journal of Applied Geophysics* **100**: 14–22. <http://dx.doi.org/10.1016/j.jappgeo.2013.10.005>.
- Delefortrie, S., Saey, T., Van Meirvenne, M., 2015. Increasing positional accuracy of surveys: correcting for spatial offset and time lag. *Near Surface Geoscience*, Papers.
- Delefortrie, S., Saey, T., De Pue, J., Van De Vijver, E., De Smedt, P., Van Meirvenne, M., 2016. Evaluating corrections for a horizontal offset between sensor and position data for surveys on land. *Precision Agriculture* **17**, 349-364. <http://dx.doi.org/10.1007/s11119-015-9423-8>
- Deszcz-Pan, M., Fitterman, D.V., Labson, V.F., 1998. Reduction of inversion errors in helicopter EM data using auxiliary information. *Exploration Geophysics* **29**, 142-146.
- Doolittle, J.A., Brevik, E.C., 2014. The use of electromagnetic induction techniques in soils studies, *Geoderma*, 223–225, 33-45. <http://dx.doi.org/10.1016/j.geoderma.2014.01.027>
- Eilers, P.H.C., Marx, B.D., 1996. Flexible Smoothing with B-splines and Penalties. *Statistical science* **11**, 89-121.
- Everett, M.E., 2012. Theoretical developments in electromagnetic induction geophysics with selected applications in the near surface. *Surveys in Geophysics* **33**: 29–63. <http://dx.doi.org/10.1007/s10712-011-9138-y>
- Everett, M.E., 2013. Near-surface Applied Geophysics. Cambridge University Press, New York.
- Farquharson, C. G., 2000, EM1DFM. University of British Columbia Geophysical Inversion Facility.

- Farquharson, C. G., Oldenburg, D. W., and Routh, P. S., 2003. Simultaneous 1D inversion of loop-loop electromagnetic data for magnetic susceptibility and electrical conductivity. *Geophysics* **68**, 1857-1869.
- Fitterman, D.V., Labson, V.F., 2005. Electromagnetic induction methods for environmental problems. In: Butler, D.K. (Ed.), *Near-surface Geophysics, Investigations in Geophysics* no. 13 (pp. 295-349). Society of Exploration Geophysicists, Tulsa, Oklahoma, USA
- Freeland, R.S., Yoder, R.E., Ammons, J.T., Leonard, L.L., 2002. Mobilized surveying of soil conductivity using electromagnetic induction. *Applied Engineering in Agriculture* **18**, 121–126
- Frischknecht, F. C., Labson, V. F., Spies, B. R., and Anderson, W. L., 1991. Profiling methods using small sources in M. Nabighian, ed., *Electromagnetic methods in applied geophysics*. Society of Exploration Geophysicists, 105-283.
- Garlick, G.S., Kanga, D.N., Miller, G.G., 1993. Vehicle offtracking: a globally stable solution. *Institute of transportation journal* **63**, 17–21
- Gebbers, R., Lück, E., Dabas, M., Domsch, H., 2009. Comparison of instruments for geoelectrical soil mapping at the field scale. *Near Surface Geophysics* **7**, 179-190. <http://dx.doi.org/10.3997/1873-0604.2009011>
- Gottfried, T., Auerswald, K., Ostler, U., 2012. Kinematic correction for a spatial offset between sensor and position data in on-the-go sensor applications. *Computers and Electronics in Agriculture* **84**, 76-84. <http://dx.doi.org/10.1016/j.compag.2012.02.021>
- Grejner-Brzezinska, 2008. Integration of the Global Positioning System (GPS) into agricultural geophysics. In: Allred, B.J, Daniels, J.J, Ehsani, M.R. (Eds.), *Handbook of agricultural geophysics* (pp. 165-198). Boca Raton, Florida, USA: CRC Press.
- Grellier, S., Florsch, N., Camerlynck, C., Janeau, J., Podwojewski, P., Lorentz, S., 2013. The use of Slingram EM38 data for topsoil and subsoil geoelectrical characterization with a Bayesian inversion. *Geoderma* **200-201**: 140–155.
- Gueguen, Y., Palciauskas, V., 1994. VII. Electrical conductivity. In: *Introduction to the Physics of Rocks*. Princeton University Press, Princeton, New Jersey.
- Guillemoteau, J., Sailhac, P., Boulanger, C., Trules, J., 2015, Inversion of ground constant offset loop-loop electromagnetic data for a large range of induction numbers. *Geophysics* **80**: E11–E21.

- Guillemoteau, J., Sailhac, P., Boulanger, C., and Trules, J., 2015. Inversion of ground constant offset loop-loop electromagnetic data for a large range of induction numbers. *Geophysics* **80**(1): E11-E21. <http://dx.doi.org/10.1190/geo2014-0005.1>
- Hilhorst, M. A., 1998. Dielectrical characterisation of soil. *Doctoral thesis*. Wageningen agricultural university
- Huang, H., 2005. Depth of investigation for small broadband electromagnetic sensors. *Geophysics* **70**(6): 135-142.
- Huang, H., SanFilipo, B., Oren, A., Won, I.J., 2006. Coaxial coil towed EMI sensor array for UXO detection and characterization, *Journal of Applied Geophysics* **61**, 3–4, 217-226. <http://dx.doi.org/10.1016/j.jappgeo.2006.06.005>
- Islam, M. M., Meerschman, E., Saey, T., De Smedt, P., Van De Vijver, E., Delefortrie, S., et al., 2014. Characterizing compaction variability with an electromagnetic induction sensor in a puddled paddy rice field. *Soil Science Society of America Journal* **78**, 579–588. <http://dx.doi.org/10.2136/sssaj2013.07.0289>
- Keller, G.V., Frischknecht, F.C., 1966. *Electrical Methods in Geophysical Prospection*. International Series of Monographs in Electromagnetic Waves Volume 10. Pergamon Press, London.
- Landau, H., Chen, X., Klose, S., Leandro, R., Vollath, U., 2009. Trimble's RTK and DGPS Solutions in Comparison with Precise Point Positioning. In: Sideris, M.G. (Ed.), *Observing our Changing Earth* (pp. 709-718), Proceedings of the International Association of Geodesy General Assembly. Heidelberg, Berlin, Germany: Springer-Verlag.
- Lange, G., Seidel, K., 2007. Electromagnetic methods. In: Knodel, J., Lange, G.; Voigt, H.-J (Eds.): *Environmental geology, handbook of field methods and case studies*. Springer-Verlag, Berlin.
- Larsson, J., 2007. *Electromagnetics from a quasistatic perspective*. American Journal of Physics **75**: 230–239.
- Lavoué, F., van der Kruk, J., Rings, J., Andre, F, Moghadas, D., Huisman, J. A., Lambot, S., Weihermuller, L., Vanderborght, J., and Vereecken, H., 2010. Electromagnetic induction calibration using apparent electrical conductivity modelling based on electrical resistivity tomography. *Near Surface Geophysics* **8**, 553-561. <http://dx.doi.org/10.3997/1873-0604-2010037>
- Lesch, S.M., Rhoades, J.D., Lund, L.J., and Corwin, D.L., 1992. Mapping soil salinity using calibrated electromagnetic measurements. *Soil Science Society of America Journal* **56**: 540-548.

- Lundgren, J., 2010. Splinefit (www.mathworks.com/matlabcentral/fileexchange/13812-splinefit), MATLAB Central File Exchange. Retrieved November 11, 2013.
- Lunne, T., Robertson, P. K., and Powell, J. J. M., 1997. *Cone penetration testing in geotechnical practice*, pp. 45-145, Blackie Academic and Professional.
- Martinelli, H.P., Robledo, F.E., Osella, A.M., and de la Vega, M., 2012. Assessment of the distortions caused by a pipe and an excavation in the electric and electromagnetic responses of a hydrocarbon-contaminated soil. *Journal of Applied Geophysics* **77**: 21-29. <http://dx.doi.org/10.1016/j.jappgeo.2011.10.016>
- Mester, A., Zimmermann, E., van der Kruk, J., Vereecken, H., Van Waasen, S., 2014. Development and drift-analysis of a modular electromagnetic induction system for shallow ground conductivity measurements. *Measurement Science and Technology* **25**: 1-13. <http://dx.doi.org/10.1088/0957-0233/25/5/055801>
- Minsley, B. J., Smith, B. D., Hammack, R., Sams, J. I., and Veloski, G., 2012. Calibration and filtering strategies for frequency domain electromagnetic data. *Journal of Applied Geophysics* **80**, 56-66. <http://dx.doi.org/10.1016/j.jappgeo.2012.01.008>
- Moghadas, D., Andre, F., Bradford, J.H., van der Kruk, J., Vereecken, H., Lambot, S., 2012. Electromagnetic induction antenna modeling using linear system of complex antenna transfer functions. *Near Surface Geophysics* **10**, 237-247.
- Nielsen, M.L., 2012. Outlier detection and removal – Hampel (www.mathworks.com/matlabcentral/fileexchange/34795-outlier-detection-and-removal-hampel), MATLAB Central File Exchange. Retrieved November 11, 2013.
- Oldenburg, D.W., Li, Y., 1999. Estimating depth of investigation in DC resistivity and in-phase surveys. *Geophysics* **64**: 403-416.
- Oldenburg, D.W., Li, Y., 2005. Inversion for applied geophysics: A tutorial. In: D. K. Butler (ed.): *Nearsurface geophysics. Investigations in geophysics*. Society of Exploration Geophysicists.
- Pearson, R.K., 2002. Outliers in process modeling and identification. *IEEE Transactions on Control Systems Technology* [**1063-6536**] **10**, 55-63.
- Pérez-Ruiz, M., Carballido, J., Agüera, J., Gil, J.A., 2011. Assessing GNSS correction signals for assisted guidance systems in agricultural vehicles. *Precision Agriculture* **12**, 639-652. <http://dx.doi.org/10.1007/s11119-010-9211-4>

- Reynolds, J.M., 1997. An introduction to applied and environmental geophysics. Wiley & Sons, New York.
- Robertson, P. K., and Campanella, R. G., 1983. Interpretation of cone penetration test: part I (sand). *Canadian Geotechnical Journal* **20**, 1-44.
- Robinson, D.A., Lebron, I., Lesch, S.M., Shouse, P., 2004. Minimizing drift in electrical conductivity measurements in high temperature environments using the EM-38. *Soil Science Society of America Journal* **68**, 339-345.
- Saey, T., Simpson, D., Vermeersch, H., Cockx, L., Van Meirvenne, M., 2009. Comparing the EM38DD and Dualem-21S sensors for depth-to-clay mapping. *Soil Science Society of America Journal* **73**: 7-12.
- Saey, T., Van Meirvenne, M., Vermeersch, H., Ameloot, N., Cockx, L., 2009. A pedotransfer function to evaluate the soil profile textural heterogeneity using proximally sensed apparent electrical conductivity. *Geoderma* **150**(3-4): 389–395. <http://dx.doi.org/10.1016/j.geoderma.2009.02.024>
- Saey, T., De Smedt, P., Monirul Islam, M., Meerschman, E., Van de Vijver, E., Lehouck, A., Van Meirvenne M., 2012. Depth slicing of multi-receiver EMI measurements to enhance the delineation of contrasting subsoil features. *Geoderma* **189**: 514–521.
- Saey, T., Islam, M., M., De Smedt, P., Meerschman, E., Van De Vijver, E., Lehouck, A., et al., 2012. Using a multi-receiver survey of apparent electrical conductivity to reconstruct a Holocene tidal channel in a polder area, *Catena* **95**, 104-111. <http://dx.doi.org/10.1016/j.catena.2012.02.001>
- Santos, F.M., 2004. 1-D laterally constrained inversion of EM34 profiling data. *Geophysics* **56**: 123-134.
- Shah, S.D., Smith, B.D, Clark, A.K., and Payne, J.D., 2008. An integrated hydrogeologic and geophysical investigation to characterize the hydrostratigraphy of the Edwards aquifer in an area of northeastern Bexar County, Texas. U.S. Geological Survey Scientific Investigations Report 2008–5181, 26 p.
- Sheets, K.R., Hendrickx, J.M.H., 1995. Noninvasive soil water content measurement using electromagnetic induction. *Water Resources Research* **31**: 2401–2409.
- Sibson, R, 1981. A brief description of natural neighbor interpolation. In: V. Barnett (ed.): *Interpreting Multivariate Data*. John Wiley, Chichester.

- Siemon, B., 2007. Levelling of helicopter-borne frequency-domain electromagnetic data. *Journal of Applied Geophysics* **67**, 206-218.
- Simpson, D., Van Meirvenne, M., Lück, E., Bourgeois, J., Rühlmann, J., 2010. Prospection of Two Circular Bronze Age Ditches with Multi-Receiver Electrical Conductivity Sensors (North Belgium). *Journal of Archaeological Science* **37**: 2198-2206.
- Simpson, D., Van Meirvenne, M., Saey, T., Vermeersch, H., Bourgeois, J., Lehouck, A., Cockx, L., Vitharana, U.W.A., 2009. Evaluating the multiple coil configurations of the EM38DD and Dualem-21S sensors to detect archaeological anomalies. *Archaeological Prospection* **16**, 91-102.
- Smith, I.E., 2013. Hampel filter in C++ (www.mathworks.com/matlabcentral/fileexchange/40147-hampel-filter-in-c++), MATLAB Central File Exchange. Retrieved November 11, 2013.
- Speckmann, H., 2000. Providing measured position data for agricultural machinery. *Computers and Electronics in Agriculture* **25**, 87–106
- Spies, B.R., 1989. Effective depth of exploration in electromagnetic sounding methods. *Geophysics* **54**: 872–888.
- Spies, B.R., Frischknecht, F.C., 1991. Electromagnetic Sounding. In: Nabighian, M. N. (Ed.): *Electromagnetic methods in applied geophysics 2, part A*. Society of Exploration Geophysicists, Tulsa.
- Sudduth, K.A., Drummond, S.T., Kitchen, N.R., 2001. Accuracy issues in electromagnetic induction sensing of soil electrical conductivity for precision agriculture. *Computers and Electronics in Agriculture* **31**, 239-264
- Tabbagh, A., 1986. Applications and advantages of the Slingram electromagnetic method for archaeological prospecting. *Geophysics* **51**: 576-584.
- Tabbagh, A., Dabas, M., Hesse, A., Panissod, C., 2000. Soil resistivity: a non-invasive tool to map soil structure horization. *Geoderma* **97**, 393-404, [http://dx.doi.org/10.1016/S0016-7061\(00\)00047-1](http://dx.doi.org/10.1016/S0016-7061(00)00047-1)
- Telford, W. M., Geldart, L.P., Sheriff, R.E., 1991. *Applied Geophysics (2nd edition)*, Cambridge University Press, 1991.
- Thiesson, J., Kessouri, P., Schamper, C., and Tabbagh, A., 2014. Calibration of frequency-domain electromagnetic devices used in near-surface surveying. *Near Surface Geophysics* **12**, 481-491. <http://dx.doi.org/10.3997/1873-0604.2014012>

- Thiesson, J., Tabbagh, A., Simon, F.-X., Dabas, M., 2017. 3D linear inversion of magnetic susceptibility data acquired by frequency domain EMI. *Journal of Applied Geophysics* **136**: 165-177. <http://dx.doi.org/10.1016/j.jappgeo.2016.10.038>
- Triantafyllis, J., Ribeiro, J., Page, D., and Monteiro Santos, F.A., 2013. Inferring the Location of Preferential Flow Paths of a Leachate Plume by Using a Dualem-421 and a Quasi-Three-Dimensional Inversion Model. *Vadose Zone Journal*, **12**(2). <http://dx.doi.org/10.2136/vzj2012.0086>
- Wait, J.R., 1962. A note on the electromagnetic response of a stratified earth. *Geophysics* **27**: 382-385.
- Wait, J.R., 1982. *Geo-electromagnetism*. Academic Press, Inc., New York.
- Ward, S.H., Hohmann, G.W., 1987. Electromagnetic Theory for Geophysical Applications. In: M.N. Nabighian (ed.): *Electro-magnetic Methods. Applied Geophysics*, vol. 1: Society of Exploration Geophysicists.
- Ward, S.H., Hohmann, G.W., 1988. Electromagnetic theory for geophysical applications. *Electromagnetic Methods in Applied Geophysics* **1**: 131–311.
- West, G.F., Macnae, J.C., 1991. Physics of the electromagnetic induction method. In: M.N. Nabighian (Ed.), *Electromagnetic methods in applied geophysics 2, parts A and B*. Society of Exploration Geophysicists, Oklahoma.
- Zhang, Q., Qiu, H., 2004. A dynamic path search algorithm for tractor automatic navigation. *Transactions of the American Society of Agricultural Engineers* **47**, 639-464
- Zhdanov, M. S., 2010. Electromagnetic geophysics: Notes from the past and the road ahead. *Geophysics* **75** (5): A49-A66. <http://dx.doi.org/10.1190/1.3483901>

Curriculum vitae

1 Personal information

Name	Samuël Delefortrie
Date of birth	February 13th, 1987
Address	Hogepontstraat 22, 9050 Gentbrugge, Belgium
Email:	Samuel.Delefortrie@UGent.be
Tel.	0032(0)488.48.34.09

2 Education

2012-2017	PhD research Ghent University, Belgium
2008-2010	Master in Geology Ghent University, Belgium
2005-2008	Bachelor in Geology Ghent University, Belgium

3 Professional experience

Employers

2012-present	Research assistant Ghent University, Belgium
2011	Geologist ERM nv, Belgium
2010-2011	Project engineer ABO nv, Belgium

Teaching experience

2012-present	Undergraduate courses taught: Earth sciences at the Faculty of Bio-engineering
--------------	---

Professional Organization Memberships

SEG - Society of Exploration Geophysicists
 EAGE - The European Association of Geoscientists and Engineers
 SSSB - Soil Science Society of Belgium
 ISPA - International Society of Precision Agriculture

Selected FDEM surveys/projects

- | | |
|-----------|---|
| 2015-2017 | FDEM data processing for precision agriculture
Commissioned by: Vandenborne Aardappelen |
| 2016 | Geophysical surveys at Avebury
Project: Living with Monuments (Investigating landscapes of residence between the 4th and 2nd millennia BC in the Avebury region, Wiltshire) |
| 2014-2016 | Geophysical surveys at Wiltshire (United Kingdom)
Project: Reconstructing the prehistoric landscape of Stonehenge through electromagnetic induction survey (UGent/FWO) & Stonehenge Hidden Landscapes (LBI et al.) |
| 2013-2016 | Geophysical surveys at Damme and Bruges (Belgium)
Project: Medieval Bruges and its outer ports. A landscape archaeological contribution to the Zwin-debate |
| 2016 | Geophysical survey at Knokke-Heist (Belgium)
Project: Expansion works Zwin
Commissioned by: Aertssen NV |
| 2016 | Geophysical survey at Birmingham (United Kingdom)
Project: Assessing sub-aqueous layer thickness of a capping layer
Commissioned by: DCI NV |
| 2014 | Geophysical survey at Knokke-Heist (Belgium)
Project: Land management Ten Bogaerde - Koksijde
Commissioned by: Grontmij Belgium NV |
| 2012 | Geophysical survey at Werendijke (Netherlands)
Project: 'Gekrompen dorpen op Walcheren' (Vanished villages at Walcheren)
Commissioned by: Stichting Landschapsbeheer Zeeland |
| 2012 | Geophysical survey at Westkapelle (Belgium)
Project: Archaeological survey along the planned 'A11' highway at Westkapelle
Commissioned by: Raakvlak |
| 2012 | Geophysical survey at Raversijde (Belgium)
Project: 'Archeologische Atlas van de 2 Zeeën' (Archaeological atlas of the 2 Seas)
Commissioned by: VIOE (Flemish heritage institute) |

4 Scientific publications

Publications in ISI-annotated journals (A1)

- Saey, T., Verhegge, J., De Smedt, P., Smetryns, M., Note, N., Van De Vijver, E., Laloo, P., Van Meirvenne, M., **Delefortrie, S.**, 2016. Integrating cone penetration testing into the 1D inversion of multi-receiver EMI data to reconstruct a complex stratigraphic landscape. *Catena* **147**, 356–371.
- Trachet, J., **Delefortrie, S.**, Van Meirvenne, M., Hillewaert, B., De Clercq, W., 2016. Reassessing surface artefact scatters. The integration of artefact-accurate fieldwalking with geophysical data at Medieval harbour sites near Bruges. *Archaeological Prospection*.
- De Smedt, P., **Delefortrie, S.**, wyffels, F., 2016. Identifying and removing micro-drift in ground-based electromagnetic induction data. *Journal of Applied Geophysics* **131**, 14–22.
- Delefortrie, S.**, Saey, T., De Pue, J., Van De Vijver, E., De Smedt, P., Van Meirvenne, M., 2016. Evaluating corrections for a horizontal offset between sensor and position data for surveys on land. *Precision Agriculture* **17**(3), 349–364.
- Trachet, J., **Delefortrie, S.**, Dombrecht, K., Dumolyn, J., Leloup, W., Thoen, E., Van Meirvenne, M., et al., 2015. Turning back the tide: the Zwin debate in perspective: a historiographical review of the medieval port system northeast of Bruges. *Revue du Nord* **97**(413), 305–321.
- Van De Vijver, Ellen, Van Meirvenne, M., Vandenhoute, L., **Delefortrie, S.**, De Smedt, P., Saey, T., Seuntjens, P., 2015. Urban soil exploration through multi-receiver electromagnetic induction and stepped-frequency ground penetrating radar. *Environmental Science-processes Impacts* **17**(7), 1271–1281.
- Van De Vijver, Ellen, Van Meirvenne, M., Saey, T., **Delefortrie, S.**, De Smedt, P., De Pue, J., Seuntjens, P., 2015. Combining multi-receiver electromagnetic induction and stepped frequency ground penetrating radar for industrial site investigation. *European Journal of Soil Science*.
- Saey, T., De Smedt, P., **Delefortrie, S.**, Van De Vijver, E., Van Meirvenne, M., 2015. Comparing one- and two-dimensional EMI conductivity inverse modeling procedures for characterizing a two-layered soil. *Geoderma* **241-242**, 12–23.
- Saey, T., Van Meirvenne, M., De Smedt, P., Stichelbaut, B., **Delefortrie, S.**, Baldwin, E., Gaffney, V., 2015. Combining EMI and GPR for non-invasive soil sensing at the Stonehenge World Heritage Site: the reconstruction of a WW1 practice trench. *European Journal of Soil Science* **66**(1), 166–178.

- Delefortrie, S.**, De Smedt, P., Saey, T., Van De Vijver, E., Van Meirvenne, M., 2014. An efficient calibration procedure for correction of drift in EMI survey data. *Journal of Applied Geophysics* **110**, 115–125.
- Islam, M. M., Meerschman, E., Saey, T., De Smedt, P., Van De Vijver, E., **Delefortrie, S.**, Van Meirvenne, M., 2014. Characterizing compaction variability with an electromagnetic induction sensor in a puddled paddy rice field. *Soil Science Society of America Journal* **78**(2), 579–588.
- Saey, T., Van Meirvenne, M., De Pue, J., Van De Vijver, E., **Delefortrie, S.**, 2014. Reconstructing mole tunnels using frequency-domain ground penetrating radar. *Applied Soil Ecology* **80**, 77–83.
- Islam, M. M., Saey, T., De Smedt, P., Van De Vijver, E., **Delefortrie, S.**, Van Meirvenne, M., 2014. Modeling within field variation of the compaction layer in a paddy rice field using a proximal soil sensing system. *Soil Use and Management* **30**(1), 99–108.
- Saey, T., **Delefortrie, S.**, Verdonck, L., De Smedt, P., Van Meirvenne, M., 2014. Integrating EMI and GPR data to enhance the three-dimensional reconstruction of a circular ditch system. *Journal of Applied Geophysics* **101**, 42–50.
- Delefortrie, S.**, Saey, T., Van De Vijver, E., De Smedt, P., Missiaen, T., Demerre, I., Van Meirvenne, M., 2014. Frequency domain electromagnetic induction survey in the intertidal zone: limitations of low-induction-number and depth of exploration. *Journal of Applied Geophysics* **100**, 14–22.
- Mujinya Bazirake, B., Mees, P., Boeckx, P., Bodé, S., Baert, G., Erens, H., **Delefortrie, S.**, et al., 2011. The origin of carbonates in termite mounds of the Lubumbashi area, D.R. Congo. *Geoderma* **165**(1), 95–105.

Publications in non-ISI indexed, peer reviewed journals (A2)

De Smedt, Philippe, **Delefortrie, S.**, & Van Meirvenne, M., 2015. Good practice in high-resolution EMI data processing for archaeological prospection. *Archeologica Polona* **53**, 586–588.

Conference proceedings

Delefortrie, S., De Smedt, P., Gillings, M., Pollard, J., Green, M., 2016. Mining and interpreting archaeo-geophysical data through excavation: a case from prehistoric Knowlton (Dorset, UK). *Poster*. Presented at NSGG 2016.

Delefortrie, S., Saey, T., De Smedt, P., Van Meirvenne, M., 2016. Potential for reconstruction of the subsurface salinity distribution using the frequency domain electromagnetic method. *Near Surface Geoscience, Papers*. Presented at the Near Surface Geoscience 2016, European Association of Geoscientists and Engineers (EAGE).

Delefortrie, S., Hanssens, D., De Smedt, P., Van Meirvenne, M., 2016. Inversion of small-loop FDEM data using bathymetrical input to monitor a sub-aqueous layer. *Poster*. Presented at EMIW 2016.

Delefortrie, S., Saey, T., Van Meirvenne, M., 2015. Increasing positional accuracy of surveys: correcting for spatial offset and time lag. *Near Surface Geoscience, Papers*. Presented at the Near Surface Geoscience 2015, European Association of Geoscientists and Engineers (EAGE).